Investigating the impact of fires on atmospheric composition using reactive gas and aerosol assimilation

Timothy David Keslake

Submitted in accordance with the requirements for the degree of Doctor of Philosophy

The University of Leeds

School of Earth and Environment

September 2017

Declaration of Authorship

The candidate confirms that the work submitted is his/her own, except where work which has formed part of jointly-authored publications has been included. The contribution of the candidate and the other authors to this work has been explicitly indicated below. The candidate confirms that appropriate credit has been given within the thesis where reference has been made to the work of others.

Abstract

The European Centre for Medium-range Weather Forecasts' (ECMWF) Composition - Integrated Forecast System (C-IFS) provides global operational forecasts and re-analyses of atmospheric composition at high spatial resolution (~80 km). In this thesis the C-IFS system, with Global Fire Assimilation System (GFAS) emissions, is used to assess the impact of fires on tropospheric ozone and aerosol concentrations. The skill of the model and the impact of data assimilation is evaluated using independent aircraft, ground and satellite observations. In particular, observations from the 2012 South American Biomass Burning Analysis (SAMBBA) field campaign is used as a case-study. This work represents the first evaluation of trace gas observations from SAMBBA.

C-IFS simulations show that 4% of the total tropospheric column is produced by fire emissions, with significantly larger contributions closer to fire sources. Compared to both SAMBBA aircraft measurements and Ozone Monitoring Instrument (OMI) satellite data (0-6 km column) O_3 concentrations are underestimated in the tropics. Evaluation of precursor emissions show that this is due to a combination of NO_x flux underestimation in GFAS and the lack of a prescribed injection height, partly acting through a subsequent limited influence of PAN. Carbon monoxide, a tracer of biomass burning transport, is well captured by C-IFS implying that GFAS detects the majority of fires although the occurrence of small ones appears underestimated.

The assimilation of satellite reactive gas measurements from OMI, Measurements Of Pollution In The Troposphere (MOPITT) and the Microwave Limb Sounder (MLS) generally improved the C-IFS comparison against SAMBBA and other independent data. The O_3 tropospheric representation was improved by MLS assimilation but a significant negative bias against OMI (0-6 km column) remained. The chemical data assimilation impacts non-assimilated species such OH with increases up to 8% in the tropics. However, compared to observations this degraded the OH Northern/Southern hemisphere ratio and the impact of the OH change on other species was minimal.

Fires in C-IFS are shown to dominate the global carbonaceous aerosol budget during the tropical fire season. Aerosol concentrations are slightly underestimated by C-IFS compared to SAMBBA. The relative contribution of black carbon (BC) and organic matter (OM) is similar to that observed in the eastern savannah but the contribution of BC is overestimated in the western deforestation region. The use of the suggested ×3.4 GFAS scaling factor leads to a large positive bias in the model aerosol compared to SAMBBA. The assimilation of aerosol optical depth (AOD) generally decreases concentrations near fire-sources, due to this scaling, but still increases concentrations in remote regions. This suggests an inaccurate model loss of aerosol is a cause of the bias. The analysis/model bias used to characterise a more realistic local scaling factor which is shown to be different for BC and OM, and for AOD metrics compared to aerosol mass.

Acknowledgements

A huge thank you to my supervisors Martyn Chipperfield, Graham Mann and Johannes Flemming for all of their help and support. None of the work in this thesis would have been possible without your guidance.

Additionally, I would like to thank my colleagues involved with the Copernicus Atmosphere Modelling Service (CAMS) and South American Biomass Burning Analysis (SAMBBA). In particular thanks to Sam Remy and Eoghan Darbyshire who gave me access to data in advance and were always very helpful.

For funding my PhD, I am very grateful to National Centre for Earth Observation (NCEO) and the Natural Environment Research Council (NERC).

I am very thankful to all my friends and colleagues throughout ICAS and in particular the TOMCAT modelling group for sharing their vast computing and scientific knowledge and for all the work and non-work based discussions.. Particular shouts outs to Bob and STEWART JENNINGS, who had to put up with living with me over the last few years, and also to Joey and Leighton, all of whom have made the last few years both bearable and a great amount of fun.

A special thanks to Alice for all of her support over the last few years, for keeping me sane and believing in me when even I did not, I'm not sure this thesis would have been possible without you.

To my wonderful grandparents, thank you for feeding me and keeping me company during the last few months of hiding in Durham to write this thesis.

Thank you to my siblings, Andrew for keeping my spirits high when Sheffield Wednesday don't manage to, Jonathan for always being a martyr and Rachael for always keeping my ego down to earth.

Finally to my parents Julie and Graeme for all of their support and love both over the last four years and beforehand. You couldn't ask for a better family, thank you for everything

Contents

List of Figures

List of Tables

Acronyms

ADM	**AD**joint **M**odel
AOD	**A**erosol **O**ptical **D**epth
BBA	**B**iomass **B**urning **A**erosol
BC	**B**lack **C**arbon
CAMS	**C**opernicus **A**tmospheric **M**onitoring **S**ervice
CCN	**C**loud **C**ondensation **N**uclei
CTM	**C**hemical **T**ransport **M**odel
C-IFS	**C**omposition **I**ntegrated **F**orecast **S**ystem
DAS	**D**ata **A**ssimilation **S**ystem
ECMWF	**E**uropean **C**entre for **M**edium-Range **W**eather **F**orecasts
EDGAR	**E**mission **D**atabase for **G**lobal **A**tmospheric **R**esearch
FRP	**F**ire **R**adiative **P**ower
GFAS	**G**lobal **F**ire **A**ssimilation **S**ystem
IASI	**I**nfrared **A**tmospheric **S**ounding **I**nterferometer
IPCC	**I**ntergovernmental **P**anel on **C**limate **C**hange
JPL	**J**et **P**ropulsion **L**aboratory
MACC	**M**onitoring **A**tmospheric **C**omposition and **C**limate
MLS	**M**icrowave **L**imb **S**ounder

MODIS	**MO**derate **R**esolution **I**maging **S**pectroradiometer
MOPITT	**M**easurements **O**f **P**ollution **I**n **T**he **T**roposphere
NASA	**N**ational **A**eronautics and **S**pace **A**dministration
NPP	**N**et **P**rimary **P**roduction
NOAA	**N**ational **O**ceanic and **A**tmospheric **A**dministration
NWP	**N**umerical **W**eather **P**rediction
OC	**O**rganic **C**arbon
OM	**O**rganic **M**atter
OMI	**O**zone **M**onitoring **I**nstrument
PAR	**P**hotosynthetically **A**ctive **R**adiation
PBL	**P**lanetary **B**oundary **L**ayer
PDF	**P**robability **D**ensity **F**unction
RMSD	**R**oot **M**ean **S**quare **D**ifference
SAMBBA	**S**outh **AM**erican **B**iomass **B**urning **A**nalysis
SSA	**S**ingle **S**cattering **A**lbedo
TLM	**T**angent **L**inear **M**odel
VOC	**V**olatile **O**rganic **C**ompound

1 Introduction

1.1 Motivation

Biomass burning is the combustion of living and dead vegetation. Such fires have a significant impact on the earth system and influence ecosystems, the carbon cycle, land surface properties, atmospheric chemistry and aerosols (Bowman et al., 2009). The ignition of fires can occur both naturally from lightning strikes or as a result of anthropogenic interactions (Crutzen et al., 1979), such as forest clearance, agricultural nutrient recycling, pest control and grassland maintenance. These fires are caused by complex interactions between climate, vegetation and people which affect the amount of fuel available, the moisture content within the plant and the ignition of fires (Hantson et al., 2016). Fire records since 1998, established from satellite observations, show a correlation between high fire activity and areas with intermediate levels of net primary production (NPP) (G. R. Van Der Werf et al., 2010), as seen Figure 1.1. In turn NPP is heavily dependent on temperature and precipitation (Bistinas et al., 2014). Recent satellite data has shown a decreasing trend in fires since 2001 (Andela et al., 2017), which compares well to long-term sedimentary charcoal and ice-core measurements. These also indicate an increase in fires since the industrial revolution until 1870 when human-initiated land management is thought to decrease the amount of fires (Marlon et al., 2008; Power et al., 2007).

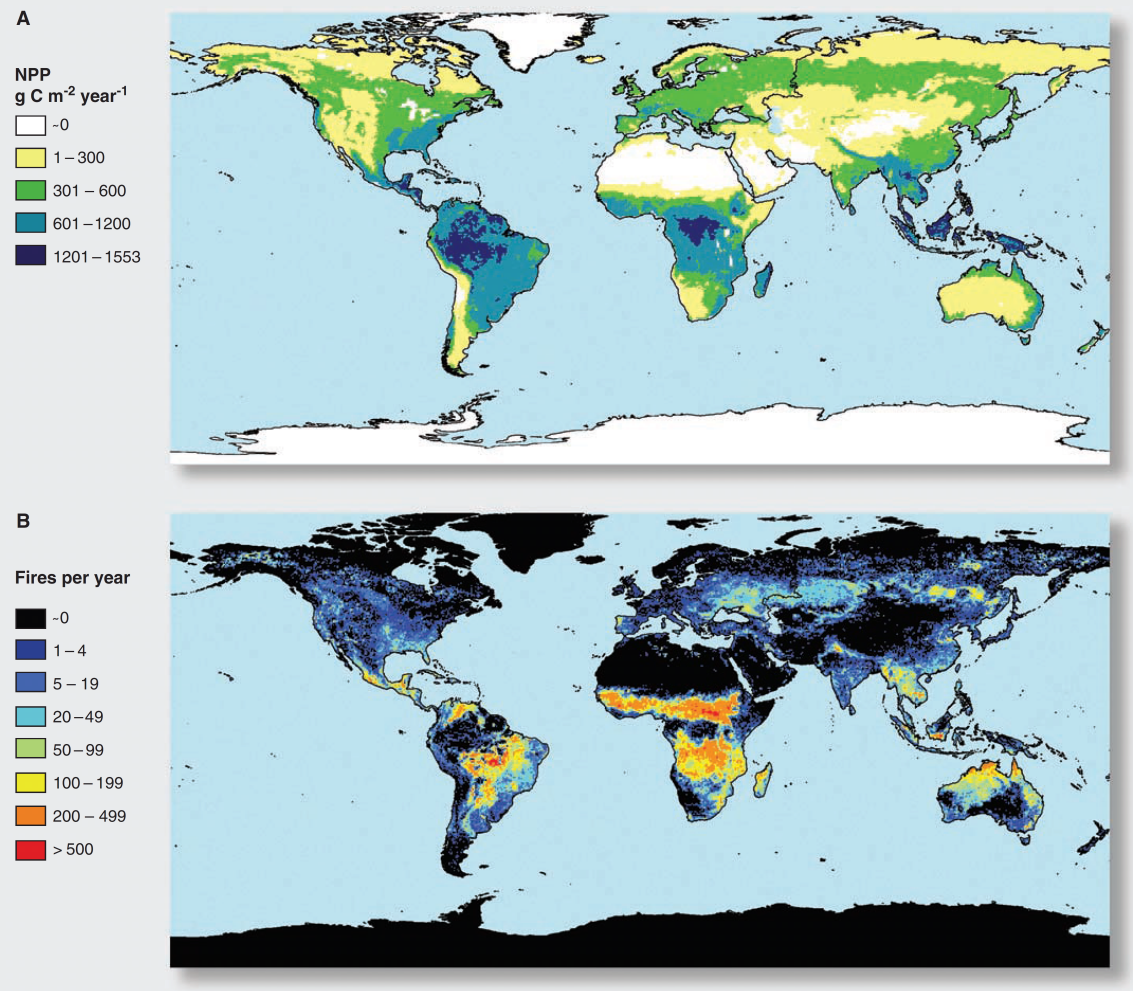

Figure 1.1 Current pyrogeography on Earth, illustrated by (A) net primary production (NPP, g C m^{-2} $year^{-1}$) from 2001 to 2006, on 1° grid cells; and (B) annual average number of fires observed by MODIS) (Bowman et al., 2009; Giglio et al., 2006).

Smoke produced by biomass burning can dominate regional atmospheric composition, influencing most radiative forcing components identified by the Intergovernmental Panel on Climate Change (IPCC) (Myhre et al., 2013). The amount and type of emitted species depends on the biomass type and the stage of combustion. Globally, fires are the second largest source of CO_2 (after fossil fuel combustion) with average emissions of 6.5-9.6 Pg $year^{-1}$ for 2002-2011 (Shi et al., 2015; Van Der Werf et al., 2010) and they also contribute 5% of total anthropogenic methane emitted into the atmosphere (Saunois et al., 2016). Fires are also a major source of ozone precursors, such as CO, NO_x and volatile organic compounds (VOCs) (Akagi et al., 2011; Andreae & Merlet, 2001; Crutzen et al., 1979). Consequently, observations predominantly show an increase in O_3 over fire-dominated

regions, with some boreal regions showing a decrease in O_3 concentrations from NO_x titration. A summary of previous near-fire O_3 observations can be found in Jaffe and Wigder (2012). Ozone has a significant impact on the troposphere acting as a greenhouse gas, contributing to the oxidative capacity of the atmosphere and affecting the concentration of the most important atmospheric oxidant OH (Seinfeld & Pandis, 2016). Surface ozone concentrations over 40 ppbv are known to impact human health and reduce photosynthesis rates by damaging plant stomata (Ainsworth et al., 2012).

Biomass burning is also a significant source of aerosol particles, which are characterised by large aerosol optical depths (AOD) leading to poor visibility. Smoke particles are composed of ~50-60% organic carbon (OC- mass of carbon in organic matter) and ~5-10% black carbon (BC) with approximately 80-90% of their volume in the accumulation mode (Reid et al., 2005). Due to this composition, the single scattering albedo (SSA), of biomass burning aerosol (BBA) particles lies close to the critical SSA, the point between net reflection and net absorption of sunlight (Haywood and Shine 1995). This is in contrast to fossil fuel emissions which have a much larger contribution of BC and are more absorbing. Globally changes in BBA since the pre-industrial period is thought to be relatively small with a combined direct radiative forcing of 0.03 Wm^{-2} (Figure 1.2). However, BBA have large aerosol radiative effects which strongly impact local radiation budgets in fire-dominated regions such as the Amazon and Central Africa (Osborne, Haywood, Francis, & Dubovik, 2004). BBA also impact the radiation budget indirectly through aerosol-cloud interactions as they form Cloud Condensation Nuclei (CCN) (Roberts et al., 2003). Local changes to the radiation budget can impact visibility, the photosynthetically active radiation (PAR), increase the diffuse fraction and impact photochemistry.

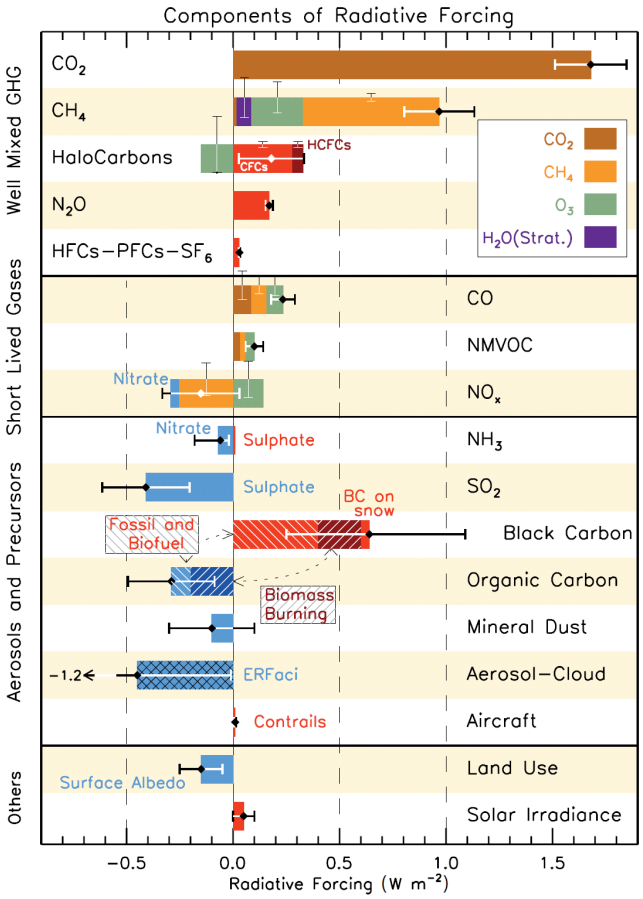

Figure 1.2 Radiative Forcing (RF) bar chart for the period 1750–2011 based on emitted compounds (gases, aerosols or aerosol precursors) or other changes. Red (positive RF) and blue (negative RF) are used for emitted components which affect few forcing agents, whereas for emitted components affecting many compounds several colours are used as indicated in the inset at the upper part the figure. The net impact of the individual contributions is shown by a diamond symbol and its uncertainty (5 to 95% confidence range) is given by the horizontal error bar. ERFaci is the effective radiative forcing (ERF) due to aerosol–cloud interaction and represents the net effect from changes of all aerosol types. BC and OC are co-emitted, especially for biomass burning emissions (given as Biomass Burning in the figure) and to a large extent also for fossil and biofuel emissions (given as Fossil and Biofuel in the figure where biofuel refers to solid biomass fuels). The vertical bars indicate the relative uncertainty of the RF induced by each component. Their length is proportional to the thickness of the bar, that is, the full length is equal to the bar thickness for a ±50% uncertainty (Myhre et al., 2013).

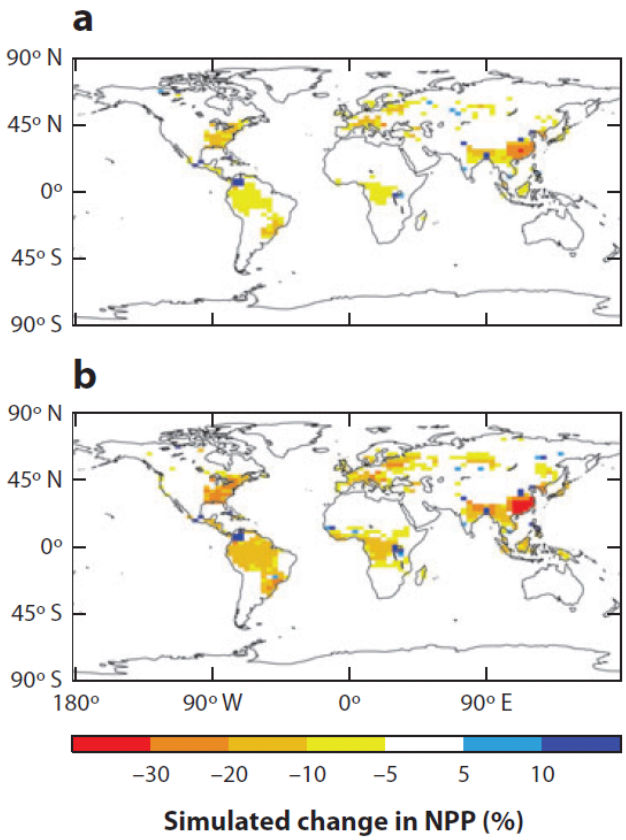

Figure 1.3 Simulated percentage change in net primary production (NPP) between 1901 and 2002 due to O_3 effects and considering changes in atmospheric CO_2 for (a) "lower" and (b) "high" O_3 plant sensitivity (Ainsworth et al., 2012).

Globally, in South America, and other tropical regions, human activities, such as deforestation, can increase the amount of fires, and as a result most tropical fire emissions are anthropogenic in origin. This is because tropical forests, in their natural state, rarely burn as moist conditions (prevalent beneath the forest canopy) act to suppress ignition, and in the dry season lightning strikes are rare (Cochrane, 2003). Amazonian fires predominantly occur during the August to October dry season and significantly change local atmospheric composition from its background conditions. In the dry season maximum, daily surface O_3 mixing ratios and aerosol mass concentrations reach values as large as 100 ppbv and 250 µg m^{-3}, compared to 12 ppb and 2.9 µg m^{-3} during the wet season (Artaxo et al., 2002, 2005; Kirkman et al., 2002). These composition changes are large enough to have an important impact on plant stomata health and PAR, altering the

local carbon budget. As seen in Figure 1.1, the Amazon is globally one of the most important regions for NPP, accounting for an estimated carbon sink of 1201-1553 g C m^{-2} $year^{-1}$, which has also been estimated to have decreased by 5-10% (depending on modelled plant sensitivity) due to O_3 between 1901 and 2002 (Ainsworth et al., 2012). Therefore, the fires in the Amazon, via the production of O_3 and by altering the radiation budget with BBA, can significantly impact the global carbon cycle by altering the NPP of one of the largest carbon sinks.

To investigate the impacts of biomass burning on atmospheric composition and the regional energy balance, and in-turn the global carbon cycle, accurate observations of emitted species are necessary. The SAMBBA (South AMerican Biomass Burning Analysis) consortium, consisting of 7 university partners, collected ground, aircraft and satellite measurements of BC, Organic Matter (OM-total mass of organic aerosol), NO_2, NO, CO and O_3 over the Amazon for the 2012 wet and dry season for both savannah and tropical fires. The main aims of the consortium were to improve our understanding of biomass burning emissions, challenge and improve the latest aerosol process models and satellite retrievals and assess biomass burning impacts on the Amazonian biosphere. Significant model work has previously be done using the SAMBBA observations, particularly focussing on the composition and impact of BBA on the radiative budget (Archer-Nicholls, Lowe, Schultz, & McFiggans, 2016; Johnson et al., 2016; Marenco et al., 2016; Reddington et al., 2016). However, there has only been limited use of O_3 and related precursor emissions to evaluate model predictions, a key aim of this thesis.

Due to the large spatial and temporal variability in biomass burning events, the monitoring and forecasting of their impacts on atmospheric composition are usually quantified by satellite data. Different satellite products relating to burned area, thermal anomalies (Giglio et al. 2006) or Fire Radiative Power (FRP) (Martin J. Wooster, Roberts, Perry, & Kaufman, 2005) are related to the dry matter flux and consequently, via emission factors (Andreae & Merlet, 2001; Akagi et al. 2011), to species emitted from fires. These emission datasets tend to produce relativity accurate emissions for common fire tracers such as CO (Andela et al., 2013; G. R. Van Der Werf et al., 2010; Wiedinmyer et al., 2010) but often fail to accurately capture other species, e.g. aerosols (Huijnen et al., 2012; J. W. Kaiser et al., 2012; Rémy et al., 2016) which are under predicted by

models. Models both with satellite-derived and bottom-up inventories have also failed to reproduce observed increase in O_3, which is thought to be due to the large number of O_3 precursors emitted from fires, the impact of aerosols on photochemistry and uncertainty in radical production (Jaffe & Wigder, 2012; Pacifico et al., 2015b; Parrington et al., 2013). In this study, emissions from the Global Fire Assimilation System (GFAS) (Kaiser et al., 2012) are used where FRP observed from MODIS satellites is used to calculate emission factors and ratios (Wooster et al. 2003 and 2005).

In this study, we combine the satellite data used in the GFAS fire emissions with composition data assimilation, to provide 'best-estimates' of atmospheric composition during the tropical fire season. Data assimilation (DA) is the process of combining observations with a numerical model in order to correct both the inherent bias in the model and the spatial limitations of the observations. This technique has a long history in meteorology and is used to produce best estimates of the current state of the atmospheric system, called an analysis, from which future forecasts are run (Bergthórsson & Döös, 1955; Bouttier, Miller, Hortal, & Isaksen, 2001; Lorenc, 1986). More recently DA has been expanded to the composition of the atmosphere with a focus on air quality forecasts, re-analysis of the past atmosphere and emission inversions (Hollingsworth et al., 2008; Miyazaki et al., 2015; Sandu & Chai, 2011). During the GEMS (Hollingsworth et al., 2008), Monitoring Atmospheric Composition and Climate (MACC) (Inness et al., 2013) and Copernicus Atmospheric Monitoring Service (CAMS) (Flemming et al., 2015) projects ECMWF's Integrated Forecasting System (IFS) data assimilation suite was expanded to include atmospheric composition elements. This included chemically reactive species (O_3, CO, NO_X and HCHO) (Flemming et al., 2009; Inness et al., 2013), greenhouse gases (CH_4 and CO_2) (Engelen, 2009) and aerosols (Benedetti et al., 2009; Morcrette et al., 2009). Global composition datasets from the CAMS system can provide a potential wealth of data on a range of atmospheric species. However, the accuracy of these huge datasets needs to be evaluated.

Composition analysis datasets have been shown to improve comparisons against long-term independent observations from satellites and ground sites (Inness et al., 2013; Flemming et al., 2015). However, there is limited evaluation against detailed in-situ observations from field campaigns, and particularly from regions involving large

deviations from background conditions e.g. fire emissions and volcanic eruptions. Additionally, by constraining one or more fields in a model, through assimilation, other fields can be modified via subsequent reactions or feedbacks. Therefore, the use of analysis fields provides an opportunity to test and further understand the physical and chemical laws of evolution used by the models (Sandu & Chai, 2011) as well as to update key air quality and climate metrics (Miyazaki et al., 2015). This study adds to the work previously done under GEMS, MACC and CAMS and uses both the GFAS-derived emissions and the collection of assimilated observations in C-IFS observations (CO, O_3, NO_2 and AOD) to create a 'best-estimate' of modelled fire emissions to be evaluated by SAMBBA observations. By doing this we can help describe the influence of fire on atmospheric composition, identify areas of model bias by highlighting key areas of model/satellite divergence and test operational assimilated datasets against in-situ SAMBBA observations.

1.2 Thesis aims

The overall aim of this PhD thesis is to assess and improve our understanding of the influence of fire emissions on the atmosphere through the combination of modelled atmospheric fields, composition satellite products and in-situ observations. To achieve this, the state-of-the-art ECMWF 4D-var data assimilation system has been used, and has been evaluated with SAMBBA composition data for the Amazon hence supporting the modelled aims of the SAMBBA flight campaign. The specific research questions of this thesis are:

- **What is the impact of fire emissions on ozone concentrations and aerosol composition?** In-situ observations of black carbon, organic carbon (OC), nitrogen oxides (NO_x) and ozone (O_3) from SAMBBA will be used to evaluate Composition-IFS (C-IFS) reactive gas and aerosol properties. With knowledge of potential limitations, the analysis can be used to quantify global and regional impacts of fires on ozone production and carbonaceous aerosol composition. The accuracy of different parameters, aerosol schemes and emissions will be tested using C-IFS sensitivity simulations.

- **How does the assimilation of global reactive gases (CO, O_3 and NO_2) change (improve or degrade) the representation of chemical fields inside a global model?** The impact of assimilation on a range of chemical species within the C-IFS model will be assessed and quantified. Through comparisons with independent observations, the extent to which assimilation improves the representation of chemical fields will be determined. The potential changes to other key species, not assimilated in the analysis, via chemical and physical coupling will also be investigated, providing information on the accuracy of the model's chemical schemes. From the analysis, best estimates of assimilated and non-assimilated fields and key metrics will be calculated and compared to other model studies.

- **How does assimilation of AOD change aerosol properties within a global model?** Through comparison with speciated aerosol mass observations (BC and OM), whether the representation of individual aerosol species in the model are improved by AOD assimilation will be investigated. Changes in different fire-dominated regions and non-fire dominated regions will be analysed. Additionally, the impact of AOD assimilation on the radiation scheme and hence the photolysis rates of reactive gases will be explored.

1.3 Thesis layout

The thesis is organised as follows. Chapter 2 contains a literature review and general background covering the impact of fire emissions on atmospheric composition. This includes trends in fire emissions, different types of fires, impacts of emissions and photochemistry in fire plumes. Chapter 3 describes the different models and observations used in this thesis while also discussing data assimilation of atmospheric composition.

Chapters 4 and 5 discuss the evaluation of both model and analysis fields against in-situ SAMBBA observations, for reactive gas and aerosol fields respectively. This includes the quantification of the amount of O_3 produced by the model and the ratio of OM to BC, both key factors in determining the impact of fire emissions on the earth system. Chapter

6 discusses the impact of assimilation on a global scale, particularly focussing on the impact of assimilation on other non-assimilated species. Finally, Chapter 7 summarises the result of the thesis, synthesises overall conclusions and makes suggestions for future work.

2 Biomass burning and the atmosphere

2.1 Motivation

This chapter aims to give a general background on the interaction between biomass burning and atmospheric composition. Section 2.2 details the physical structure of the atmosphere and briefly describes transport processes that impact atmospheric composition. Section 2.3 explores the role of fire in the earth system, describes recent trends in biomass burning emissions and explores the impacts of humans and climate on emission. Section 2.4 describes the different species emitted from biomass burning into the atmosphere and describes their role in air quality and climate. Subsections 2.4.1-2.4.3 describe general distribution of fire emissions, both horizontally and vertically, while exploring how emissions are considered in atmospheric transport models. Subsections 2.4.5-2.4.7 describe short-lived trace gas emissions emitted from fires, namely CO, VOCs and NO_x. Section 2.4.8 describes ozone formation and Section 2.4.9 describes aerosol emissions.

2.2 Structure of the atmosphere

An atmosphere is a layer of gas surrounding a planet that is held in place by the planetary body. The atmosphere of earth is commonly known as air, which maintains the planet's ability to sustain life. By volume, earth's dry air atmosphere is predominantly made up of nitrogen (78%), oxygen (21%) and argon (0.93%). The atmosphere also contains variable amounts of water vapour, which is as high as 1% at the surface but with a mean value of 0.4% of the entire atmosphere. Other gases which make up a smaller contribution in the atmosphere are known as trace gases, and although they have relatively small atmospheric concentrations, they play a large role in determining the earth's climate and can significantly impact the biosphere. A detailed description of the physical structure of the atmosphere can be found in (Seinfeld & Pandis, 2016).

2.2.1 Vertical structure

Atmospheric pressure is the term given to the force exerted by the weight of the atmosphere above any measurement point, this decreases exponentially with altitude as there is less overlying atmospheric mass. The temperature of the atmosphere has a more complex structure, with reversals of the temperature gradient classifying the atmosphere into five distinctive vertical layers, each with different compositions as well as physical and chemical properties, which can be seen in Figure 2.1.

The troposphere is the lowest region of the atmosphere containing 85% of its total mass. In the troposphere temperature decreases with height, until the upper bound of the troposphere known as the tropopause. The altitude of the tropopause is highly dependent on latitude and season, sitting around 8-18 km above the earth's surface. Close to the surface is a section of the troposphere called the planetary boundary layer (PBL), which extends upwards to a couple of kilometres. This region is characterised by rapid and turbulent atmospheric mixing due to the warming from the planet and the orography of the surface. Emissions from biomass burning mostly impact the lower troposphere, with the majority of fire plumes not penetrating beyond the PBL.

The stratosphere sits above the troposphere and is characterised by temperature increasing with altitude due to the absorption of solar radiation by ozone. The stratosphere temperature profile creates very stable atmospheric conditions and so lacks the weather producing turbulence of the troposphere. Above the stratopause (~50 km) temperature once again decreases with altitude in a section called the mesosphere, although the temperature gradient is not as steep as the troposphere. Just below the mesopause (80-85 km), the mesosphere is the coldest place on Earth with an average temperature of 188 K. The thermosphere sits above the mesopause where temperatures rise sharply again up to 500-2000 K due to strong solar absorption of UV radiation by the main atmospheric constituents N_2 and O_2.

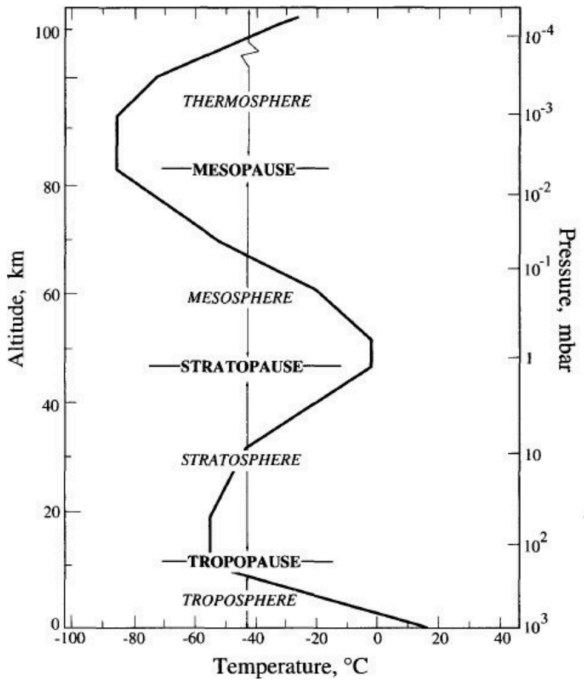

Figure 2.1 Vertical structure of the atmosphere subdivided by changes in the temperature gradient (Seinfeld & Pandis, 2016).

2.2.2 Transport

Advection

Advection is the transport of a substance by bulk motion, which in the atmosphere is the large-scale transport of air known as wind. Wind is the flow of air from high pressure areas to lower pressure and is responsible for most of the large-scale transport of air around the globe. Advection is responsible for the transport of trace gases away from their source.

Convection

Convection is responsible for the rapid vertical transport of air in the atmosphere. Free convection occurs due to the solar heating of the earth's surface, which causes a vertical air density gradient known as a thermal, which forces air to rise. Due to the temperature

dependence of free convection, its effect is generally greatest in tropical latitudes, with decreasing effects towards the poles. Forced convection can occur for a number of reasons. It may be due to the orography of the land surface, weather fronts or the convergence of horizontal winds, which causes air to rise.

2.3 Fire in the earth system

The earth is a flammable planet with carbon-rich vegetation, atmospheric oxygen (between 13-30% of atmospheric concentrations is required for burning), seasonally dry climates and widespread lighting and volcanic ignition events (Bowman et al., 2009). Fires have burnt ecosystems on earth since the first appearance of plants on land 420 million years ago (Scott & Glasspool, 2006). As such, fires are a natural part of the earth system sustaining biodiversity and accelerating the natural cycle of net primary production and respiration. Fire can be seen as a key component of floral evolution, with different global fire regimes promoting the growth of different plant types, to an extent that fire has been described as the 'global herbivore'(W. J. Bond & Keeley, 2005). Despite natural fire patterns and regimes, large or catastrophic fires can devastate local wildlife and human populations.

Fires on earth need a source of ignition, combustible material to burn and favourable weather to spread. These factors are driven by complex interactions between climate, vegetation and people (Hantson et al., 2016). Attributing the impact of these various influences on fires has been difficult due to their complex interaction with one another and the inability to observe and fully comprehend the extent of the fire system, until the modern satellite era.

2.3.1 Distribution and diversity

Recent advancements in satellite technology have enabled studies on the global scale of fires, their distribution and their impact. Two different earth observation approaches have been used in attempt to estimate the amount of fuel biomass combusted. One is to measure the amount of area burned by a fire and the other is to directly measure the fire-emitted energy. Measurements of overall thermal emissions rate integrated over all wavelengths

and angles, so called Fire Radiative power (FRP), is used in this thesis to estimate the amount of fuel biomass emitted. Within the GFAS emission data set FRP is estimated using observation of thermal radiation around 3.8 and 11µm wavelengths (Wooster et al., 2005).

The global mean distribution of fires for 2000 to 2005 is shown in Figure 2.2, in terms of fire radiative power (FRP). FRP is a quantitative. The majority of biomass burning events occur in the tropics, although studies have shown the impact of boreal regions (Goode et al., 2000). In terms of average regional combustion budget [Tg(C) yr^{-1}] during 2003-2008, Africa dominates with 44%, with 17% from South America, 11% from North Asia and about 28% distributed around the rest of the world (J. W. Kaiser et al., 2012).

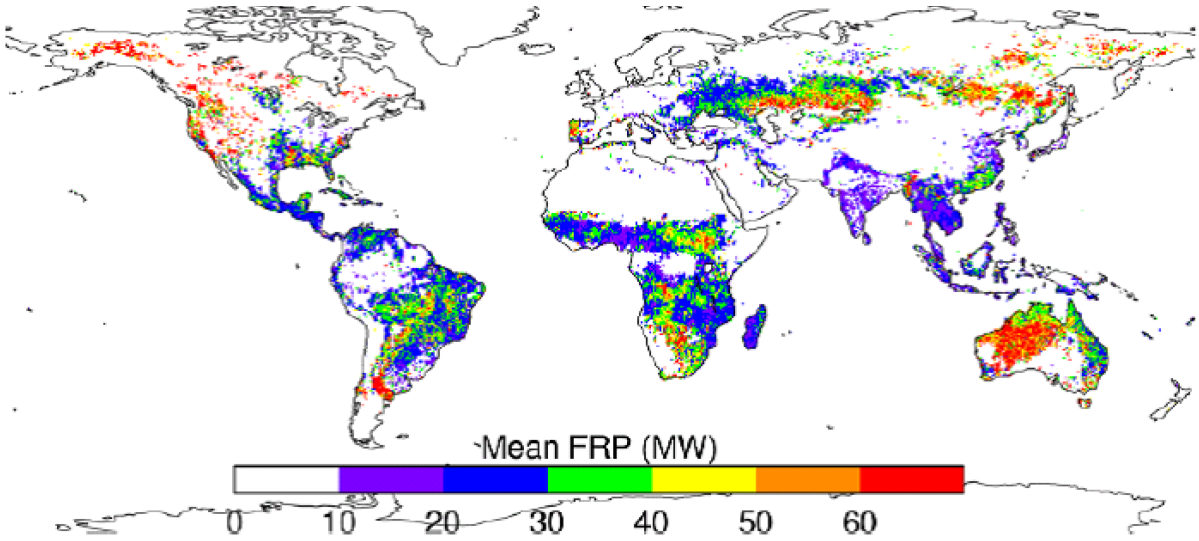

Figure 2.2 Mean annual fire radiative power (FRP) for Terra MODIS (November 2000 to October 2005) (Louis Giglio et al., 2006).

Analysing fire trends using satellite records has shown a correlation between high fire activity and areas with intermediate levels of both net primary production (NPP; 500-100 g C m^{-2} yr^{-1}) and precipitation (1000-2000 mm yr^{-1}) (Van Der Werf et al., 2008). This is due to dry environments having low NPP, indicating little plant growth, and therefore limited fuel available to burn while wet environments, despite having high NPP, being too wet to ignite and burn. Seasonality plays a large role as areas with varying seasonal

climates can accumulate ‘fuel’ in the wet season before ‘drying-out’ and burning in the dry season. Along with precipitation and gross primary production (GPP), temperature also influences fires due to its impact on GPP and by determining how quickly the vegetation dries.

Fires burn with different intensities and frequencies, leading to many diverse effects on the earth system. To capture this diversity ‘fire regimes’ are used to group fire types based on a range of variables including vegetation type, ignition and local climate. In terms of human-controlled ‘fire regimes’ there exists two different types: deforestation and agricultural (Bowman et al., 2009). Deforestation fires are classified as the permanent destruction of forests or woodlands in order to produce timber or make land available for urbanisation, crop and pastoral farming. Agricultural fires or stubble burning is the burning of crop residue after grains have been harvested.

Wildfires are generally classed by biome and meteorological conditions with the most important examples including grassland, savannah, woodland, forest and peat fires. Savannah vegetation is classified as a mixed ecosystem of woodland and grassland with an open canopy allowing an unbroken herbaceous surface area. Woodland vegetation is a small area of trees with around 40% canopy closure (60% or more of the sky is visible). The term ‘forest’ is generally reserved for a relativity large area of trees with a dense canopy (as low as 20% in some definitions) (Thomas & Packham, 2007). Peat fires is the burning of peat soil, a semi-fossilised accumulation of partially decayed vegetation or organic matter which is highly flammable, once ignited by surface fuel combustion peat can smoulder and can burn undetected under the underground peat layer, becoming particularly difficult to extinguish. Peat fires are thought to be the largest under-sampled biomass burning source and primarily occur in boreal and tropical forests, especially in Indonesia and Malaysia (Stockwell et al., 2016). The recent burning of peat bogs in Indonesia during the 2015 El Nino, emitting 11.3 Tg CO_2 per day, exceeding the fossil fuel emissions of the European Union (EU 28) (8.9 Tg CO_2 per day) (Huijnen et al., 2016).

The distribution of these different fire regimes is shown in Figure 2.3. Burnt area datasets, produced by MODIS for 2001-2009 show that of the 2.0 Pg C yr^{-1} produced by fires, most carbon emissions were from grasslands and savannas fires (44%) with smaller contributions from tropical deforestation and degradation fires (20%), woodland fires (mostly confined to the tropics, 16%), forest fires (mostly in the extratropics, 15%), agricultural waste burning (3%), and tropical peat fires (3%) (G. R. Van Der Werf et al., 2010). These values indicate that wildfires are responsible for 70% of global biomass burned annually. However, agricultural fires are most likely underestimated in this analysis; they are relativity small and are difficult to pick up on the native 500-metre resolution of MODIS. A recent study using the geostationary satellite, Himawari-8 Advanced Himawari Imager (AHI) over Asia, detected more small agricultural fires than MODIS, due to both its greater resolution and 144 observation opportunities a day compared to 4 (Xu et al., 2017).

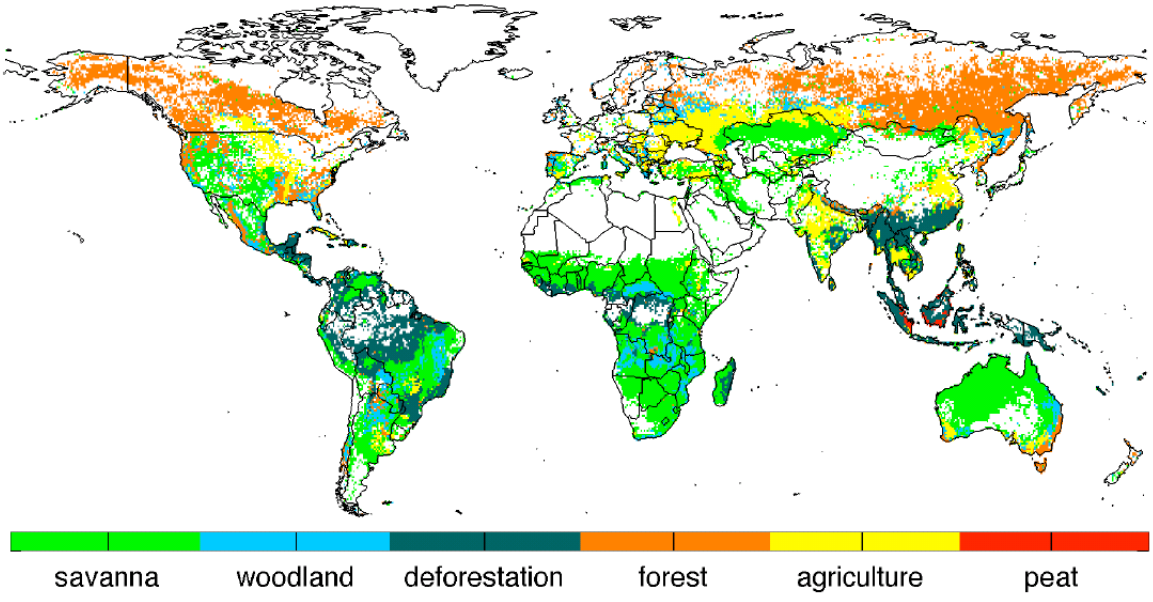

Figure 2.3 Dominant fire type in each 0.5° grid cell based on carbon emissions. Savannah fires include grassland fires; deforestation includes degradation. Woodland and savannah fires were separated based on the relative contribution from woody or herbaceous fuels to total emissions, respectively (G. R. Van Der Werf et al., 2010).

2.3.2 Climate and human drivers

Trends in fire emissions over the past millennia have been assumed from global sedimentary charcoal record, formed from lake sediments and peats (Marlon et al., 2008; Power et al., 2007), and from Antarctic ice-core measurements of CO, O_3 and their isotopic ratios (Wang, et al., 2008). Results from both datasets are summarised in Figure 2.4. Large variations are seen in the degree of biomass burning over the past 800 years, with precipitation being the main driver (Marlon et al., 2008). After the industrial revolution in 1750, both charcoal and CO concentrations increase, indicating that climate change and increasing temperatures was the primary driver of fire activity during this time period. This was the case until 1870 where a decline in biomass burning is observed until the end of each record, which is opposite to the expected effect of rising CO_2. This time period does coincide with a large increase in population growth suggesting that human activities in the industrial era have reduced biomass burning through agricultural expansion, increased pastoral land use and active fire management which are all thought to reduce biomass burning.

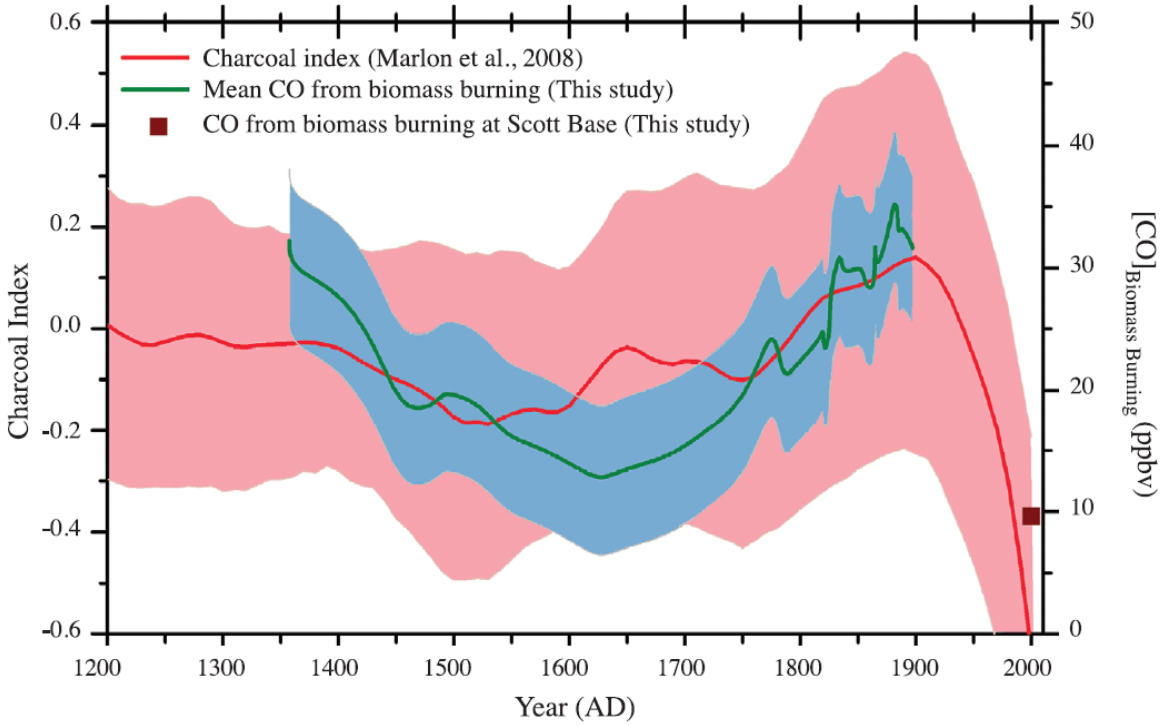

Figure 2.4 Correlation between the derived CO from biomass burning (green line) and the sedimentary charcoal record compilation in the tropics (30°N-20°S) (red line). The

red shaded area represents charcoal index measurement uncertainties. The blue shaded area represents divergent scenario run results and uncertainties. Also shown is the MOZART-4 simulated CO from biomass burning emission at Scott Base for the modern atmosphere (Marlon et al., 2008; Wang et al., 2008).

Trends in burnt area from 1998 to 2015, derived from MODIS (MODerate-resolution Imaging Spectroradiometer) are shown in Figure 2.5. During this time period, after removing inter-annual variability from precipitation, there was a 24% reduction in global burnt area (Andela et al., 2017), supporting the decreases seen in the charcoal and ice-core datasets. The majority of this decrease is thought to be down to change in livestock density and cropland area rather than just population increase. This is likely a consequence of fire suppression to protect crops, livestock, homes, infrastructure and air quality (M. A. Moritz et al., 2014). Conversely, these activities, by expanding crop and pasture areas through deforestation, increase fire activity in and around tropical rainforests, which in their natural state rarely burn due to moist conditions beneath the canopy and the rarity of dry lightning (Cochrane, 2003). In regions less dominated by land management, wild fires are still driven by increasing temperature attributed to climate change (Bowman et al., 2009).

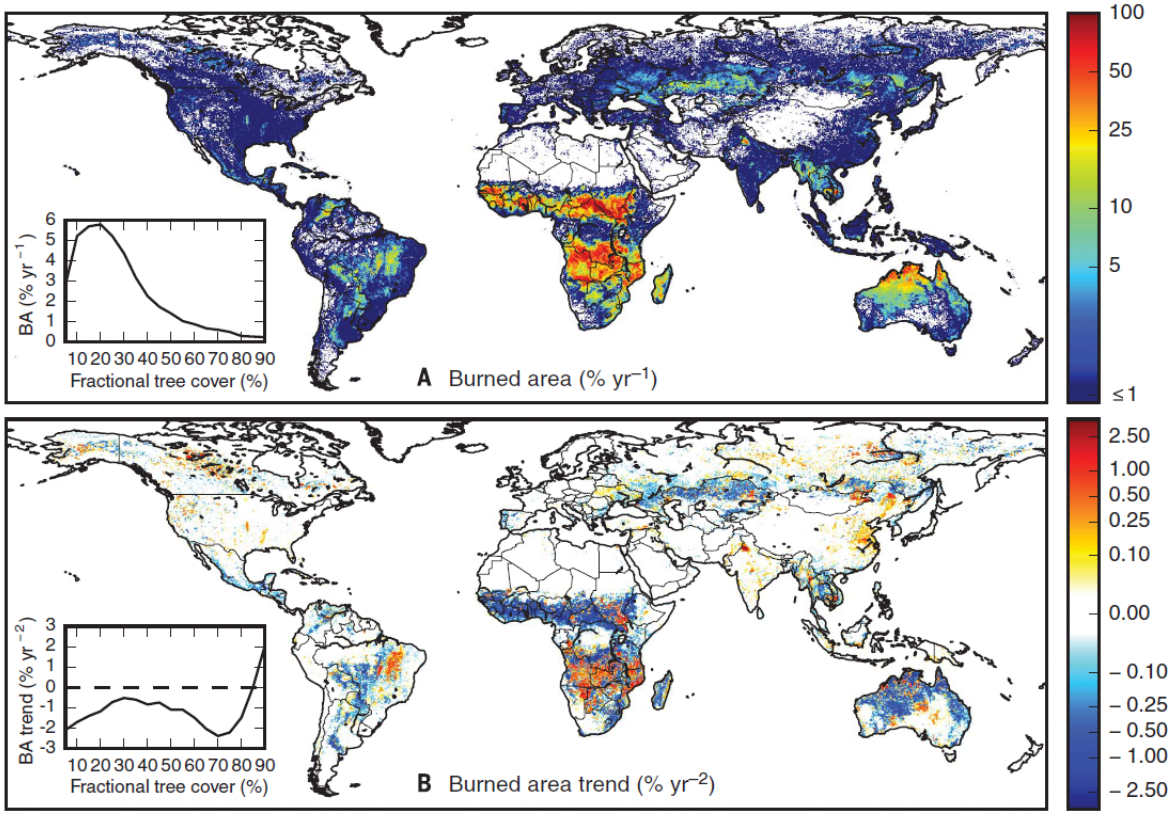

Figure 2.5 Satellite observations showing the global trend in fire activity. (A) Mean annual burned area and (B) trends in burned area (GFED4s, 1998 through 2015). Line plots (inset) indicate global burned area and trend distributions by fractional tree cover (Andela et al., 2017).

The importance of GPP, precipitation and temperature to wildfires means that climate is an important driver of fire inter-annual variability. Changes in rainfall and the length of the dry season both influence fires. An increase in rainfall or decrease in length of the dry season decreases the amount of area burnt on short timescales, but can lead to an increase in area burnt in subsequent years, due to a build-up of vegetation (Archibald et al., 2010). Climate modes, such as the El Nino-Southern Oscillation (ENSO), significantly impact precipitation and length of the dry season. During the La-Nina phase of ENSO fire occurrence increases in the south United States and Argentina, while in the El Nino phase a marked increase is observed in tropical rainforests. Drought years associated with

ENSO events devastate large number of forests worldwide (Saatchi et al., 2013; Swetnam et al., 1990), with 20 million ha burned in Latin America during the 1997-1998 El Nino event.

Future climate scenarios suggest an increasing risk of fires as an impact of rising temperature from climate change (Pechony & Shindell, 2010), particularly due to increasing length of fire seasons (Jolly et al., 2015). However, fire models, used to predict the future fires, do not currently capture the influence of socio-economic development on fire dynamics, meaning current trends in fires, driven by fire suppression in agricultural and pastoral regions, may continue (Andela et al., 2017). A sharp decrease in fire activity, while significant in counteracting the short-term impact of fires on humans and ecosystems , the reduction in this key ecological disturbance allows the build-up of fuel making some areas more vulnerable to future catastrophic fires (Moritz et al., 2012). Increases in large-scale fires have already been seen, instigated by strong ENSO years, in Indonesia, Australia, United States and Portugal over the last couple of years, the intensity and frequency of which is larger than the previous fire record.

2.4 Impacts and emissions of fires

Fires can have a significant impact on the carbon cycle and climate change by emitting carbon dioxide, the main compound produced by any combustion process of organic material. Biomass burning is also a major source of chemical species which react on much shorter timescales such as nitrogen oxides, carbon monoxide and volatile organic compounds (VOCs), which is particularly the case in tropical regions (Crutzen et al., 1979). These species also lead to the production of ozone and as such can impact net primary production, human health and the oxidation capacity of the atmosphere (Jaffe & Wigder, 2012; Monks et al., 2009). Carbonaceous aerosols are also emitted from biomass burning, directly impacting air quality and both local and global radiative properties (Reid et al., 2005).

2.4.1 Process of combustion and emission

The composition of fuel as well as the chemical and physical processes during the combustion process, determine the various constituents of smoke. The carbon content of fuels shows limited variability between biomes and as such the emission of different hydrocarbons is largely determined by the combustion process. The emissions of minor substances e.g. nitrogen, sulfur and halogens, is determined by the concentrations of these elements in the fuel. Vegetation material is generally made up of cellulose, hemicelluloses, lignin, proteins, nucleic acids and amino acids. With minerals making up approximately 10% of volume and controlling the emissions of many trace species. The water content, which can account for 60% of the total mass, determines fire propagation and the extent of combustion.

The different stages of combustion- ignition, glowing, flaming and smouldering- emit different species (Lobert & Warnatz, 1993). Ignition stage refers to the small-scale ignition of fires by an external source or adjacent burning biomass. After ignition, thermal degradation, dries the plant emitting water and volatile contents, this is followed by temperature-caused cracking called pyrolysis which produces gaseous material which feed the flame. When temperatures exceed 350 K, the process becomes exothermic, further increasing temperatures at ~800 K glowing combustion begin, producing more complex mix of tar and gas products, which diluted in the air, form a flammable mixture. Flaming combustion occurs when this mixture ignites converting C, H, N and S in the fuel into highly oxidised molecules such as CO_2, H_2O, NO_x and SO_2 (Akagi et al., 2011). After most volatiles have been released, flaming combustion ceases and smouldering combustion begins. This phase corresponds to a gas-solid reaction between oxygen and carbon at the fuel layer with temperatures above 850 K. Due to the chemisorption of O_2 on tar, rather than a deficiency in O_2, smouldering emits large amounts of incompletely oxidised products such as CO, CH_4, NMVOC (non-methane VOC) and primary organic aerosol and is generally the mode of combustion with the largest diversity of emissions (Yokelson et al., 1997).

Vegetation fires are typically dynamic and due to a moving fire front, most of these combustion processes are present at any given time. The combustion efficiency (CE)- the fraction of fuel carbon converted to CO_2- can be used to determine the relative

contribution of flaming and smouldering fires (Sinha et al., 2003). Flaming tends to dominate emissions early on with smouldering becoming increasing more important with time. Smouldering combustion can last for weeks after ignition, meaning emission studies might not capture the full breadth of fire activity and might be biased towards flaming combustion. However, the majority of emissions take place within ~4-8 hours of ignition, limiting this bias (Ward et al., 1992). Modified combustion efficiency (MCE) is often used instead of CE (MCE= CO_2 /(CO + CO_2)), with values generally between 0.8 and 1, fires with MCE values closer to 0.8 represent a higher proportion of smouldering fires while values approaching 1.0 represent fires becoming increasingly more dominated by flaming combustion (Jaffe & Wigder, 2012).

2.4.2 Emission factors and fire emissions

Two different metrics are commonly used to measure concentrations of trace species emitted during different biomass burning regimes, each relating emissions of each trace species to a reference measurement. Emission ratios relate the emission of a particular species to that of a reference species, normally CO_2 or CO during smouldering combustion. Alternatively, the emission ratio can be determined via a regression slope between the two species. Emission factors use the mass of a species emitted (M_x) to the amount of dry fuel combusted ($M_{biomass}$) expressed in units of g kg^{-1}. Calculation of this parameter requires knowledge of the carbon budget of the fire which can be assumed by adding measured concentrations of CO_2, CO, hydrocarbons and particulate carbon. The emission factor can be expressed as seen in equation 2.1, where (M_c) is the mass of carbon emitted.

$$EF_x = \frac{M_x}{M_{biomass}} = \frac{M_x}{M_c}[C]_{biomass} \qquad (2.1)$$

Table 2.1 shows emission factors for key species from each biome, collected from multiple different studies compiled in (Andreae & Merlet, 2001) and subsequently updated in (Akagi et al., 2011). Emission factors where used as the key metric in both these studies as it provides the most direct estimation of gas and aerosol released per

amount of biomass burned, where fuel and residue data is not available a fuel carbon content of 45% was assumed to derive emission factors from ratios.

Biomass burning and the atmosphere

Species	Tropical forest	Savanna	Crop residue	Pasture maint.	Boreal forests	Temporal forest	Extratropical forests
Carbon Dioxide (CO_2)	1643 (58)	1686 (38)	1585 (100)	1548 (142)	1489 (121)	1637 (71)	1509 (98)
Carbon Monoxide (CO)	93 (27)	63 (17)	102 (33)	135 (38)	127 (45)	89 (32)	122 (44)
Methane (CH_4)	5.07 (1.98)	1.94 (0.85)	5.82 (3.56)	8.71 (4.97)	5.96 (3.14)	3.92 (2.39)	5.68 (3.24)
Acetylene (C_2H_2)	0.44 (0.35)	0.24 (0.10)	0.27 (0.08)	0.21 (0.29)	0.18 (0.10)	0.29 (0.10)	0.19 (0.090)
Ethylene (C_2H_4)	1.06 (0.37)	0.82 (0.35)	1.46 (0.59)	1.28 (0.71)	1.42 (0.43)	1.12 (0.35)	1.38 (0.42)
Ethane (C_2H_6)	0.71 (0.28)	0.66 (0.41)	0.91 (0.49)	0.95 (0.43)	1.79 (1.14)	1.12 (0.67)	1.70 (1.05)
Ethylene (C_2H_4)	1.06 (0.37)	0.82 (0.35)	1.46 (0.59)	1.28 (0.71)	1.42 (0.43)	1.12 (0.35)	1.38 (0.42)
Ethane (C_2H_6)	0.71 (0.28)	0.66 (0.41)	0.91 (0.49)	0.95 (0.43)	1.79 (1.14)	1.12 (0.67)	1.70 (1.05)
Propylene (C_3H_6)	0.64 (0.43)	0.79 (0.56)	0.68 (0.37)	0.85 (0.66)	1.13 (0.60)	0.95 (0.54)	1.11 (0.61)
Isoprene (C_5H_8)	0.13 (0.056)	0.039 (0.027)	0.38 (0.16)	0.12 (0.055)	0.15	–	0.15
Benzene (C_6H_6)	0.39 (0.16)	0.20 (0.084)	0.15 (0.04)	0.70 (0.32)	1.11	–	1.11
Toluene ($C_6H_5CH_3$)	0.26 (0.13)	0.080 (0.058)	0.19 (0.06)	0.34 (0.15)	0.48	–	0.48
Methanol (CH_3OH)	2.43 (0.80)	1.18 (0.41)	3.29 (1.38)	5.84 (3.42)	2.82 (1.62)	1.93 (1.38)	2.70 (1.75)
Phenol (C_6H_5OH)	0.45 (0.088)	0.52 (0.36)	0.52 (0.14)	1.68 (3.34)	2.96	0.33 (0.38)	2.60 (3.00)
Formaldehyde (HCHO)	1.73 (1.22)	0.73 (0.62)	2.08 (0.84)	1.90 (1.11)	1.86 (1.26)	2.27 (1.13)	1.92 (1.14)
Acetaldehyde (CH_3CHO)	1.55 (0.75)	0.57 (0.30)	1.24 (0.28)	2.40 (1.08)	–	–	–
Acetone (C_3H_6O)	0.63 (0.17)	0.16 (0.13)	0.45 (0.07)	1.05 (0.47)	0.75	–	0.75
Acetyl ($C_3H_6O_2$)	1.13 (0.12)	0.45 (0.24)	3.77 (0.91)	6.18 (5.60)	–	–	–

Formic Acid (HCOOH)	0.79 (0.66)	0.21 (0.096)	1.00 (0.49)	0.20 (0.64)	0.57 (0.46)	0.35 (0.33)	0.54 (0.47)
Acetic Acid (CH_3COOH)	3.05 (0.90)	3.55 (1.47)	5.59 (2.55)	10.4 (6.8)	4.41 (2.66)	1.97 (1.66)	4.08 (2.99)
Hydrogen Cyanide (HCN)	0.42 (0.26)	0.41 (0.15)	0.29 (0.38)	0.46 (0.45)	1.52 (0.82)	0.73 (0.19)	1.41 (0.60)
Ammonia (NH_3)	1.33 (1.21)	0.52 (0.35)	2.17 (1.27)	1.47 (1.29)	2.72 (2.32)	0.78 (0.82)	2.46 (2.35)
Hydrogen (H_2)	3.36 (1.30)	1.70 (0.64)	2.59 (1.78)	–	–	2.03 (1.79)	2.03 (1.79)
Sulfur Dioxide (SO_2)	0.40 (0.19)	0.48 (0.27)	–	0.32 (0.14)	–	–	–
Nitrogen Oxides (NO_x as NO)	2.55 (1.40)	3.9 (0.80)	3.11 (1.57)	0.75 (0.59)	0.90 (0.69)	2.51 (1.02)	1.12 (0.69)
PM 2.5	9.1 (3.5)	7.17 (3.42)	6.26 (2.36)	14.8 (6.7)	15.3 (5.9)	12.7 (7.5)	15.0 (7.5)
PM10	18.5 (4.1)	–	–	28.9 (13.0)	–	–	–
Black Carbon (BC)	0.52 (0.28)	0.37 (0.20)	0.75	0.91 (0.41)	–	–	0.56 (0.19)
Organic Carbon (OC)	4.71 (2.73)	2.62 (1.24)	2.3	9.64 (4.34)	–	–	8.6–9.7

Table 2.1 Emission factors (g kg^{-1}) for species emitted from different types of biomass burning, brackets indicating estimates of natural variation (Akagi et al., 2011).

Three different satellite-based emission datasets use emission factors derived from either (Akagi et al., 2011) or (Andreae & Merlet, 2001), combing them with MODIS fire products, to produce global datasets of fire emissions on daily timescales. These data sets include: Global Fire Emissions Database version 3 (GFED3; (G. R. Van Der Werf et al., 2010)), the National Center for Atmospheric Research Fire Inventory version 1.0 (FINN1; (Wiedinmyer et al., 2010)) and the Global Fire Assimilation System version 1.0 (GFAS1; (J. W. Kaiser et al., 2012)).

GFED provides daily mean fire emissions from 2003 at 0.5◦ × 0.5◦ resolution. Fire emissions are estimated from burnt area time series from Giglio et al., 2010 containing a 500 m burned areas mapping algorithm based on a burn sensitive vegetation index, active-fire detections and plant productivity from MODIS imagery. Total carbon emissions are then calculated using the Carnegie–Ames–Stanford–Approach biogeochemical model. These carbon emission fluxes can then be used, by re-arranging equation 2.1., to calculate trace gas and aerosol emissions using emission factors

FINN provides daily mean fire emissions from 2003 at 1 km × 1 km resolution. MODIS Thermal Anomalies Product (Giglio et al., 2003) is used to determine the location and timing of fires while MODIS Land Cover Type product is used to specify land cover classes. The emissions of a certain species E_i is estimated using equation 2.2.

$$E_i = A(x,t) \times B(x) \times FB \times ef_i \qquad (2.2)$$

With *A(x, t)* being the burned area at time *t* and location *x*, *B* the biomass loading fraction, *FB* the fraction of biomass that is burnt by the fire, and ef_i the emission factor for the species.

GFAS provides daily fire emission since 2001 at 0.5◦ × 0.5◦ resolution. GFAS uses the NASA fire product MOD14, a quantitative observation of the fire radiative power, which has been linked to the combustion rate (Martin J. Wooster et al., 2005) of fire. Fires are observed by the satellite in terms of Watt for each satellite system, before being aggregated onto the 0.5◦ × 0.5◦ resolution global grid. A drawback of using FRP is that thermal radiation cannot penetrate clouds, thus limiting the observations to cloud-free areas. This is accounted for by assuming the same FRP areal density throughout the grid cell. Additionally, a Kalman filter data assimilation system fills in observation gaps by assuming FRP persistence in past observations. FRP is converted to the combustion rate of dry matter using land-specific data based on GFED. Emissions are then calculated as they are in GFED.

Biomass burning and the atmosphere

A key difference between the emission datasets is that GFED and GFAS both use an older compilation of emissions from Andreae & Merlet, 2001, while FINN uses the updated Akagi et al., (2011). Akagi et al., (2011) benefits from 10 more years of observations and studies of emission factors, with new avaliable technology to quantify both new and old species more accurately.

GFED fire emissions are known to underestimate contributions from smaller fires due to the 500 m detection limt of the MODIS global burned area product (G. R. Van Der Werf et al., 2010). Thermal anomalies from small fires (smaller than 100 ha) can be picked up meaning emissions datsasets that use active fire measuremnts (GFAS and FINN) will capture fires more accurately than GFED. Part of GFAS ability to detect small fires is limited by the need to use GFED data to calculate dry matter. Additionally, FINN assumes much larger burnt area for individual agricultural fires than GFED and GFAS in order to compensate for missing fire detections. Field data and retrievels of fire radiative power show that the majority of fires are smaller, particularly in tropical regions, suggesting that burned area estimeas from MODIS proably underestimate global burned area (Schultz & Wooster 2008).

Measurements of FRP are also generally limited to cloud-free regions, and are affected by the time of satellite overpass and obstructions of line-of-sight to the fire, for example if fires occur underneath the forest canopy (Kaiser et al., 2012). This can lead to biases in fire emissions in some regions of the globe (Andela et al., 2013). Comparisons of different emissions datasets during the 2012 SAMBBA campaign showed that FRP-derived emissions showed lower fluxes over deforestation regions compared to bottom-up inventories while providing higher concentrations over the eastern savannah dominated and soybean farming regions (Pereira et al., 2016).

2.4.3 Vertical distribution of emissions

Energy emitted from the intense burning of biomass results in heating of the local ambient air, increasing convection and creating a rising plume which transports smoke emissions away from the surface. The variability of the heat flux from fires (due to fire size, type and meteorological conditions) and different ambient atmospheric conditions (stability and humidity) makes the manner in which fire emissions are injected into the atmosphere highly variable. The height at which emissions are injected into the atmosphere significantly impacts their longevity, chemical conversion and fate (Freitas et al., 2006). Of particular importance is whether smoke constituents are released below or above the planetary boundary later (PBL).

Factors which control plume dynamics are shown in Figure 2.6 and include: the buoyancy flux inducted by the heat flux, the size of the combustion zone that interacts with the atmosphere, atmospheric stratification (e.g. height of the planetary boundary layer), degree of turbulent mixing causing entrainment/detrainment, the wind shear and the latent heat realised from the condensation of water (Paugam, et al., 2016).

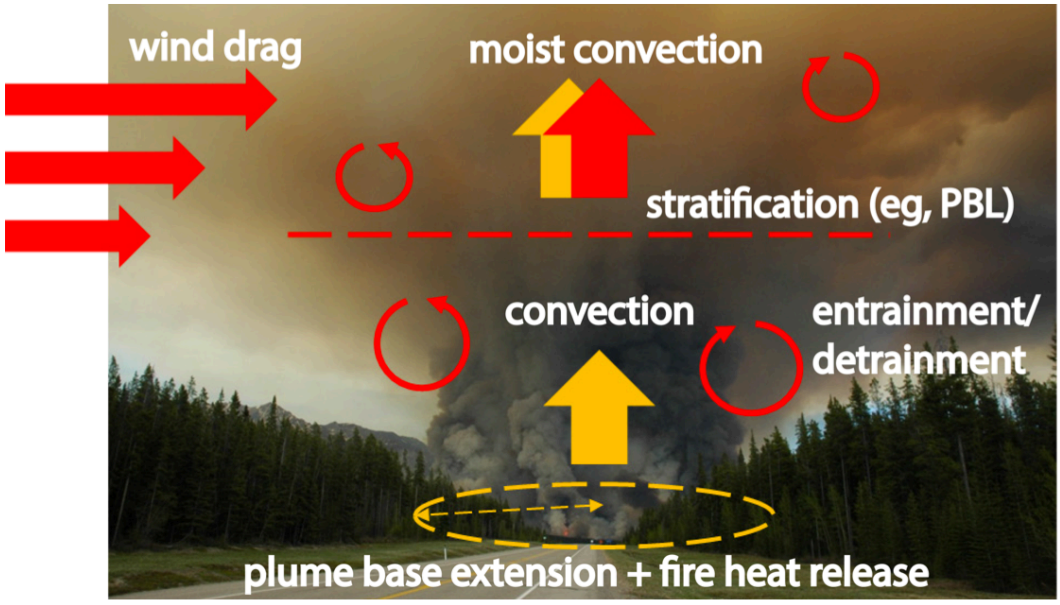

Figure 2.6 Schematic view of the physical processes involved in fire plume dynamics. Red and yellow labels indicate atmospheric and fire-induced mechanisms respectively (Paugam, et al., 2016).

Biomass burning and the atmosphere

Satellite data can be used to estimate smoke plume height. The two most commonly used instruments are the Cloud-Aerosol Lidar with Orthogonal Polarization (CALIOP) on board CALIPSO and the Multi-angle Imaging Spectro-Radiometer (MISR) on the TERRA satellite. Both datasets suggest that the majority of detected plumes are trapped in the planetary boundary layer, but the fraction of plumes that are injected above the PBL is dependent on geographical location and land cover type (Martin et al., 2010).

A number of studies have implied that atmospheric models misrepresent emission transport due to little or no representation of plume injection height. Many different plume injection height parameters exist and are discussed in Paugam, et al., (2016). However, apart from simulations based on single plume events, modelling injection height is still difficult, leading to inaccuracies in modelling emission transport. This is due to the necessity for both accurate fire emissions and local atmospheric conditions, which is difficult in a large-scale atmospheric model.

2.4.4 Carbon dioxide and methane

According to the 2013 IPCC report, combined CO_2 emissions from wildfires/biomass, are approximately 1-2 Gt C yr^{-1} (Bellouin, Quaas, Morcrette, & Boucher, 2013). Tropical biomass burning dominates the total carbon emissions. If climate and fire regimes equilibrate, the CO_2 emissions are counter-balanced by the regrowth or regeneration of vegetation. Deforestation fires, which relate to vegetation burning for land use do not contribute to this re-growth and are a net-source of CO_2 (Achard et al., 2002). Deforestation and land use change, are estimated to have released 180 Gt C between 1750 and 2011, which has also lead to an increase in land surface albedo, RF of -0.15 [-0.25 to -0.05] W m^{-2}. Fires are also a major source of methane, the second most important greenhouse gas.

Methane has a significant role in atmospheric chemistry: it is a strong infrared absorber, second most important greenhouse gas, influences tropospheric OH concentration and directly affects stratospheric ozone chemistry. Biomass burning is the third largest source for CH_4, contributing about 40 Tg yr^{-1} to the global emission rate.

2.4.5 Carbon monoxide

Colourless, odourless and poisonous, carbon monoxide is one of the major air pollutants. Carbon monoxide is the second most abundant species emitted during the combustion of both biomass burning and fossil fuels. It is either emitted directly during combustion or produced in-situ by oxidation of methane or other volatile organic compounds (e.g. isoprene, terpenes).

CO is often used as a tracer for transport processes of pollution due to its relatively well-known chemistry and large departure from background conditions (compared to CO_2). Its intermediate lifetime (~2 months), longer than volatile compounds and aerosols emitted from fires but shorter than for example CH_4, makes CO traceable as it travels between continents (Koppmann et al., 2005).

Impacts

The main sink for CO in the atmosphere is its reaction with OH radicals, with soil uptake and transport into the stratosphere being minor routes. Reaction (2.5) shows the production of HO_2 from this main sink and why CO is a dominant species in determining tropospheric HO_2/OH partitioning. In turn, CO is the primary sink of tropospheric OH and helps form O_3, therefore having a significant impact on the oxidising capacity of the troposphere. (Forster et al. 2007). CO can influence the global radiative forcing directly by absorbing and emitting infrared wavelengths between 1800-2300 cm^{-1}. However, studies have shown this is relatively small compared to the global average forcing (Evans and Puckrin, 1995) (Sinha and Toumi, 1996). More importantly, CO can affect the global radiative forcing indirectly by chemically altering the abundance of other radiatively active gases, notably CH_4, O_3 and CO_2 (Daniel and Solomon, 1998).

$$HCHO + hv \rightarrow 2HO_2 + CO \quad (2.3)$$

$$HCHO + OH \rightarrow HO_2 + CO \quad (2.4)$$

$$CO + OH \xrightarrow{O_2} CO_2 + HO_2 \quad (2.5)$$

Biomass burning and the atmosphere

Sources and trends

The Measurements of Pollution in the Troposphere (MOPITT) on board the EOS-TERRA satellite is the longest running satellite sensor measuring atmospheric CO globally, observing since 2000 using both thermal infrared and near infrared (NIR) (Deeter et al., 2003). The simultaneous use of NIR and TIR provides greater sensitivity to the lower troposphere, which is a common limitation of other instruments (e.g. TES and IASI).

A review of global emissions inventories of CO for 1980 to 2010 (Claire Granier et al., 2011) suggest that anthropogenic emissions (500-600 Tg yr^{-1}) are the main source of CO with relatively stable emissions for the time period. The second largest source was biomass burning (300-600 Tg yr^{-1}), which showed greater variability and determines interannual variability. Natural or background concentrations of surface CO, observed by MOPITT, are around ~100 ppb, with concentrations around ~300-400 ppb observed in urban (Clerbaux et al., 2008) and fire-dominated regions (Edwards et al., 2004). Figure 2.7 shows how CO concentrations have been decreasing since the start of the MOPITT record, even in highly polluting areas such as China (Worden et al., 2013). Decreases in anthropogenic and biomass burning emissions sources are considered the most likely cause for this decline (Jiang et al., 2017), although trends in OH may also play a role.

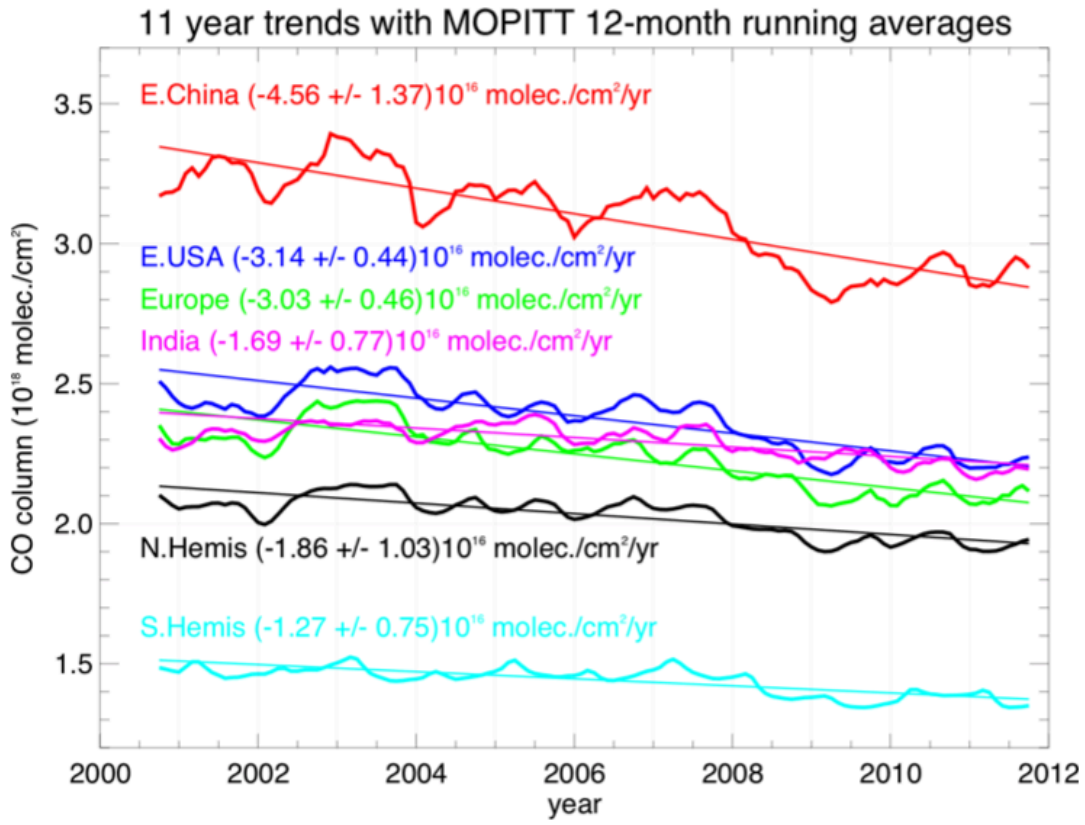

Figure 2.7 MOPITT 11-yr regional trends in total CO column change per year. Regional time series with 12-month running average and corresponding linear trends are indicated by the different colours, with slope and 1σ error given in molecules/cm^2 yr^{-1} (Worden et al., 2013).

Emissions from biomass burning

As a major carbon species emitted from fire , there are sufficient surface measurements of CO available to provide some confidence in calculated emission factors for each fire type Andreae & Merlet, 2001. In the update of emission factors in Akagi et al., (2011), there was only minor changes to CO with smaller factors associated with boreal forests and larger factors from agricultural residue.

A comparison of the three daily fire emission inventories is shown in Figure 2.8 (Andela et al., 2013). Generally, GFAS and GFED show similar concentrations, apart from where

small fires dominate and GFAS has higher concentrations than GFED, with FINN having even higher values still (e.g. agriculture and deforestation). The impacts of the different emission factors in Akagi et al., (2011) can also be seen in the agricultural and boreal regions. The largest differences however, are for fires associated with Savannah and peat. Peat fires are treated differently in the three inventories as estimating dry matter burned is particularly inaccurate for peat fires. While the assumed fire size of FINN (0.75 km^2) is probably too small for the humid savannah region (Reddington et al., 2016).

GFED and GFAS emissions in C-IFS were compared to MOPITT and IASI total columns where the model captured the seasonal and inter annual variability of CO, although negative biases were seen in boreal region and a positive bias in Northern Africa. Huijnen et al., 2012 evaluated that during the Russian fire episode of 2010 GFAS CO fire emissions gave good consistency with MOPITT observations, unlike aerosol species emitted by fires.

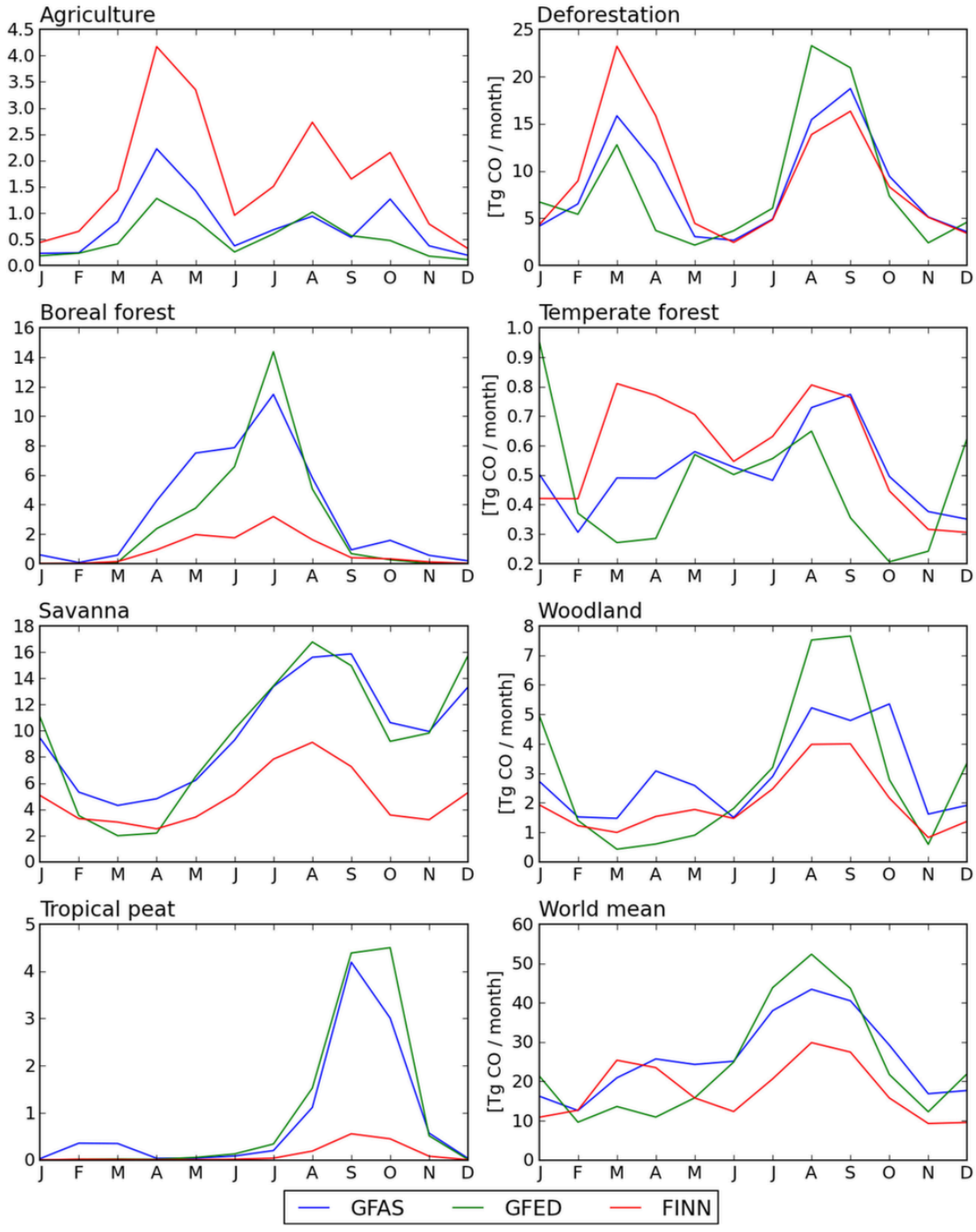

Figure 2.8 Mean seasonal CO emissions for 7 biomes associated with dominant fire type in GFED (see *Figure 2.3*) and the world mean for 2003 until 2011. Emissions are shown for three different fire emission inventories: GFAS, GFED and FINN (Andela et al., 2013).

2.4.6 Other hydrocarbons

Due to the thermal cracking of vegetation multiple different NMVOC (non-methane organic carbon) species have been identified in fire plumes. Observations of smoke plumes have identified over 90 individual NMOC compounds in smoke, with around 60-80% of total emission being oxygenated volatile organic compounds (OVOCs), a range of oxygen-containing vapour-phase atmospheric organics with an impact on atmospheric chemistry, particularly O_3 formation. Examples of OVOCs produced in biomass burning events include methanol, formaldehyde, acetaldehyde, acetone, acetonitrile, formic acid and acetic acid. However, there is still significant uncertainty on the molecular form of many of the oxygenated compounds (Warneke et al., 2011).

In emission inventories the sum of non-identified NMOCs is often give with emission factors in Akagi et al., 2011 of 51.9, 24.7, 58.7 and 23.7 g kg^{-1} of fuel for tropical forests, savannah, boreal and temperate forests, respectively. A large amount of work is still required to identify OVOCs in fire plumes and quantify the contribution of each different species.

2.4.7 Nitrogen oxides

NO_X is a general term for the nitrogen oxides most relevant for atmospheric chemistry, air quality and climate, namely nitric oxide (NO) and nitrogen dioxide (NO_2). Nitrogen oxides have a large influence on tropospheric chemistry, due to their influences on tropospheric ozone (see Section 2.4.8) (Jaffe and Wigder, 2012), the hydroxyl radical (OH) and the formation of nitrate aerosol. It is also significant in terms of air quality not only as a toxic gas –exceeding 200 μg/m^3- but also as a marker for other pollutants relating to combustion such as PM, benzene and O_3 (World Health Organization, 2006). The lifetime of NO_x is on the order of hours to days and is dependent on numerous factors including OH concentrations and hydrocarbons, temperature, humidity and sunlight (Lamsal et al., 2010). Due to the short lifetime of NO_x and the spatial inhomogeneity of its emissions, its concentrations vary significantly in the troposphere.

Photochemistry

A summary of tropospheric NO_x chemistry is shown in Figure. Reactions (2.6-2.8) show the photochemical NO_x null cycle, which controls O_3 formation/destruction in the troposphere, where $O(^3P)$ is the ground electronic state of the oxygen atom. The photochemistry of O_3 is discussed in more detail in Section 2.4.8. At night reaction 2.6 cannot occur and a consequent oxidation of NO_2 by O_3 can occur to produce NO_3, an important night-time oxidant.

$$NO_2 + h\nu \rightarrow NO + O\ (3P) \quad (2.6)$$

$$O(3P) + O_2 + M \rightarrow O_3 + M \quad (2.7)$$

$$NO + O_3 \rightarrow NO_2 + O_2 \quad (2.8)$$

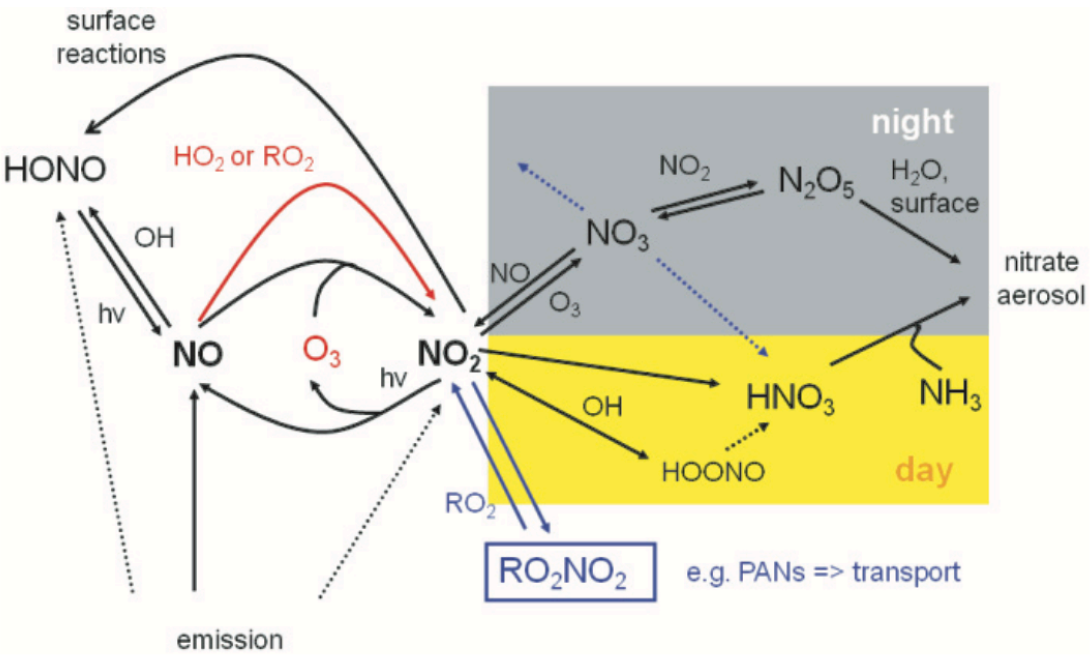

Figure 2.9 Simplified sketch of the chemistry of NO_x in the troposphere (Richter, 2009).

NO_x can also react with OH to create HNO_3 via an irreversible reaction, which can easily be taken up by droplets and aerosols as nitrate (NO_3^-). Nitrate aerosol can also be formed

at night as NO_2 reacts with NO_3 forming N_2O_5 and subsequent hydrolysis on surfaces and droplets. Nitrate acidifies aerosol and cloud droplets contributing to acid rain.

Peroxyacetyl nitrate (PAN) is an important long-term reservoir of NOx and can be formed by the temperature-dependent reversible reaction between NO_2 and the peroxyacetyl radical ($CH_3C(O)OO$) (2.9). The radical is produced through the reaction of an acetyl group ($R\text{-}C(O)CH_3$), e.g. acetone and acetaldehyde, with OH and O_2. When PAN is formed at the surface it can be uplifted into the cold upper troposphere, where it has a lifetime of several months (Talukdar et al., 1995). When these upper troposphere air masses descend and warm, PAN can break down producing NO_2, which can lead to the photochemical production of O_3 away from source regions (Pope et al., 2016).

$$CH_3C(O)OO + NO_2 + M \rightarrow PAN + M \qquad (2.9)$$

Sources and trends

Anthropogenic sources of NO_x include fossil fuel, anthropogenic biofuel combustion, power plants, automobiles, ships, aircraft and industry. Natural sources of NO_x include, soil, biomass burning and lightning. A compilation of emission datasets in (Schumann & Huntrieser, 2007) show that anthropogenic emissions dominate, contributing 49% of the total NO_x flux with natural emissions biomass burning, soil and lightning contributing 24%, 13% and 12%, respectively. However, bottom-up inventories from different sources and regions contain large uncertainties and the wide range of emission estimates in the literature suggest incomplete knowledge of the contribution of different sources to NO_x emissions (Oikawa et al., 2015).

Miyazaki et al., 2016 derived trends in NO_2 emissions from 2005 to 2014 using multi-satellite data assimilation. The USA (-38% decade^{-1}), western Europe (-8.8% decade^{-1}) and southern Africa (-8.2% decade^{-1}) showed decreases in emissions, while India (+29% decade^{-1}), China (+26% decade^{-1}) and the Middle East (+20% decade^{-1}), showed increasing emissions. Despite the large regional changes, the global NO_x emissions remained relatively constant from 47.9 Tg N yr^{-1} in 2005 to 47.5 Tg N yr^{-1} in 2014. The

a-priori and a-posteriori results of the emission inversion of NOx using OMI from K. Miyazaki et al., 2012 are shown in Table 2.2. The largest change is seen in regions where anthropogenic emissions dominate (China, eastern USA, southern Africa and central-western Europe) suggesting that anthropogenic emissions are the most underestimated emissions (using the EDGAR emission inventory). Significant underestimations are also seen in several biomass burning regions, particularly during their respective dry seasons, such as South-East Asia in April and South America in October (using GFED emissions).

	A priori	A posteriori
E-China	3.1	5
Europe	5.5	4.6
E-USA	2.6	3.4
S-America	0.7	1.1
N-Africa	3.1	2.6
C-Africa	2	1.9
S-Africa	0.2	0.5
SE-Asia	0.4	0.7
Globe	41.6	45.4

Table 2.2 The 4-month mean (January, April, July, and October in 2005) global and regional NOx emissions (in TgN yr^{-1}) showing the changes from a priori emissions, to posteriori emissions following the assimilation of the DOMINO OMI NO_2 product (K. Miyazaki et al., 2012).

Emissions from biomass burning

A large number of gaseous nitrogen compounds have been identified in biomass burning plumes including N_2O, NH_3, HONO, HNO_3, NO, NO_2, HCN, CH_3CN, amines ($ReNH_2$) and nitrates ($R\text{-}ONO_2$) (Akagi et al., 2011; Andreae & Merlet, 2001). Table 2.1 implies nitrogen compounds are produced in much smaller quantities in BB plumes than organic

compounds. Nitrogen/CO_2 emission ratios are reported between 0.5 and 3.5% (Andreae & Merlet, 2001). The nitrogen content of vegetation varies considerably, with laboratory measurements ranging from 0.2 to 4% (McMeeking et al., 2009), although there does not appear to be a systematic difference in nitrogen content per biome (Laursen et al., 1992).

NO_x is primarily emitted from wildfires as NO and is quickly converted to NO_2 (Lobert & Warnatz, 1993). Along with nitrogen content of fuels, another main influence on NO_x emissions is the combustion efficiency of the fire. Flaming combustion produces more NO, N_2 and N_2O due to the greater oxidation of fuel nitrogen, while smouldering combustion produces more reduced compounds such as NH_3 and HCN (Andreae & Merelt, 2001; Goode et al., 1999).

Andreae & Merlet, 2001 derived average emission factors for NO of 1.6, 3.9 and 3.0 g NO kg^{-1} dry fuel burned for tropical, savannah/grass- lands and extra-tropical forests, respectively. Akagi et al., 2011 report values of 2.6, 3.9 and 1.2 g NO kg^{-1} fuel burned for tropical, savannah and extra-tropical fires, respectively. These values show that Savannah fires emit more NO_x emissions than other biomes, due to having larger MCE values and a greater percentage of fuel nitrogen released by fires (89%) (Hurst et al., 1994) compared to other fire types (69%) (Goode, et al., 1999). The increase in tropical emission factors is thought to be an impact of more studies focussing on young plumes while the decrease in extra-tropical fires are due observations suggesting a larger contribution of smouldering fires in boreal regions.

2.4.8 Tropospheric ozone

Ozone (or trioxygen) is an inorganic molecule with the chemical formula O_3, its name is derived from the Greek word *ozein* meaning “to smell” due to its distinctively pungent smell. In the atmosphere, the majority of ozone is located in the lower stratosphere (~90%), at approximately 20-30 km altitude in the ‘ozone layer’. This absorbs 97-99% of the sun’s medium-frequency ultraviolet radiation (200-315 nm), which would otherwise damage plant and animals at the surface. This absorption drives the ozone/dioxygen (O_2) cycle called the Chapman cycle, with O_2 molecules absorbing wavelengths up to 242 nm and dissociating via reaction 2.10. The unstable O_3 molecules

dissociate back into O_2 following absorption of wavelengths throughout the ultraviolet part of the spectrum (2.11).

$$O_2 + h\nu \rightarrow 2O^{\cdot} \quad (2.10)$$

$$O^{\cdot} + O_2 \leftrightarrow O_3 \quad (2.11)$$

Ozone is a powerful oxidiser, much more so than dioxygen, and has many industrial and consumer applications. This oxidising potential causes ozone to damage mucous and respiratory tissues in animals and also plant tissue, and as such tropospheric ozone is considered a significant air-pollutant, with the WHO (World Health Organization, 2006) air quality guideline suggesting concentrations of O_3 should remain under 100 μg/m^3 (or ~50 ppb). O_3 is also an important greenhouse gas and significantly impacts the concentrations of OH, the most important atmospheric oxidiser. O_3 concentrations in the planetary boundary layer are regulated by atmospheric transport, chemical production/destruction and dry deposition.

Tropospheric photochemistry

Due to the absorption of UV wavelengths in the ozone layer, tropospheric O_3 is not formed via the Chapman cycle and is dependent on other photolytic reactions, based the interaction of NO_x and NMVOCs. The production of O_3 in the troposphere via the interaction of O_3-VOC (CH_4)-NO_x is shown in Figure 2.10. Fundamentally the production of tropospheric O_3 relies on reactions (2.7-2.8), the photolysis of NO_2 followed by the association of O(^{3}P) with O_2 through a termolecular interaction with a third body (M).

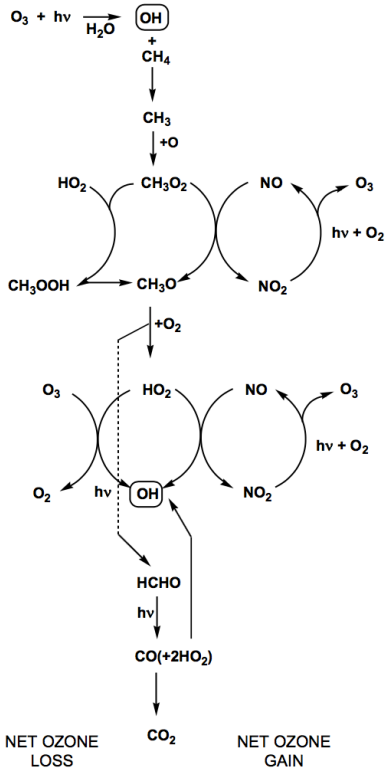

Figure 2.10 Simplified mechanism for the photochemical oxidation of CH_4 in the troposphere (Lightfoot et al., 1992).

The VOCs (illustrated here by CH_4) control the formation of the peroxide radical (HO_2) (2.12), which can react with NO to form NO_2 and OH (2.13). Reaction (2.13) influences the NO_x cycle, impacting the net amount of O_3. In a high-NO_x concentration environment reaction (2.8) dominates and the concentration of HO_2 radical controls the production of O_3. In a low-NO_x environment reaction (2.7) dominates and NO_x concentrations control the production of O_3.

$$CH_4 + OH\ (+O_2) \rightarrow CO_2 + HO_2 \qquad (2.12)$$

$$HO_2 + NO \rightarrow NO_2 + OH \qquad (2.13)$$

For reaction 2.12 O_3 is the source of the hydroxyl radical (OH), which is formed by reaction 2.17. However, the presence of VOCs and NOx allow OH to be regenerated

therefore promoting the formation of NOx through NO_2 photolysis (2.6). This is called OH-initiated O_3 formation.

.

$$O_3 + h\nu \rightarrow O_2 + O \quad (2.14)$$

$$O + O_2 \xrightarrow{[M]} O_3 \quad (2.15)$$

$$O(1D) + M \rightarrow O + M \quad (2.16)$$

$$O(1D) + H_2O \rightarrow OH + OH \quad (2.17)$$

Figure 2.11 shows the non-linearity of O_3-VOC-NOx system. Regions where there is net O_3-destruction top left (A) and bottom right (B) are referred to as VOC-limited and NOx-limited regimes, respectively. In VOC-limited environments there is no recycling of NO_2 via 2.14, leading to O_3 titration via 2.8. In a NO_x-limited environment 2.12 dominates as there is excess HO_2 and no loss via reaction 2.14, leading to O_3 destruction.

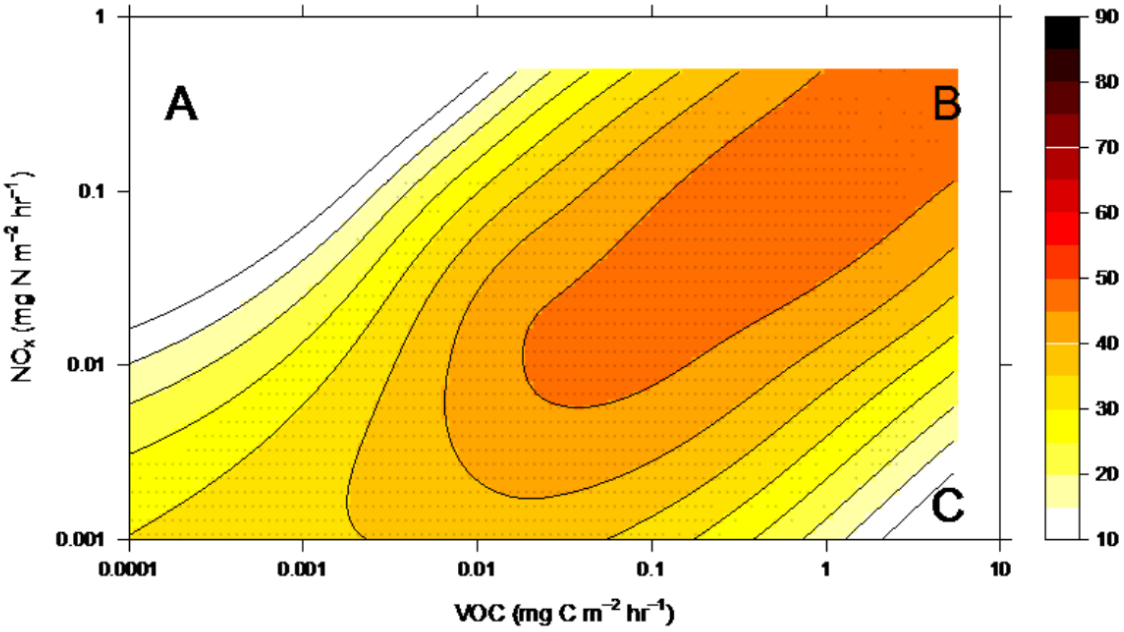

Figure 2.11 O_3 mixing ratios (ppb) as a function of VOC and NO_x emissions as computed using the UKCA model of atmospheric chemistry. Three main regions are identified. Top left corner (A): region of NO_x saturation and O_3 titration. Bottom right corner (C) region of VOC saturation and O_3 destruction. Diagonal elements A-B and A-C show efficient conversion of NO-NO_2 and hence O_3 production increasing with increasing VOC and NO_x emissions. (NB: $\log_{10}$ scales for emissions) (A. T. Archibald et al., 2011).

This general mechanism of OH-initiated O_3 formation can be expanded to more complex VOCs forming organic peroxy radicals RO_2 instead of HO_2 in reaction 2.12. Here R represents allyl, alkyl, allyl or aryl organic functional groups which all possesses the ability to oxidise NO to NO_2. The fate of these radicals is often more complicated than HO_2 and remains a great challenge in fully understanding tropospheric O_3 formation (Monks et al., 2009).

Models have assessed that the chemical production in the troposphere contributes 5000 Tg yr^{-1} to global tropospheric ozone, while stratospheric-tropospheric exchange is estimated to contribute 550 Tg yr^{-1} (Monks et al., 2015).

Ozone formation and removal is central to the chemistry of the troposphere through the catalytic production of the OH radical, as well as other photochemical reactions (Seinfeld and Pandis, 2006). OH, is the most important reactive species in the troposphere due to its high reactivity and relatively large concentration. Reaction 2.14 shows the photolysis of O_3 leading to the production of ground state O, that quickly reforms back to O_3. Occasionally the excited $O(^1D)$ is produced, as the transition to the ground state is spin forbidden, it is able to react with other atmospheric species. On reaction with N_2 or O_2, $O(^1D)$ quenches back to its ground state (2.16), however on collision with two OH radicals are formed (2.17). This is the only gas-phase reaction in the troposphere able to break the H-O bond in H_2O. At night NO_2 can no longer be photolysed so is able to react further with O_3, producing the nitrate NO_3 radical, an important night-time atmospheric oxidant. Ozone, along with the hydroxyl and nitrate radicals, determine the oxidative capacity of the troposphere (Gauss et al. 2003).

Current and future ozone trends

Ozone concentrations are currently higher in the northern hemisphere than the southern hemisphere, reflecting the anthropogenic dominance of O_3 precursor emissions (Monks et al., 2015). O_3 concentrations can vary significantly region by region and are very dependent on the season, as seen in Figure 2.12. Concentrations in the Northern Hemisphere peak during boreal summers (JJA) at mid-latitudes while Southern Hemisphere concentrations peak in the austral spring (SON) between South America and Africa (Cooper et al., 2014).

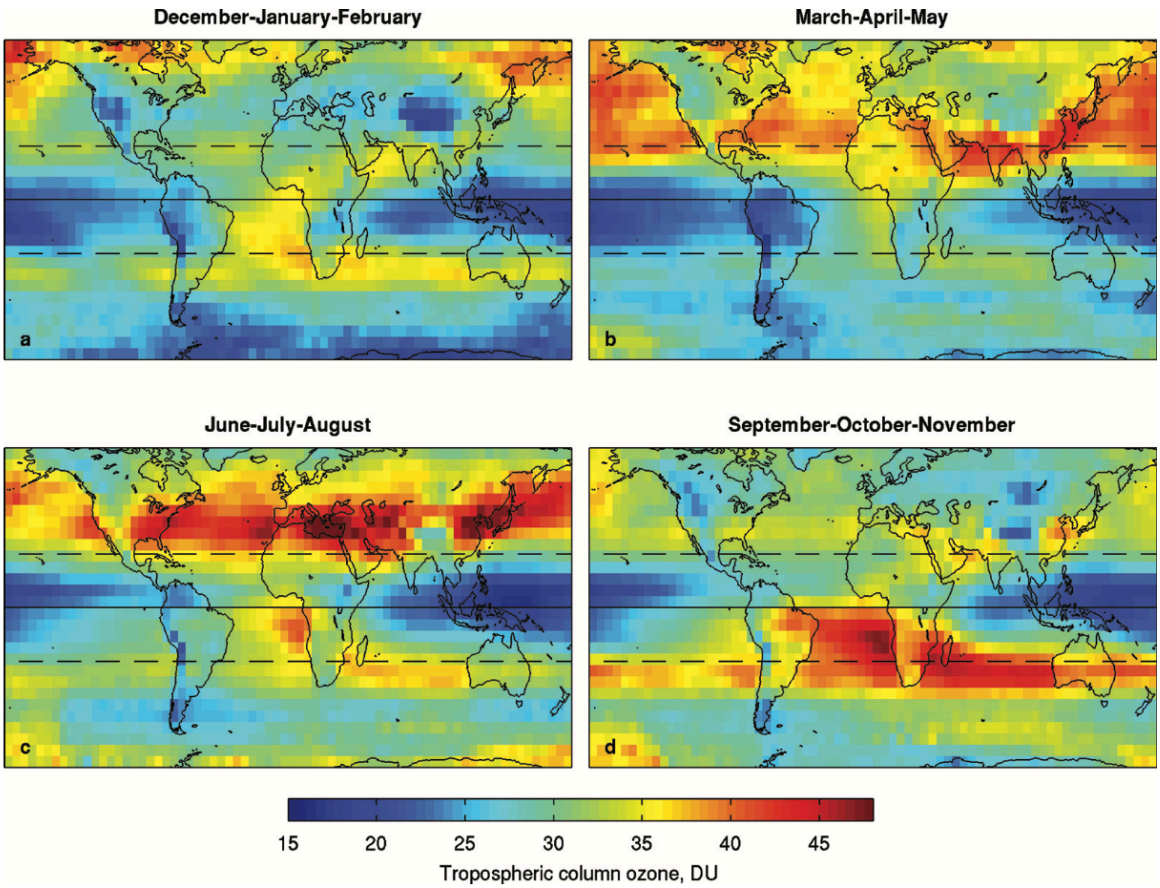

Figure 2.12 OMI/MLS tropospheric column ozone (DU) by season. Averaged data for October 2004 – December 2010 and reported at 5° × 5° horizontal resolution. Locations of the equator (solid horizontal line) and tropics (dashed horizontal lines) are indicated (Cooper et al., 2014).

Modelling studies have suggested that the tropospheric ozone burden in 1850 was 30% less than today, but there are problems validating observations from this time period (Young et al., 2013). Observations in Western Europe show a factor of 3-5 increase from the late 1800s to late 1900s and an increase by a factor of 2 between the 1950s and 1990s. Ozone trends from 1990 to 2010 have varied significantly from region to region. Western Europe and the US show decreasing surface O_3 while concentrations in east Asia continue to rise (Cooper et al., 2014).

Biomass burning and the atmosphere

Air quality impact

Ozone is an important trace gas in the troposphere as it has a substantial impact on air quality. Anenberg et al., 2010 used cardiopulmonary and lung cancer mortality rates along with a global atmospheric transport model to estimate approximately 0.7 million ± 0.3 million respiratory mortalities annually worldwide from atmospheric O_3. The majority of these mortalities (75%) occurred in densely populated and heavily polluted regions of the Asian continent. Time-series studies indicate an increase in daily mortality of 0.3-0.5% for every 100 $\mu g/m^3$ increment in 8-hour ozone concentrations above 70 $\mu g/m^3$ (World Health Organization, 2006). O_3-related deaths are estimated to make up between 5-20% of all those related to air pollution (Silva et al., 2013).

Deposition and plant health

The main loss processes of tropospheric O_3 is dry deposition at the surface with a net removal of about 1000 ± 200 Tg yr^{-1} (Stevenson et al., 2006), which is an order of magnitude greater than that to marine surfaces. The majority of dry deposition is controlled by stomata opening and there is a strong correlation between stomatal conductance and potential O_3 damage (Ainsworth et al., 2012). Stomata open to take up CO_2 for photosynthesis and close to reduce water loss and as such stomata opening is influenced by light, CO_2 concentrations, soil water content and temperature. Non-stomatal uptake does, however, play a role as ozone reacts and oxidises external surfaces of vegetation and soil, visible O_3 leaf damage has been seen globally at current ambient concentrations (Ashmore, 2005). In-canopy photochemistry can also have a significant impact on available O_3 for deposition as vegetation emits highly reactive VOCs which can rapidly deplete concentrations immediately above the canopy (Neirynck et al., 2012).

Through the impacts on the productivity and biodiversity, ozone has become the most important pollutant threat to terrestrial ecosystems (Monks et al., 2015). Typical ozone effects on vegetation include reduced growth, less seed production, lower functional leaf area and earlier leaf senescence. Studies have shown the impacts of ozone on multiple agriculture crops and tree species. A compilation of laboratory studies shows that current ambient O_3 (40 ppb) has reduced biomass by 7% with concentrations of 64 ppb and 97 ppb showing 11% and 17% decreases, respectively (Wittig et al., 2009). While studies

have used accumulated O_3 exposure above 40 ppb as a metric of O_3 damage on vegetation (Felzer et al., 2005) it has long been recognised that the plant response is more closely linked to the instantaneous flux of ozone through the plant stomata than ambient O_3 concentrations (Emberson et al., 2000). This is partly due to the complex relationship between O_3 concentrations and stomatal conductance, the rate which CO_2 enters the stomata, as O_3 damages a plant it supresses the net leaf photosynthesis which in turns impacts stomatal conductance reducing the instantaneous ozone flux. The O_3 flux can also be impacted by other factors that impact dry deposition such as the topography of the surface, the type of vegetation and the presence of water (Wesely and Hicks, 2000).

Tropical forests, specifically, may be particularly sensitive to surface O_3, due to their high stomatal conductance, accounting for as much as 50% of the global net primary productivity, and having evolved in some of the lowest O_3 concentrations on the planet (Pacifico et al., 2015a). Conversely, the dry season of August, September and October are the months when biomass burning and surface O_3 are highest over the Amazon forest, but are also the months where water limitations reduce the plants productivity (Rummel et al., 2007).

The impact of climatic conditions on plant stomata opening leads to variable impact of similar O_3 concentrations globally (Ashmore, 2005). The reduction of the carbon sink due to forest O_3 damage represents a substantial contribution to the indirect radiative forcing of O_3 (Sitch et al., 2007) and the potential impact of rising O_3 concentrations on this forcing is seen in Figure 2.13.

The lifetime of O_3 in the lower atmosphere is highly variable depending on available sinks, primarily photochemical destruction. In polluted urban regions where concentrations of its precursors are high it has a lifetime on the scale of hours, while in the free troposphere its lifetime is on the order of several weeks, allowing for intercontinental transport (Stevenson et al., 2006; Young et al., 2013).

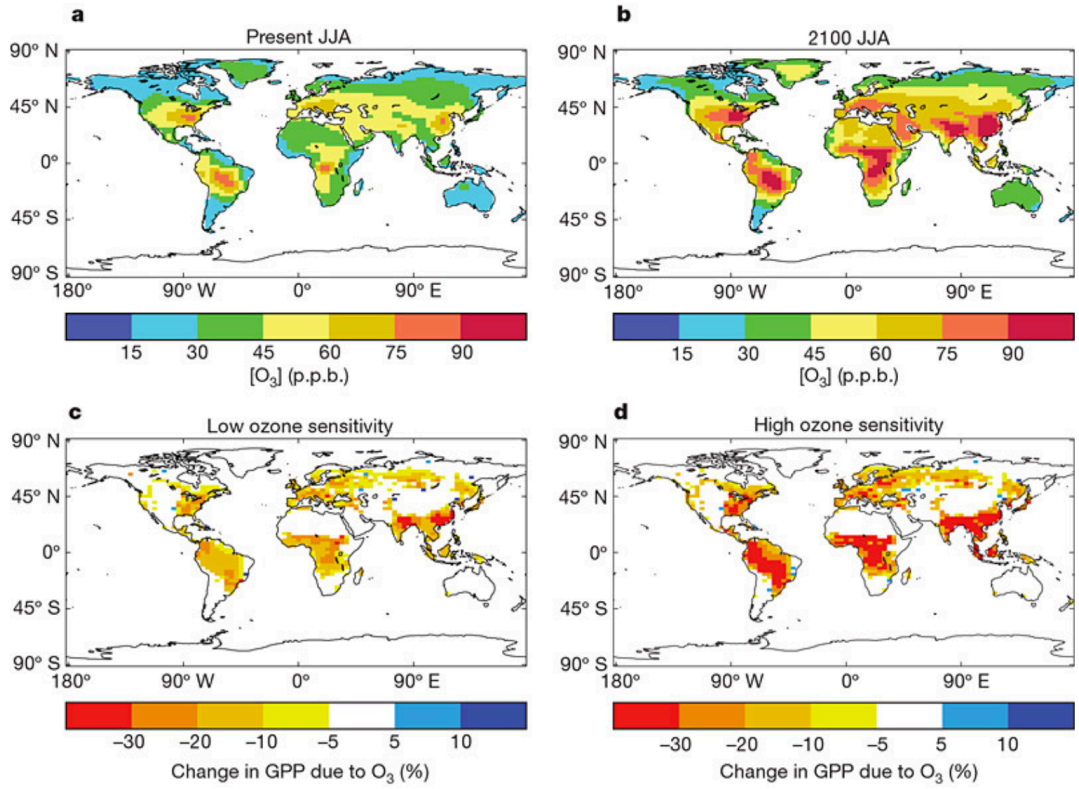

Figure 2.13 Modelled diurnal (24 h) mean surface [O3] in ppb averaged over June, July and August (JJA) for the present day (a) and the year 2100 under the highly polluted SRES A2 emissions scenario (b). (c, d) Simulated percentage change in gross primary productivity (GPP) between 1901 and 2100 due to O_3 effects at fixed pre-industrial atmospheric [CO_2] for "low" (c) and "high" (d) ozone plant sensitivity (Sitch et al., 2007).

Greenhouse gas

Ozone acts as a greenhouse gas absorbing infrared radiation emitted from earth. On a molecule by molecule basis, O_3 has a radiative effect roughly 1000 times as strong as CO_2, although it has a much shorter lifetime and therefore a smaller radiative impact. O_3 is estimated to have a radiative forcing of 0.4 W m^{-2} compared to 0.544 and 1.66 W m^{-2} for CH_4 and CO_2 (Myhre et al., 2013). It is estimated to have been responsible for 5%–16% of the global temperature change since preindustrial times (Forster, Ramaswamy, Artaxo, Berntsen, & Betts, 2007).

Production from fire emissions

Most observations suggest that biomass burning is a significant source of O_3. This is due to the emissions of substantial amounts of primary O_3 precursors, NMVOCs and NO_X, (see Sections 2.4-2.6) (Akagi et al., 2011; Andreae & Merlet, 2001; Crutzen et al., 1979). O_3 production in biomass burning is thought to be NO_x-limited due to the low concentrations of nitrogen containing compounds in plants compared to organics. The average molar ratio of emitted NMOC/NOx in savannah, tropical, temperate and boreal forests is 15, 50, 20 and 150, respectively (Jaffe & Wigder, 2012).

Some studies, however, have indicated either a minimum increase or even a depletion in tropospheric O_3 in plumes, mainly in boreal regions (Tanimoto et al., 2008). Lower production in boreal regions is thought to be due to the cooler temperatures of high latitudes and fires with lower MCE. This leads to larger emissions of NMOCs enabling significantly more NO_x to be converted into PAN. The rapid conversion of NOx to PAN is one of the key limits on local O_3 production, although PAN will eventually decompose leading to O_3 production downwind. Mason et al. (2006) used box models to study both boreal and savannah fires both showed significant O_3 production and NO_x loss however, O_3 production took place within an hour over Africa and up to several hours in the Alaskan case. This was due to 6ppb of PAN being formed in Alaska compared to 1ppb in Africa, indicating that PAN significantly impacts the rate of O_3 production.

In a POLIMIP comparison it was found that during the summer Arctic Ozone is sensitive to high initial PAN, and PAN precursor, concentrations from high latitude biomass burning (Arnold et al., 2015). The models used in the comparison were impacted significantly by the metrological data used to drive the model, indicting the influence of the atmospheric transport of species such as PAN. C-IFS was used in this POLIMIP comparison and had the largest PAN enhancement and largest overall positive bias (+40%) against high-latitude observations.

Aerosols and clouds can also impact O_3 production rates in plumes by reducing the amount of solar radiation available in the plume and limiting photochemistry. This can either increase or decrease net O_3 production by impacting both the production and loss

rates. Duncan et al., 2003 found decreases of 10-20% in NO_2 and O_3 photolysis rates over Indonesia during the strong 1997 El-Nino fires, with the reductions dependent on aerosol concentrations, SSA and size distributions. The net impact of lower photolysis rates on O_3 production remains unclear (Real et al., 2007).

To characterise O_3 production in plumes, O_3 concentrations are often correlated to CO, by quantifying the excess concentrations of both species $\Delta O_3/ \Delta CO$, the difference between the ambient background concentrations and the values measured in the smoke. This ratio can be calculated either by using a linear regression of observed data or calculating the enhancement above an assumed background value. However, regardless of method it is assumed that background concentrations do not vary over the range of observations.

Close to plume fire sources O_3 concentrations are normally low due to NO_x being emitted as NO and O_3 being titrated out through reaction (2.8), making $\Delta O_3/ \Delta CO$ low. This ratio then tends to increase with plume age until NOx decreases to very low concentrations (<0.1 ppb). In the free troposphere O_3 concentrations are generally stable, but can increase as PAN thermally decomposes back to NO_x, making $\Delta O_3/ \Delta CO$ large. Tropical and equatorial regions tend to have large $\Delta O_3/ \Delta CO$, due to greater NO_x emissions associated with higher MCE values.

O_3 production is very efficient at low NOx mixing ratios. Hudman et al., 2004 and Fischer et al., 2010 found O_3 production in excess of 40 ppb per ppb of NO_x in the free troposphere based on observations and modelling. This suggests that the thermal decomposition of PAN to NOx, while only producing of just over 0.1 ppb can explain high $\Delta O_3/ \Delta CO$ in aged plumes. However, at this age plumes may also be influenced by the mixing of other air masses (e.g. from urban sources) and by the photochemical destruction of CO which can be up to 20% over a week.

Modelling O_3 production from fire faces additional challenges to the modelling of urban O_3 due to the large range of emitted species from fires, the difficulty in modelling plume dynamics and chemistry on a model spatial grid and the uncertainty in emission heights. Mason et al. (2006) showed, using a box model, that NMOC emission data was the most significant cause of uncertainty in African and Alaskan fires while Cook et al. (2007) and

Biomass burning and the atmosphere

McKeen et al. (2002) showed discrepancies between modelled and observed PAN, NO_x and O_3 for boreal fires. More recently a POLIMIP comparison of Arctic O_3 using the FINN emission inventory, showed significant enhancement of summer tropospheric O_3 over the Arctic from biomass burning, with $\Delta O_3/ \Delta CO$ comparable to observations. The meteorological data used to drive the model was identified as the most important factor controlling simulated PAN enhancements, with ECMWF-driven models comparing more accurately to observations (Arnold et al., 2015). Modelling accurate emission heights is also important for capturing O_3 concentrations with Leung et al., (2007) noting much higher O_3 concentrations when NOx emissions are dispersed above the boundary layer.

Biomass burning makes a significant contribution to O_3 both regionally and globally, with an estimated global production of 175 Tg $year^{-1}$, which is 3.5% of all tropospheric O_3 production (Jaffe & Wigder, 2012; Monks et al., 2015). In the tropics, biomass burning is the major source of tropospheric O_3 (157 Tg yr-^{1}), where seasonal cycles of O_3 are in phase with the local biomass season (South America and South Africa 17 Tg $month^{-1}$ during the dry season (Mauzerall et al., 1998)). O_3 production also occurs at a faster rate in the tropics than at higher latitudes, with a fire in South Africa showing enhancements of 98 ppb in less than 30 minutes (Mason et al., 2006). Extremely rapid production of O_3 appears to happen in the presence of very reactive VOCs such as HONO and formaldehyde, which are key sources of the HO_x radical.

In the Amazon, surface O_3 varies from 12 ppb, during the wet season, to values as high as 100 ppb in the biomass-burning-affected dry season (Kirkman et al., 2002; Sigler et al., 2002; Artaxo et al., 2002, 2005; Rummel et al., 2007). Pacifico et al., (2015) predicts that the impact of ozone damage on the carbon cycle in the Amazon is equal to that of carbon dioxide released from the fire. Bela et al., 2015 and Pacifico et al., 2015 show that models overestimate O_3 concentrations in the Amazon away from polluted regions, particularly at night, and do a better job of capturing polluted plumes. This is thought to be due to both an underestimated of the dry deposition flux and inaccurate VOC reactivity for biogenic emissions which deplete O_3 concentrations immediately above the canopy.

2.4.9 Atmospheric aerosols

An aerosol is a colloid of solid particles or liquid droplets dispersed in a gas; in the case of atmospheric aerosols it refers to solid or liquid particles dispersed in the air. Aerosols can either be anthropogenic (e.g. haze, dust, particulates or smoke) or natural (e.g. fog, forest exudates or steam) in origin. The main sources of anthropogenic emissions occur in industrial or urban areas and include traffic (exhaust emissions, road surface abrasion, brake and tyre wear, particle resuspension from paved roadways), different industrial activities (emissions from power plants, oil refineries, mining), building (excavations, soil movement, demolitions) and emissions from housing (heating, food cooking). There is also a significant impact of anthropogenic emissions in rural areas from biomass burning and farming activities. The main natural sources of aerosol include the seas and oceans, deserts, soil, volcanoes, vegetation, wildfires and lightning (Calvo et al., 2013).

Regardless of whether anthropogenic or naturally emitted, aerosols originate from two different pathways: emissions of primary particulate matter and formation of secondary particulate matter from gaseous precursors. Atmospheric aerosol can be made up of inorganic species (e.g. sulfate, nitrate, ammonia, and sea salt), organic species, black carbon, mineral species and primary biological particles.

Size classification

The diameter of aerosol particles in the atmosphere span 4 orders of magnitude from a few nm to 100 μm. This significant variety in size requires aerosol to be measured both in terms of aerosol mass and aerosol number to fully understand aerosol properties, as the mass of a 10 μm diameter particle is equivalent to the mass of 1 billion 10-nm particles. Combustion-generated particles from biomass burning, fossil fuels and automobiles have a large variety of sizes from a few nm to as large as 1 μm. Natural primary aerosols such as windblown dust, pollens, plant fragments and sea salts are generally larger than 1 μm. Secondary aerosol, produced photochemically in the atmosphere, are generally smaller particles under 1 μm (Seinfeld & Pandis, 2016).

Biomass burning and the atmosphere

Particles with a diameter less 2.5 μm are referred to as “fine” particles and those with diameters greater than 2.5 μm are called “coarse” particles. These particle modes have different origins, transform separately, are removed from the atmosphere via different mechanisms, different chemical composition, different optical properties and have different impacts on the respiratory tract. Their properties are summarised in Figure 2.14. The fine mode can be further divided into the nuclei mode (0.005 μm < d < 0.01 μm), Aitken mode (0.01 μm < d < 0.1 μm) and accumulation mode (0.1 μm < d < 2.5 μm). The Aitken and nuclei mode account for the majority of particles by number but only a few percent of the aerosol mass. The nuclei mode is formed from the condensation of hot vapours during the combustion processes and the nucleation of atmospheric gases to form fresh secondary aerosol particles. The majority of particles in the nuclei mode coagulate with larger particles until they reach the accumulation mode, which accounts for the majority of the aerosol surface area and a more significant contribution to the aerosol mass. The accumulation is the mode where particle removal mechanisms are least efficient, causing particles to accumulate. Coarse particles have sufficiently large sedimentation velocities and settle out of the atmosphere with a reasonably short lifetime (Seinfeld & Pandis, 2016).

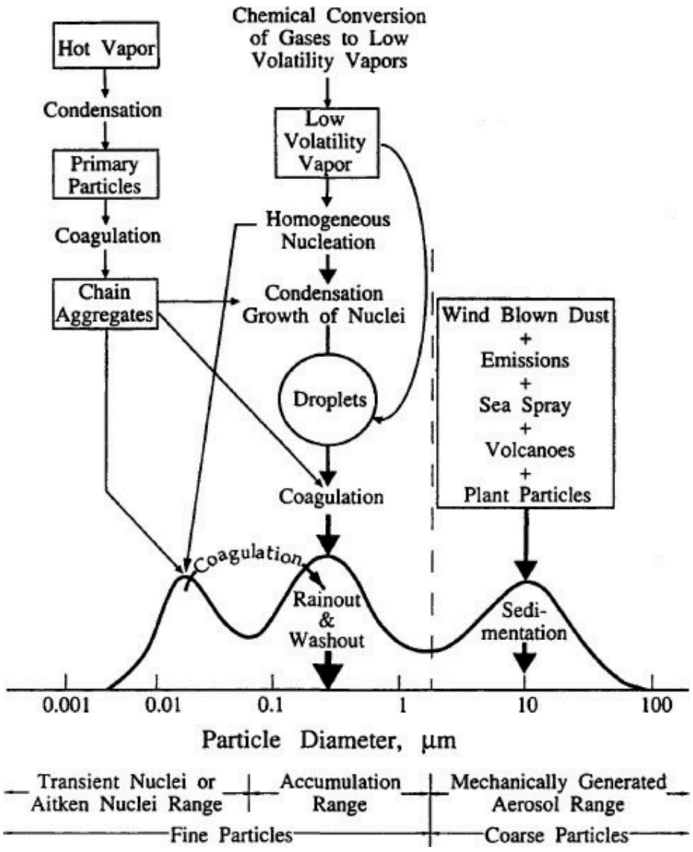

Figure 2.14 Idealised schematic of the distribution of particle surface area of an atmospheric aerosol. Principal modes, sources, and particle formation and removal mechanisms are indicated (Seinfeld & Pandis, 2016).

Impact on climate

Atmospheric aerosol is the greatest uncertainty in anthropogenic climate forcing, with man-made aerosol particles predicted to have an overall cooling effect around -0.5 Wm^{-2} (Boucher et al., 2013). Aerosols can affect the climate in multiple complex ways through their interactions with radiation and clouds. Aerosols can impact solar radiation through both scattering, which leads to less radiation reaching the surface therefore leading to localised cooling, and absorption which heats the aerosol but cools the surface as it receives less radiation. On larger timescales, atmospheric circulation and mixing processes spread the cooling from aerosol scattering and the warming from aerosol absorption horizontally and vertically as thermal energy is redistributed . These aerosol-

radiation changes can also alter the climate indirectly by altering the flows of the internal energy in the system. This is called rapid adjustments and affects cloud cover and other components of the climate system.

The radiative forcing from aerosol-radiation interactions (RFari) is the change in radiative flux caused by the combined scattering of aerosols, this includes both the direct effect and the impact of radiation by the rapid adjustments. The RFari for each aerosol type is summed up in Figure 2.15. This calculation requires knowledge of the spectrally variant single scattering albedo and phase function which is dependent on aerosol size distribution, shape, chemical composition and mixing state.

Aerosols also serve as condensation and ice nucleation sites on which cloud droplets and ice particles form. Clouds influenced by more aerosol particles tend to have more but smaller droplets, leading to a brighter cloud which increases their reflectance of the cloud and cooling the climate. There are many other pathways in which aerosols can impact clouds, particularly in ice or mixed water clouds, where phase changes are sensitive to aerosol concentrations and properties. All of these effects and any rapid adjustments resulting from these interactions make up the effective radiative forcing from aerosol-cloud interactions (ERFci), which is very difficult to quantify (Boucher et al., 2013).

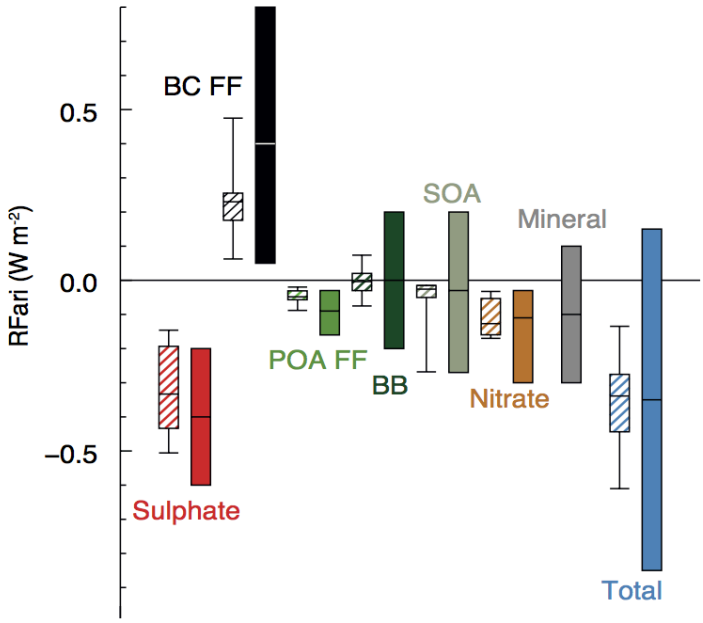

Figure 2.15 Annual mean top of the atmosphere radiative forcing due to aerosol–radiation interactions (RFari, in W m^{-2}) due to different anthropogenic aerosol types, for the 1750–2010 period. Hatched whisker boxes show median (line), 5th to 95th percentile ranges (box) and min/max values (whiskers) from AeroCom II models (Myhre et al., 2013) corrected for the 1750-2010 period. Solid coloured boxes show the AR5 best estimates and 90% uncertainty ranges. BC FF is black carbon from fossil fuels and biofuels, POA FF is primary organic aerosol from fossil fuels and biofuels, BB is for biomass burning aerosols and SOA is for secondary organic aerosols (Boucher et al., 2013).

Impact on air quality

The size of the particle is the most important factor in determining the health impact of a particle. Larger particles (> 10 μm) are filtered out by the cilia and mucus, while particles under 10 μm (PM_{10}) can penetrate the lungs, and particles < 2.5 μm ($PM_{2.5}$) can penetrate the gas exchange in the lungs impacting other organs. Epidemiological and human exposure studies show that both long-term and short-term exposure to PM correlate with increasing cardiovascular and respiratory diseases as well as increased mortality. In 2005 $PM_{2.5}$ and O_3 was estimated to be responsible for 773,000 deaths from respiratory

diseases, 186,000 deaths from lung cancer and 2 million deaths from cardiovascular disease (Lelieveld, Evans, Fnais, Giannadaki, & Pozzer, 2015). In 2012 the World Health Organisation estimated that ambient air pollution was responsible for 3.7 million deaths (WHO 2014). The guidelines set by the WHO are that concentrations of $PM_{2.5}$ and PM_{10} should remain under 10 and 20 $\mu g/m^3$ (annual mean), respectively, to minimise the health impacts (WHO 2006). Though air quality guidelines solely rely on mass concentrations, carbonaceous aerosol (black and organic carbon) are more toxic than crustal material, nitrates and sulfates (Tuomisto, Wilson, Evans, & Tainio, 2006).

Sea spray

Sea spray is a natural aerosol, produced at the sea surface by bubble bursting which are entrained by the wind stress, mostly from whitecap formation in waves. Wind speed is the key parameter in determining the production rate. Sea salt aerosols mainly consist of the ions of sodium chloride (Na^+ Cl^-) but many other chemical ions are common in sea water e.g. K^+, Mg^{2+} and Ca^{2+}. They are generally larger particles than in the coarse and accumulation modes, meaning they can sediment out of the atmosphere. Due to this size and hygroscopic nature, they readily act as cloud condensation nuclei (CCN) (Andreae & Rosenfeld, 2008). They are light scattering molecules decreasing the amount of radiation absorbed by the oceans as 0.08-6 W m^{-2} (Jaegle et al. 2011).

Sea spray aerosol dominates the mass concentrations of marine aerosol, particularly away from anthropogenic sources. It is one of the dominant aerosol globally in terms of mass emitted into the atmosphere. The source and composition of sea spray is a significant uncertainty in the aerosol number concentration of the atmosphere as estimates of its flux vary from 1400-6800 Tg yr^{-1} (Jaegle et al. 2011).

Mineral dust

Mineral dust particles or *aeolian dust* is produced mainly from arid and dry regions where high velocity winds can remove larger soil particles into the atmosphere. It consists mostly of metal oxides, clays and carbonates. The magnitude of dust emitted into the atmosphere depends on the surface wind speed and many soil-related factors such as its texture, moisture and vegetation cover. Around 75% of dust is from natural origin and 25% is anthropogenic (primarily agricultural) (Ginoux et al., 2001). Dust particles are

one of the largest atmospheric aerosol type by mass and mostly exists in the coarse mode, meaning they can sediment out in the atmosphere (Textor et al., 2006). Dust has a large impact on the radiative budget due to both absorbing and scattering of both solar and infrared radiation, with an estimated top of the atmosphere forcing between -0.03 and -0.25 W m^{-2} (Balkanski, Schulz, Claquin, & Guibert, 2007). Estimates of dust emissions vary from 1000-4000 Tg Yr^{-1} (Huneeus et al., 2011).

Sulfate aerosols

Sulfate aerosols are a suspension of fine solid particles or tiny droplets of sulfate (SO_4^{2-}), which are formed from the reaction between sulfuric acid (H_2SO_4), and ammonia (NH_3), see reaction 2.18. H_2SO_4 can be emitted as either primary aerosol from sea salt (19%) or as a secondary aerosol by the oxidation of SO_2 by OH from anthropogenic (74% - mostly fossil fuel burning) or volcanic emission (7%) or from other sulfur gases (such as dimethyl sulfide (DMS)) (Haywood & Boucher, 2000). Estimates of global SO_2 emissions range from 66.8 to 92.4 TgS yr^{-1} (Vautard et al., 2006).

Sulfate aerosols are very hygroscopic, are very important in the growth of aerosol particles by nucleation and are cloud condensation nuclei (CCN) active. They are entirely a scattering aerosol across the solar spectrum with a SSA of 1 and have a RFari of -0.31 W m^{-2} (Boucher et al., 2013).

$$NH_3 + H_2SO_4 \rightarrow NH_4HSO_4 + NH_3 \rightarrow (NH_4)SO_4 \qquad (2.18)$$

Nitrate aerosols

Nitrate aerosols are a suspension of solid or droplet nitrate (NO_3^-), a salt of nitric acid (HNO_3) and are formed by reaction 2.19 if sulfate aerosol is fully neutralised and there is excess ammonia. Nitric acid itself is a secondary aerosol produced by the oxidation of NO_x. The amount of nitrate aerosol is therefore sensitive to atmospheric concentrations of ammonia, sulfate and nitrogen oxides (see Section 2.4.7).

Nitrate aerosols are hygroscopic and cloud condensation nuclei (CCN)-active, but to a lesser degree than sulfates. They are light scattering particles with an estimated RFari of -0.11 W m^{-2} (Boucher et al., 2013).

$$NH_3 + HNO_3(NH_4) \leftrightarrow NO_3 \quad (2.19)$$

Black carbon

Black carbon (BC) also known as elemental carbon or soot, is a distinct type of carbonaceous material that has a graphite-like structure (Novakov and Corrigan, 1995) and is formed from the incomplete combustion of fossil and biomass burning fuels. It is distinguishable from other forms of carbon and carbon compounds due to having a unique combination of physical properties (Bond et al., 2013). BC strongly absorbs visible light with a mass absorption cross section of at least 5 m^2g^{-1} at a wavelength of 550 nm. It is refractory, retains its basic format very high temperatures, has a vaporization temperature near 4000 K, is insoluble in water, organic solvents and in other components of atmospheric aerosol and exists as an aggregate of small carbon spherules.

The estimated total global emissions of BC, using bottom-up inventories are 7500 Gg yr^{-1} (for the year 2000) (Bond et al., 2013). Sources of BC are distributed as 42% from open biomass burning (forest and savanna burning), 18% residential biofuel burned with traditional technologies, 14% diesel engines for transportation, 10% diesel engines for industrial use, 10% from industrial processes and power generation and 6% residential coal burned with traditional technology.

BC has a significant climatic impact as it is a strong absorber of solar radiation; the best estimate for the BC direct radiative forcing in the industrial era is +0.71 W m^{-2} with an uncertainty range of +0.08 to +1.27 W m^{-2}. There are also significant indirect influences of BC on climate through the indirect effect, semi-direct effect and the altering the melting of snow and ice cover. Overall the best estimate of all forcing mechanisms is +1.1 W m^{-2} with 90% uncertainty of +0.17 to +2.1 W m^{-2} (T. C. Bond et al., 2013).

Condensation of gas-phase compounds on BC and coagulation with other particles alter the mixing state of BC and in urban polluted air internally mixed BC can be produced in around 12 hrs. The resulting BC-containing particles can become hygroscopic, allowing wet deposition and thereby reducing both their atmospheric lifetime and loading.

Organic aerosols

Organic aerosol (OA) is a broad term indicating all hydrocarbon compounds in the liquid or solid phase. It can either be emitted as primary organic aerosol (POA) or created in the atmosphere as secondary organic aerosol (SOA). Both primary and secondary organic aerosol are influenced by natural and anthropogenic emission sources. The anthropogenic sources are the same combustion processes as BC, as all sources that emit BC also emit POA and SOA precursors, due to the break-up of organic material. Natural sources include continental and marine ecosystems and biogenic emissions.

Organic carbon (OC) refers solely to the mass of carbon in organic aerosol. While OA is more relevant for climate and air quality, OC has more often been measured during field campaigns. The ratio of OA to OC varies from 1.1 to 2.2 and depends on the amount of oxygen incorporated into the organic compound (Russell, 2003). In atmospheric models a value for POA/OC of 1.3 or 1.4 is often used (Dentener et al., 2006).

OA particles are generally reflective in nature and as such have a RFari of -0.12 W m^{-2} (Boucher et al., 2013). However, some OA particles are light absorbing and are called brown carbon (BrC) particles. Brown carbon lacks an analytical definition, but is distinguishable from black carbon due to being less absorbing (1 m^2g^{-1}), having a strong wavelength dependence on absorption and being soluble in organic solvents.

Biomass burning aerosols

Biomass burning aerosol (BBA) are characterized by large aerosol optical depths (AOD) and poor visibility. BBA particles and the associated haze, perturb regional radiation budgets by their light-scattering effects and on their influences on cloud microphysical processes. Globally the RFari of BBA is estimated as +0.0 (-0.2 to +0.2) W m^{-2} as OM and BC radiative effects cancel out. Locally, however, there can be a significant impact on radiation and BBA it is thought to play a more important role, for example over Amazonia the average total solar flux was reduced by up to 37% by smoke aerosol, due to extremely large aerosol optical depths and strong particle absorption (Schafer et al., 2002).

The single scattering albedo (SSA) of BBA generally lies close to the critical SSA, the point between net reflection and net absorption of sunlight (Haywood and Shine, 1995).

Therefore, many of the effects of BBA depends on its SSA, which in turn is related to the fraction of OC (scattering) and BC (absorbing) in the particles (Boucher et al., 2013). BB emissions are the largest global source of black carbon (BC). BBA are generally composed of 50-60% organic carbon and 5-10% black carbon (Reid et al., 2005). 80 − 90% of their volume is in the accumulation mode (particle diameter (dp) < 1 μm). Global emissions estimated from open burning range between 2000 and 11,000 Gg yr^{-1} for BC between 18,000 and 77,000 Gg yr^{-1} for OC in average years, as summarized by (Schultz et al., 2008), with most recent studies falling into the range of 2000 to 6000 Gg yr^{-1} for BC and 20,000 to 27,000 Gg yr^{-1} for OC (Lamarque et al., 2010; G. R. Van Der Werf et al., 2010).

The impact of aerosol on local radiation can significantly impact the biosphere. In the presence of optically thin smog, direct photosynthetically active radiation (PAR) decreases while the diffuse fraction increases (Doughty et al., 2010; Oliveira et al., 2007; Roderick et al., 2001). An increase in diffuse radiation provides more light to parts of the canopy that would be shaded. The net effect of the smog on photosynthesis is the balance between the decrease in direct radiation and the diffuse effect. This value has the largest positive effect on photosynthesis in the tropics where canopy carbon assimilation is low at midday due to the oversaturation of direct sunlight leading to closing of the plant stomata. Diffuse sunlight decreases the impact of sunlight saturation on photosynthesis. Rap et al. 2015 showed using a radiative transfer model and a land surface model that aerosol particles in the Amazon increase diffuse radiation by 3.4-6.8% increasing NPP by 1.4-2.8%.

BBA also has a significant influence on cloud condensation nuclei (CCN), with greater than 10,000 cm^{-3} observed during the Amazon dry season (Roberts et al., 2003). In BBA, organic compounds and BC are frequently internally mixed with ammonium, nitrate and sulfate (Deboudt et al., 2010) (Pratt and Prather, 2010). The aerosol mixing state can alter particle size distribution and hygroscopity and hence the aerosol optical properties and ability to act as CCN (Wex et al., 2010).

Satellite-based emission estimates (e.g. GFAS, GFED, and FINN) show a significant and persistent underestimation of aerosol optical depth (AOD) in most tropical biomass burning regions. Due to this bias modelling studies have required biomass burning

aerosol emissions to be scaled by factors ranging from 1.5 to 6, in order to match ground and satellite based AOD (J. W. Kaiser et al., 2012; Reddington et al., 2016; Rémy et al., 2016). This underestimation is thought to be attributed to a number of factors including the underestimation of biomass burning emission fluxes, errors in atmospheric distribution of aerosols, modelling of aerosol ageing in smoke aerosols and the calculation of AOD (Andela et al., 2013; J. W. Kaiser et al., 2012). Reddington et al., 2016 show that in South America, there is a smaller bias when evaluating modes with ground-site PM 2.5 instead of AOD. Rémy et al., 2016 in turn shows that the bias between AOD from satellite and model is very different depending on the proximity to fires, with different errors calculated for both OM and BC.

Difference in emission factors between Andreae & Merlet , 2001 and Akagi et al., 2011 are within 20% of one other on average (Janhäll et al., 2010). Despite this, FINN shows much higher OC emissions in the tropics, being 47% higher that GFAS and 30% higher than GFED. This leads to a much larger OC:BC ratio for FINN of 10.0, with 7.9 for GFED and 7.1 for GFAS, suggesting very different radiative effects for each emission inventory (Reddington et al., 2016).

2.5 Summary

Overall biomass burning has been shown to have a substantial impact on local and regional climates and air quality. Recent trends have shown decreases in fires in changing landscapes round the globe and a key area of future research is identifying how this effect will balance with future increases in temperature.

Accurate modelling of the impact of fire emissions on the troposphere is important to fully understand their impacts on the earth system. Without accurate modelling of O_3 and aerosols the total impact on the carbon sink cannot be calculated in an earth system model. Difficulties in modelling include determining the location of the fire, the type of vegetation being burnt and increasingly how the emissions are distributed vertically in plumes. Recent use of satellite-based top down emissions has improved the modelling of major species, such as CO_2 and CO, by providing daily emissions with accurate locations, but significant uncertainties remain in terms of identifying small fires and requiring

accurate emission factors for trace species such as aerosols. Ozone concentrations have an added difficulty due to the multitude of different VOCs emitted by fires affecting O_3 photochemistry and their unknown composition. In regions such as tropical South America observations of different trace species can be sparse and detailed observation of different vegetation types and meteorological conditions are needed to fully understand the regional impacts on plant health, photosynthesis and, in regions with growing populations, public health.

An additional way to better quantify the impact of fires in models is to use satellite data not only to locate fires but to also alter composition fields in models with trace-gas and aerosol observations and provide more accurate model metrics. The following chapter discusses some “data assimilation” methods for combining satellite and model data, and describes the finding of previous studies using composition data assimilation to more accurately capture fire emissions.

3 Models, observations and data assimilation

3.1 Introduction

This chapter provides a general background to composition data assimilation, i.e. the combining of a state-of-the-art model with observations to provide a 'best estimate' of the atmospheric state. In particular, this chapter also describes the Composition – Integrated Forecast System (C-IFS), a general circulation model (GCM), with coupled chemistry modules, that is used throughout this work. Section 3.2 describes the general theory of data assimilation and briefly summarises the two most widely used techniques in composition studies: Variational methods (3D + 4D) rooted in control theory, and ensemble Kalman filters rooted in statistical representation theory. Section 3.3 describes the C-IFS model including information on model parameters and emissions. Section 3.4 describes the Global Fire Assimilation System (GFAS) including information on the plume rise mode. Section 3.5 discusses the composition assimilation scheme within C-IFS, including details of assimilated satellite columns (MOPITT CO, OMI O_3, MLS O_3, OMI NO_2 and MODIS). Finally, section 3.6 details the SAMBBA flight campaign.

3.2 Data assimilation

Data assimilation is a term that encompasses a number of techniques, each estimating the true nature of a system by assimilating three different sources of information and their associated errors: The model, the observations and the previous best estimate. There is a tradition of employing data assimilation within numerical weather prediction, ocean modelling and oil reservoir simulation (Courtier, P., 1998; Daley, 1991; Kalnay, 2002; Navon, 2009). More recently, atmospheric composition data assimilation has started to play an important role in both air quality forecasts and composition studies, leading to improvements in initial and boundary conditions as well as refined top-down emission estimates (Inness et al., 2013; K. Miyazaki et al., 2015; Sandu & Chai, 2011). These composition data assimilation systems (DAS) combine the theoretical chemical and

physical laws of evolution with the available (but limited) distribution of trace gases/aerosol measurements, to provide a formal best-estimate of reality.

3.2.1 Methodology and notation

This section outlines the generalised methodology and identifies key terms used in data assimilation studies, a more thorough description of data assimilation can be found in Kalnay, 2002. Data assimilation optimally fuses three different sources of information:

1. The observations **y**: observed concentration of a trace gas or aerosol.

2. The model state vector $\mathbf{X^m}$: model encapsulating physical and chemical laws that govern the atmospheric composition over time.

3. $\mathbf{X^b}$ the *a priori* or background state: best estimate of the true state of a system $\mathbf{X^T}$ before any measurements are considered, generally either the previous best model estimates or an analysis field from a previous time step.

The *a priori* has an associated error matrix **B**, also known as the background error covariance matrix, which expresses the random error in the background and the correlation between these errors elsewhere. Observations, in-situ or satellite, represent a particular atmospheric metric at a discrete time and location, often indirectly, and therefore an observation operator **H** is needed to calculate the model equivalent of the assimilated observations (e.g. satellite retrievals of atmospheric composition). The observation error **R** accounts for both the error in the observation and the representative error associated with **H**, arising from different resolutions between model and observations. The weighting between the background error covariance and the observations error determines the influence of the *a priori* and observation on the analysis $\mathbf{X^a}$.

These three sources of information, and their associated errors, are used to compute the posterior estimate $\mathbf{X^a}$ also known as the 'analysis' state, a best estimate of the true state of a system $\mathbf{X^T}$. Different approaches to this calculation are rooted in different theories; variational methods based in control theory and Kalman filters based in statistical

representation. These different approaches and their computational costs are discussed in the following sections.

The data assimilation problem can be formulated in a Bayesian framework, where the analysis probability density, or posterior distribution, $P(X^a)$ can be expressed as:

$$P(X^a) = P(x^b/y) = \frac{P(y/X^b)\, P(X^b)}{P(y)} \tag{3.1}$$

Where $P(x^b)$ is the prior distribution and $P(y/x^b)$ is the likelihood function or the probability that the observations are conditioned by the model (the probability that the observation error **B** assume the values $\mathbf{H(X^B) - y)}$. P(y) is calculated by integrating over all values of X^b, as shown in equation 3.2.

$$P(y) = \int P(y/X^b)\, P\left(X^b\right) dX^b \tag{3.2}$$

In large-scale models this direct application of Bayes theorem to describe the posterior is not possible due to the large number of variables (for a general atmospheric chemistry model ~10^8) and hence the multi-dimensional probability densities of $\mathbf{X^b}$. Approximations are therefore needed to represent the posterior (Sandu & Chai, 2011).

3.2.2 Variational methods

Variational methods solve the data assimilation problem by looking for the most probable state or mode for the posterior probability density function (PDF). The minimum of a cost function **J** is used to find this maximum value of the posterior.

$$P(x^b/y) \propto \exp[-\frac{1}{2}J] \tag{3.3}$$

$$J(x) = \frac{1}{2}\left(x^m - x^b\right)^T B^{-1}\left(x^m - x^b\right) + \frac{1}{2}\left(y - H(x^m)\right)^T R^{-1}\left(y - H(x^m)\right) \quad 3.4)$$

In order to find the optimal state vector, the value of the cost function **J**, the misfit between the model state and the observations, needs to be minimised in a least-square sense. In 3D variational (3D-var) data assimilation observations are considered sequentially in time and the 3D problem is solved at each time step.

4D-var considers all observations simultaneously over a certain assimilation window and solves the problem at the beginning of the time window. The difference between 3D and 4D-var data assimilation is shown in Figure 3.1. The 4D-var cost function includes all observations over the assimilation window, the number of model time steps is denoted by **M**;

$$J(x) = \frac{1}{2}\left(x^m - x^b\right)^T B^{-1}\left(x^m - x^b\right) + \sum_{tobs=1}^{M} \frac{1}{2}\left(y_i - H_i(x^m)\right)^T R^{-1}\left(y_i - H_i(x^m)\right) \quad (3.5)$$

This non-linear cost function is minimised iteratively where initial conditions at the start of the window are varied. Adjusting theses initial values instead of changing the state directly in model time reduces the complexity of the calculation. The model then propagates these optimised initial states to produce a posterior 'analysis' over the whole-time window, before the next iteration. The large-scale optimisation required for 4D-var is achieved when the gradient of **J**, with respect to the state vector is equal to zero;

$$\nabla_x J(x) = B^{-1}\left(x^m - x^b\right) + (x^m)^T[R^{-1}\left(y - H(x^m)\right) \quad (3.6)$$

In 4D-var the observation operator **H** includes the transposed derivatives of future state with respect to the initial conditions, the adjoint matrix. In reality **H** is not solved directly,

the model outputs are interpolated to each observation and the adjoint matrix is replaced by an adjoint model, created directly from the forward model.

After the minimisation, the state vector is updated and the model propagates these optimised initial states to produce a new background $\mathbf{X^B}$ for the whole-time window, before the next iteration. Eventually, the norm of the gradient reaches a certain threshold value or convergence criteria, which is chosen as the close-to-optimal state as desired.

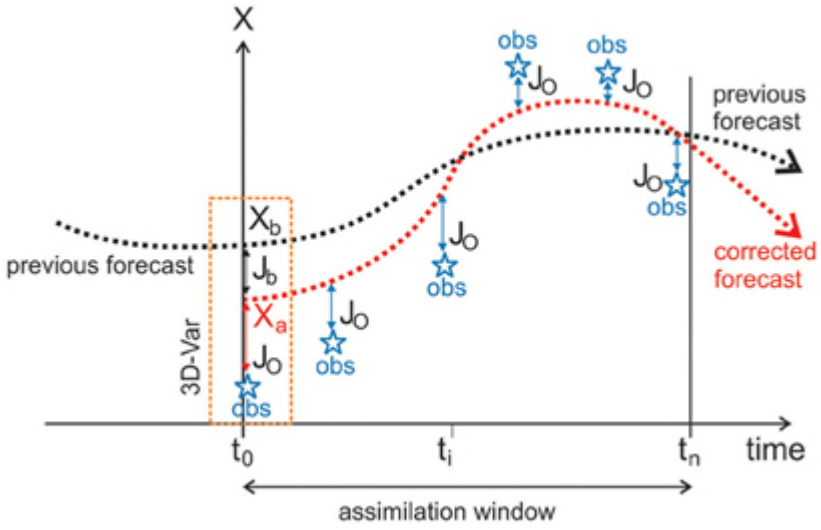

Figure 3.1 Schematic diagram illustrating both 3D and 4D-var data assimilation (Lahoz & Schneider, 2014).

3.2.3 Previous composition assimilation studies

In the 8-year (2003-2010) dataset of the MACC reanalysis (Inness et al., 2013), total column O_3, CO and NO_2 fields compared well to independent satellite observations, but profiles showed biases in the boundary layer close to large urban and fire emissions, with over-estimation of NO_x over Africa and under-estimation over South America. NO_x generally showed smaller changes via assimilation, due to its shorter lifetime (~days in the free troposphere to ~hours during the summer in the PBL). The assimilation was also shown to impact the non-assimilated species formaldehyde (HCHO) when compared to SCIAMACHY. The impact of MODIS AOD assimilation in the IFS is discussed in

Benedetti et al., (2009) and showed improvements in the model from assimilation, against AERONET ground observations of AOD.

Another long-term (2005-2012) tropospheric chemistry reanalysis using the DAS-CHASER ensemble Kalman-filter (Miyazaki et al., 2012), showed similar comparison to independent data-sets but by including the simultaneous adjustment of emissions and concentrations of various species as well as including a whole range of non-assimilated chemical species in the state vector. More significant changes from NO_x assimilation were observed using the simultaneous adjustment (Miyazaki, et al. 2015). Including OH in the state-vector showed increases in OH in the tropics (5%) and decreases in the northern mid-latitudes (3%) and a more realistic comparison in NH/SH ratio to OH observations derived from chloroform (Patra et al., 2014).

3.3 C-IFS model

During the GEMS (Hollingsworth et al., 2008), MACC (Inness et al., 2013) and Copernicus Atmospheric Monitoring Service (CAMS) (Flemming et al., 2015) projects ECMWF's IFS data assimilation system was expanded to include atmospheric composition elements. This included chemically reactive species (O_3, CO, NO_X and HCHO) (Flemming et al., 2009; Inness et al., 2013), greenhouse gases (CH_4 and CO_2) (Engelen, 2009) and aerosols (Benedetti et al., 2009; Morcrette et al., 2009).

C-IFS refers to the inclusion of atmospheric composition modules within ECMWF's general circulation model (IFS). In preparation for the CAMS IFS was extended to include chemically reactive gases (Flemming et al., 2009; Inness et al., 2013), aerosols (Benedetti et al., 2009; Morcrette et al., 2009) and greenhouse gases (Inness et al., 2013). This implementation enables: (1) the use of detailed meteorology in the simulation of composition constituents, (2) simulation of feedback processes between atmospheric composition and weather and (3) the use of 4D-var data assimilation system within IFS to assimilate observations of atmospheric composition (Flemming et al., 2015). Analysis data from C-IFS is often used as boundary conditions for regional model studies (Archer-Nicholls et al., 2015; R. J. Pope et al., 2014) with Pope et al., (2014) showing large changes within the regional model depending on which analysis product is assimilated.

The following section describes the framework and background of the C-IFS, the implementation of composition elements inside the IFS model. The transport simulated by the IFS is discussed in 3.3.1, composition emissions in 3.3.2 and the chemical scheme in 3.3.4. The two aerosol schemes, IFS-GEMS and IFS-GLOMAP, are discussed in Sections 3.3.5 and 3.3.6, respectively.

3.3.1 IFS: transport and grid

The IFS is a semi-Lagrangian semi-implicit Numerical Weather Prediction (NWP) model that includes representations of cloud fraction, cloud liquid water, cloud ice, rain and snow in the simulation of the hydrological cycle (Forbes, 2012). Initially the three-dimensional advection is calculated, then the tracers are vertically distributed in the diffusion scheme and convective mass fluxes. The diffusion scheme also includes both the injection of emissions at particular heights and the loss via dry deposition at the surface. Finally, the sink and source terms due to chemical conversion, wet deposition and prescribed surface and stratospheric boundary conditions are calculated.

The advection, convection and turbulent diffusion of the chemical tracers in C-IFS use the same algorithms as those used for the transport of water vapour. A Lagrangian description of advection follows individual air parcels along their trajectories as opposed to the Eulerian description, which considers the exchange of tracer mass between grid boxes. The IFS uses a three-dimensional semi-Lagrangian scheme, which includes a Eulerian framework but uses discrete equations from the Lagrangian perspective. This applies a quasi-monotonic cubic interpolation of the departure values with a global mass fixer, to conserve mass. The vertical turbulent transport in the boundary layer is calculated by a first-order k-diffusion closure and by convection as part of the cumulus convection (Flemming et al., 2015).

Chemical and related processes and species are represented in grid-point space (Hortal & Simmons, 1991). Global fields can be calculated at varying vertical and horizontal levels. In this thesis, the simulations are achieved at spectral truncation at wavenumber 255 (T255), corresponding to a reduced Gaussian grid of about 80 km horizontal resolution. The vertical discretization uses 60 hybrid sigma- pressure levels, with a model top at 0.1 hPa.

3.3.2 Emissions

C-IFS uses various emission inventories, which are injected as a lower boundary flux in the diffusion scheme. Anthropogenic surface emissions are given by MACCity (Claire Granier et al., 2011), developed as an extension of the Atmospheric Chemistry and Climate Model Intergovernmental Panel (ACCMIP) from the Fifth IPCC assessment report (AR5). Aircraft emissions of a total of ~0.8 Tg N/yr were applied to the anthropogenic emissions (Lamarque et al., 2010). Natural emissions from soils and oceans were taken from the POET database for 2000 (Granier et al., 2005; Olivier et al., 2003). Biogenic emissions come from the Model of Gases and Aerosols from Nature (MEGAN-2) (Guenther et al, 2006). Fire emissions were produced by the Global Fire Assimilation system (GFAS), which is discussed in Section 3.4. Example anthropogenic, biogenic and biomass burning emission totals for 2008 are shown in Table 3.1 (Flemming et al., 2015).

3.3.3 Dry deposition

Dry deposition is an important removal mechanism for many atmospheric gases and aerosols, particularly in the absence of precipitation. Dry deposition velocities are highly dependent on both the diffusion at the surface and the topography of the surface particularly the type of vegetation and the presence of water (Wesely and Hicks, 2000). In C-IFS the turbulent transfer of particles to the surface is based on a resistance model (Wesely et al., 1989) which calculates the total resistance, which is the inverse of the deposition velocity $\mathbf{V_d}$. The total resistance comprises aerodynamic resistance, resistance in quasi-laminar sublayer and the canopy or surface resistance. The dry deposition flux $\mathbf{F_d}$ is related via equation (3.9) to the $\mathbf{V_d}$, mass mixing ratio $\mathbf{(X_s)}$ of the tracer and the air density at the surface $\boldsymbol{\rho_s}$;

$$F_d = V_D X_S \rho_s \qquad (3.7)$$

Species	Anthropogenic emissions (Tg)	Biogenic and natural emissions (Tg)	Biomass burning emissions (Tg)
CO	584	96	325
NO	70.2 +1.8	10.7	9.2 +12.3 (LiNO)
HCHO	3.4	4.0	4.9
CH_3OH	2.2	159	8.5
C_2H_6	3.4	1.1	2.3
C_2H_5OH	3.1	0	0
C_2H_4	7.7	18	4.3
C_3H_8	4.0	1.3	1.2
C_3H_6	3.5	7.6	2.5
Paraffins (Tg C)	30.9	18.1	1.7
Olefins (Tg C)	2.4	0	0.7
Aldehydes (Tg C)	1.1	6.1	2.17
CH_3COCH_3	1.3	28.5	2.4
Isoprene	0	523	0
Terpenes	0	97	0

Table 3.1 Annual emissions from anthropogenic, biogenic and natural sources and biomass burning for 2008 in Tg for a C-IFS (CB05) run at T255 resolution. Anthropogenic NO emissions contain a contribution of 1.8 Tg aircraft emissions and 12.3 Tg (5.7 Tg N) lightning emissions (LiNO) is added in the biomass burning columns (Flemming et al., 2015).

The dry deposition velocities in this study are calculated from monthly mean values for a one-year simulation of the TM5 model, using surface input data such as wind speed, temperature, surface roughness and soil wetness as described in Michou et al., (2005).

For large aerosols, the most efficient removal process is gravitational settling (sedimentation). This is calculated in IFS following the approach described in Morcrette et al., (2009) for ice sedimentation.

3.3.4 Wet deposition

Wet deposition is the removal of soluble and scavenged constituents by precipitation. It includes in-cloud scavenging, evaporation by rain or snow and below-cloud scavenging by precipitation. In C-IFS wet deposition is based on the Harvard wet deposition scheme where both convective and large-scale precipitation are simulated in the same way (Jacob, , Liu, , Mari, & , Yantosca, 2000).

The input fields are calculated in the IFS cloud scheme (Forbes et al., 2003) and include total cloud and ice water content, rain water content, snow water content, precipitation fraction and cloud fraction. Washout, evaporation and rainout are calculated after each other and the amount of trace gases dissolved in cloud droplets is calculated using Henry's-law-equilibrium with the coefficients taken from Sander et al., (2003).

3.3.5 CB05 chemical scheme

Due to the complexity of the chemical mechanisms required for simulations of reactive gases, a coupled system with a chemical transport model (CTM) (MOZART) and the IFS using the OASIS4 coupler software was initially developed, known as IFS-MOZART. The IFS provided the meteorological data and updated mixing ratios for the tracers while, the coupled CTM providing initial fields and chemical production and loss rates for reactive gases (Flemming et al., 2009). The coupled system (Stein et al., 2012) has been successfully used to create a long-term reanalysis of atmospheric composition (Inness et al., 2013) and forecasts as well as for several case-studies such as the intense 2010 biomass burning fires in Russia (Huijnen et al., 2010). The coupled approach is, however, computationally expensive due to the numerous interpolations between the two models and the duplicate simulation of transport in both the IFS and MOZART.

Consequentially C-IFS was developed to include the chemistry and physical processes of the CTM into the IFS directly (Flemming et al., 2015). C-IFS is intended to be able to run several chemistry schemes for both the troposphere and the stratosphere. The chemical scheme used in this thesis is a modified version of the CB05 scheme (Carbon Bond mechanism 5), originating from the TM5 CTM (Huijnen et al., 2010). For implementation in C-IFS, CBO5 was modified to include additional reactions and updated reaction rates, these changes are further described in Flemming et al., (2015). In total there are 36 transported chemical species in CB05 and 16 non-transported short-lived chemical species, mainly free radicals. The scheme also adopts a lumping approach for organic species, by defining a separate tracer for each functional group.

For the calculation of photolysis rates an on-line parameterisation for the derivation of actinic flues is used. It applies a Modified Band Approach (Landgraf and Crutzen, 1998), modified for CTMs, which uses 7 absorption bands across the spectral range 202-695 nm with different absorption bands used for cases of large solar zenith angles. The model includes an online radiative transfer calculation using the absorption and scattering components of gases, aerosols and clouds. This allows the Mie-scattering components of clouds and aerosols to be considered. For aerosols either a climatology field or online aerosol fields can be used in the photolysis calculation.

CB05 is not suited for stratospheric chemistry, as it includes no halogens and no photolytic destruction at wavelengths below 220 nm. To obtain realistic stratospheric boundary conditions stratospheric O_3 is parameterised through a Cariolle scheme (Cariolle & Teyssèdre, 2007).

Gas-aerosol partitioning is calculated using a version of the Equilibrium Simplified Aerosol Model (EQSAM) (Metzger et al., 2002a, 2002b), with only the partitioning between HNO_3 and the nitrate aerosol (NO^-_3) and between NH_3 and the ammonium aerosol (NH^+_4) is calculated. SO_4^{2-} is assumed to remain completely in the aerosol phase, because of its low vapour pressure.

3.3.6 IFS-AER aerosol scheme

As part of the GEMS, MACC and now CAMS project the IFS has been extended to include a number of tracers representing aerosols which are advected by the model dynamics and interact with various physical processes. A complete description of the IFS-AER aerosol scheme is included in Morcrette et al., (2009).

The physical parameterisation of aerosols in IFS-AER is based on the LOA-LMDZ model (Reddy et al., 2005). Five different types of aerosol are included sea salt, dust, organic carbon, black carbon and sulphate aerosols. A bin representation is used for sea salt, 3 bins with limits of 0.03, 0.5, 5 and 20 μm, and for dust, 3 bins with limits of 0.03, 0.55, 0.9 and 20 μm. These limits are chosen to roughly represent 10%, 20% and 70% of the total mass of each aerosol type. For organic and black carbon, hydrophobic and hydrophilic components are considered with the hydrophobic part transformed to the hydrophilic with a time constant of 1.16 days. Therefore, aerosol mixing, unlike reality, is only treated implicitly. A simplified representation of the sulphur cycle is included with two variables sulphur dioxide (SO_2) and sulphate aerosol (SO_4^{2-}).

Sea-salt production in IFS-AER is parameterised from the 10-m wind speed at the free ocean surface following (Monahan et al., 1986). For the production of dust a parameterisation from (Ginoux et al., 2001) is considered, based on the surface wind and the areas likely to produce dust are diagnosed as snow-free land with at least 10% bare soil and the soil moisture below the wilting point. Sources for the other aerosol types are taken from emission inventories described in Section 3.3.2. Organic matter is emitted as 50% hydrophobic and 50% hydrophilic, while for black carbon 80% is hydrophobic and 20% hydrophilic. Organic carbon is related to organic matter with a ratio of 1.5. The different loss processes in IFS-GEMS are based on the sedimentation, dry and wet deposition schemes described in Sections 3.3.4 and 3.3.5.

3.4 Global fire assimilation system (GFAS)

Emission fluxes in GFAS are calculated using Fire Radiative Power (FRP) from the MODIS instrument on the Terra and Aqua satellites and fire-type dependent emission factors, the method for this is summarised here but a detailed description can be found in Kaiser et al., (2012). Daily GFAS (v1.2) biomass burning emissions are used in this study and comparisons to other emission datasets are discussed in Chapter 2.

The MODIS instruments on the polar orbiting satellites AQUA and TERRA observe thermal radiation around 3.9 and 11 μm which is used to produce the NASA fire product MOD14 (Louis Giglio et al., 2006) which contains quantitative measurement of FRP, representing fires observed by the satellite in units of Watts for each satellite pixel. The model aggregates observed FRP observations onto a global grid of 0.5^{o} and then performs a clustering process to sensor pixels with valid observations to correct for the MODIS bow-tie effect and partial cloud/ice/snow/water cover of a grid cell.

The two MODIS sensors on terra and aqua satellites provide 4 daily overpasses over most places on the earth, although data at the edge of the swath show significant degradation. As there are gaps in FRP observations due to the sun-synchronous orbit of Terra and Aqua satellites and cloud cover a Kalman filter is used to obtain additional information from earlier observations. The model assumes persistence of FRP from one timestep to another as little information can be assumed about the day-to-day variability. The timestep for the model is a single day so errors in the diurnal cycle of fires does not contribute to the error. This leads to an emission file with data with a one day temporal resolution, which is averaged into 6 hour emission files when implemented into C-IFS. This leads to a poor diurnal cycle of fire emissions, which is known to vary sharply between day and night, and consequently leads to emissions being too large during the night and too small during the day (Andela, et al., 2015) . Additionally, this would mean less photochemical production of O_3 as more of its precursors will be emitted into the model when photochemistry cannot occur. The underlying assumption used in GFAS is that the electromagnetic radiation emitted by fires is related to the consumption of burned biomass (Giglio et al., 2006). FRP has been quantitatively linked to the dry matter combustion rate through a universal factor of 0.368 kg MJ^{-1} (Martin J. Wooster et al.,

2005) calculated from ground-based experiments linking FRP observations directly to the fuel consumption. Linear regressions between GFAS FRP and GFED dry matter combustion rates have been used to determine conversion factors to create dry matter combustion rate for eight different land cover classes (Heil, Werf, Wooster, Schultz, & Gon, 2010). However, this requires the assumption that GFED describes the real-fire activity sufficiently accurately to interpret the conversion factors. Using emission factors (Andreae & Merlet, 2001), the dry matter combustion rate can be used to calculate emission fluxes of different species.

3.4.1 Plume rise model

GFAS version 1.2 provides information from a Plume Rise Model (PRM) which is solved offline and provides information that can be used by a CTM to estimate the injection height of a fire plume. Figure 3.2 shows a schematic sketch of how a fire plume is modelled showing the two kinds of inputs required, information about the environment (temperature and wind) and about the fire (FRP and fire areas) and the injection height parameters outputted for models (top of the plume, mean height of max injection and bottom of the plume). Plume detrainment is the quantity of smoke shed by the plume to the environment and the mean height of max injection is defined as the plume height where detrainment exceeds half of its maximum value.

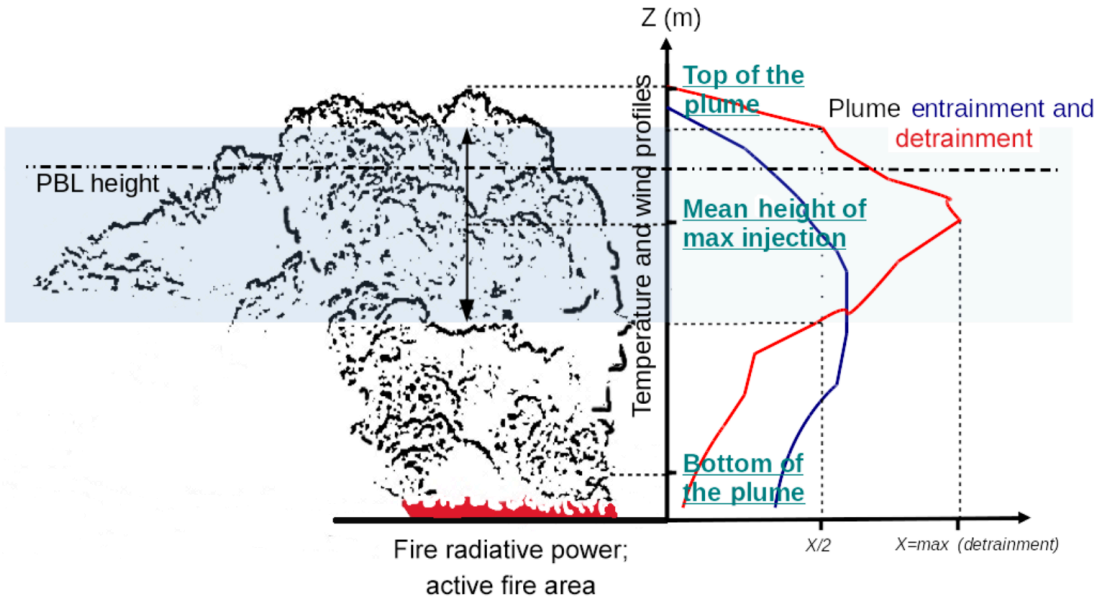

Figure 3.2 Schematic of an algorithm estimating plume injection height parameters. The fire input (fire radiative power and fire area) and the environmental input (temperature and wind profiles) are shown, as well as the possible output of the model: detrainment and entrainment profiles, with the derived quantities (bottom of the plume, top of the plume, mean height of maximum injection), or injection height, usually defined as the top of the plume (Rémy et al., 2016).

The PRMv2 used in this study is described in (Paugam, Wooster, & Atherton, 2015) and compared to other injection height models in (Paugam et al., 2016). The mode consists of a one-dimensional cloud-resolving model (Freitas et al., 2007; Freitas, Longo, Trentmann, & Latham, 2010) based on the original plume model of (Latham, 1994) in which equations for vertical momentum, first thermodynamic law and continuity of water phases are solved explicitly. The model is also forced at the surface by satellite-derived fire parameters Convective Heat Flux (CHF) and active fire area. The model output is four prognostic variables: vertical velocity, temperature, horizontal plume velocity and the radius of the plume are forecast by the PRM and are used to calculate the parameters seen in Figure 3.2. For this study, the PRM is run at 100m vertical resolution with a maximum height of 20 km, atmospheric profiles are taken from 3-h European Centre for Medium-Range Forecasts (ECMWF) data, with the fire derived parameters derived from GFAS (Rémy et al., 2016).

3.5 Composition data assimilation in C-IFS

The IFS has used an incremental formulation of 4-D variational data assimilation since 1997 (Inness et al., 2013). 4D-var is described in detail in Section 3.2.2, the incremental approach is a method to reduce the calculation cost of 4D-var for operational implementation in numerical weather prediction (Courtier, 1994). The full 4D-var problem is approximated by a series of minimisations of complex quadratic equations by describing them with simpler models at a lower resolution, known as tangent-linear models. This minimisation has been shown to provide a similar analysis to full 4D-var, with differences dependent on the variability of the observations (Lawless, 2005). In its incremental formulation, the minimisation problem is written as a function of the correction **δX** from an initial first guess $\mathbf{X^g}$;

$$\mathrm{J}(\delta \mathrm{x}) = \frac{1}{2}(\delta \mathrm{x} + \mathrm{b})^{\mathrm{T}}\,\mathrm{B}^{-1}(\delta \mathrm{x} + \mathrm{b}) + \sum_{tobs=1}^{M} \frac{1}{2}(\mathrm{H}\delta \mathrm{x} + \mathrm{d})^{\mathrm{T}}\mathrm{R}^{-1}\,(\mathrm{H}\delta \mathrm{x} + \mathrm{d}) \qquad (3.8)$$

Where $b = \mathrm{x}^{g} - \mathrm{x}^{\mathrm{b}}$ and $d = \mathrm{Hx}^{g} - \mathrm{y}$.

In IFS a non-linear integration of the first guess $\mathbf{X^g}$ provides the departures **d,** from the observations **y**, as well as the trajectory about which the tangent linear model and adjoint model can be linearized. Using the trajectory and **B** the linearized cost function (equation 3.7) is minimised at low resolution using a iterative algorithm based on Lancozos conjugate gradient algorithm (equation 3.6) This is known as the inner loop and the resulting increment **δX** is interpolated back to high resolution and added to the current first guess $\mathbf{X^g}$. This is known as the outer loop, which is repeated until the analysis $\mathbf{X^a}$ is obtained (Trémolet, 2007), via convergence criteria outlined in (Fisher, 1998).

3.5.1 Total column reactive gas assimilation

O_3, CO, NO_x and HCHO were chosen for assimilation into C-IFS due to their key roles in the chemistry of the atmosphere, described in Section 2.2.2, and because they have been measured by space-borne instruments with sufficient density and continuity for assimilation. The implementation of chemistry modules in C-IFS is discussed in Section

3.4. For the previous IFS analysis, the 8-year MACC analysis (Inness et al., 2013), many different satellite profiles were used in the assimilation. Even though the benefits of correlations between different assimilated species has been shown (K. Miyazaki et al., 2015), the assimilation of the different species in C-IFS are at the moment univariate i.e. compounds are assimilated independent of one another. The different satellite products assimilated in this study are shown in Table 3.2.

Instrument	Satellite	Species	Type
MODIS	EOS-AQUA/TERRA	AOD, FRP	Column
MLS	EOS-AURA	O_3	Profiles
OMI	EOS-AURA	O_3	Total column
MOPITT	EOS-TERRA	CO	Total column
OMI	EOS-AURA	NO_2	Total column

Table 3.2 Composition satellite data assimilated in 'analysis' experiments for this study.

The Ozone Monitoring Instrument (OMI) is a nadir-viewing imaging spectrograph sensitive to wavelengths from 270 to 500 nm at 0.5 nm resolution (Levelt et al., 2006). OMI is on board the NASA Aura satellite which is part of a formation of sun-synchronous-orbit satellites that cross the equator around 13:30, named the A (afternoon) Train. OMI maps O_3 and NO_2 profiles at 36 × 48 km spatial resolution. The Earth Observing System Microwave Limb Sounder (EOS-MLS) is a limb-sounding instrument that provides information on the Earth's upper troposphere, stratosphere and mesosphere (Waters et al., 2006). The instrument observes thermal emission in 6 broad spectral regions centred near 118, 190, 240 and 650 GHz and 2.5 THz. By assimilating both MLS data, with vertical resolved information of stratospheric O_3, and total column O_3 from OMI tropospheric O_3 can also be constrained.

MOPITT (Measurements Of Pollution In The Troposphere) is a nadir-sounding instrument, which measures IR radiation from the Earth, using correlation spectroscopy to calculate total column observations and profiles (Deeter et al., 2010). The MOPITT

instrument is mainly sensitive to free-tropospheric CO, especially in the middle troposphere and its averaging kernels are included in the observation operator.

In order to solve the cost function for the reactive gases, observation operators, observation error covariance matrices and background error covariance matrices need to be calculated for each tracer. The observations used in C-IFS are all column or partial column satellite data. Therefore, the observation operator is a simple vertical integral of the background model between the top and bottom pressure of the satellite column at the time and location of the observation. Averaging kernels, when provided with the observations, are also used in the observation operator, to remove the impact of the retrieval first guess in the assimilation. By transforming the model field to have the same vertical resolution and background dependence as the satellite data, the model field and retrieved quantity can be compared without influence from the satellite *a priori*.

3.5.2 AOD assimilation

The aerosol information assimilated in C-IFS is aerosol optical depth (AOD), a measure of the extinction of the solar beam by aerosol particles. It is a dimensionless number that is related to the amount of aerosol in the vertical column between the instrument and the surface. The AOD product assimilated is the 550-nm band from MODIS (Moderate Resolution Imaging Spectroradiometer). The MODIS instrument provides high radiometric sensitivity in 36 spectral bands between 0.4 and 14.4 μm at nadir. Like MOPITT, MODIS is on the Aqua and Terra satellites, with sun synchronous orbits. Different retrievals with different accuracies are used for MODIS AOD over land and ocean with an additional retrieval, deep blue, used over bright land surfaces. MODIS AOD, along with fire emission datasets, has been used to characterise biomass burning emissions (Paton-walsh et al., 2012). In comparisons between observed MODIS AOD and PM2.5 ground-sites an underestimation in MODIS AOD has been identified from severe fire events, this is due to its cloud removal algorithm often identified thick (AOD >4.0) fire plumes as clouds (Donkelaar et al., 2011).

A full description of the aerosol assimilation system is documented in Benedetti et al., (2009).The background aerosol covariance matrix **B** was derived from forecast

differences. Six months of 2-day forecasts were run and the differences between the 48-h and the 24-h are used as statistics to estimate the background error (Benedetti et al., 2009). The observation operator for AOD is based on pre-determined aerosol optical propertires for each of the individual aerosol species using Mie theory (i.e. all particles are assumed spherical in shape). Mass extinction coefficents for each species are retrieved for the computed relative humidty at 500 nm and then multiplied by the aerosol mass at the observation time and location before being integrated vetically. The total AOD is the sum of the single species optical depths.

$$T_\lambda = \sum_{t=1}^{N} \int_{Psurf}^{0} \alpha_{ei}(\lambda, RH(p)) r_i(p) \frac{dp}{g} \tag{3.9}$$

Where **N** is the total number of aerosol species **α** is the mass extinction coefficient, **r** is the mass-mixing ratio, **dp** is the pressure of the model layer, **psurf** is the pressure at the surface and **g** is the gravitational constant.

IFS-AER (Morcrette et al., 2009) is the current operational aerosol scheme used in C-IFS. The aerosol assimilation in IFS-AER uses the total aerosol mixing ratio, the sum of the 11-aerosol species, as the control variable. Including all 11 tracers as control variables to use in the minimisation would constitute a heavy burden on the analysis, increasing the size of the control vector and background error statistics. The total column aerosol approach requires two assumptions, (1) that aerosol mass in the model needs to be conserved over the 12-h assimilation window and (2) the relative contribution of a single species to the total mixing ratio needs to remain constant.

The mixing ratios of all the species are then used to calculate the total optical depth using the pre-calculated optical properties. The tangent linear run is started from the background $\mathbf{X^B}$, to compute the perturbation in the optical depth, compared to MODIS. The perturbation in optical depth is then passed through the adjoint routine to compute the gradient for each individual species. The total aerosol mixing ratio gradient is then obtained based on the gradient of each individual mixing ratio and their fractional contribution to the total mass. The gradient with respect to the total mixing ratio is then

used in the minimisation and the resulting increment is used to update the individual species. This is repeated until the convergence criteria are met.

3.6 SAMBBA flight campaign

The SAMBBA (South AMerican Biomass Burning Analysis) was a field campaign using the FAMM BAe-146 aircraft based in Porto Velho, the capital of the Brazilian state Rondonia, in the upper Amazon river basin. This is a region with extensive biomass burning due to forest clearance. The campaign involved nineteen flights between September 14 and October 3, 2012. 2012 was not an EL Niño year and as such was not a major drought year, with the total fire emissions similar to the average burned area of previous years (Andela et al., 2017; Pereira et al., 2016).

3.6.1 Instrumentation

The suite of aircraft instruments used in this study is summarised in Table 3.4. For aerosols, the sub-micron non-refractory aerosol composition was measured by an Aerodyne Research (Billerica, MA, USA) compact Time of Flight Aerosol Mass Spectrometer (cToF-AMS) (Drewnick et al., 2005), providing information on the physical nature of the major non-refractory aerosol species, measurement uncertainties are approximately 30% (Middlebrook et al., 2012).

The Single Particle Soot Photometer (SP2), developed by Droplet Measurement Technologies (Boulder, CO, USA), was used to measure number and mass concentrations of refractory black carbon (rBC). The measurement uncertainty is approximately 30%.

For the gas-phase, carbon monoxide (CO) was measured using an Aero-Laser AL5002 VUV resonance fluorescence gas analyser, developed by Aero Laser (Garmisch-Partenkirchen, Germany), with an uncertainty of 2%. Ozone (O3) was measured using the Thermo Environmental Instruments (TE149C) developed by Thermo Fisher Scientific (Waltham, MA, USA), the measurement uncertainty is measured at 5%. Nitric oxide and nitrogen dioxide were measured from air collected using a GC-MS from the University of York, with uncertainties calculated to be 15% for NO and 20% for NO_2.

4 Instrument	Measurement	Units	Temporal resolution
SP2	BC	μg sm^{-3}	1s
cToF-AMS	OM	μg sm^{-3}	~30s in level runs ~10s during profiles
AL5002-VUV	CO	ppbv	1s
TE149C	O_3	ppbv	1s
GCMS	NO	ppbv	1s
GCMS	NO_2	ppbv	1s

Table 3.3 Table of instrumentation used during SAMBBA flight. Full instruments names are Single Particle Soot Photometer (SP2), compact Time of Flight Aerosol Mass Spectrometer (*cToF-AMS),* Aero Laser (AL5002-VUV), Thermo Environmental Instruments (TE149C) and The Gas Chromatograph- Mass Spectrometer (GC-MS)

3.6.2 Flight information

The key locations during the flight campaign are shown along with the flight track from the 19 flights in Figure 3.3. The flights covered a large geographical area spanning different biomes, shown in Figure 3.4. Based on these different biomes the flight data can be divided into 3 different regions. The majority of flights took place over the Western Amazon (longitudes 67.9°W to 54.5°W) and mainly characterised by tropical forest fires from fire clearance. Flights B741-B743 flew over Eastern Brazil, spanning longitudes 49.25°W to 46.0°W characterised by cerrado (savannah) vegetation and a fire regime. Additionally, Flight B735 flew from Porto Velho to Manaus sampling the background

biogenic emissions in the Northern Amazon, a remote region of pristine rainforest, away from major fire hotspots.

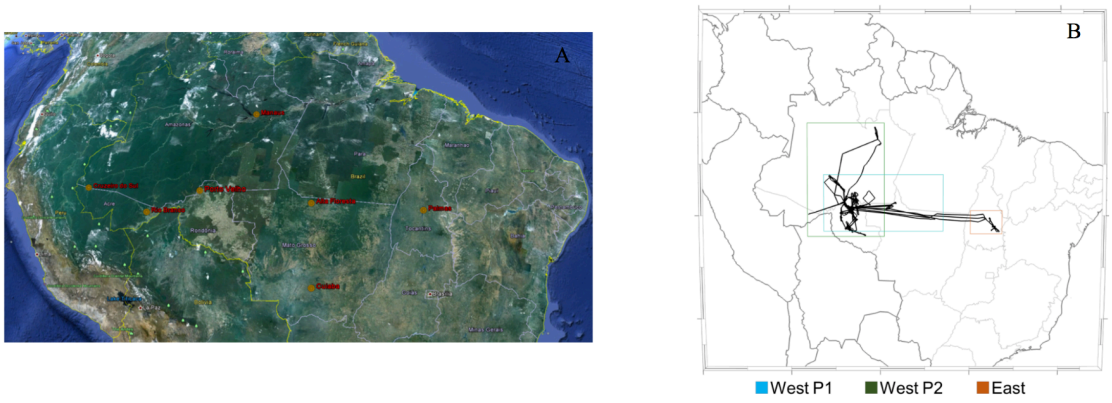

Figure 3.3 Flights and key locations during the SAMMBA campaign Sept-Oct 2012. (a) Key locations during the campaign © Google Earth. (b) Flight tracks of the 19 SAMBBA flights with colours indicating the different phases of the campaign (Darbyshire & Johnson, 2012).

The western flights can be further divided based on the meteorological conditions during the campaign, with Phase I (04/09/12 - 22/09/12) during the height of dry season, and Phase II (23/09/12 - 03/10/12) during the wet-to-dry transition (Brito et al., 2014). Precipitation from TRMM during the two different phases is shown in Figure 3.5. Unlike the western region, the eastern region remains relatively dry during Phase II of the aircraft campaign.

The SAMBBA flights can also be characterised by the broad flight operation type, which have been manually identified by Darbyshire et al. (2016) and are illustrated by

1) **Profile:** ascents and descents.

2) **SLR:** Straight and Level Runs within the convective boundary layer (coarsely defined as <4.25 km).

3) **HALT:** High ALtitude Transits, straight and level runs above the convective boundary layer.

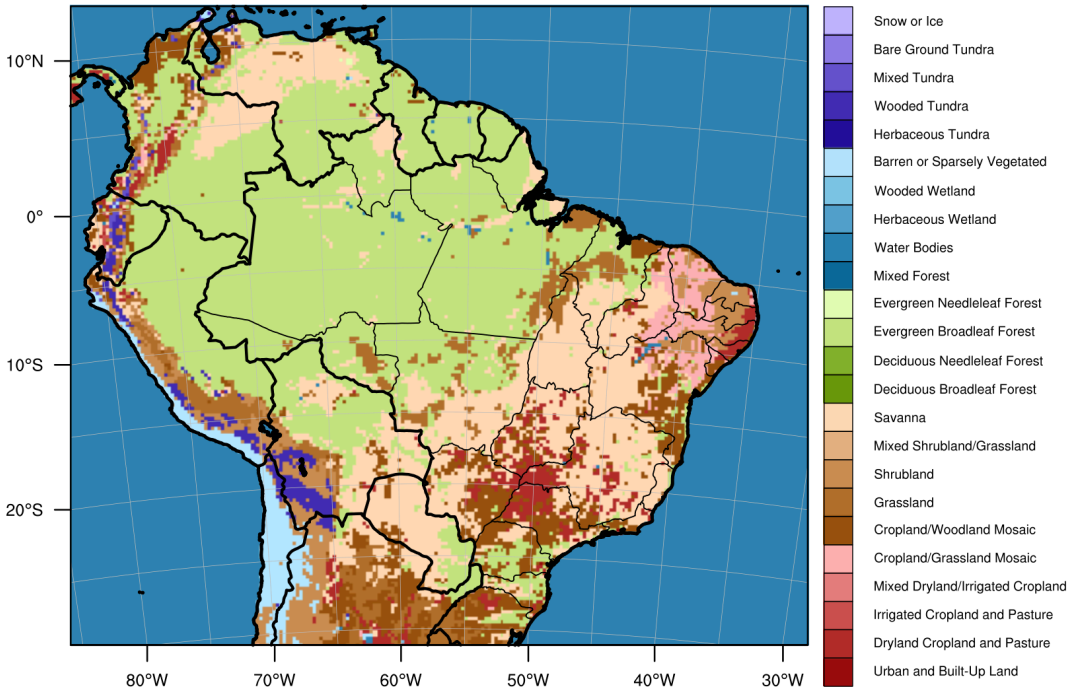

Figure 3.4 The Amazon coloured by 24 USGS land use categories. The southern Amazon, coloured green, is the main region of deforestation burning, corresponding to the West-central Brazilian states and northern Bolivia. The East-central Brazilian states, coloured pale-brown, are the main regions of cerrado burning. Figure taken from Archer-Nicholls et al., (2015).

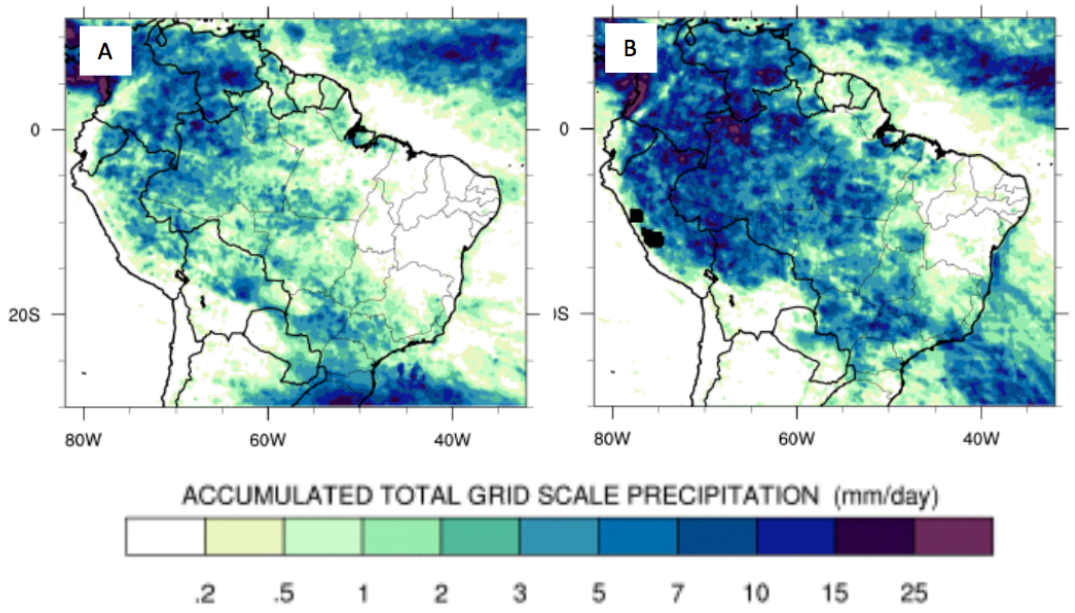

Figure 3.5 Precipitation during the SAMBBA campaign from Tropical Rainfall Measuring Mission (TRMM). A: (04/09/12 - 22/09/12): Representative of dry season Fire radiative power. B, Phase 2 (23/09/12 - 03/10/12): Transition to the wet season. Taken from Archer-Nicholls et al., (2015).

3.6.3 Individual flights

A list of the different flights detailing their locations and main flight objectives that were classified in Section 3.6.2 are shown in **Error! Reference source not found.**. As can be seen in Figure 3.6b the majority of flights took place around the Rondonia region of Brazil around Porto Velho where the campaign was situated. From Porto Velho the aircraft could cover radial distances of 200-300km or a single high-altitude journey of 800km.

#	Flight	Date	Departure /Return (Z)		Take Off /Land		Duration	Objectives Achieved
1	b731	14/09/2012	14:00	18:35	PVH	PVH	03:47	Regional haze (elevated and BL), and fresh smoke.
2	b732	15/09/2012	14:30	18:40	PVH	RBR	05:32	Regional haze (elevated and BL), mid-level cloud sampling.
3	b733	16/09/2012	12:00	15:55	RBR	PVH	00:54	Regional survey of aerosols and clouds (lidar)
4	b734	18/09/2012	12:00	16:15	PVH	PVH	03:56	Radiative closure, radiometric inversion of size distribution, regional haze (elevated and BL), fresh smoke sampling, IRC images, plume rise
5	b735	19/09/2012	12:00	15:40	PVH	MAO	03:40	Biogenic emissions, characterization of Amazonian "background" / inflow, comparisons with Manaus tower
6	b736	19/09/2012	17:10	19:15	MAO	PVH	01:26	Regional survey of aerosols and clouds (lidar).
7	b737	20/09/2012	14:45	18:45	PVH	PVH	03:48	IR fire images, plume rise, fresh smoke emissions, transformations in plume, CALIPSO validation, regional haze, radiometric inversion of size distribution.
8	b738	22/09/2012	16:00	19:30	PVH	PVH	01:59	Regional haze (BL)
9	b739	23/09/2012	12:00	16:00	PVH	PVH	03:56	Fresh smoke (BL), IR fire images, smouldering emissions.
10	b740	25/09/2012	11:45	15:00	PVH	PVH	03:05	Regional haze (elevated and BL).
11	b741	26/09/2012	13:00	16:30	PVH	PMW	03:15	Regional survey of aerosol, cloud (lidar) and meteorology (dropsondes).
12	b742	27/09/2012	13:00	16:30	PMW	PMW	03:26	Fresh smoke from Savanah fires, plume rise, regional haze (elevated & BL), radiometric inversion of size distribution.
13	b743	27/09/2012	18:00	21:30	PWM	PVH	03:26	Regional survey of aerosol, clouds (lidar) meteorology (dropsondes) and plume rise.
14	b744	28/09/2012	13:00	16:30	PVH	PVH	03:45	Biogenic emissions over Rondonia national park forest, chemical transformations and BL processes through the diurnal cycle. Elevated haze layers. Radiometric inversion of size distribution.
15	b745	28/09/2012	18:00	21:30	PVH	PVH	03:27	
16	b746	29/09/2012	13:00	17:00	PVH	PVH	03:44	Fresh smoke from smouldering emissions, IR fire images, regional haze (elevated & BL), regional survey of aerosol ,cloud (lidar) and meteorology (dropsondes).
17	b747	01/10/2012	15:00	16:30	PVH	PMW	03:09	Regional survey of aerosol, clouds (lidar) meteorology (dropsondes).
18	b748	02/10/2012	13:00	17:00	PMW	PVH	03:25	Regional survey of aerosol, clouds (lidar) meteorology (dropsondes). Fresh smoke from smouldering emissions. Radiometric inversion of size distribution. IR fire images.
19	b749	03/10/2012	14:00	17:30	PVH	PVH	03:47	Biogenic emissions over Amazonian rainforest, chemical transformation and BL processes through the diurnal cycle. Characterization of Amazonia "background" / clean inflow.
20	b750	03/10/2012	19:00	22:30	PVH	PVH	03:09	

PVH - Porto Velho PMW - Palmas MAO - Manaus BRB - Rio Brancho

SAMPLING BIOMASS BURNING EMISSIONS | SAMPLING OF BIOGENIC EMISSIONS | HIGH ALTITUDE REMOTE SENSING

Table 3.4 Summary of SAMBBA flights and objectives achieved. Colours indicate the main focus of the flight (Darbyshire & Johnson, 2012).

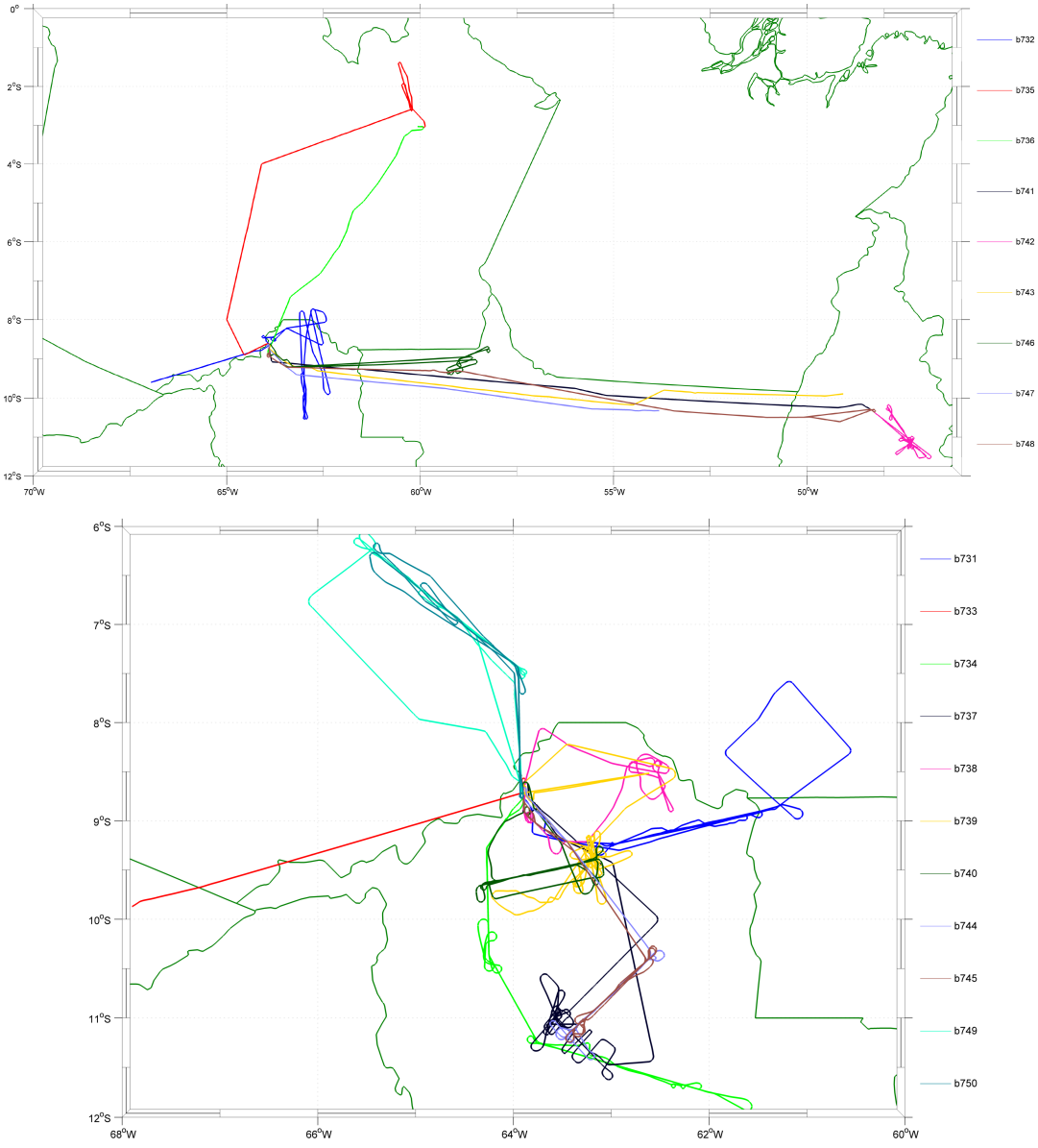

Figure 3.6 Flight maps for the SAMBBA flight campaign. a) shows the long distance flights during the campaign which sample regions close to Las Palmas and Rio Brancho, the plotted box has dimensions of 2700x667km. b) shows flight local to Porto Velho, the plotted box has dimensions of 880x667 km. Originally from (Darbyshire & Johnson, 2012).

3.6.4 Data processing

For this work, an offline analysis tool was developed to compare C-IFS output to SAMBBA aircraft measurements. This analysis grouped and averaged the observations into either 1-minute or 10-minute means, to account for the different temporal scale of the instruments and to reduce the overall number of data points. First, the closest C-IFS model grid point (in terms of latitude and longitude) for each grouped observation point is found and then the model fields are linearly interpolated to both the time and altitude of the averaged reading. The 1-minute means were used to create vertical profiles, flight-tracks and averages while the 10-minute means were used as individual data points for model-observation correlations.

Raw data from flights B737, near Porto Velho and B742, near las Palmas is shown in Figure 3.7. Averaged data for comparison can be seen in Chapter 4 and 5. The very large in plume concentrations of BC, OM and CO are not generally seen in the flight averaging and generally reduce the observed concentrations in plume. However, due to the coarse temporal resolution of the model this averaging provides a more suitable comparison.

Additionally, a limitation of this study is the use of a global model with 80x80km resolution. This makes the modelling of fire plumes, which are generally smaller than a km in width, very difficult as the high concentration gradients of these plumes are washed out by low background concentrations. This, as with the coarse temporal resolution, is helped by the averaging of the SAMBBA data which reduces the impact of the large concentrations of species in-plume. However, despite this the coarse resolution of the model will have consequences on the model's chemistry as nitrogen oxide concentrations will be more spread out over a model grid. This would lead to more ozone formation away from the plumes and smaller chances of ozone titration by excess nitrogen oxides within plumes.

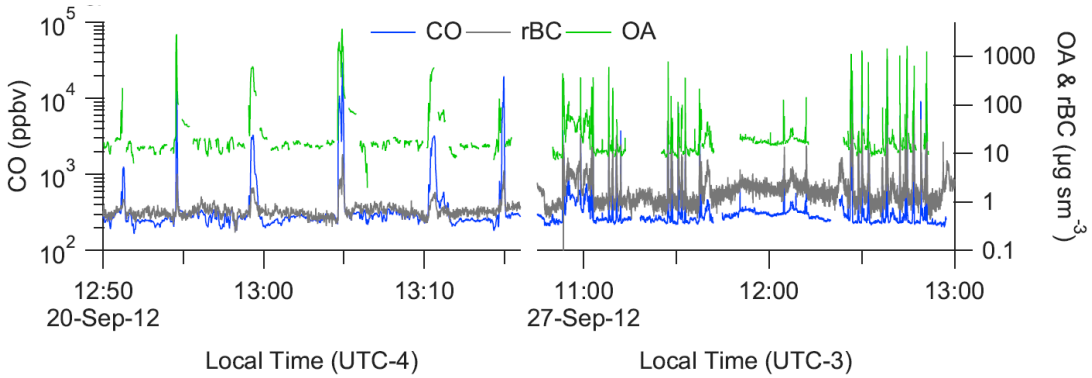

Figure 3.7 Raw data time series of CO, rBC and OA during the near-field fire sampling periods of SAMBBA flights b737 (left) and B742 (right). Orginally from (Hodgson et al., 2017).

4 Fire influences on tropospheric ozone during the SAMBBA flight campaign

4.1 Introduction

This chapter investigates the impact of fire emissions on ozone formation over the Amazon rainforest using models, satellite data and in-situ observations from ground sites and the SAMBBA aircraft campaign. The use of the 4D-var data assimilation system in the C-IFS model also provides an opportunity to combine model and satellite data to produce analysis fields for O_3, CO and NO_x providing an opportunity to evaluate the analysis against independent observations and calculate more accurate fire related metrics using analysis data.

Previous studies (Ainsworth et al., 2012; Pacifico et al., 2015) have shown, using earth system models the impact of O_3 concentrations on gross primary production (GPP) in South America. Evaluated against surface observation sites these ESM show an overestimation of surface O_3, particularly at night. These surface observation and flux tower sites are sparse in South America, making it difficult to observe the impact of different regions and observe the influence of fires on O_3 formation in older plumes downwind of fires, which have shown to be more efficient and can impact both vegetation and people downwind of fires as well as heavily changing the oxidative capacity of the local troposphere. Without detailed observations of O_3 and its precursors, it is difficult to validate the skill of fire emission databases, and the accuracy of modelled O_3 chemistry. The in-situ observations from the SAMBBA campaign and the new tropospheric OMI O_3 retrievals provide an opportunity to accurately estimate O_3 concentrations over the Amazon and provide an opportunity for model validation.

The use of Global Fire Assimilation System (GFAS) fire emissions in this study provides daily fire emission derived from satellite observations rather than historical or monthly mean emissions used in previous studies (Pacifico et al., 2015a). This should reduce the uncertainty of O_3 precursor emissions associated with fire location, seasonality and

magnitude. Earlier validation work with the GFAS fire emissions have focussed on carbonaceous aerosol and CO rather than NO_x, the most important O_3 precursor in this region, and have suggested significant biases associated with emission factors used in GFAS (Huijnen et al., 2012; Johannes W Kaiser et al., 2011; Rémy et al., 2016).

The chapter is structured as follows. Section 4.2 summarises the different C-IFS and TOMCAT simulations used. Section 4.3 describes the impact of fire emissions on CO, NO_x and O_3 model fields during the flight campaign. Section 4.4 compares C-IFS CO, NO_x and O_3 to satellite observations and discusses the impact of composition assimilation. Section 4.5 looks at observations from the SAMBBA flight campaign, comparing values to previous campaigns and using the observations to validate C-IFS model and analysis fields. Section 4.6 describes the TOMCAT sensitivity experiments, varying NO_x emission and injection and investigating the impact on O_3 concentrations. Section 4.7 summarises the results from this chapter.

4.2 Model experiments

Information on the different experiments used in this chapter is shown in Table 4.1. Two different types of model experiments are used in this chapter, the analysis mode and the forecast mode. The analysis mode contains the 4D-var data assimilation system described in Chapter 3 while the forecast mode runs forward in time from an analysis without being constrained any further by observations. In these retrospective runs the forecast meteorology is relaxed to ERA-Interim, to maintain accuracy at a smaller computational cost. Even without composition assimilation, the analysis mode is computationally expensive so the forecast mode has been used to test different model parameters and emission scenarios. For an accurate assessment of the impact of assimilation, two different analysis experiments were run, one with composition and meteorological data assimilated (AN_METCOM) and one with only meteorological data assimilated (AN_MET).

Name	Type	Emissions	Injection	Description
AN_METCOM	analysis	GFAS	Surface	Composition and meteorology data assimilated.
AN_MET	analysis	GFAS	Surface	Only meteorological data assimilated.
FOR	forecast	GFAS	Surface	Relaxed forecast.
FOR_NBB	forecast	GFAS	Surface	No biomass burning emissions.

Table 4.1 Experiments run over the SAMBBA campaign period September - October 2012. Experiments designated 'analysis' are run in the analysis mode where observations constrain certain model parameters, the 'forecast' experiments are run using the forecast mode and the meteorology is relaxed to ERA-INTERIM.

4.3 Impact of fire emissions

4.3.1 Carbon monoxide

CO is used in this chapter as a proxy for biomass burning emissions due to being a moderately long-lived species, with a lifetime on the order of months (IPCC 2014). This is long enough to permit long-range transport into the upper troposphere but short enough to not be thoroughly mixed throughout the troposphere (Koppmann et al., 2005). As a major carbon species emitted from fire, CO there was sufficient literature data available in Andreae & Merlet, 2001 to calculate emission factors for each fire type. Additionally, it is used as a reference species to extrapolate emission data for other species when there is no published data (Johannes W Kaiser et al., 2011). Overall, this means that CO GFAS emission factors and fluxes are relatively accurate compared to other emitted species. We can therefore assume that large biases in CO emissions indicate a more systematic bias in GFAS such as fire detection or emission injection height rather than a species specific bias such as emission factors, as CO emission factors are generally well constrained.

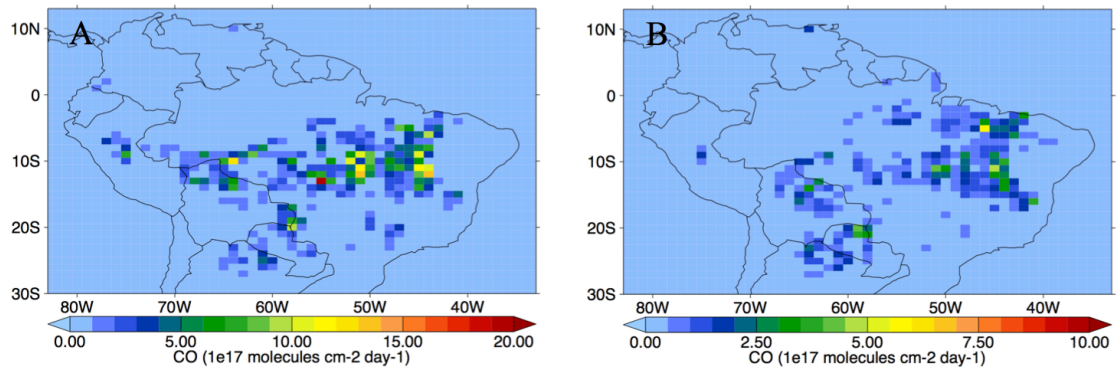

Figure 4.1 CO fire emissions during different SAMBBA flight campaign phases. Average GFAS CO fire flux (molecules cm^{-2} day^{-1}) during the SAMBBA flight campaign during (a) the dry season (September 1-22) and (b) the dry-to-wet transition (September 23 – October 31).

Figure 4.1 shows the average CO fire emissions during the SAMBBA campaign estimated from experimentally measured emission factors (Andreae & Merlet, 2001) and observed Fire Radiative Power (FRP) from MODIS. The eastern cerrado region has a predicted larger CO flux than the western forest fires due to a higher observed FRP and a larger number of observed fires. The decreases in the CO fire flux from the dry season to the dry-to-wet transition, is more substantial in the western region as there is a more significant increase in rainfall. Pereira et al., 2016 compares CO fluxes over the SAMBBA campaign from multiple different emission inventories, GFAS generally had larger emissions than non-FRP based inventories in the eastern region, but tended to underestimate in the Amazon deforestation area.

Figure 4.2 shows the C-IFS CO field and the impact of fire emissions on CO concentrations during the two campaign phases. The CO concentrations are higher in the west as easterly trade winds push the increases from fires towards the Andes mountain barrier. Figures 4.2e and f show that fires contribute between 40-60% of the total CO in the western Amazon. Higher concentrations of CO are seen during the main fire season with a 19% average reduction from the dry to the wet season. The effect of decreasing fire emissions from the dry to the wet season is seen in Figures 4.2c and Figures 4.2d

with the contribution in the western tropics having a larger decrease than the eastern cerrado. Small contributions of fires are predicted by C-IFS over the southern Atlantic are unlikely from Amazonian fires due to the strongly easterly winds and relate to transported CO from sub-Saharan African fires.

Figure 4.3 shows longitude by height cross section of CO concentrations in C-IFS over the SAMBBA flight domain. As with the total columns, decreases are seen between the dry and the wet season. The largest CO concentrations are near the surface which are significantly impacted by fire emissions, with the eastern cerrado showing larger concentrations than the western tropical fires. Conversely, in the free troposphere (1-3 km) larger concentrations are seen west of 55W with a sharp gradient between the boundary layer and the troposphere predicted in the east. Model predicts only a small contribution of fire emissions to CO concentrations above 4 km. However, this may be impacted by an inaccurate injection height. Overall, fire emissions are a dominant contributor to CO concentrations in C-IFS during the dry season, leading to increased concentrations across South America. As a tracer of biomass burning transport, C-IFS suggest the majority of fire emissions emitted from the Amazon remain over South America.

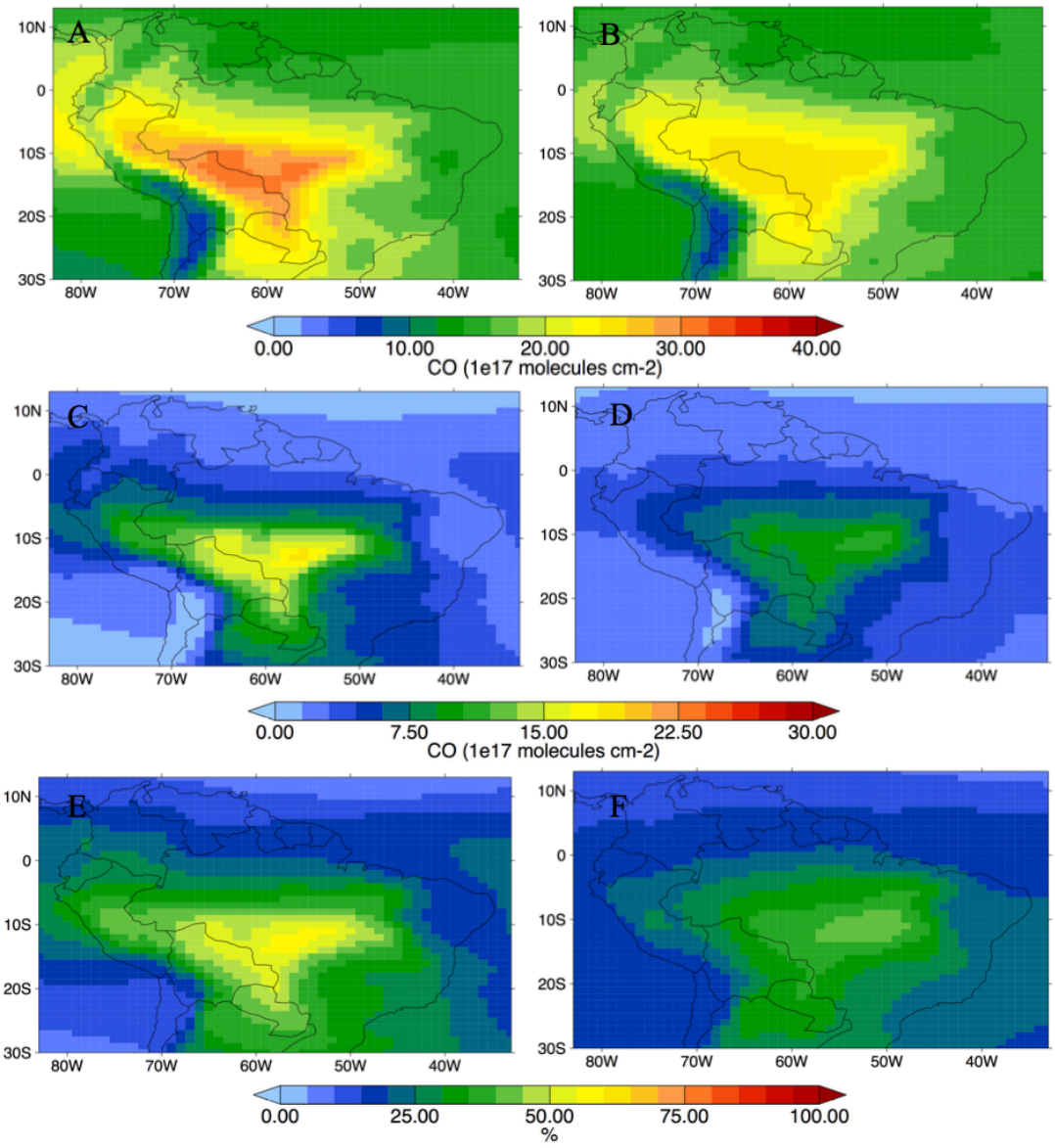

Figure 4.2 The impact of fires on C-IFS simulated CO tropospheric column during the SAMBBA campaign. The left column shows average results from the dry season (September 1-22) and the right column shows equivalent results from the dry-to-wet transition (September 23 – October 31). (a, b) Total column CO (molecules cm^{-2}) from C-IFS simulation FOR. (c, d) Difference in CO column between simulations FOR and FOR_NBB. (e, f) Percentage difference in column CO for panels (c) and (d), respectively.

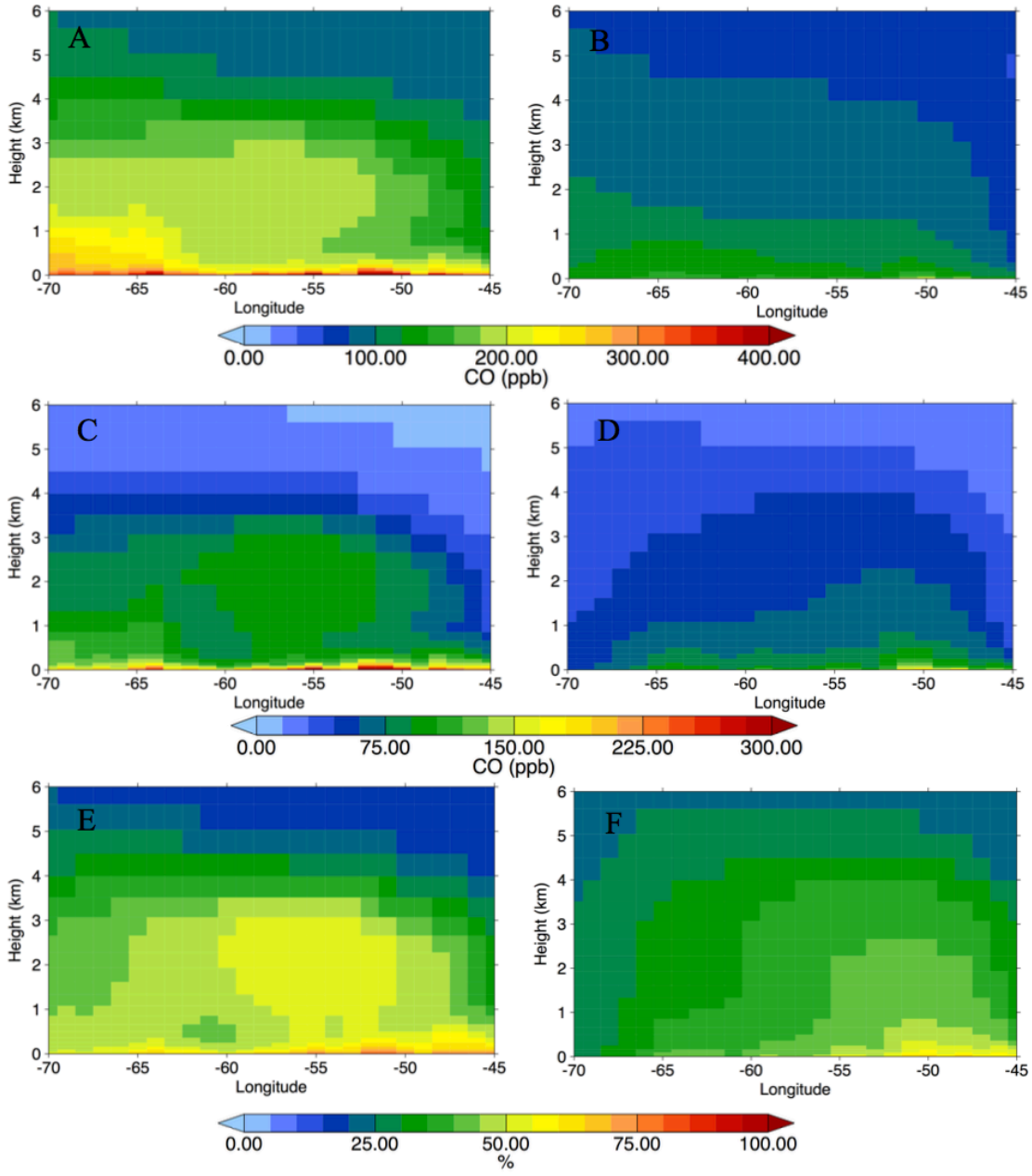

Figure 4.3 The impact of fires on the C-IFS CO latitude/height zonal mean cross section over the latitudes sampled by the SAMBBA flights (-5.5º to -12º). The left column shows average results from the dry season (September 1-22) and the right column shows equivalent results from the dry-to-wet transition (September 23 – October 31). (a, b) CO (ppb) from C-IFS simulation FOR. (c, d) Difference in CO concentrations between simulations FOR and FOR_NBB. (e, f) Percentage difference in CO for panels (c) and (d), respectively.

4.3.2 Nitrogen oxides and O_3 formation

Figure 4.4 shows GFAS NO_x emission fluxes during the SAMBBA campaign. These have the same spatial pattern as the CO fluxes seen in Figure 4.1 as they are derived from the same MODIS FRP product. Compared to the total emission flux, a larger NO_x flux is seen in the eastern region than the CO flux. This is due to larger NO_x emission factors for cerrado/savannah fires (3.9 ± 2.4) compared to tropical forest fires (1.6 ± 0.7) (Andreae & Merlet, 2001). The impact of this flux can be seen in Figure 4.5 (c and d), as larger concentrations of NO_2 are predicted by C-IFS over the cerrado, with wet seasons concentrations of ~3.2 1e15 molecules cm-2 in the east and ~1.0 1e15 molecules cm-2 in the west.

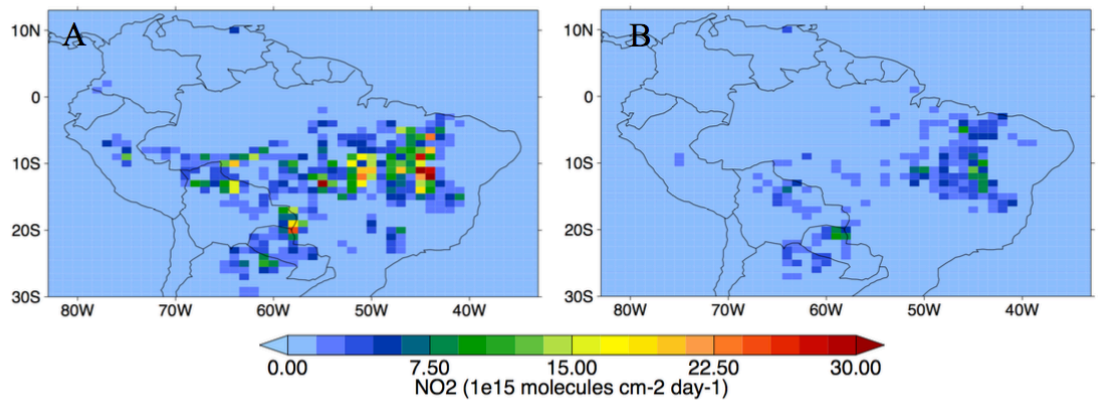

Figure 4.4 NO_x fire emissions during different SAMBBA flight campaign phases. Average GFAS NO_x fire flux (molecules cm^{-2} day^{-1}) (a) during the dry season (September 1-22) (b) dry-to-wet transition (September 23 – October 31).

Figure 4.5 (e and f) indicate that modelled NO_2 over South America is almost entirely from fire emissions. Around 80-90 % of NO_2 concentrations over the Amazon are from fire emissions, in the dry-to-wet transtion this contribution decreases to 55% for the western region and 75% for the Eastern region.

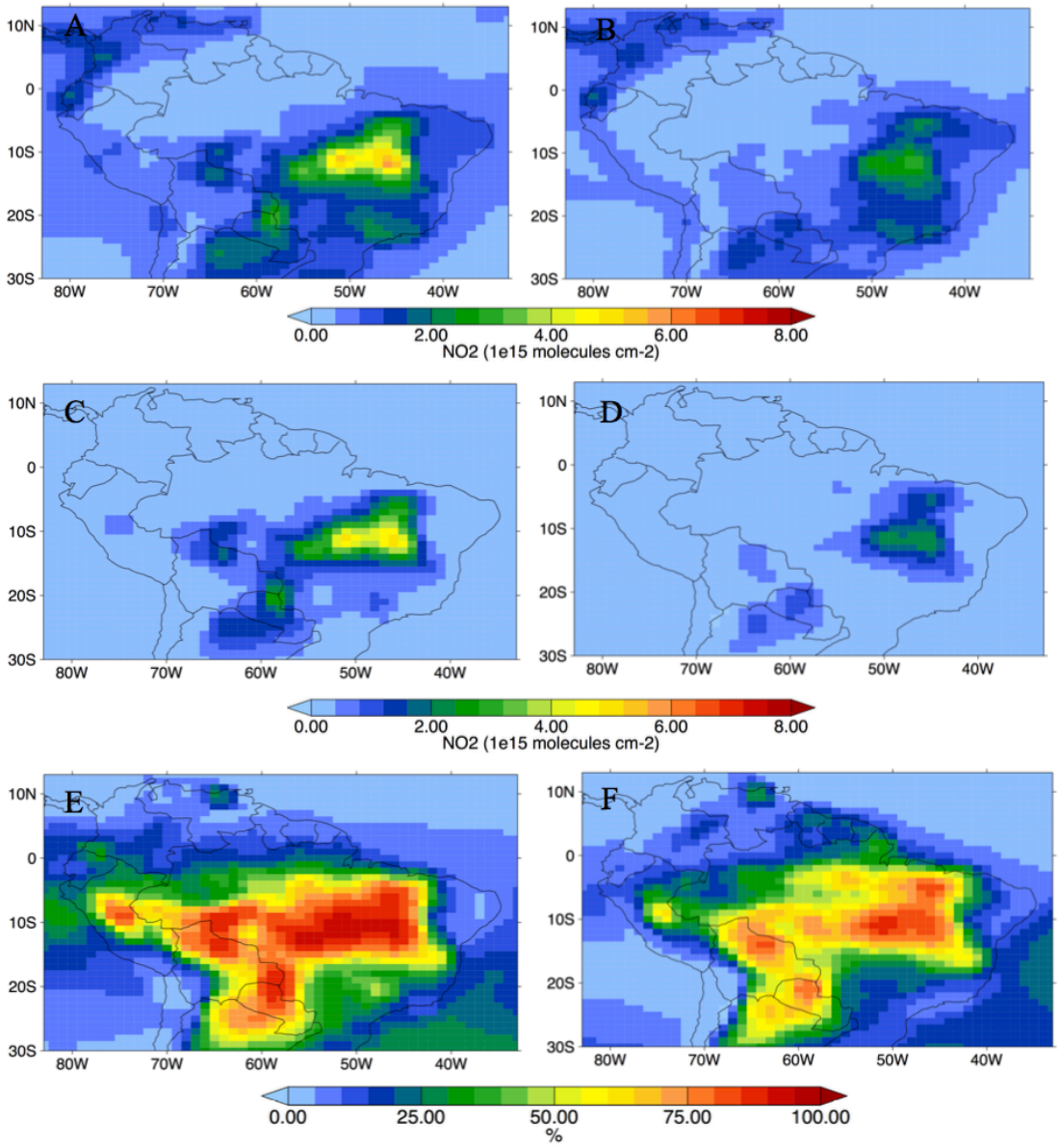

Figure 4.5 The impact of fires on NO_2 tropospheric column during the SAMBBA campaign. The left column shows average results from the dry season (September 1-22) and the right column shows equivalent results from the dry-to-wet transition (September 23 – October 31). (a, b) Total column NO2 (molecules cm^{-2}) from C-IFS simulation FOR. (c, d) Difference in NO_2 column between simulations FOR and FOR_NBB. (e, f) Percentage difference in column NO_2 for panels (c) and (d), respectively.

Impact of fires on ozone

NO_x emission fluxes are large compared to the NO_2 tropospheric column as emitted NO_x stays near the surface, due to the short lifetime of NO_2 compared to CO. The short life time of NO_x also means that NO_2 has less transport westwards than CO. The distribution of NO_2 fire emissions vertically is show in Figure 4.6, modelled surface NO_2 concentrations can be as high as 5 ppb, with concentrations lower than 0.1 ppb, predicted above 2kms, suggesting limited O_3 formation at these altitudes in these NO_x limited regime. The NO_2 concentrations associated with cerrado fires are higher both at the surface and within the first few kilometres, this is despite the emissions only being injected at the surface. Despite the low concentrations, percentage-wise increase of NO_2 in the free troposphere is almost entirely from fire emissions, indicating that other emission sources of NO_2 are not present in the model.

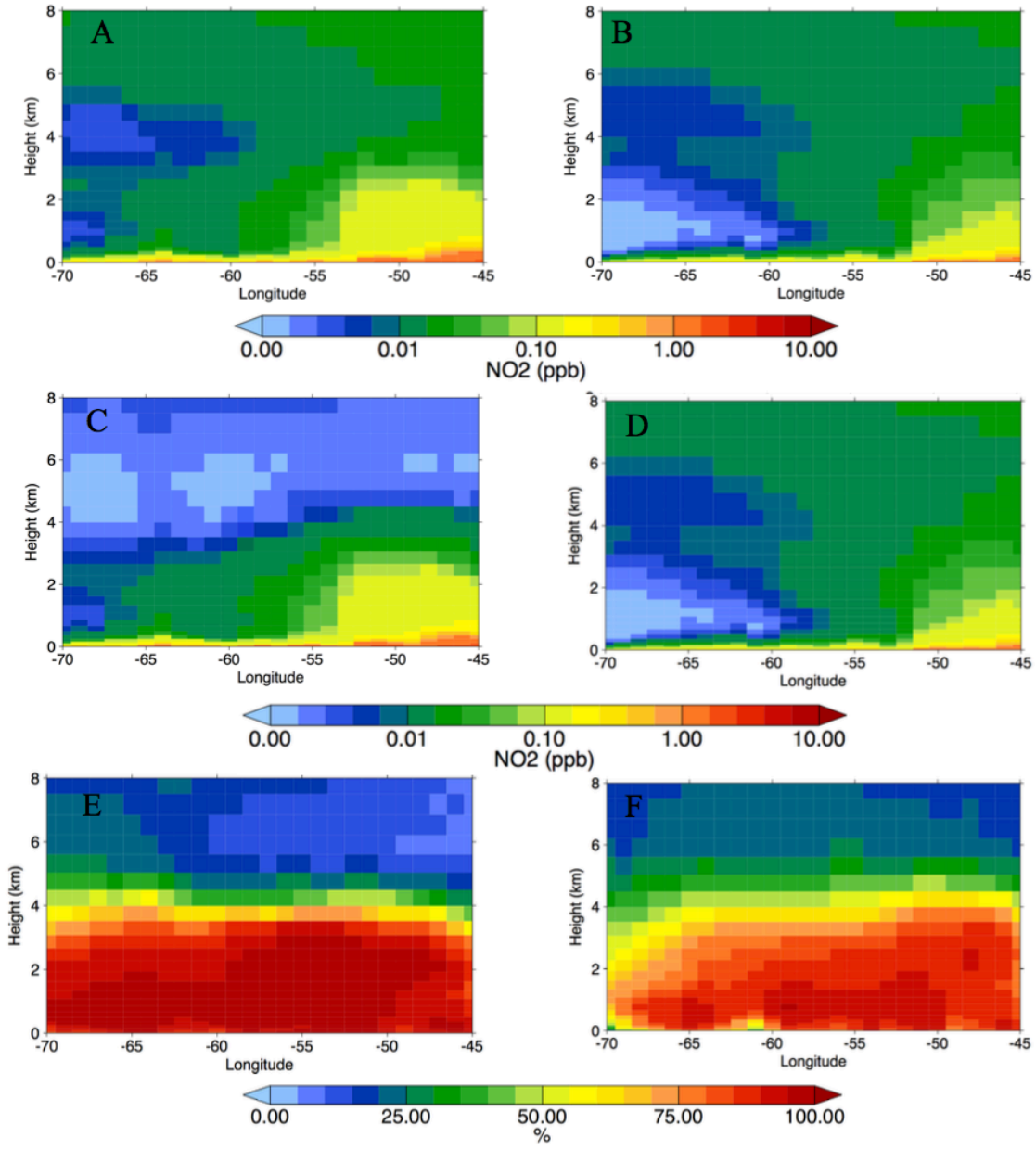

Figure 4.6 The impact of fires on the C-IFS NO_2 latitude/height zonal mean cross section over the latitudes sampled by the SAMBBA flights (-5.5° to -12°). The left column shows average results from the dry season (September 1-22) and the right column shows equivalent results from the dry-to-wet transition (September 23 – October 31). (a, b) NO_2 (ppb) from C-IFS simulation FOR. (c, d) Difference in NO_2 concentrations between simulations FOR and FOR_NBB. (e, f) Percentage difference in NO_2 for panels (c) and (d), respectively.

Impact of fires on ozone

Figure 4.7 shows the calculated impact of different fire emissions on O_3 concentrations during the SAMBBA campaign. There is a significant impact of fire emissions on O_3, particularly over the eastern cerrado region where model values show that 20-35% of the total tropospheric column is formed from fires emissions. Despite being a product of fire emissions, rather than a directly emitted species, O_3 concentrations are higher in the dry season compared to the dry-to-wet transition with values in the east decreasing from ~40 DU to ~30 DU.

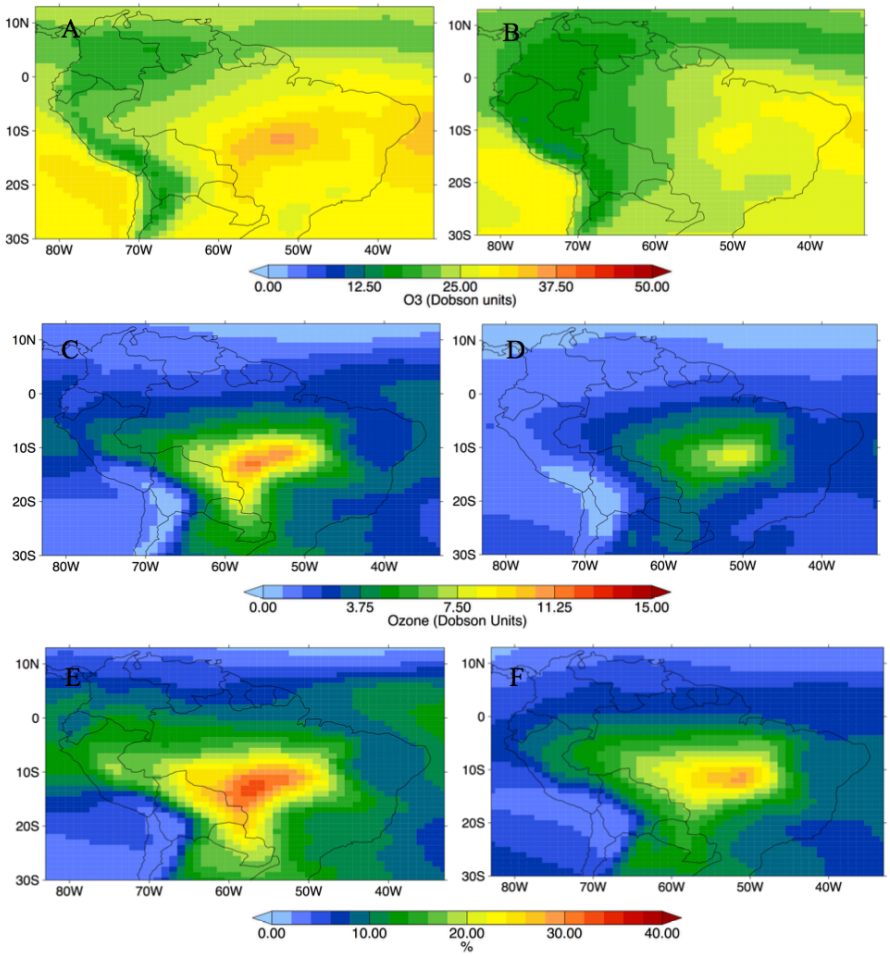

Figure 4.7 The impact of fires on O_3 tropospheric column during the SAMBBA campaign. The left column shows average results from the dry season (September 1-22) and the right column shows equivalent results from the dry-to-wet transition (September 23 – October 31). (a, b) Total column O_3 (molecules cm^{-2}) from C-IFS simulation FOR. (c, d) Difference in O_3 column between simulations FOR and FOR_NBB. (e, f) Percentage difference in column O_3 for panels (c) and (d), respectively.

Impact of fires on ozone

Figure 4.8 shows the vertical structure of O_3 and the impacts of O_3, in the first 3 kms throughout the flight domain 50-60% of O_3 concentrations are from fire emissions, however concentrations are higher in the East, surface concentrations of ~50 ppb than the west, surface concentrations of ~30 ppb. The highest O_3 concentrations, below 4km, correlate with the largest contribution from fire emissions and are 2-3 km above the eastern cerrado region. During the dry season, more O_3 is formed in the free troposphere and is generally correlated with CO concentrations, i.e. emissions being transported westwards, in the dry-to-wet season increases in O_3 concentrations generally occur within the PBL, with the largest increases near the eastern region with the larger NO_x emissions.

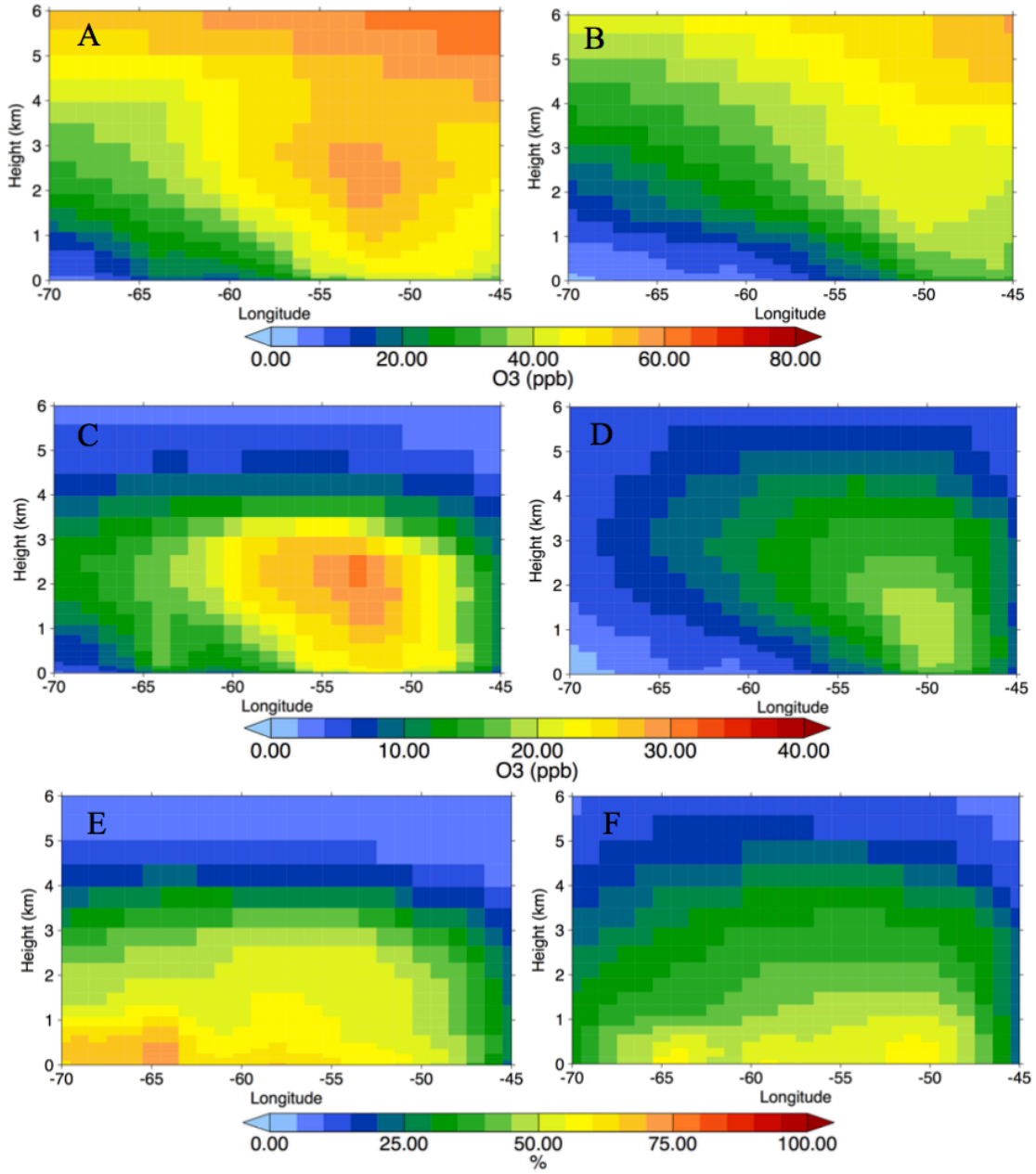

Figure 4.8 The impact of fires on the C-IFS O_3 latitude/height zonal mean cross section over the latitudes sampled by the SAMBBA flights (-5.5º to -12º). The left column shows average results from the dry season (September 1-22) and the right column shows equivalent results from the dry-to-wet transition (September 23 – October 31). (a, b) O_3 (ppb) from C-IFS simulation FOR. (c, d) Difference in O_3 concentrations between simulations FOR and FOR_NBB. (e, f) Percentage difference in O_3 for panels (c) and (d), respectively.

4.4 Satellite comparison and assimilation

4.4.1 MOPITT CO

The impact of assimilating total column MOPITT data into the C-IFS is shown in Figure 4.9. In 4D-var data assimilation analysis increments refers to the cumulative increments over an assimilation window, in the case of C-IFS this is every 12 hours. The AN_METCOM-AN_MET, or the difference from assimilation (ANDIF), refers to the difference between a model run without composition.

There is only a small difference in the average AN_MET and AN_METCOM field for September-October 2012, suggesting the model compares well to observations. The cumulative analysis increments show that most significant differences between the model and the analysis, at the end of each 12hr analysis window, is not the main fire source regions, but further east towards the more heavily populated coast. The lack of a significant bias suggests that the majority of the fires and their associated fluxes are observed by MODIS FRP and are considered in the GFAS emission inventory.

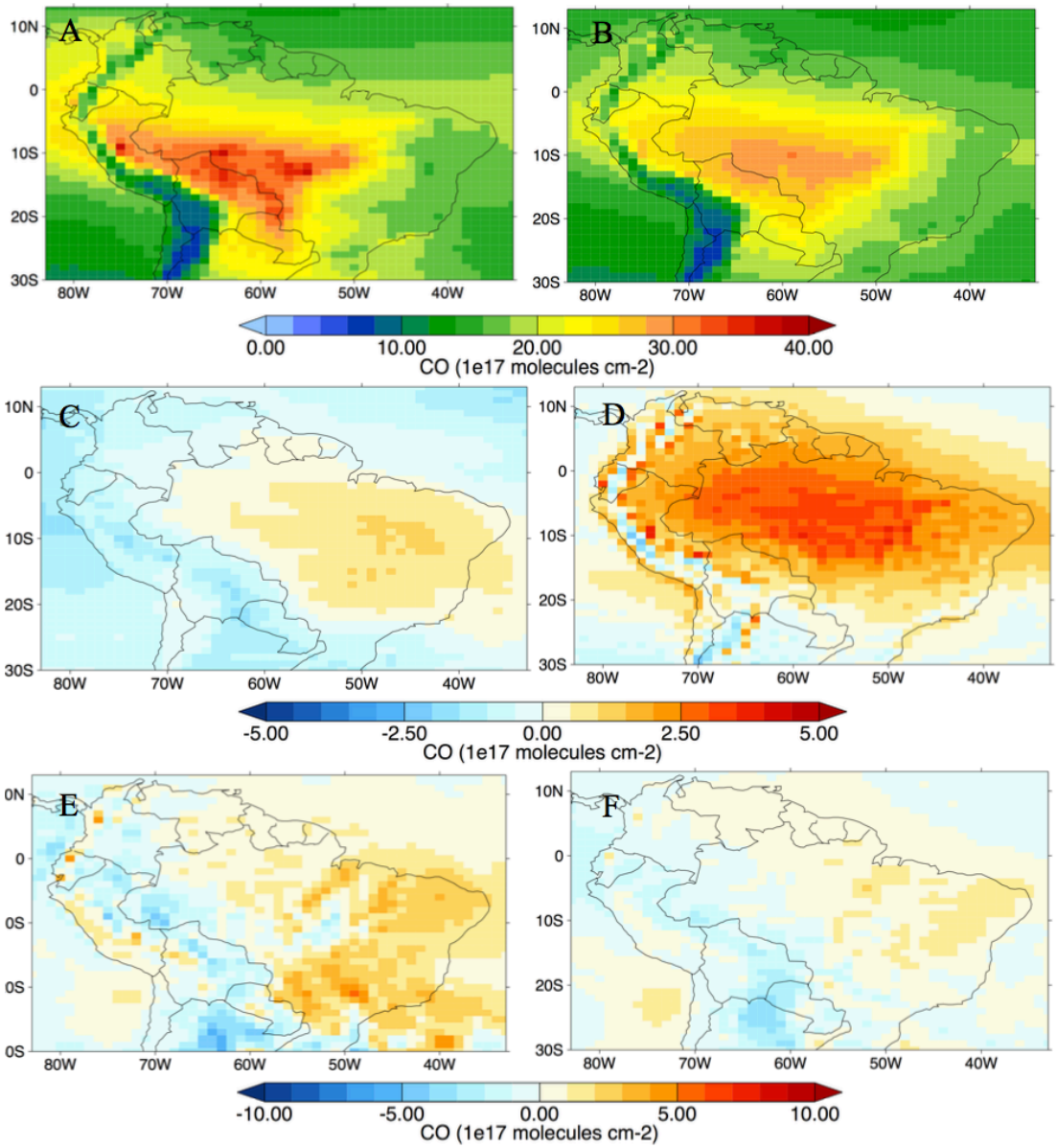

Figure 4.9 Impact of MOPITT CO assimilation on C-IFS for the 2012 tropical biomass burning season (Sept-Oct). The left column shows average results from the dry season (September 1-22) and the right column shows equivalent results from the dry-to-wet transition (September 23 – October 31). Panels (a, b) show mean analysis tropospheric CO columns (molecules cm^{-2}) from the C-IFS simulation AN_METCOM. Panels (c, d) is AN_METCOM – AN_MET, or the average impact of assimilation at each 6 hour timestep. Panels (e, f) shows the average CO analysis increments from simulation AN_METCOM, for each 12 hour analysis step.

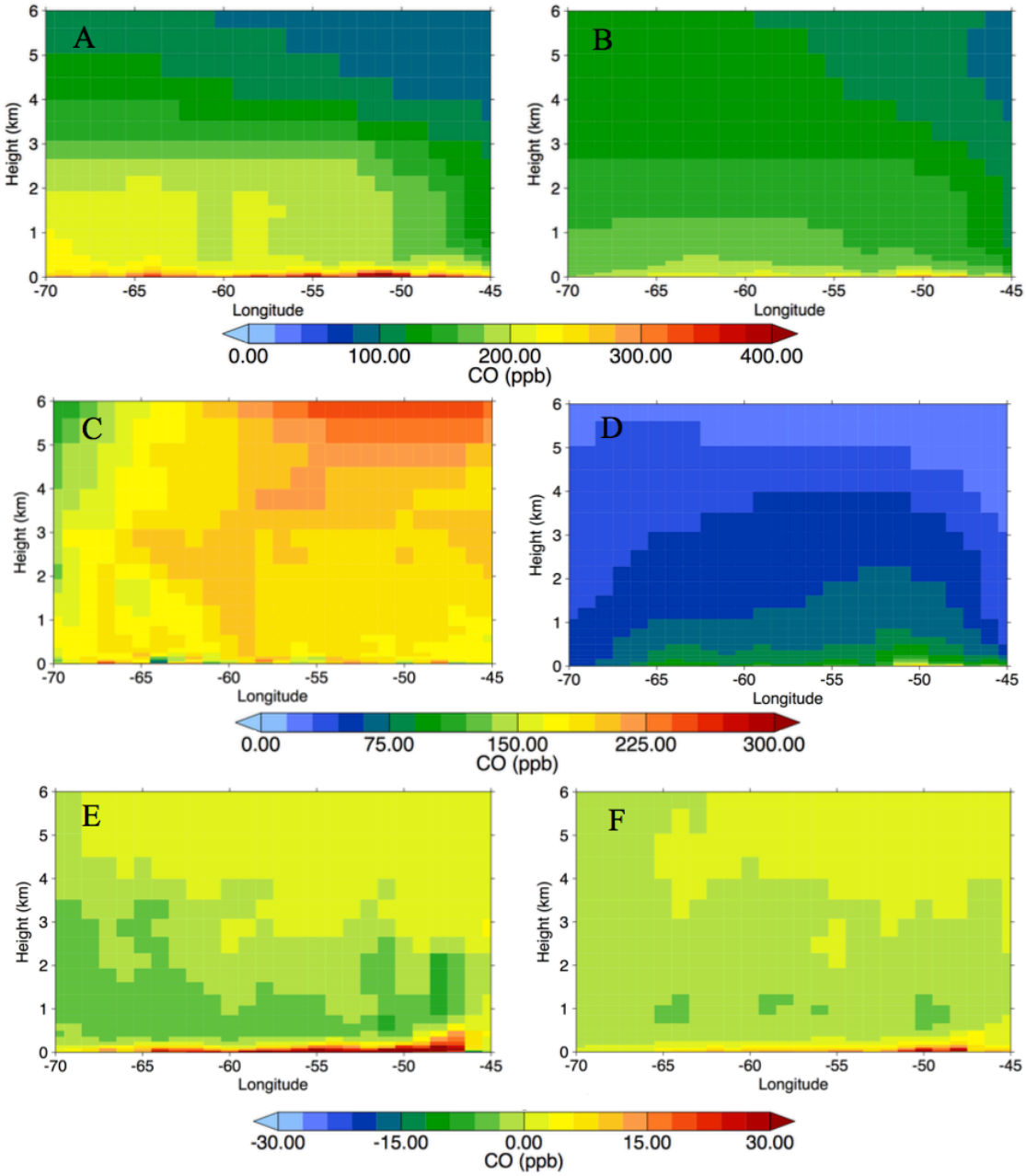

Figure 4.10 Impact of MOPITT CO assimilation on C-IFS CO latitude/height zonal mean cross section over the latitudes sampled by the SAMBBA flights (-5.5° to -12°). The left column shows average results from the dry season (September 1-22) and the right column shows equivalent results from the dry-to-wet transition (September 23 – October 31). Panels (a, b) show mean analysis CO (ppb) from the C-IFS simulation AN_METCOM. Panels (c, d) is AN_METCOM – AN_MET, or the average impact of assimilation at each 6 hour timestep. Panels (e, f) shows the average CO analysis increments from simulation AN_METCOM, for each 12 hour analysis step.

4.4.2 OMI NO_2

Figure 4.11 shows an underestimation of NO_2 by C-IFS (AN_MET) compared to OMI, over most of South America, with the black lines indicating locations where this bias is outside the error range associated with OMI. The highest concentrations of observed NO_2 are over savannah vegetation regions in both Eastern Brazil and Paraguay, as predicted by the model. Over the western tropical forest region, associated with deforestation fires, OMI observers lower NO_2 concentrations but is still larger than the near-zero concentrations predicted in C-IFS. On average, over South America, C-IFS underestimates OMI by a factor of 3.2. AN_METCOM is C-IFS analysis constrained by OMI NO_2 and is compared directly to the NO_2 observations in Figure 4.12. While there is an increase in NO_2 concentrations after the assimilation these values are still significantly smaller than the directly observed OMI concentrations. The only region which no longer has a bias outside the satellite error, is the eastern cerrado region where the model predicted NO_x is highest.

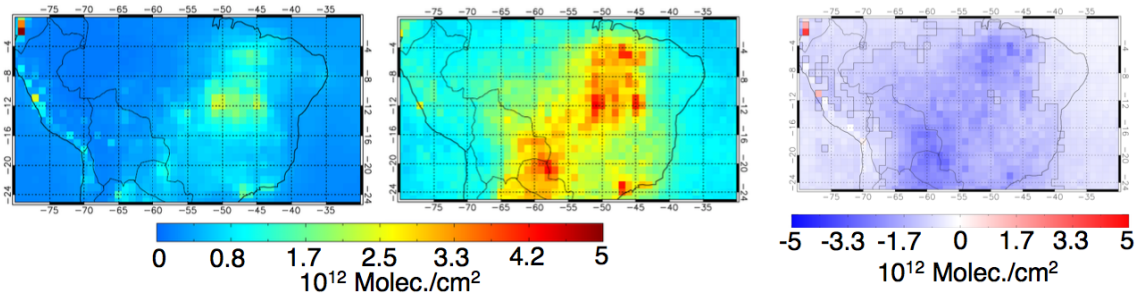

Figure 4.11 Comparisons of C-IFS to OMI NO_2. Average tropospheric NO_2 column (molecules cm^{-2}) September-October 2012 from (a) C-IFS simulation AN_MET and (b) OMI satellite observations. Panel (c) shows the difference between panel (a) and (b).

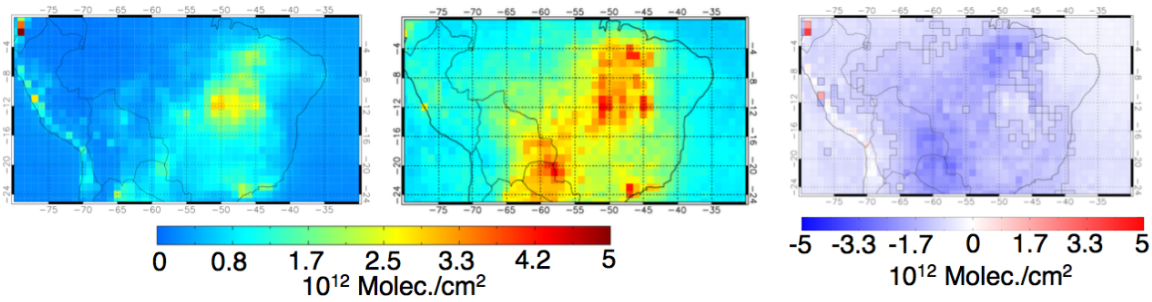

Figure 4.12 Comparisons of C-IFS, with OMI NO_2 assimilated, to the directly observed OMI NO_2 product. Average tropospheric NO_2 column (molecules cm^{-2}) September-October 2012 from (a) C-IFS simulation AN_METCOM and (b) OMI satellite observations. Panel (c) shows the difference between OMI and simulation AN_METCOM.

The impact of the assimilation is shown in Figure 4.13 where both the AN_METCOM/AN_MET difference and the analysis increments show large increase in this eastern region and little to no change over the west. The increase in NO_2 from OMI assimilation is, compared to the tropospheric column, is more significant than MOPITT CO. The cumulative analysis increments show that the assimilation adds a large amount of NO_2 into the model, despite the average NO2 field remaining significantly lower than the observations.

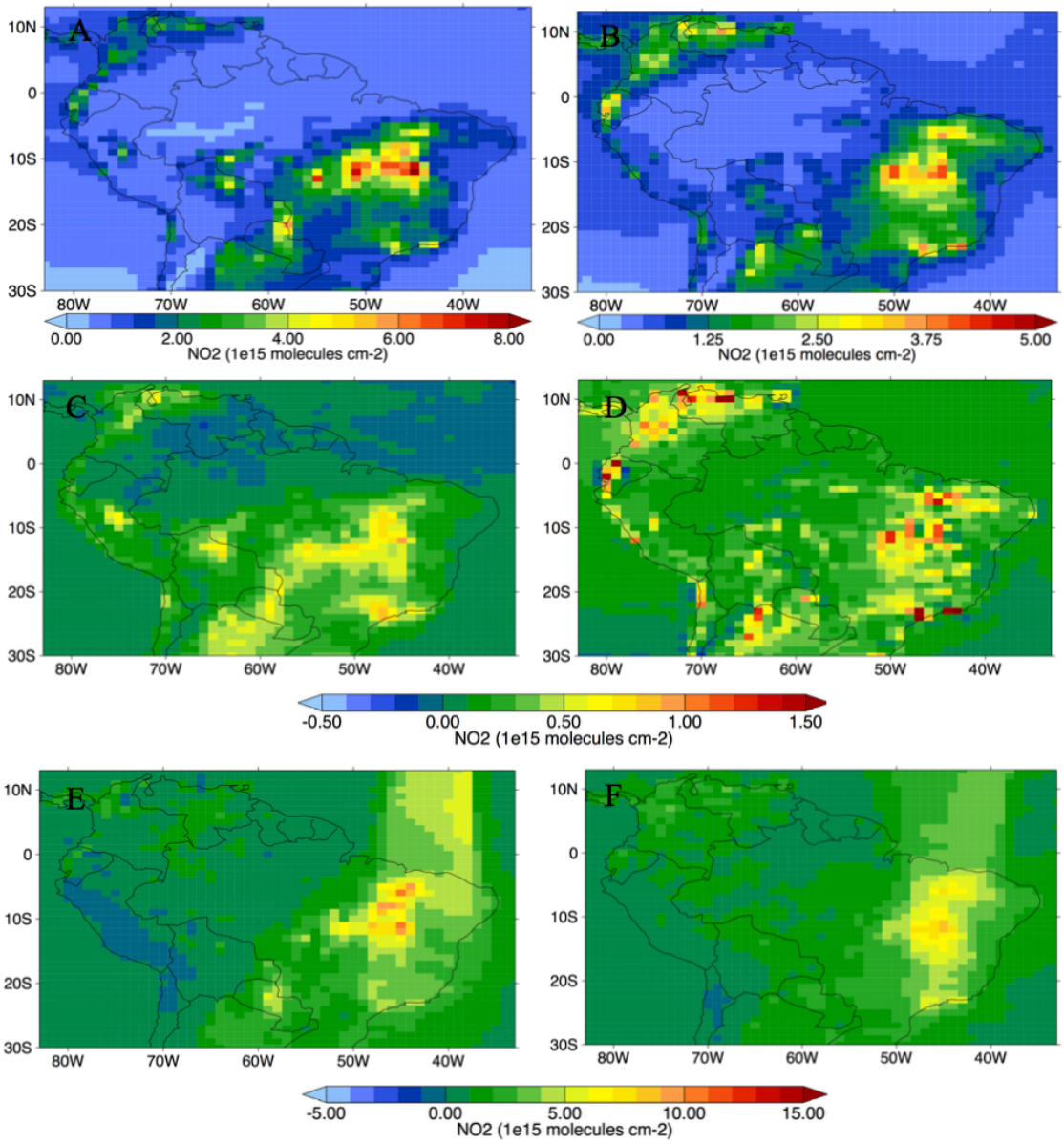

Figure 4.13 Impact of OMI NO_2 assimilation on C-IFS for the 2012 tropical biomass burning season (Sept-Oct). The left column shows average results from the dry season (September 1-22) and the right column shows equivalent results from the dry-to-wet transition (September 23 – October 31). Panels (a, b) show mean analysis tropospheric NO_2 columns (molecules cm^{-2}) from the C-IFS simulation AN_METCOM. Panels (c, d) are AN_METCOM – AN_MET, or the average impact of assimilation at each 6-hour timestep. Panels (e, f) show the average NO_2 analysis increments from simulation AN_METCOM, for each 12 hour analysis step.

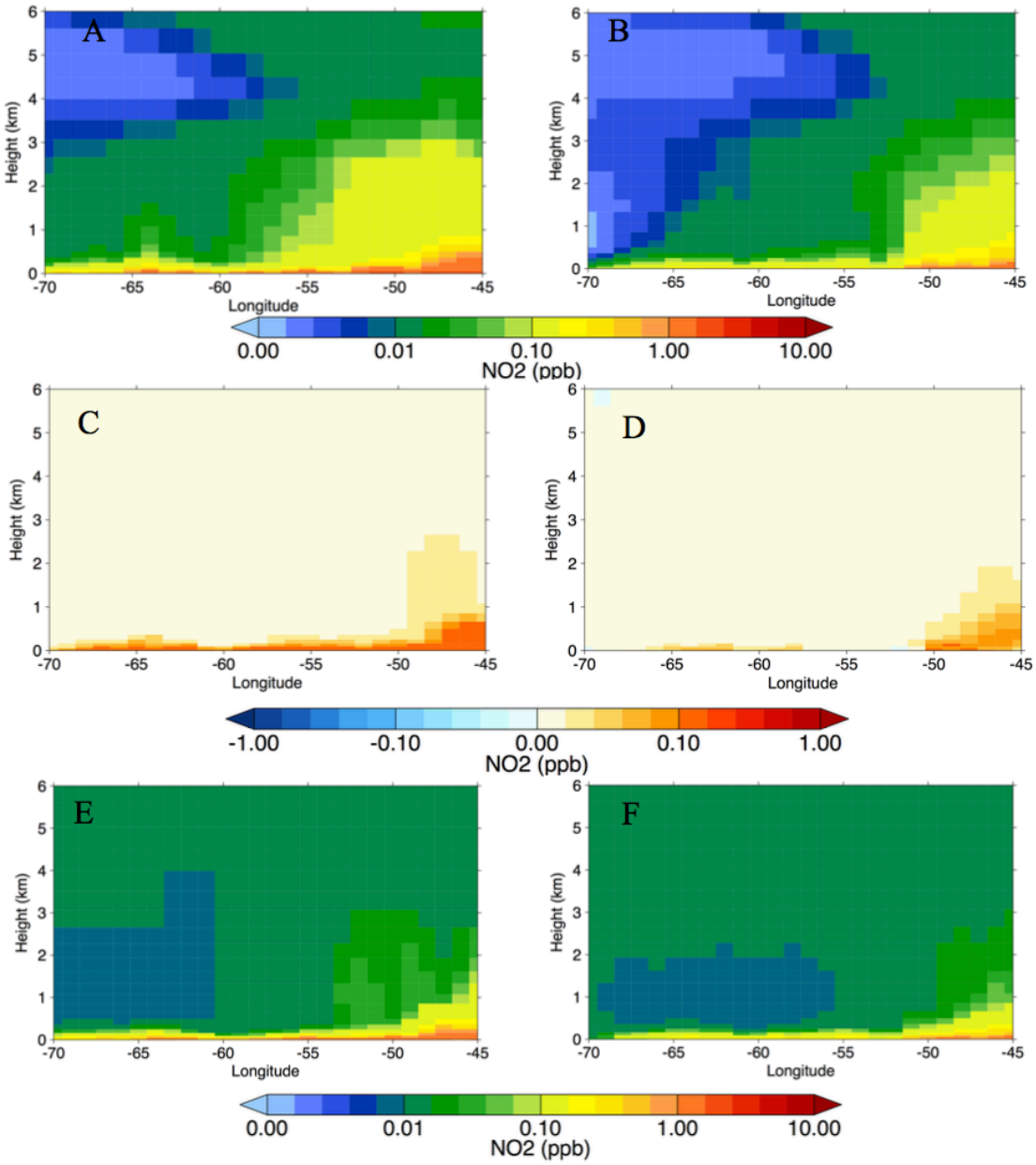

Figure 4.14 Impact of OMI NO_2 assimilation on C-IFS NO_2 latitude/height zonal mean cross section over the latitudes sampled by the SAMBBA flights (-5.5º to -12 º). The left column shows average results from the dry season (September 1-22) and the right column shows equivalent results from the dry-to-wet transition (September 23 – October 31). Panels (a, b) show mean analysis NO_2 (ppb) from the C-IFS simulation AN_METCOM. Panels (c, d) are AN_METCOM – AN_MET, or the average impact of assimilation at each 6-hour timestep. Panels (e, f) show the average NO_2 analysis increments from simulation AN_METCOM, for each 12 hour analysis step.

The scale of the impact from NO_x assimilation, compared to fire emissions, is shown in Figure 4.15. Over the SAMBBA campaign domain 0.056 g m^{-2} $month^{-1}$ is added by assimilation compared to 0.015 g m^{-2} $month^{-1}$ from the fire emissions, with the majority over the cerrado region. The western region comparatively has little change after assimilation and is comparable to previous studies investigating NO_2 assimilation in C-IFS where only a small change in NO_2 was seen after assimilation (Inness et al., 2013).

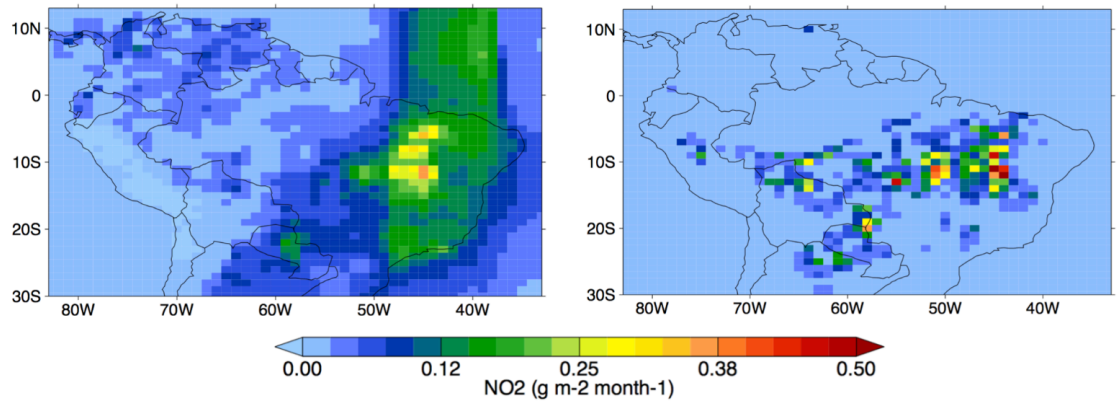

Figure 4.15 Mass of NO_2 added by OMI assimilation (g m^{-2} $month^{-1}$) during September-October 2012 compared to NOx fire emission fluxes. (a) Average monthly NO_2 column analysis increments and (b) GFAS fire emission fluxes.

4.4.3 Ozone

A comparison of AN_MET to partial column retrievals from both OMI and GOME-2 is shown in Figure 4.16. The partial columns are formed from 0-6 km profiles and hence are different from the GOME-2 and OMI total columns assimilated in AN_METCOM. GOME-2 and OMI satellite products have significant differences between one another with GOME-2 suggesting O3 concentrations 20 DU higher than OMI over the Amazon. This is thought to be due to an error in GOME-2 caused by a degradation in the instrument and as such OMI is considered here as the more accurate observation. With the individually applied averaging kernels C-IFS underestimates the partial tropospheric column compared two OMI by between 10-20 DU over the Amazon, representing a significant negative bias. AN_METCOM only shows a slight increase in the partial column and still shows small concentrations compared to OMI.

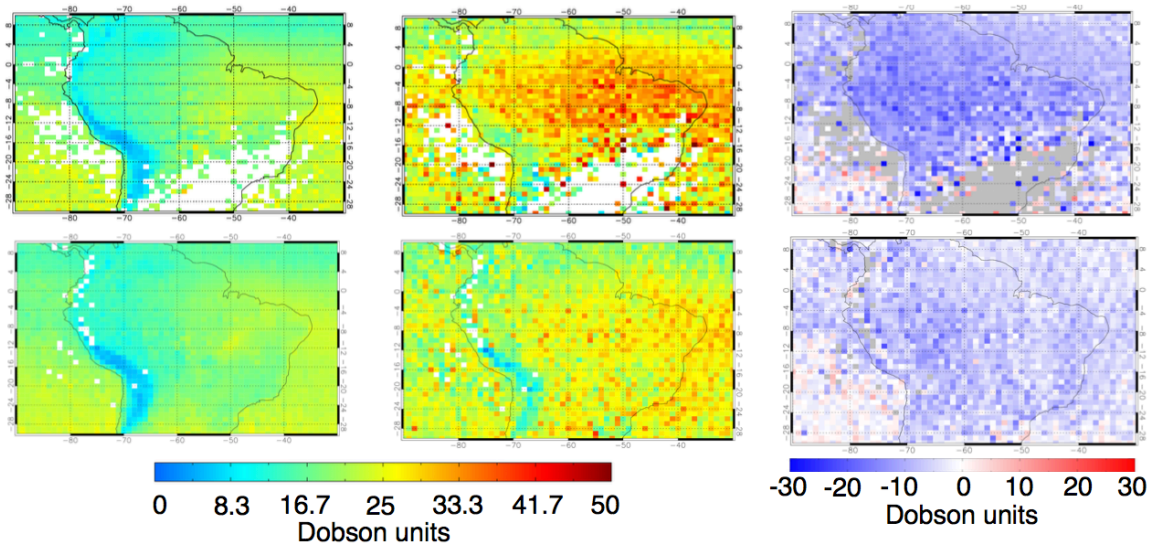

Figure 4.16 Comparison of C-IFS to OMI and GOME-2 partial tropospheric columns (0-6 km). AN_MET partial O_3 column (0-6 km) compared to GOME-2 (top row) and OMI (bottom row). (a, b) C-IFS partial column with applied averaging kernels. (c, d) Satellite partial column. (e, f) Difference between model and satellite partial column.

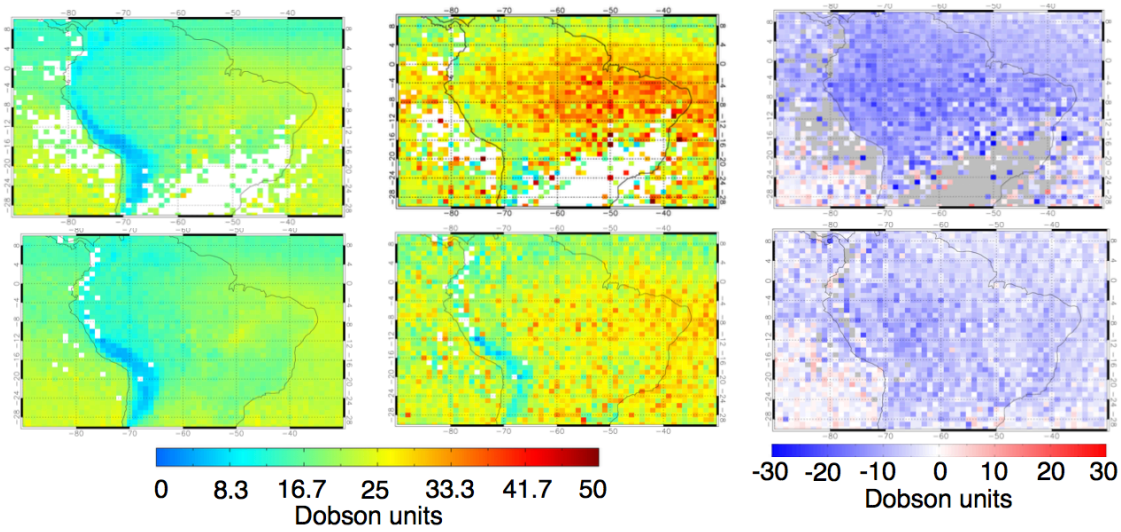

Figure 4.17 AN_METCOM partial O_3 column (0-6 km) compared to GOME-2 (top row) and OMI (bottom row) partial column satellite products. (a, b) C-IFS partial column with applied averaging kernels. (c, d) Satellite partial column. (e, f) Difference between model and satellite partial column.

Impact of fires on ozone

The impact of the assimilation of OMI total column as well as MLS partial columns on the tropospheric column are shown in Figure 4.18. As this figure shows total tropospheric column rather than partial column the difference between the AN_MET and AN_METCOM experiments are larger than seen in Figure 4.17 and fairly evenly distributed over the continent. Significant differences are seen for October compared to September as OMI data was not available for September. This leads to a significant increase in assimilation in October compared to September with the average difference between AN_MET and AN_METCOM increasing from 1.36 to 5.71 DU. The impacts of assimilation on O_3 zonal mean is shown in Figure 4.19 and shows how the majority of the impacts are related to troposphere/stratosphere exchange.

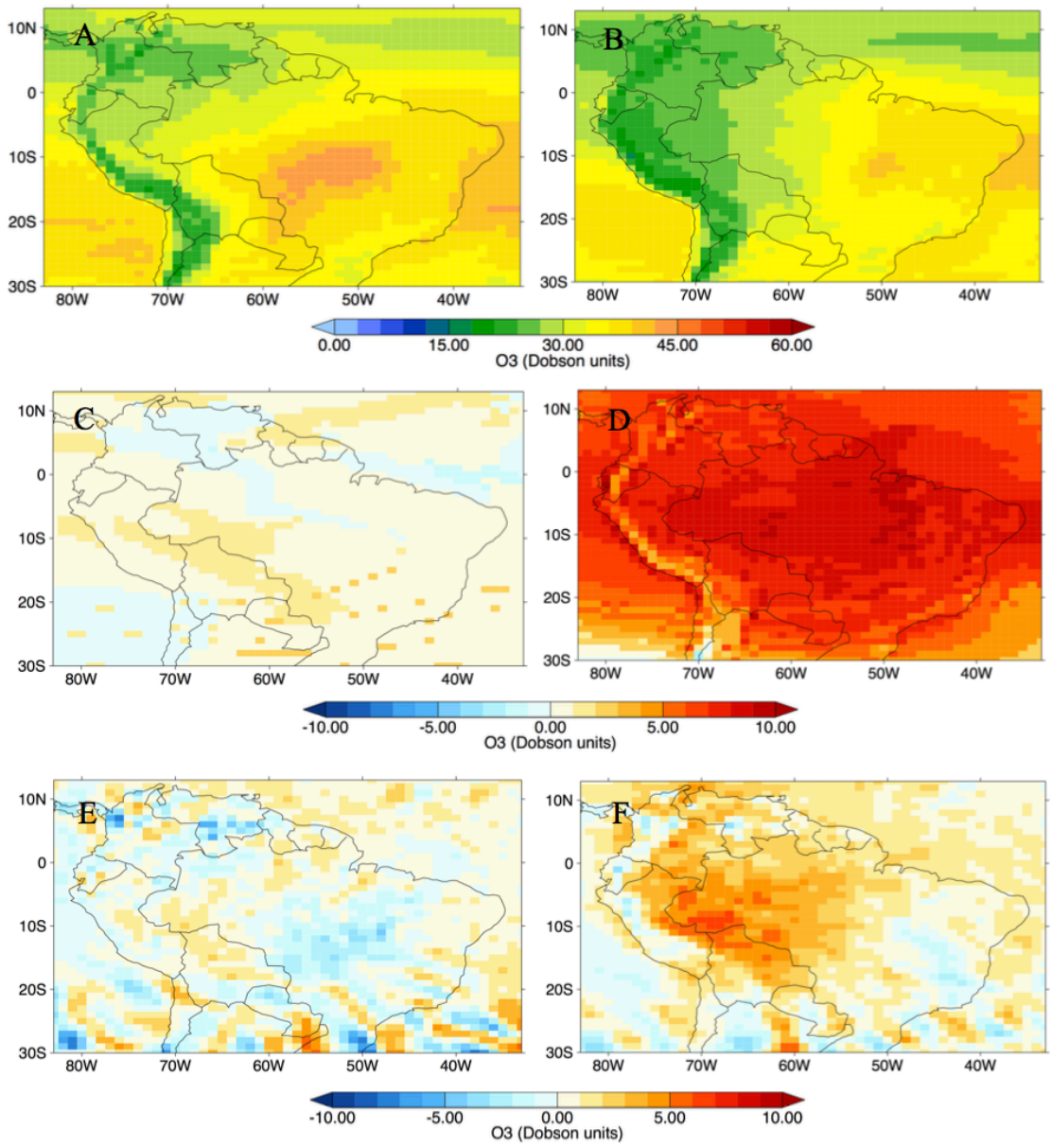

Figure 4.18 Impact of O_3 assimilation on C-IFS for the 2012 tropical biomass burning season (Sept-Oct). The left column shows average results from the dry season (September 1-22) and the right column shows equivalent results from the dry-to-wet transition (September 23 – October 31). Panels (a, b) show mean analysis tropospheric O_3 columns (Dobson units) from the C-IFS simulation AN_METCOM. Panels (c, d) are AN_METCOM – AN_MET, or the average impact of assimilation at each 6-hour timestep. Panels (e, f) show the average O_3 analysis increments from simulation AN_METCOM, for each 12-hour analysis step.

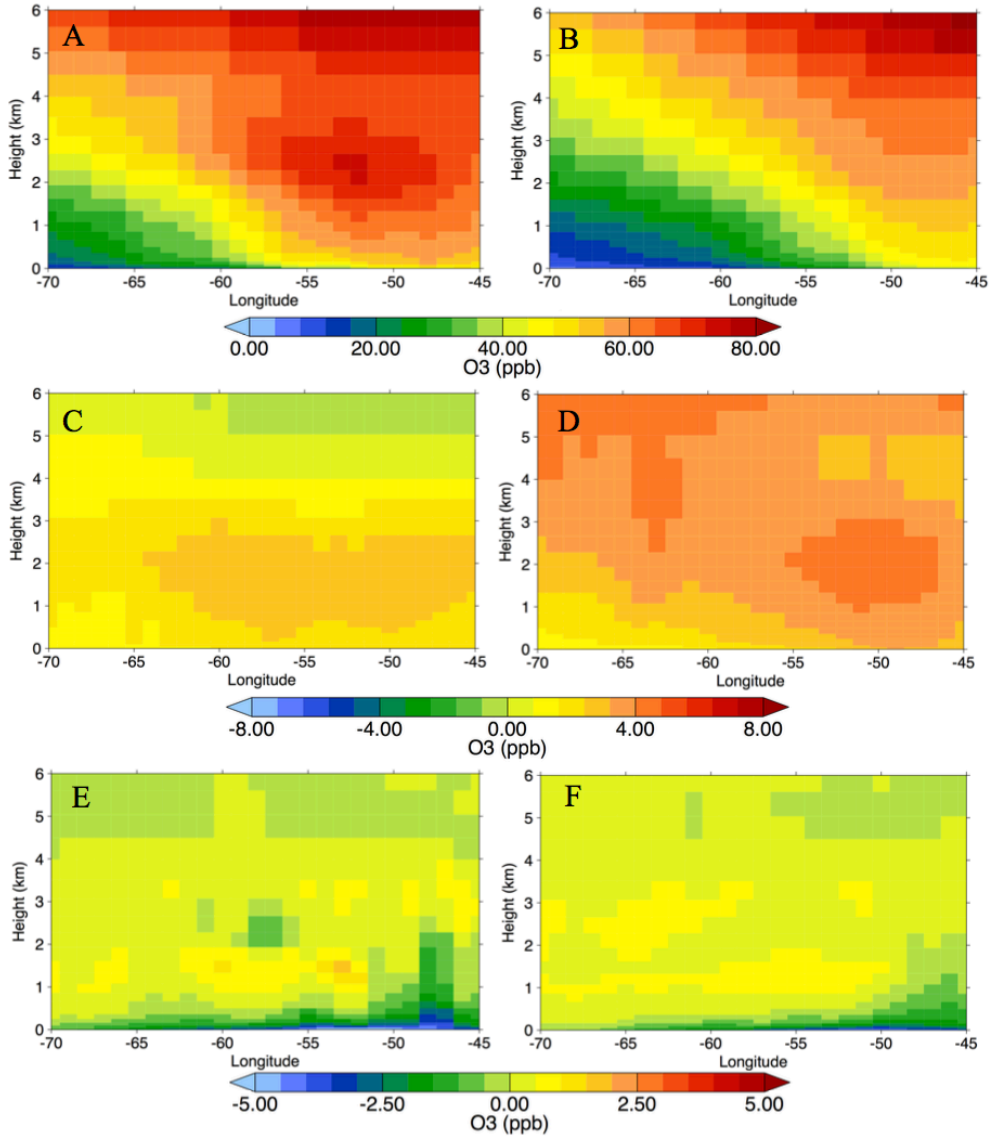

Figure 4.19 Impact of O_3 assimilation on C-IFS O_3 latitude/height zonal mean cross section over the latitudes sampled by the SAMBBA flights (-5.5º to -12 º). The left column shows average results from the dry season (September 1-22) and the right column shows equivalent results from the dry-to-wet transition (September 23 – October 31). Panels (a, b) show mean analysis O_3 (ppb) from the C-IFS simulation AN_METCOM. Panels (c, d) are AN_METCOM – AN_MET, or the average impact of assimilation at each 6-hour timestep. Panels (e, f) show the average O analysis increments from simulation AN_METCOM, for each 12-hour analysis step.

4.5 SAMBBA comparisons

.

4.5.1 Carbon monoxide

Figure 4.20 shows results from 19 of the 20 SAMBBA flights with CO concentrations from the campaign and C-IFS simulations AN_METCOM, AN_MET and FOR_NBB. The SLR (Straight and Level Runs) flights, which sampled the boundary layer, show CO concentrations ranging from 150-1000 ppb with the highest values observed in proximity to fires during the dry season and the start of the transition to the wet season. Concentrations identified as inside the plume by the flight logs encompass the largest CO mixing ratios while values outside the plumes tend not to exceed 500 ppb. The lowest concentrations were seen at the end of the dry-to-wet transition and over the pristine Northern region.

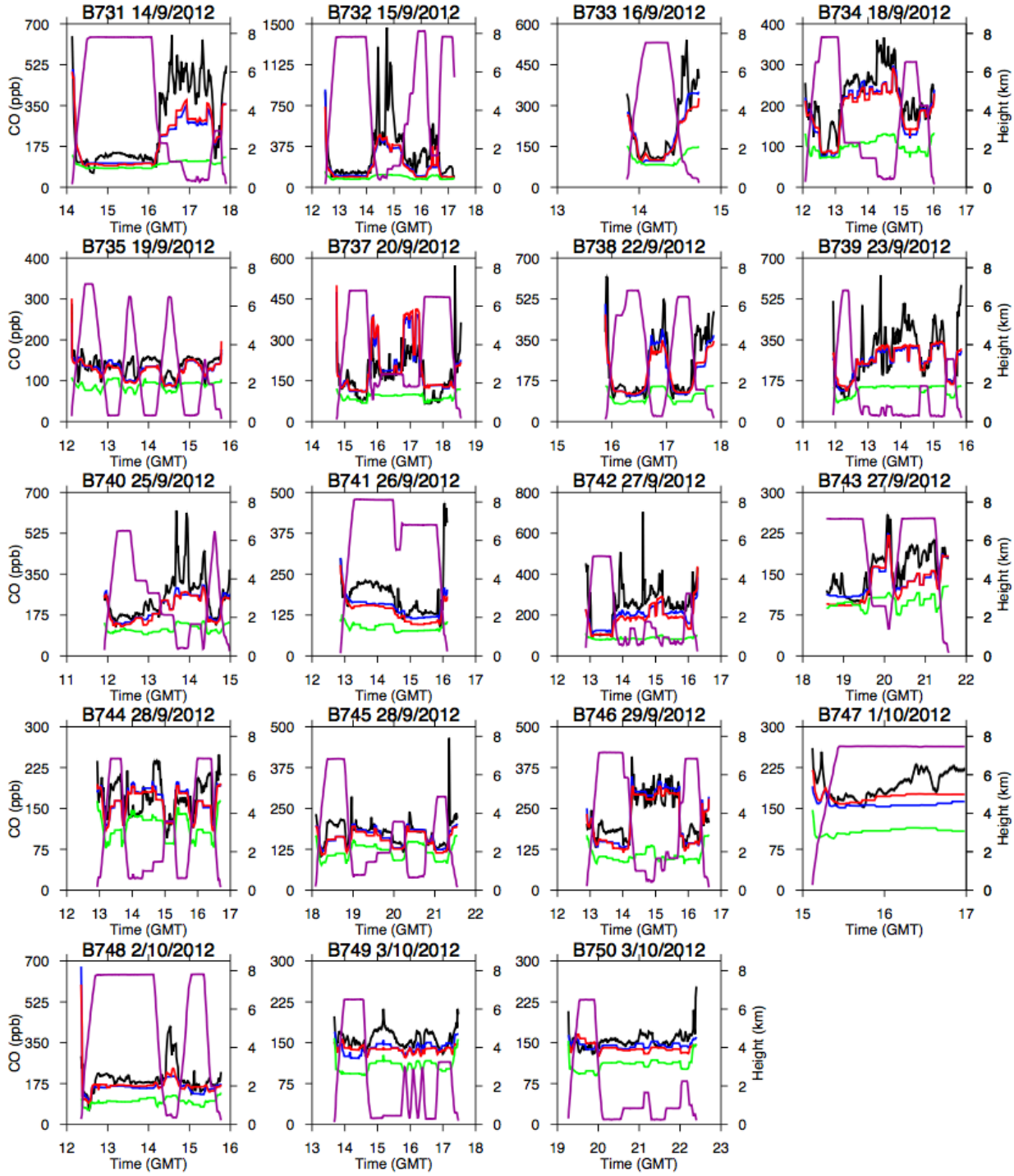

Figure 4.20 Observed CO concentrations (black) during the SAMBBA aircraft campaign compared to AN_MET (red), AN_METCOM (blue) and FOR_NBB (green) for 19 of the 20 SAMBBA flights. Purple indicates the altitude of the aircraft. Note the different y-axis ranges.

Impact of fires on ozone

Near-fire plumes from flight B738 (16:45-17:15 GMT), B746 (14:00-16:00 GMT) correspond to large smouldering fires (~300 ppb) fire plumes B732 (14:00-15:30 GMT) corresponds to a large fresh fire, with CO concentrations up to 1000 ppb, and B743 (19:30-20:00 GMT) sampled concentrations above and around a large fire, these fires are associated with an increase in modelled CO concentrations with surface or near-surface concentrations generally well captured by C-IFS.

Figure 4.21 shows average CO vertical profiles from the SAMBA observations and simulations, AN_METCOM and AN_MET for each flight. Away from the surface high CO concentrations were observed at elevated layers of around 1-2km for flights B732, B733, B738, and B743 but, these concentrations are underestimated by the model leading to biases in the modelled average vertical profiles seen in Figure 4.21. For the plume sampling flights B732 and B738 show the model overestimating the near-surface aircraft observations, showing the importance of accurate injection height modelling. However, flights B733 does not show higher concentrations near the surface, and could suggest that the total CO flux is too low.

The older smouldering fires B746 and B732 however, show a more accurately modelled vertical structure, particularly flight B732, most likely due to the modelled emissions having more time to mix within the boundary layer. The fact that older fires, not penetrating the boundary layers, are better captured vertical suggests that the CO flux may not be underestimated, at least for these fires. Figure 4.3 shows the large discrepancy between the surface layer and the rest of the boundary layer, if the emissions are solely emitted at the surface, and during flight B733 didn't sample plumes to as low an altitude as the other flights. This could also suggest that the surface CO concentrations in the model are a lot higher than reality and the injection is the sole bias for these fires.

Near-fire plumes close to small and medium scale fires, identified as (<100m) and (<500m) respectively, were sampled in flights B731 (16:15-17:45 GMT), B739 (12:45-16:00 GMT) and B740 (13:00-15:00 GMT) showing CO concentrations similar to the larger fires. These fires do not show as definitive of a layer around 1-2 km as the larger fires and even near-surface concentrations (< 1km) from these fires were generally lower than the fresh larger fires (e.g. b738) but are similar in concentration to the older smouldering fires. C-IFS generally underestimated by the observed concentrations of

these fires, even close to the surface, with the vertical profiles in Figure 4.21 showing biases all the way to the surface. This is in line with the small GFAS emissions compared to non-FRP based inventories in the western deforestation area seen in Pereira et al., (2016). Due to the small nature of these fires and considering that model underestimates emissions even at the surface, where all of the fire emissions in the model are emitted, these fires are likely too small to be accurately captured by the GFAS emissions inventory, due to its dependence on GFED dry matter flux or obstructions to the line-of-sight of the satellite observation of FRP for example by tall trees in forested regions (Kaiser et al., 2012).

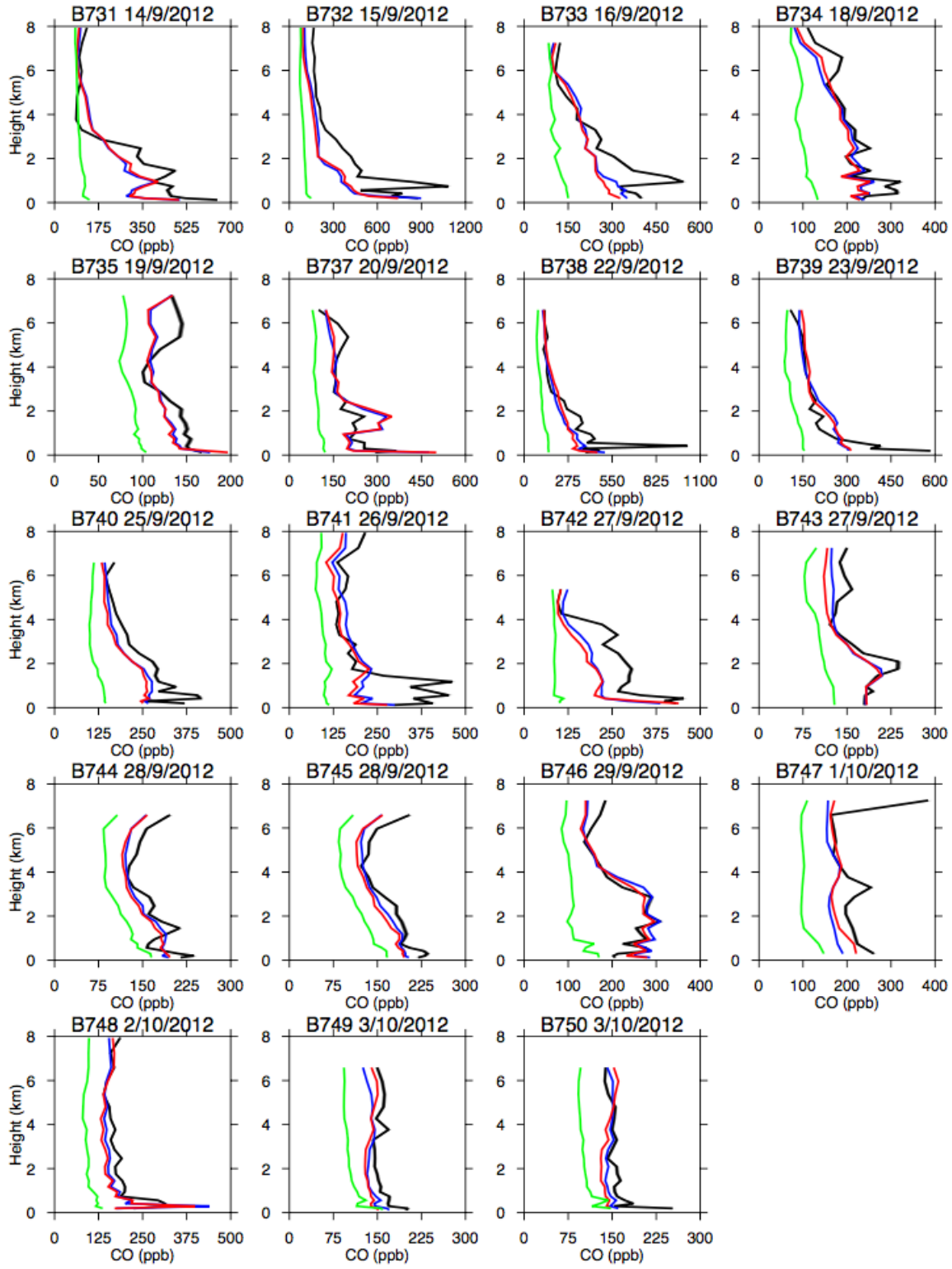

Figure 4.21 Average CO profiles ppb (black) from the SAMBBA aircraft campaign compared to AN_MET (red), AN_METCOM (blue) and FOR_NBB (green) for 19 of the 20 SAMBBA flights.

Impact of fires on ozone

Higher CO concentrations are seen in the HALT (High ALtitude Transits) parts of the flight in B741 and B743 than at the start of the campaign in flights B731 and B732, increasing from ~150ppb to ~175ppb. This increase is not observed in the model, with the HALT segment of flights B731 and B732 more accurately captured than the later flights B741 and B743. This suggests that the transport of emissions in the model is not accurately capturing the elevated concentrations of CO above the boundary layer. The general rapid mixing in the boundary layer may account for a lack of modelled injection height in the boundary layer e.g. flight B732, but plumes which penetrate above the boundary layer are not adequately represented by the model without an injection height and the atmosphere above this altitude is likely to be less pristine than the model indicates.

Flight B734 sampled an aged plume, identified by lidar, around Porto Velho, before descending into a smaller fire. Elevated CO concentrations were observed in the aged plume that were slightly underestimated by C-IFs, as with the HALT flights, but the bias was largest when sampling the small plume. Flight B737, also sampled aged plumes as well as background concentrations around fresh plumes. During 16:00-17:00 GMT the flight flew close to fire plumes without directly sampling them and is the only time and location during the flight campaign where the model overestimates observed CO concentrations. This positive bias is probably a model representation error i.e. the model resolution is too coarse to separate out the background CO concentrations from the fresh plumes. This bias also suggests that model representation error may have played a role in the underestimation of the model concentrations through the flight campaign, particularly when sampling smaller fresh plumes.

Flights sampling the pristine northern regime (flights B735, B749, B750) and flights near Porto Velho after the dry-to-wet transition (B747 and B748), showed lower CO concentrations than other flights and these relatively more pristine conditions were more accurately captured by the model. Although, a small fire was sampled during B748, which like previous small fires, was not captured by the model. This flux discrepancy could either be due to an underestimation in the emissions or the relatively coarse model resolution.

Flight B741 flew from Porto Velho to Las Palmas, with Flight B743, being the return flight. Figure 4.20 shows during the HALT portion of these flights, observations show a

decreasing gradient in CO concentrations from west to east in the free troposphere. C-IFS also shows this decrease in concentrations from west to east, but as with other flights underestimates the impact of biomass burning on CO concentrations in the free troposphere. Flight B742, sampled plumes near-fires in the savannah region around Las Palmas, these moderately sized fires, were generally flaming compared to the predominantly smouldering fires observed in the East, and as such generally produced less CO, highest near surface concentrations (< 1km) of 554 ppb compared to the comparable eastern sized fire in B731 of 650 ppb.

Figure 4.22 shows the difference between the flights in the east and west, showing the lower concentrations in the eastern region compared to the first phase of the western region. The fires in the eastern region however, showed a larger injection height than the west with concentrations above 200 ppb observed up to 4 km. The increased model bias in the eastern region is most likely due to this larger injection height, which has also previously been associated with savannah fires.

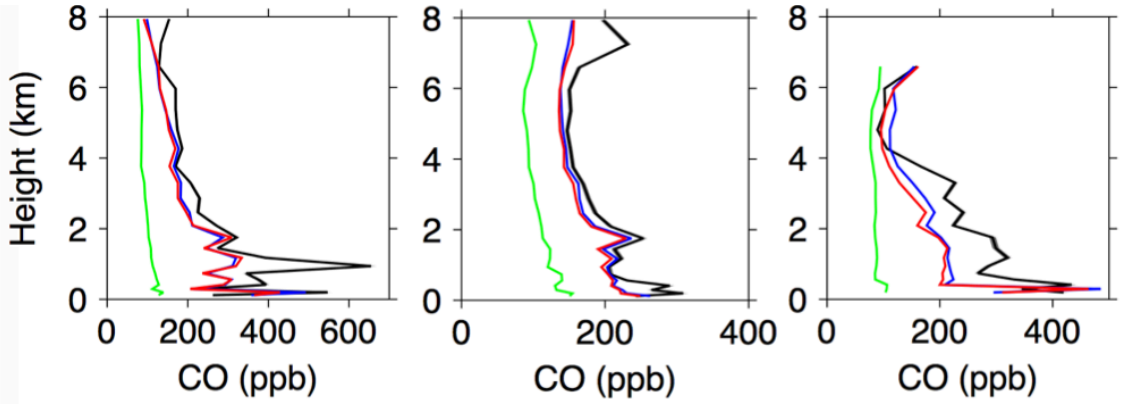

Figure 4.22 Comparison of mean CO profiles (ppb) between SAMBBA observations (black) and C-IFS simulations AN_METCOM (blue) and AN_MET (red). The three panels from left to right represent: the western region phase 1, the western region phase 2 and the eastern region.

Figure 4.23 shows the correlation between modelled and observed CO for the different flight phases. Flights during the wet-to-dry transition (WR2) show the smallest MFB (-11%) while observations in the eastern region have the highest (-26%). The correlations

show that the largest biases are associated with high CO concentrations above 300 ppb, although some elevated concentrations are well captured by the model. Figure 4.23b shows the correlations after MOPITT assimilation, with both MFB and NMB both marginally improved after assimilation. The largest improvement is seen in the eastern region where the injection height is largest and, as seen in Figure 4.22, the assimilation improves CO throughout the profile.

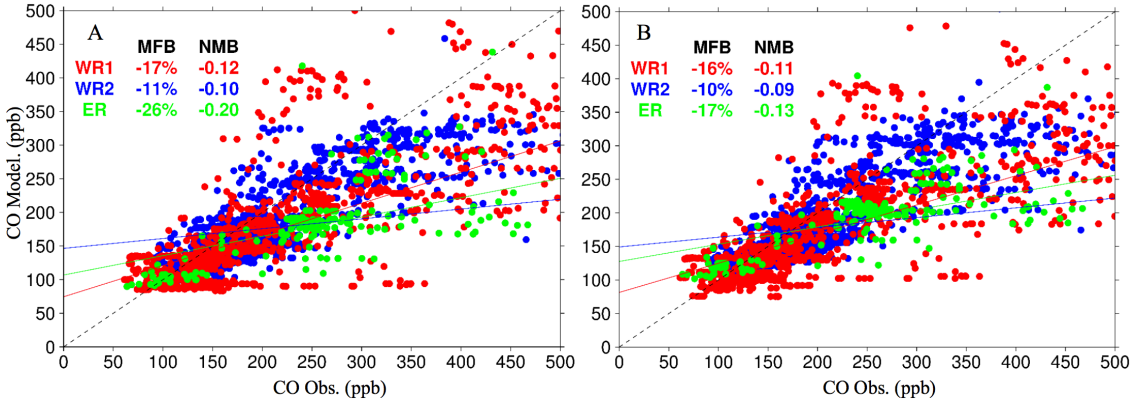

Figure 4.23 Correlation between SAMBBA CO (ppb) observations and C-IFS simulations (a) AN_MET and (b) AN_METCOM. WR1 and WR2 refer to the first and second phases of the flights over the western regions and ER represents the Eastern cerrado region. MFB is the mean fractional bias (%) between the observation and the model and NMB is the normalised mean bias.

4.5.2 Nitrogen oxides

Figure 4.24 shows results from 16 of the 20 SAMBBA flights with NO_x concentrations from the campaign and C-IFS simulations AN_METCOM, AN_MET and FOR_NBB. Concentrations throughout the flight campaign are generally above 0.1 ppb which is suggested to be necessary for O_3 formation in previous studies of fire emissions in a remote NO_x limited environment (Jaffe & Wigder, 2012). SLR flights, outside the plume had, a mean concentration of 0.42 ppb, with concentrations between 1-10 ppb observed in fire plumes. These concentrations are higher than those measured at Porto Velho outside of the fire season.

Impact of fires on ozone

In contrast to the CO comparison, C-IFS NO_x concentrations are significantly lower than that observed during SAMBBA. Increases in NO_x, in and around plumes, do correspond with increases in CO, although the negative bias is greater. Significantly, unlike CO, the background NO_x concentrations are poorly captured by C-IFS. Flights sampling the pristine northern regime (flights B735, B749, B750) and flights near Porto Velho after the dry-to-wet transition (B747), show negligible concentrations in the model while observations suggest concentrations around 0.1 ppb. This could suggest either a missing background non-fire source, potentially lightning or soil, or an underestimation of the impact of PAN in transporting NO_x emitted from near-fires to the remote regions. This underestimation of background NO_x is in contrast to the well captured NO observations from the 2009 BARCA campaign in Bela et al., 2015, using 3BEM fire emissions. These flights however, sampled more pristine regions than those observed during SAMBBA, with much lower background NO concentrations.

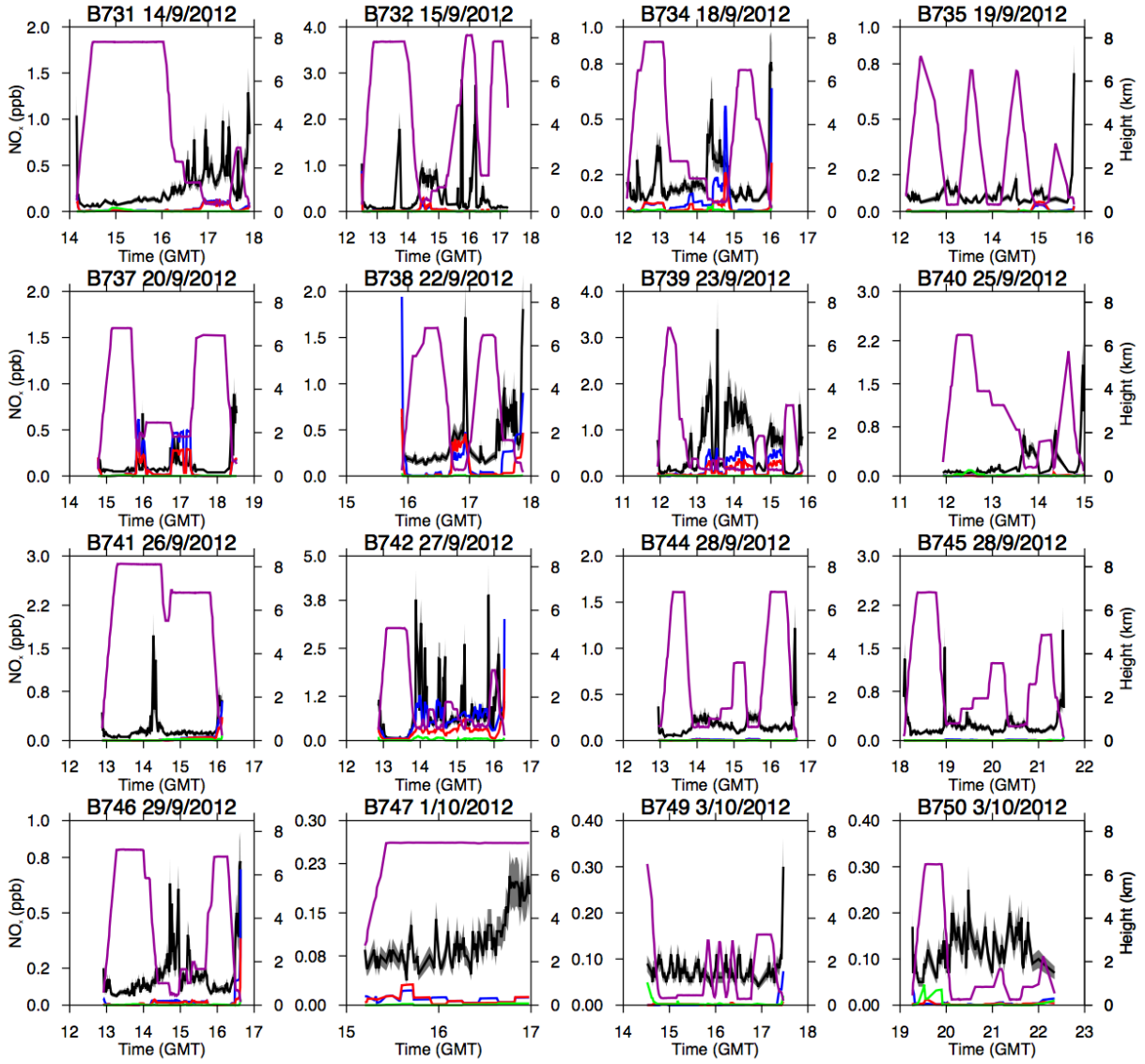

Figure 4.24 Observed NO_x concentrations (black) during the SAMBBA aircraft campaign compared to AN_MET (red), AN_METCOM (blue) and FOR_NBB (green) for 16 of the 20 SAMBBA flights. Purple indicates the altitude of the aircraft. Note the different y-axis ranges.

Flight B744 and B745 sampled areas of previous deforestation fires, showing significant perturbations in CO (>180 ppb) and NO_x concentrations. While C-IFS generally captured the background CO in the boundary layer, C-IFS NO_x concentrations were negligible. These elevated concentrations are likely to be biomass burning in source due to this

corresponding CO increase and suggests either an underestimation of the impact of PAN on NOx concentrations after fires or low NO_x emissions.

The average NO_x profile for each flight is shown in Figure 4.25. In the western region, as with CO, the larger fires captured by the model compare better to observations near the surface. However, the vertical structure of NO_x is still underestimated throughout the profile, even at the surface, where the model emits all fire emissions. This suggests that the total NO_x flux in the west is underestimated by the emission inventory and the model uncertainty isn't solely down to an inaccurate injection or missing small fires. As with the flights in the remote regions, C-IFS NO_x is underestimated in the free troposphere, above the maximum height of injection predicted by MODIS, further suggesting a missing NO_x source. The highest observed NO_x concentrations, in the free troposphere, is in flight B732 at ~6km, this flight occurred as a strong convective system moved in from the west and could be due to lightning NO_x emissions associated with this convection.

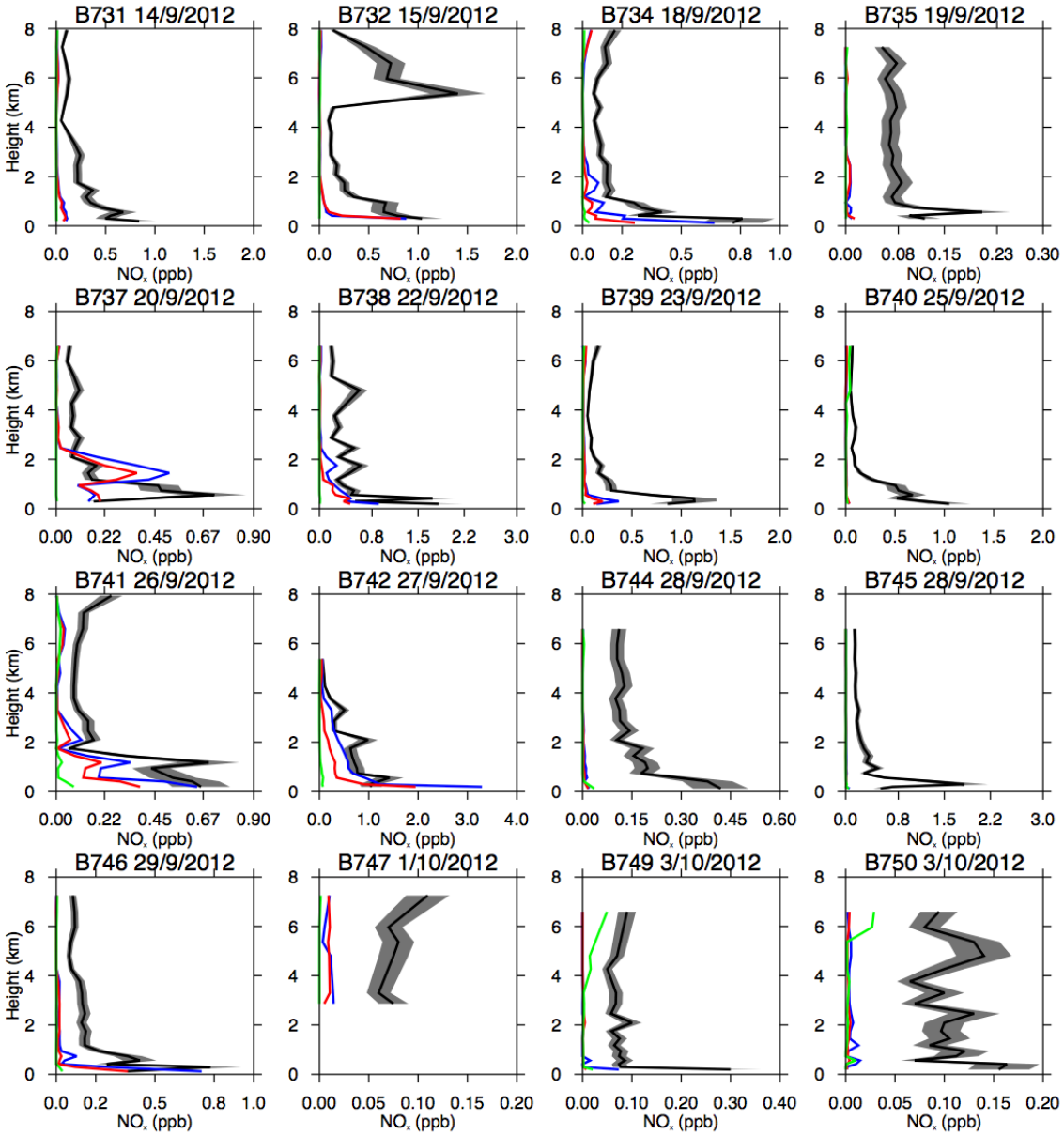

Figure 4.25 Average NO_x profiles ppb (black) from the SAMBBA aircraft campaign compared to AN_MET (red), AN_METCOM (blue) and FOR_NBB (green) for 19 of the 20 SAMBBA flights.

Figure 4.25 shows the difference in NO_x concentrations between the 3 different flight phases and in particular the difference between the western and eastern regions. As with the satellite observations there are higher observed concentrations of NO_x in the eastern region. The maximum mean observed eastern NO_x concentrations was 1.5 ppb, in an

elevated layer of ~1km, this compares to the averaged maximum of 0.75 ppb in the west. This corresponds well to previous studies showing higher NO_x emissions associated with savannah fires compared to tropical fires and supports the higher emission factors suggested in (Akagi et al., 2011; Andreae & Merlet P, 2001). This is due to the higher proportion of flaming fires in the savannah which is was seen by the increase in flaming fires observed by flight B732 during SAMBBA. The higher injection height over the eastern savannah region, seen in CO observations, is also seen in the NO_x observations as concentrations above 0.5 ppb were observed at ~4km. C-IFS shows higher NO_x concentrations in the eastern region, but as with the satellite comparison, there is still a significant negative bias.

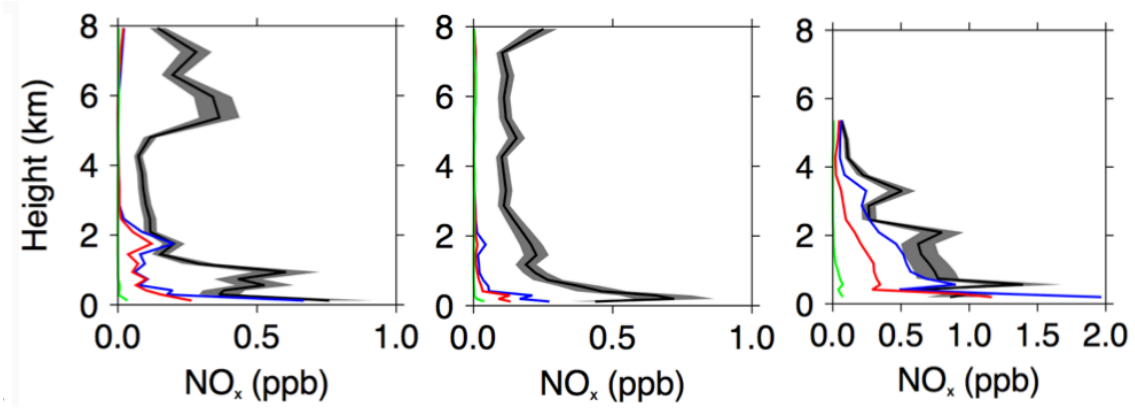

Figure 4.26 Comparison of mean NO_x profiles (ppb) between SAMBBA observations (black) and C-IFS simulations AN_METCOM (blue) and AN_MET (red). The three panels from left to right represent: the western region phase 1, the western region phase 2 and the eastern region.

As seen in Section 4.4.2 the assimilation of OMI NO_2 increases the NO_x values in both the western and eastern region to a greater extent than MOPITT did for CO and this can also be seen by the comparison of AN_METCOM to the SAMBBA observations. The assimilation generally improved concentrations compared to SAMBBA, at least close to fire sources where concentrations where highest (Flight B734, B738, B741, B742 and B746), due to the lack of injection height in the model however, the majority of this increase is at the surface. This leads to an overestimation of near-surface concentrations and an underestimation away from the surface after assimilation, as seen for CO.

However, the shorter lifespan of NOx, compared to CO, means an inaccurate injection height has a larger impact on model bias, as the rapid mixing in the boundary layer is less effective at counteracting the bias. This leads to the inaccurate model vertical profile in flight B738 for NO_x, even though the vertical structure for CO during this flight was well captured by C-IFS.

The assimilation of OMI does little to improve the underestimation of background concentrations, both in the free troposphere and in the pristine regions. The assimilation considers both the model and satellite values, the fact that modelled NO_x concentrations are negligible in these background conditions, adds a bias to the analysis product as the increments will be applied in a region where the model predicts NO_x concentrations rather than in a location it does not. This is particularly the case for the bias in the free troposphere (4-8 km) over the western region, where the vertical distribution of the NO_2 increments following the assimilation of total column OMI data, would solely be dependent on the vertical information provided by the model. This suggests that these elevated NO_x concentrations are causing the bias between the analysis data, after the assimilation of OMI, to the RAL OMI product seen in Section 4.4.2.

Figure 4.27 shows correlation values between modelled and observed NO_x for the different flight phases. The AN_MET comparison shows the large underestimation of the background model compared to the aircraft observations. The assimilation of OMI in AN_METCOM, decreases the MFB from -141% in the eastern region to -19% after OMI NO_2 is assimilated. Both simulations AN_MET and AN_METCOM have errors in the western of over -100%, although, some improvement from assimilation is seen for the higher NOx concentrations during western region phase 1.

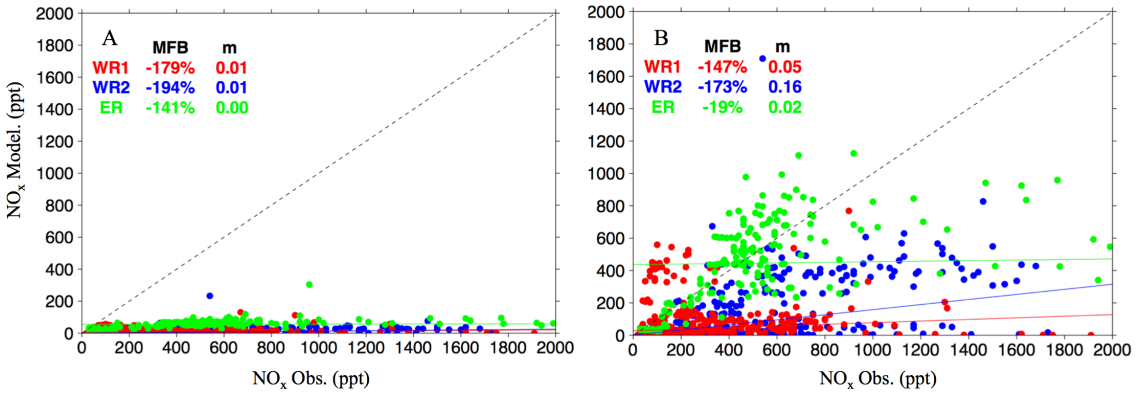

Figure 4.27 Correlation between SAMBBA NO_x (ppt) observations and C-IFS simulations (a) AN_MET and (b) AN_METCOM. WR1 and WR2 refer to the first and second phases of the flights over the western regions and ER represents the Eastern cerrado region. MFB is the mean fractional bias (%) between the observation and the model and NMB is the normalised mean bias.

4.5.3 O_3 formation

Figure 4.24 shows results from 19 of the 20 SAMBBA flights with O_3 concentrations from the campaign and C-IFS simulations AN_METCOM, AN_MET and FOR_NBB. Average O_3 concentrations outside the plumes during the SLR flight operations was 40 ppb over the western region during the first phase, 62 ppb over the eastern region and 36 ppb during the second phase of the campaign. These concentrations are around the ~40 ppb mark known to impact plant health, although lower concentrations may damage sensitive forest regions (Pacifico et al., 2015a) and are significantly higher than literature background concentration of 12 ppb. The flights sampling the pristine northern region (flights B735, B749, B750), observed lower concentrations of O_3 compared to the perturbed regions, but showed an increase from 18 ppb to 25 ppb from phase 1 to phase 2 in the SLR operation.

The average vertical profile for each flight is shown in Figure 4.29, and shows the large predicted contribution of biomass burning emissions to O_3 concentrations in C-IFS, during the flight campaign. Increases in C-IFS NO_x, in and around plumes, correspond with a modelled increase in O_3, but as NO_x is underestimated compared to the SAMBBA

flight observations, so is O_3. Due to the uncertainty in background NO_x concentrations, it is unclear if this bias is down to an underestimation of fire emissions or a different NO_x source. However, a higher contribution of fires to O_3 concentrations can be expected in B731, B739 and B740, where the model does not adequately account for the observed smaller fires, as such emissions are low and C-IFS O_3 concentrations have a more significant bias than the larger fires in B732, B738 and B742. Likewise, these larger fires show a larger bias in C-IFS above the surface due to inaccurate emission injection of NO_x. The underestimation of NO_x in regions after fire activity in flights B744 and B745 also corresponds to a large bias in O_3.

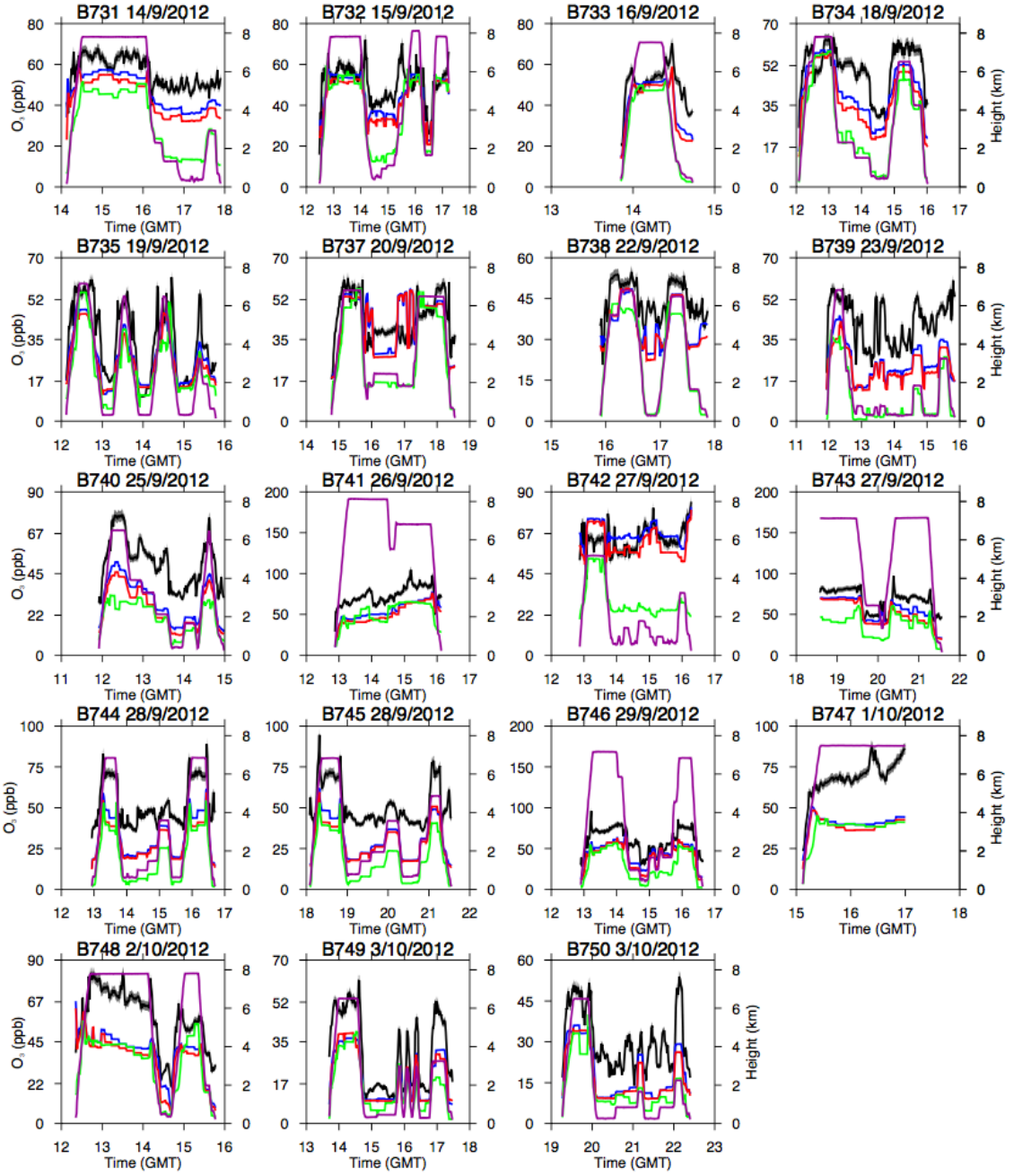

Figure 4.28 Observed O_3 concentrations (black) during the SAMBBA aircraft campaign compared to AN_MET (red), AN_METCOM (blue) and FOR_NBB (green) for 19 of the 20 SAMBBA flights. Purple indicates the altitude of the aircraft. Note the different y-axis ranges.

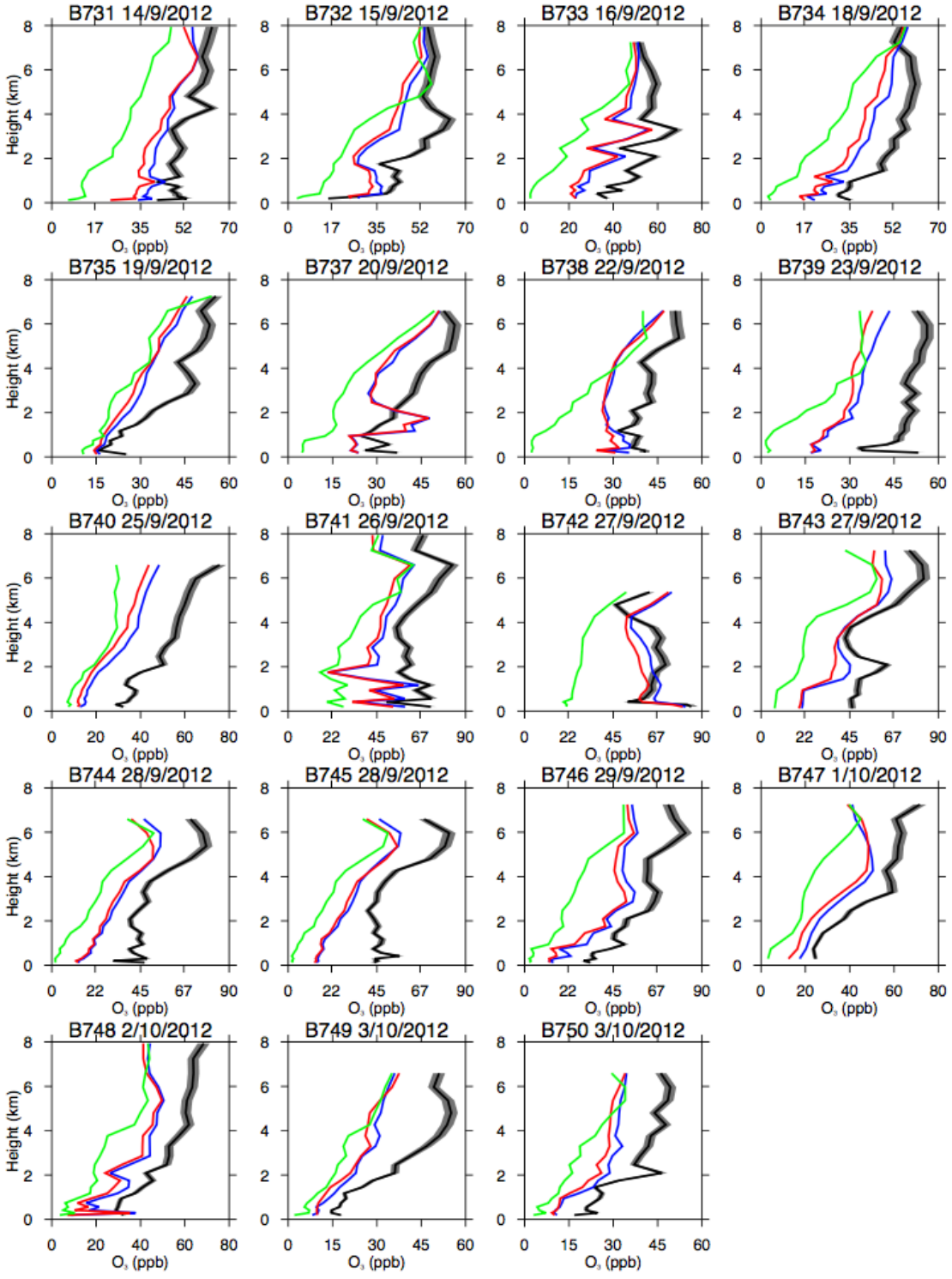

Figure 4.29 Average O_3 profiles ppb (black) from the SAMBBA aircraft campaign compared to AN_MET (red), AN_METCOM (blue) and FOR_NBB (green) for 19 of the 20 SAMBBA flights.

Impact of fires on ozone

Figure 4.30 shows average O_3 vertical profiles from the SAMBA observations and C-IFS simulations, AN_METCOM AN_MET and FOR_NBB for each flight phase. The highest O_3 observations are seen in the eastern region, where NO_x concentrations are also highest see Figure 4.25, with 1.5 ppb of NO_x. O_3 concentrations in the free troposphere (> 4 km) increase in the west during the dry-to-wet transition and while boundary layer concentrations remain similar the negative bias in C-IFS increases. Differences between simulations FOR_NBB and AN_MET show the impact of fire emissions on O_3 concentrations with ~40 ppb formed in the eastern region, 10-20 ppb in the western region.

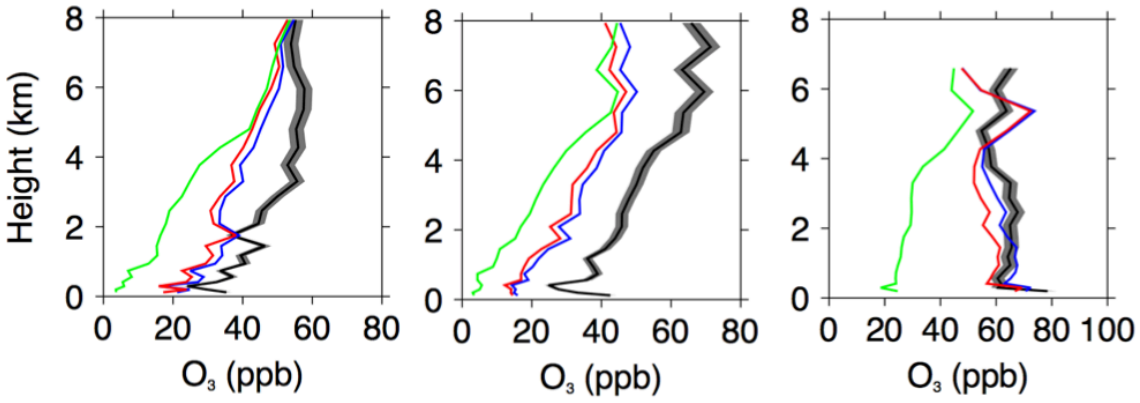

Figure 4.30 Comparison of mean O_3 profiles (ppb) between SAMBBA observations (black) and C-IFS simulations AN_METCOM (blue) and AN_MET (red). The three panels from left to right represent: the western region phase 1, the western region phase 2 and the eastern region.

Figure 4.31 shows correlation values between modelled and observed O_3 for the different flight phases. In all three phases the model underestimates the observed O_3 concentrations with the largest bias in the dry-to-wet transition (MFB -53%).

As mentioned in earlier chapters, the lack of MLS assimilation during September 2012 severely limited the impact of direct O_3 observations on the tropospheric part of the analysis product as stratospheric data could not be removed from the total column. As such changes in the analysis during the first phases of the flight campaign are most likely due to the assimilation of OMI NO_2. The impact of the assimilation of composition observations on O_3 is seen in Figure 4.31 AN_METCOM and reduces the MFB (-45%)

and NMB in the Western region. In the eastern region, the assimilation sees the largest change, AN_MET has a small underestimation (MFB -4%) while AN_METCOM has a small overestimation (MFB 4%). The O_3 profiles in Figure 4.30 show that this overestimation is near the surface and is most likely related to the overestimation of surface NO_x values in the analysis. The increases in O_3 after assimilation in AN_METCOM corresponds to the changes in NO_2 from OMI assimilation suggesting, as in Section 4.4.2, the assimilation of OMI NO_2 is having the largest impact on O_3 concentrations.

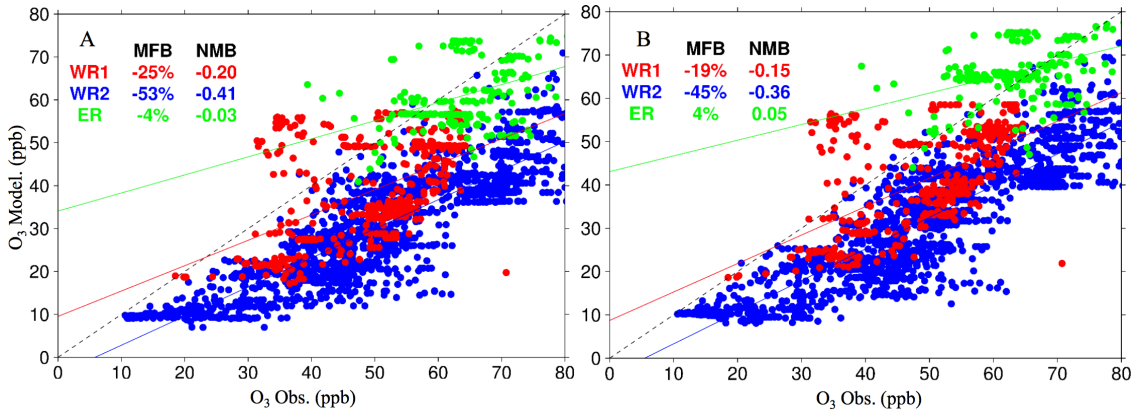

Figure 4.31 Correlation between SAMBBA O_3 (ppb) observations and C-IFS simulations (a) AN_MET and (b) AN_METCOM. WR1 and WR2 refer to the first and second phases of the flights over the western regions and ER represents the Eastern cerrado region. MFB is the mean fractional bias (%) between the observation and the model and NMB is the normalised mean bias.

Figure 4.32 shows surface O_3 concentrations taken at Porto Velho during September-October 2012. The average day time average at the surface site is 28 ppb, which is lower than the average near-surface concentrations observed during the flight campaign and only 7 days out of the 2 month time period pass the 40ppb threshold identified in Ainsworth et al., 2012. Compared to the previous comparison to the Porto Velho ground-sties in Pacifico et al., 2015 C-IFS does a better job of capturing O_3 concentrations instead of overestimating the observations, but places the day time maximum earlier than

the observations. The night time concentrations are still overestimated by the model suggesting an overestimation of either chemical or dry deposition of O_3 in the model.

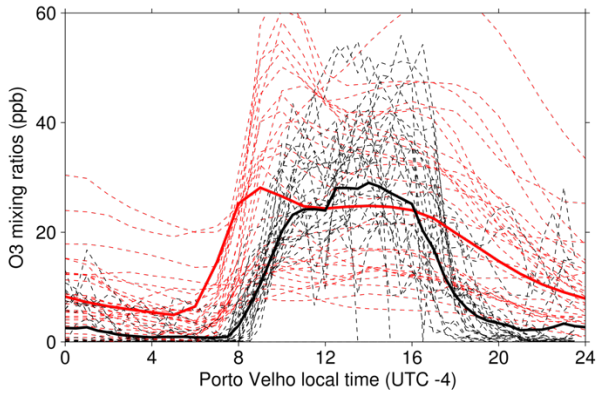

Figure 4.32 Surface O_3 over Porto Velho during September-October 2012, ground site observations (black) and AN_MET (RED). Dotted lines indicate diurnal cycle for each day and solid represents the mean.

4.6 TOMCAT sensitivity runs

In order to quantify the extent to which either NO_x emissions factors in GFAS or an inaccurate injection height cause the bias in NO_x and O_3 concentrations compared to satellite and SAMBBA observations, sensitivities experiments were run with the TOMCAT CTM. Monthly mean fire emissions were used instead of the daily fire emissions used in C-IFS as the runs were used to roughly estimate the results of different parameters on O_3 formation and the current fire emission input in TOMCAT uses monthly means as its generally used to run simulations over a longer time-scale. During the first half of the campaign the monthly mean emissions are larger than the daily emission files as the campaign took place near the end of the dry season and there were plenty of high emission data before the campaign started. For the second half of the campaign, average emissions are smaller than the daily emission files used in C-IFS as

the campaign takes place at the start of the wet-season and the amount of fires drops of considerably by the end of October.

Two sensitives experiments are discussed in this section and are summarised in Table 4.2, with TOM_3.4 referring to NOx GFAS emissions scaled by 3.4, the bias between the OMI NO_x field and AN_METCOM, and TOM_INJ with a prescribed injection height where emissions are injected into the model as they were observed during the flight B742, the flight sampling savannah fires in the eastern region with NO_x emissions observed up to 4km. For each experiment,.

Name	Type	Emissions	Injection	Description
TOM	CTM	GFAS	Surface	Tomcat simulation with daily GFAS emissions.
TOM_3.4	CTM	GFAS×3.4	Surface	TOMCAT stimulation with daily GFAS NOx emissions multiplied by 3.4.
TOM_INJ	CTM	GFAS	Prescribed	TOMCAT simulation with a prescribed injection height.

Table 4.2 TOMCAT Experiments run over the SAMBBA campaign period September - October 2012.

Figure 4.33 shows the impact of the prescribed injection height on NOx concentrations during the two different flight phases. Lower concentrations are seen in TOM_INJ at the surface, with the injection height, while higher concentrations in the rest of the boundary layer, with NOx concentrations above 0.1 ppb up to 4 km. Even with this injection height, concentrations above the boundary layer (>4km) are still small.

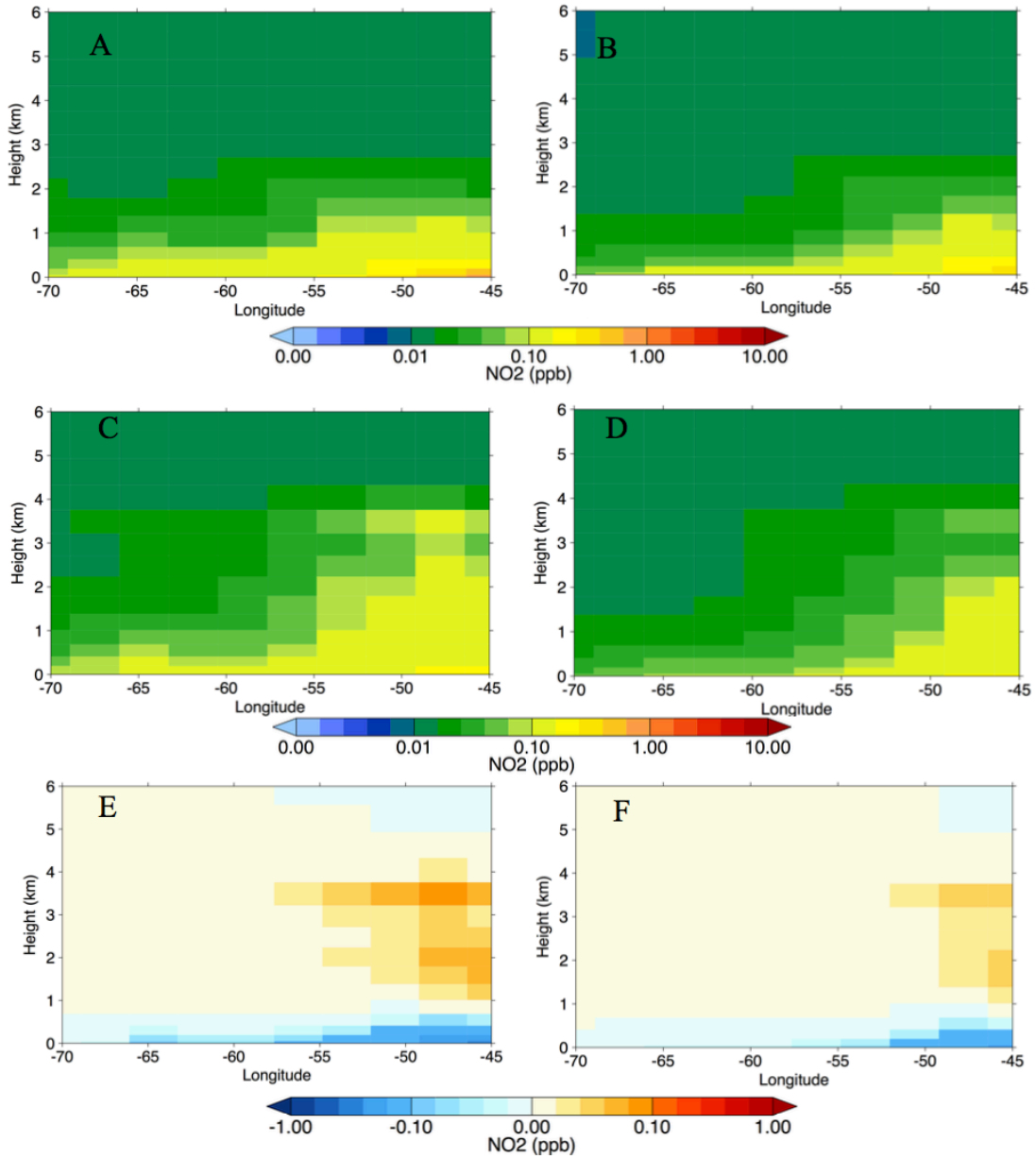

Figure 4.33 Impact of prescribed injection height on NO_2 latitude/height zonal mean cross section over the latitudes sampled by the SAMBBA flights (-5.5º to -12º) in TOMCAT for the 2012 tropical biomass burning season (Sept-Oct). The left column shows average results from the dry season (September 1-22) and the right column shows equivalent results from the dry-to-wet transition (September 23 – October 31). Panels (a, b) show mean NO_2 concentrations (ppb) from the TOMCAT simulation TOM. Panels (c, d) show mean NO_2 concentrations (ppb) from the TOMCAT simulation TOM_INJ. Panels (e, f) show the mean difference between TOM_IN and TOM.

Impact of fires on ozone

Figure 4.34 shows the evaluation of the three different TOMCAT experiments against the three average SAMBBA profiles for each flight phase. Increasing fire emissions by 3.4, leads to an overestimation of the eastern region profile at the surface, but still underestimates NOx concentrations through the rest of the profile. The prescribed injection in TOM_INJ, leads to a decrease in NOx concentrations at the surface and an increase, but a more accurate vertical structure in the eastern region. In the western region surface concentrations are still lower than the observed concentrations, despite an increase in fire emissions by 3.4, the injection height, as it is prescribed for the eastern region does not generally improve the vertical structure in the west. Interestingly, despite this larger injection height there is still no increase in NOx concentrations above 4 km.

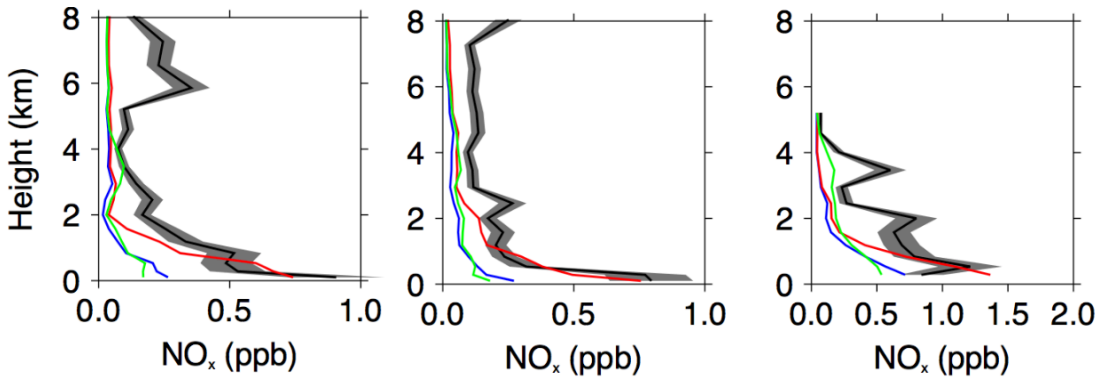

Figure 4.34 Comparison of mean NO_x profiles (ppb) between SAMBBA observations (black) and TOMCAT simulations TOM (blue), TOM_3.4 (red) and TOM_INJ (green). The three panels from left to right represent: the western region phase 1, the western region phase 2 and the eastern region.

Figure 4.35 shows the evaluation of the three TOMCAT experiments against average O_3 profiles for the three flight phases. For the enhanced emission experiment O_3 concentrations are higher in the model than the observed concentrations for the first few kilometres, before underestimating O_3 concentrations above 3 km. However, there is a significant increase in O_3 concentrations above 3 km in the TOM_3.4 experiment compared to the standard TOMCAT experiment. The prescribed injection height for NOx emissions leads to an improved vertical structure for the first 4 km and also leads to

increases in the free troposphere in all three regions, despite still being lower than the enhanced emission experiment.

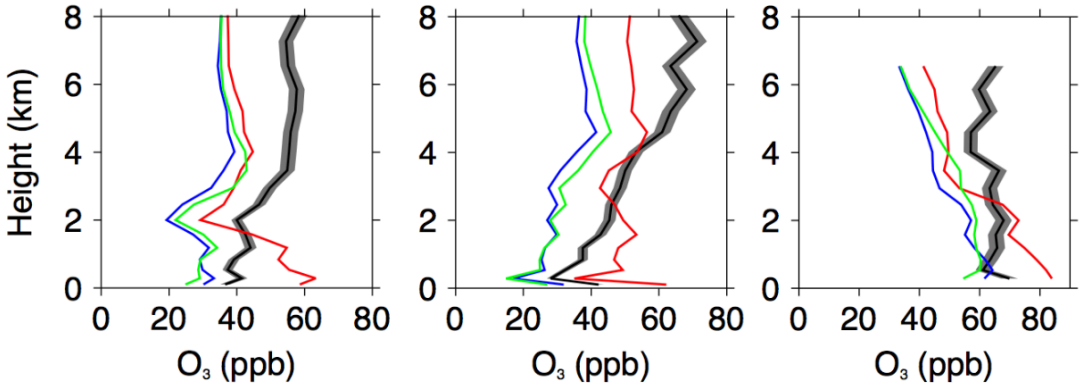

Figure 4.35 Comparison of mean O_3 profiles (ppb) between SAMBBA observations (black) and TOMCAT simulations TOM (blue), TOM_3.4 (red) and TOM_INJ (green). The three panels from left to right represent: the western region phase 1, the western region phase 2 and the eastern region.

4.7 Summary

CO concentrations are generally well captured by C-IFS with GFAS emissions, particularly close to large fires. Smaller fires in the western region are, however, not accurately seen by the emissions and the vertical structure is poor for all fires due to the modelled emissions being solely injected at the surface. The inaccurate injection is particularly important over the eastern savannah region, where fires have a higher injection height, and for enhanced CO concentrations in the free troposphere. The underestimation of CO concentrations during the first phase of the western region flights is due to the underestimation of smaller fires either due to the reliance of GFAS on GFED dry-matter fluxes or the in-ability of FRP measurements to observe these fires. This is also the likely cause of the bias for FRP-based emissions compared to other emission inventories over deforestation region seen in Pereira et al., 2016. Additionally, part of the underestimation near-fires may be down to a model representation error as the resolution of C-IFS is not fine enough to completely resolve a near-source fire plume, which can be seen by misplaced fires in certain flights. During the dry-to-wet transition and over the

pristine northern region the vertical structure and magnitude of observed CO, is captured by the model, suggesting that background CO is accurate in the model and confirms that fire emissions are the main source of the small CO model bias.

NO_x concentrations are not accurately captured by either C-IFS or TOMCAT with GFAS emissions, with significant biases seen in both the west and the east. Similar biases to the CO evaluation are seen, with smaller fires not correctly accounted for and a poor vertical structure. However, the vertical structure is less well captured for NO_x than CO and negative biases are seen near the surface for larger fires, despite emissions being solely injected at the surface. An accurate injection height is more important for NO_x than CO due to its shorter lifetime and improvements are seen compared to the SAMBBA vertical profile and OMI total column when an emission height is prescribed in TOMCAT. However, the injection height is not the only source of bias in both models with total fluxes low in both models compared to SAMBBA. This is particularly the case in the western region where increasing GFAS emissions by 3.4, still leads to an underestimation of observed NO_x near the surface.

Background NO_x concentrations are also underestimated by the model with concentrations in both the free troposphere and the pristine northern regions being negligible in the model with observations suggesting concentrations around 0.1 ppb. It is unclear whether this bias is down to a missing emission source or an insufficient representation of PAN formation from NO_x leading to subsequent increases in NO_x concentrations away from fires by PAN decomposition. The higher observed NO_x concentrations correspond to elevated CO concentrations after a main fire event, where the model captures CO but not NO_x, suggesting an underestimation of the impact of PAN within the boundary layer. Increases in NO_x in the free troposphere, corresponding to increases in observed CO suggests a missing impact in the free troposphere. However CO is also biased low in the model at this altitude suggesting this bias is mainly due to transport. It should be noted that the flight during a major convective event B733, observed high NO_x concentrations in the free troposphere and a large negative bias in C-IFS and could suggest that lightning NO_x is also a significant contributor to the bias in the free troposphere.

Impact of fires on ozone

High surface concentrations are observed in both the western region (~40 ppb) and the eastern region (~60 ppb) and correspond to high observed NO_x concentrations, with 20-40% of these concentrations predicted by C-IFS to be caused by fires. Compared to previous model studies the use of daily GFAS fire emissions seems to provide more accurate surface O_3, with day-time O_3 concentrations at Porto Velho well captured by C-IFS. However, there is still a positive bias during the night time suggesting a bias in either the chemical or dry deposition sink. O_3 concentrations during the flight campaign are well captured by C-IFS in the eastern region, but in the west O_3 concentrations are poorly captured above the first 2 km, and concentrations after the dry-to-wet transition are also underestimated. This corresponds with low NO_x concentrations away from main fire sources and most likely an underestimation of the impact of PAN in C-IFS. Increasing surface NO_x concentrations in TOMCAT, to match observations, leads to an overestimation of O_3 and suggests that modelled O_3 production might be too sensitive to increased NO_x concentrations, which may have contributed to the overestimation of O_3 in previous studies (Bela et al., 2015; Pacifico et al., 2015a).

Assimilating reactive gas total columns general improves the C-IFS correlation to SAMBBA observations and satellite data as near-fire concentrations are increased by the assimilation. Due to the assimilation of total column satellite products rather than profiles, the vertical structure of CO, NO_x and O_3 is generally not improved by assimilation as the vertical distribution is down to the model error co-variance matrixes. The largest increases are seen in NO_x concentrations after OMI NO_2 assimilation, as the assimilation corrects for the large underestimation of NO_x seen in the comparison to the OMI product. This is in contrast to previous work using the C-IFS assimilation system which suggested only minor changes from OMI assimilation. OMI assimilation does a better job in correcting for the eastern region due to the higher concentrations observed by satellite and that the high concentrations observed in the west over the free troposphere are incorrectly distributed by the assimilation as the model predicts little-to-no NO_x concentrations above 2 km. There is also evidence of OMI NO_2 assimilation improving the O_3 field as the analysis increments for O_3 are very different to the AN_METCOM-AN_MET differences and a significant increase in C-IFS O_3, after assimilation, is seen in the eastern region, where NO_2 increments are highest. This increase in O_3 in the east after assimilation, leads to a small positive bias compared to the aircraft observations and

further suggests that O_3 production is too sensitive to the increase in NO_x from assimilation.

Satellite and in-situ concentrations show that the majority of NO_x is emitted from the eastern cerrado (savannah) region and there is a strong evidence of westerly trade winds pushing PAN concentrations from these fires over the deforestation and pristine regions, increasing O_3 concentrations over both the west and east. The predicted future 'savanna-fication' of the Amazon, due to more frequent and powerful droughts, and the already observed increase in burnt area in the eastern cerrado region from 1998 till 2015 (Andela et al., 2017), suggests that NOx emissions and subsequent O_3 concentrations over the Amazon will increase in the near future, potentially increasing the positive climatic feedback on GPP.

5 Impact of fires on carbonaceous aerosol during the SAMBBA campaign

5.1 Introduction

This chapter investigates the impact of fire emissions on carbonaceous aerosol during the SAMBBA flight campaign using models, satellite data and in-situ observations. A particular focus is on how aerosol optical depth (AOD) assimilation modifies predicted speciated aerosol concentrations (i.e. black carbon (BC) and organic matter (OM)) and to assess whether the technique also improves these more specific and "non-assimilated" aerosol properties. In so-doing, the investigation is used as a means to identify potential sources of aerosol model uncertainty during the emission-dominated Amazonian fire season, particularly focussing on aerosol fire emissions, impact of injection height and carbonaceous aerosol lifetime.

Previous studies using GFAS fire emissions have highlighted significant increases in aerosol fields with AOD assimilation, attributing model underestimation to low emission fluxes and inaccurate injection heights (Huijnen et al., 2012; Johannes W Kaiser et al., 2011; Rémy et al., 2016). To counteract the low emission fluxes, GFAS recommends that a 3.4 scaling factor is applied (Kaiser et al., 2012) to carbonaceous aerosol fire fluxes in non-constrained model runs or forecasts, where AOD from MODIS is not assimilated. This is despite a total column metric, AOD, calculated with fixed model optical properties for each aerosol type as discussed in Chapter 3 (Section 3.4.2), being used to infer this model/analysis difference and the subsequent changes to aerosol emissions. The original work (Kaiser et al., 2012) and later studies (Huijnen et al., 2012; Rémy et al., 2016) identify that this scaling does not fully account for the model/analysis difference and show that the model/analysis AOD errors vary by location and proximity to fires, suggesting the increase in emissions is an over-simplified approach.

In this study both model and analysis fields are compared to independent observations of speciated mass concentrations from the SAMBBA aircraft campaign. This indicates the

accuracy of aerosol model fields, particularly the BC/OM ratio, and whether AOD assimilation improves modelled aerosol mass concentrations compared to independent observations. The model bias for species compared to the analysis and SAMBBA observations (Darbyshire et al., 2017) will be compared to the AOD-based scaling factor, and new values will be calculated for South America. Additionally, to identify the impact of the emission injection height on the vertical structure and regional distribution of aerosol mass simulations, an injection height parameterisation from the Plume Rise Model (PRM) (Paugam et al., 2015) implemented in C-IFS in (Rémy et al., 2016) is compared to the standard C-IFS setup where the emissions are injected at the surface level.

The chapter is structured as follows. Section 5.2 summarises the different model simulations used in this chapter. Section 5.3 discusses the impact of fire emissions in C-IFS during the campaign. Section 5.4 describes the impact of AOD assimilation on modelled fields over the Amazon. Section 5.5 validates model and analysis experiments against independent SAMBBA observations. Section 5.6 identifies the impact of the injection height scheme on the model skill against the independent observations. Finally, section 5.7 summarises the results from this chapter.

5.2 Model experiments

Name	Type	Emissions	Injection	Description
AN_METCOM	analysis	GFAS × 3.4	Surface	Composition and meteorology data assimilated.
AN_MET	analysis	GFAS × 3.4	Surface	Only meteorological data assimilated.
AN_INJ	analysis	GFAS × 3.4	Paugam (2016)	Injection height parameterisation.
AN_NINJ	analysis	GFAS × 3.4	Surface	Standard injection on same branch as AN_INJ.
FOR	forecast	GFAS × 3.4	Surface	Relaxed forecast.
FOR_NSCF	forecast	GFAS	Surface	No GFAS scaling factor applied.
FOR_NBB	forecast	GFAS	Surface	No biomass burning emissions.

Table 5.1 Experiments run over the SAMBBA campaign period September - October 2012. Experiments designated 'analysis' were run in the analysis mode where observations constrain certain model parameters, the 'forecast' experiments were run using the forecast mode with the meteorology relaxed to ERA-INTERIM.

Information on the different experiments used in this chapter are shown in Table 5.1. Two different types of experiment are used, the analysis mode and the forecast mode. The analysis mode contains the 4D-var data assimilation system described in Chapter 3 while the forecast mode runs integrate forward in time from an analysis but without further use of observations. In these retrospective runs the forecast meteorology is relaxed to ERA-Interim, to lessen the computational cost. Different sensitivity runs looking at the impact of injection height and the GFAS scaling factor have also been run.

5.3 Impact of fire emissions

Figure 5.1 shows the average BC and OC fire emissions during the SAMBBA campaign estimated from experimentally measured emission factors (Andreae & Merlet, 2001) and observed Fire Radiative Power (FRP) from MODIS. As with the emissions of CO and

NOx discussed in Chapter 4, the eastern cerrado (savannah) region has a larger flux for both BC and OC than the western forest fires. This is due to a higher observed FRP and a larger number of observed fires, despite the smaller aerosol emission factors for savannah compared to tropical forest fires. In addition to the aerosol savannah/tropical difference, OC carbon emissions have a larger emission factors than BC and as such has a much larger flux than BC. One other key difference between the eastern (cerrado) and western (forested) regions relates to the fact that the SAMBBA campaign had two distinct phases: the first phase (between 04 Sep and 22 Sep), was still in the dry season, whereas the 2nd (between 23 Sep and 3 Oct) was in the transition into the wet season. This temporal shift had a much larger decrease in emissions flux from the dry season to the dry-to-wet transition in the western region as there was a much more extensive region of rainfall.

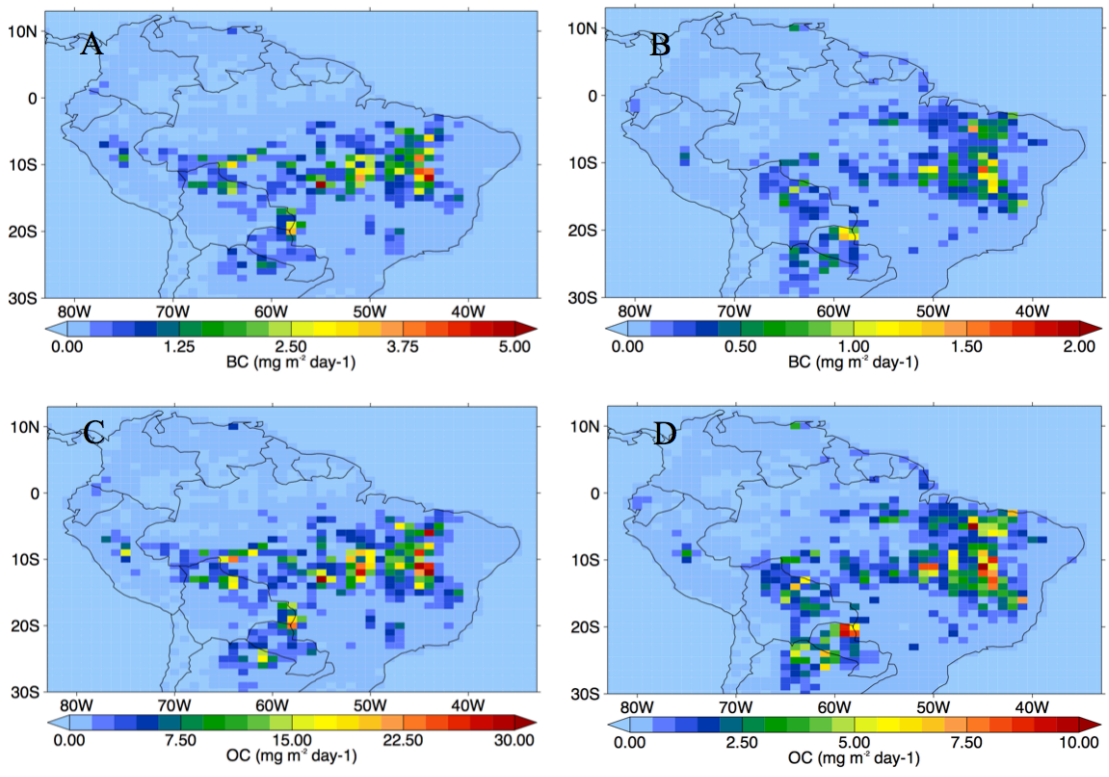

Figure 5.1 BC and OC fire emissions during different SAMBBA flight campaign phases. Average GFAS OC fire flux (mg cm^{-2} day^{-1}) during the SAMBBA flight campaign during (a, c) the dry season (September 1-22) and (b, d) the dry-to-wet transition (September 23 – October 31).

Figure 5.2 and Figure 5.3 show the C-IFS BC and OM fields, respectively, during these two distinct phases of the SAMBBA flight campaign and also the impact of GFAS fire emissions on carbonaceous aerosol concentrations after the application of the 3.4 scaling factor. As with CO concentrations in Section 4.2, BC and OM concentrations are, throughout the campaign, higher in the west, despite more emissions in the east, as easterly trade winds transport the aerosols towards the Andes mountain barrier. Figure 5.2e and f show for BC (and Figure 5.3e and f for OM respectively) the ratio between simulations FOR_NBB and FOR, thereby isolating the dominant contribution that fire emissions make to simulated column BC and OM burdens over the Amazon. Throughout the SAMBBA domain, the vast majority of the carbonaceous aerosol originates from biomass burning with also modest impacts on BC from urban sources on the populated east coast and a significant contribution of biogenic sources to OM seen in the 'pristine' north. Higher concentrations are seen during the main fire season with the total OM burden over all of South America decreasing from 0.27g to 0.21g from the dry to the wet season and the BC burden decreasing from 0.039g to 0.035g.

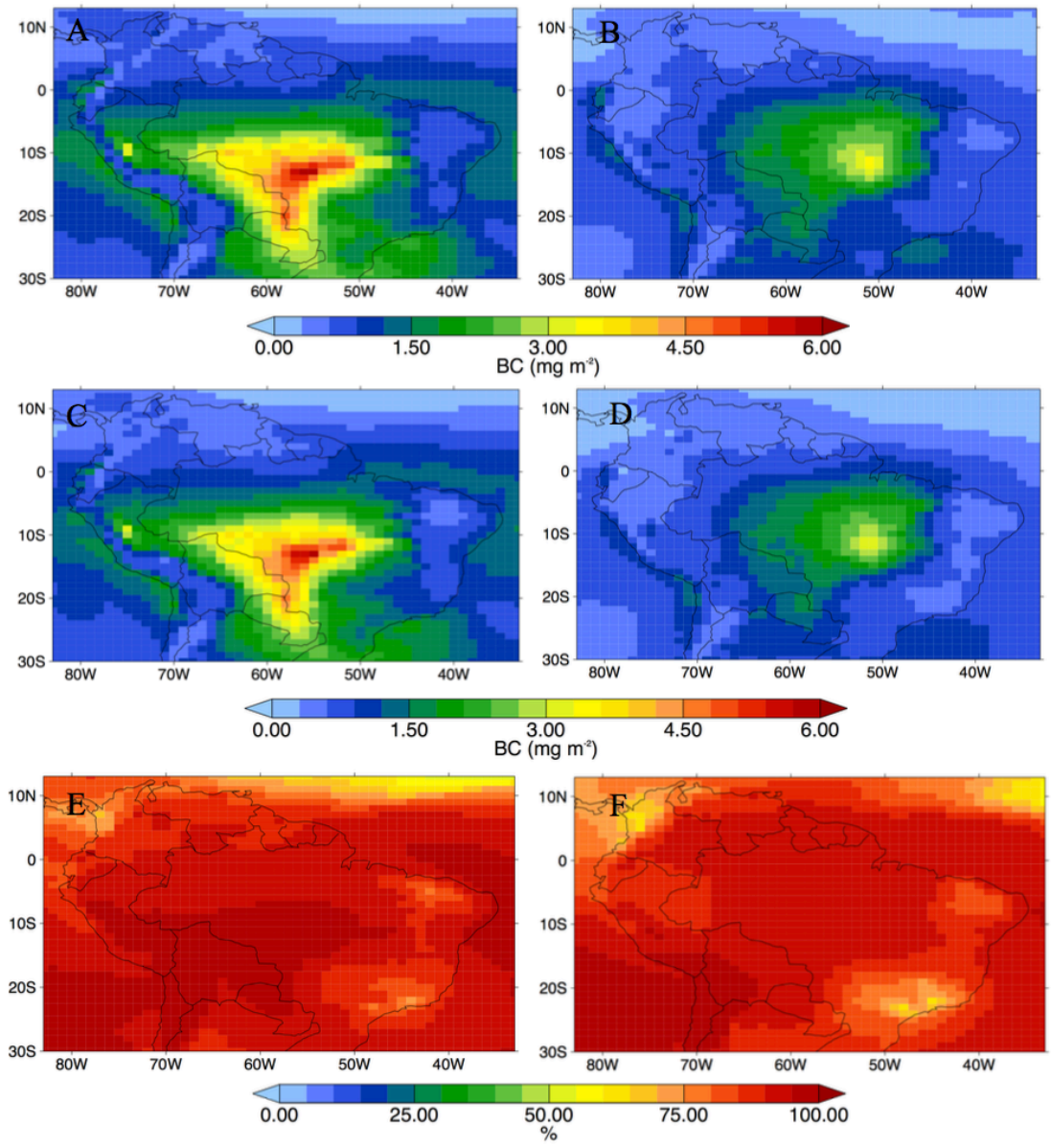

Figure 5.2 The impact of fires on C-IFS-simulated BC tropospheric column during the SAMBBA campaign. The left panels show average results from the dry season (September 1-22) and the right panels show equivalent results from the dry-to-wet transition (September 23 – October 31). (a, b) Total column BC (mg cm^{-2}) from C-IFS simulation FOR. (c, d) Difference in BC column between simulations FOR and FOR_NBB. (e, f) Percentage difference in column BC for panels (c) and (d), respectively.

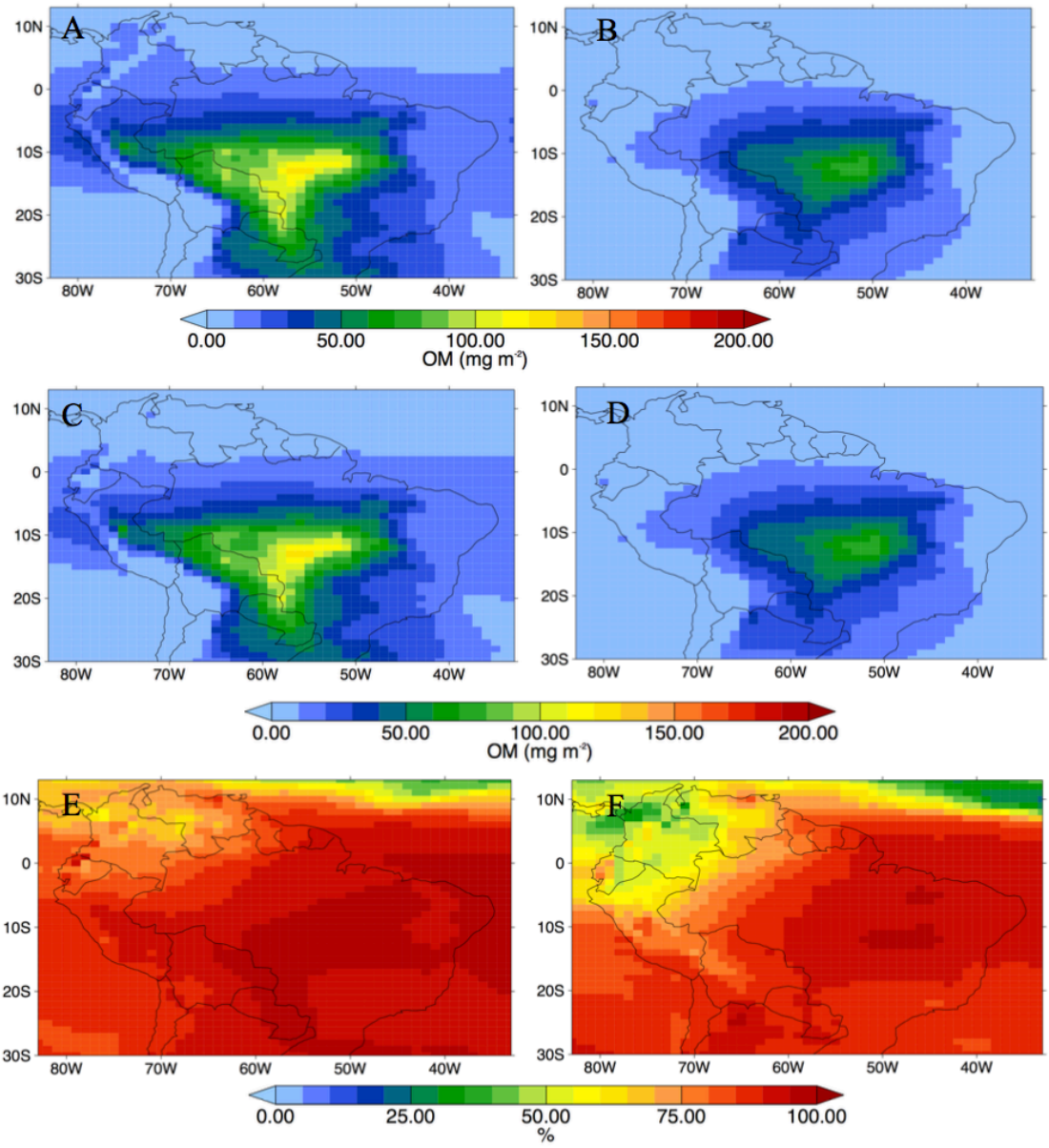

Figure 5.3 The impact of fires on C-IFS simulated OM tropospheric column during the SAMBBA campaign. The left panels show average results from the dry season (September 1-22) and the right panels show equivalent results from the dry-to-wet transition (September 23 – October 31). (a, b) Total column OM (mg cm^{-2}) from C-IFS simulation FOR. (c, d) Difference in OM column between simulations FOR and FOR_NBB. (e, f) Percentage difference in column OM for panels (c) and (d), respectively.

Impact of fires on carbonaceous aerosol

Figure 5.4 and Figure 5.5 show longitude-height cross sections of BC and OM concentrations in C-IFS respectively, over the SAMBBA flight domain (latitude range 12S to 5.5S). As with the total columns, decreases are seen between the dry and the wet season. The aerosol concentrations generally follow the pattern of CO (Section 4.2) with the largest concentrations near the surface which are significantly impacted by fire emissions, with the eastern cerrado showing larger concentrations than the western tropical fires. The transport of aerosol concentrations eastwards can be seen in the free troposphere (1-3 km); larger concentrations are seen west of 55^{o}W with a sharp gradient between the boundary layer and the troposphere predicted in the east. The model predicts no carbonaceous aerosol concentrations above 4 km.

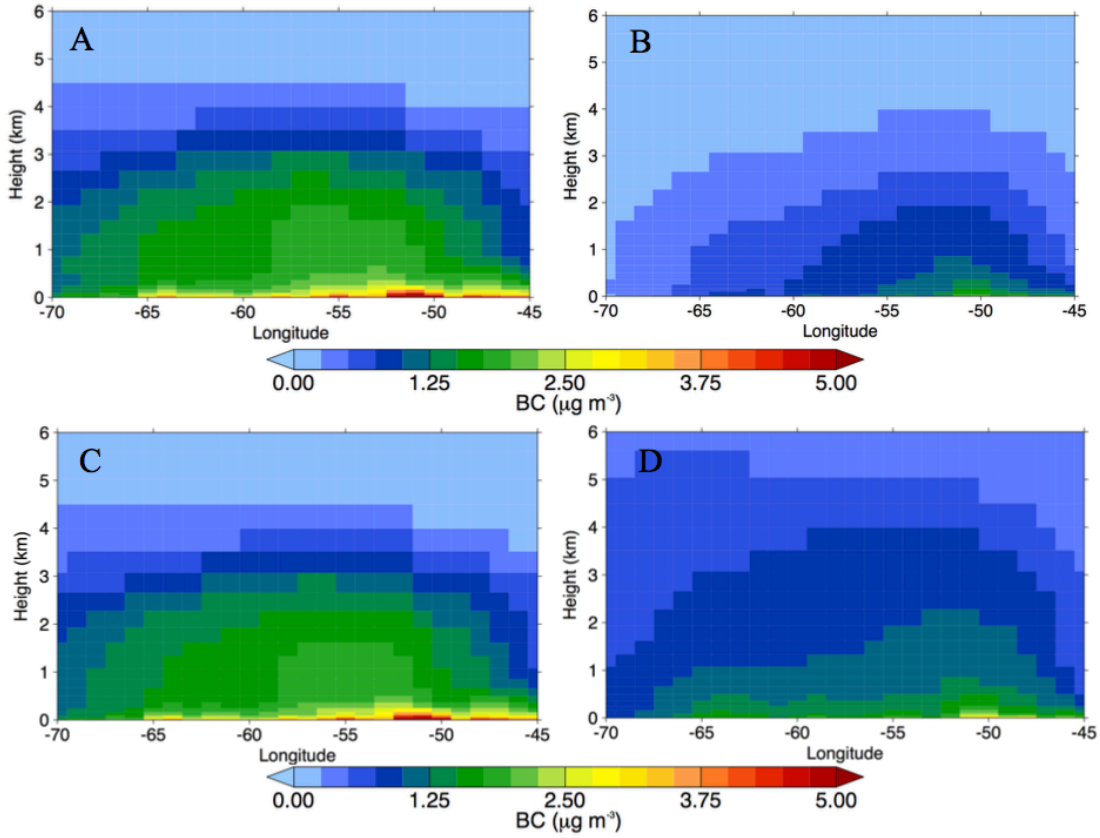

Figure 5.4 The impact of fires on the C-IFS BC latitude/height zonal mean cross section over the latitudes sampled by the SAMBBA flights (5.5°S to 12 °S). The left panels show average results from the dry season (September 1-22) and the right column shows equivalent results from the dry-to-wet transition (September 23 – October 31). (a, b) BC (µg cm^{-3}) from C-IFS simulation FOR. (c, d) Difference in BC concentrations between simulations FOR and FOR_NBB.

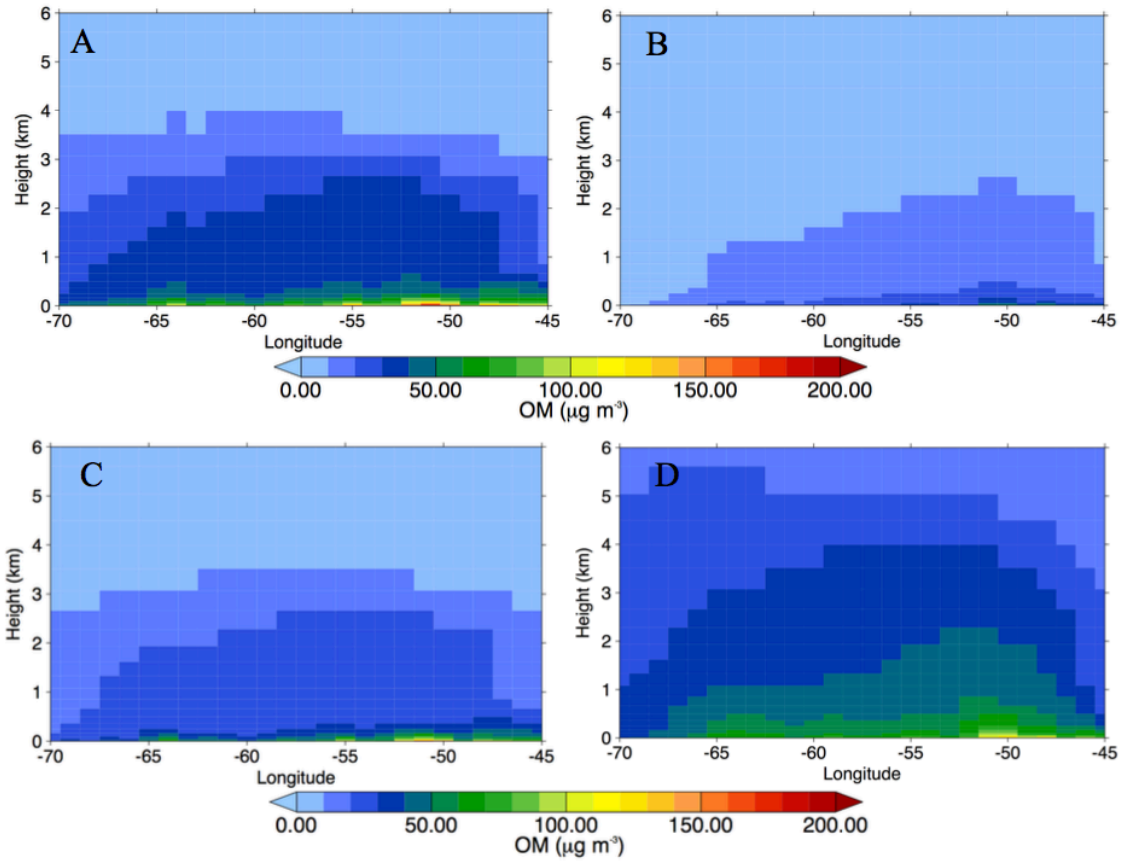

Figure 5.5 The impact of fires on the C-IFS OM latitude/height zonal mean cross section over the latitudes sampled by the SAMBBA flights (5.5ºS to 12 ºS). The left panels show average results from the dry season (September 1-22) and the right column shows equivalent results from the dry-to-wet transition (September 23 – October 31). (a, b) OM (µg cm^{-3}) from C-IFS simulation FOR. (c, d) Difference in OM concentrations between simulations FOR and FOR_NBB..

5.4 Influence of AOD assimilation

Figure 5.6 shows the impact of AOD assimilation on mean campaign concentrations of BC and OM mass concentrations. Figure 5.6a, d and g show concentrations from the C-IFS experiment FOR_NSCF, the standard C-IFS run, which exhibits a large underestimation compared to the analysis product AN_METCOM (Figure 5.6c, f and i) This is comparable to the results from AOD comparisons during both the original implementation of GFAS aerosol emissions (J. W. Kaiser et al., 2012) and in an earlier

C-IFS/SAMBBA evaluation (Rémy et al., 2016). Figure 5.6b, e and h show aerosol concentrations from the C-IFS experiment FOR where GFAS carbonaceous aerosols emissions are increased by a factor of 3.4, as is standard in C-IFS and other models using GFAS. This change has a significant impact on regional concentrations and generally improves the comparison to AN_METCOM, although concentrations are now larger than that seen in that simulation, at least over the main fire-regions.

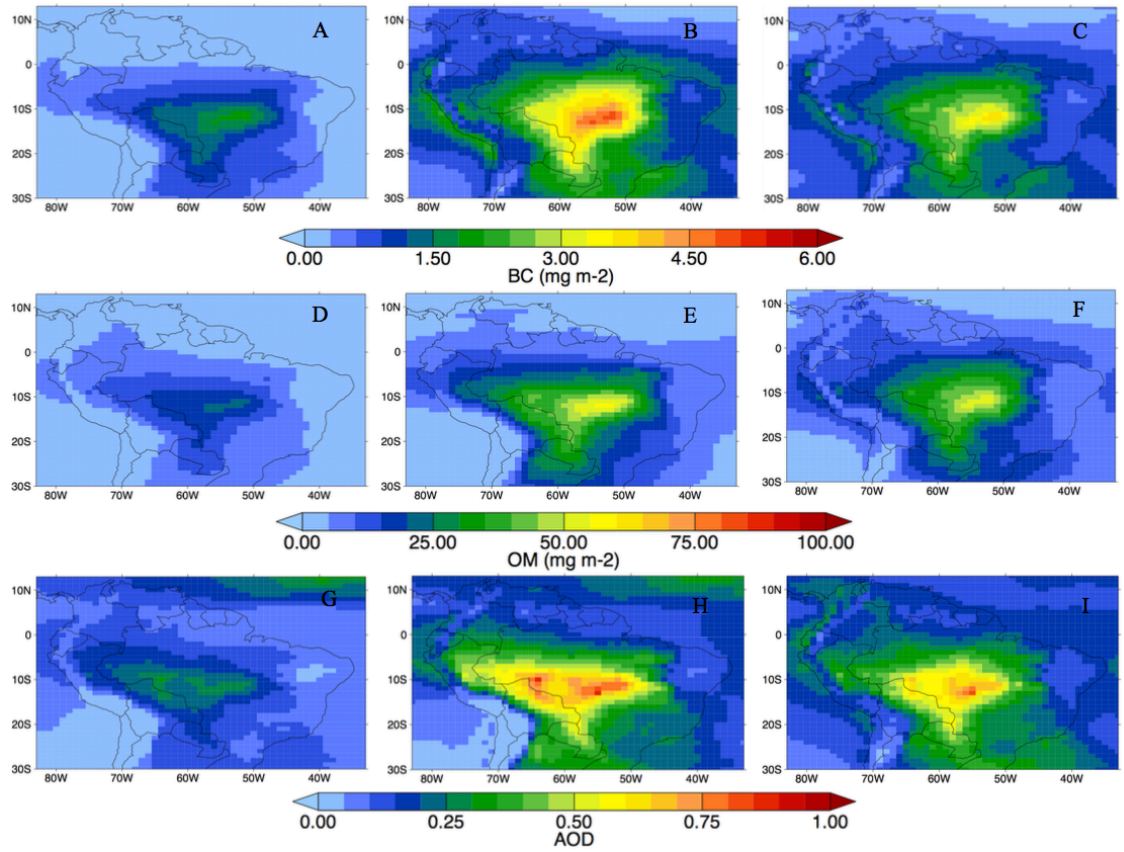

Figure 5.6 Impact of assimilation on C-IFS tropospheric BC mass burden (mg m^{-2}) (a, b,c), OM mass burden (d, e, f) and AOD (g, h, i). Average for the 2012 tropical biomass burning season (Sept-Oct). (a, d, g) C-IFS forecast (FOR_NSCF) (b, e, h), C-IFS forecast with GFAS emissions multiplied by 3.4 (FOR) (c, f, i), C-IFS with assimilated AOD (AN_METCOM).

Table 5.2 shows the ratio between results from simulations AN_METCOM and FS_NSCF for different carbonaceous aerosol metrics. The South America BCAOD +

OMAOD (BBAOD) bias is similar to that seen in Kaiser et al., (2012) (a factor of 4.1). Significant differences from this scaling factor is seen for BCAOD (17.8) and OMAOD (2.36) also suggested in Rémy et al., 2016, although a much larger BCAOD bias is seen in this study. This implies that the biases are different for OM and BC, either relating to their separate emission factors or loss processes. Furthermore, while the bias for the OM burden is similar to OMAOD, the BC burden bias is significantly smaller than BCAOD suggesting that assumed optical properties used to calculate the BCAOD are contributing to the bias. The bias for OM is also largest in the eastern region, where the fire emissions are largest, while the bias for BC is larger when considering all of South America rather than just the emission dominated regions, suggesting that loss processes are contributing to the increased negative bias in BC.

Species	SAmerica	Western region	Eastern region
BC	3.31	2.88	3.24
OM	2.48	2.20	2.85
BCAOD	17.8	18.86	15.45
OMAOD	2.36	2.09	2.67
BBAOD	4.2	3.8	4.54
AOD	1.99	2.16	2.53

Table 5.2 Ratios of C-IFS model and analysis experiments (AN_METCOM/FOR_NSCF) for different aerosol metrics during the tropical fire season (Sept-Oct 2012). SAmerica is the average over the whole of South America, Western region is the average over the tropical forest region and the eastern region is the average over the savannah (cerrado) region. BBAOD denotes BCAOD+OMAOD.

Figure 5.7 and Figure 5.8 show the difference between AN_METCOM and AN_MET (i.e. the difference due to composition assimilation) as well as the analysis increments for both BC and OM, respectively. AN_METCOM, although assimilating MODIS AOD has aerosol GFAS emissions scaled by 3.4. In principle this is done to provide a more accurate model field for assimilation. However, negative analysis increments are calculated over fire emission source regions for both OM and BC, suggesting that aerosol emissions are

too large in C-IFS when this scaling factor is applied. This leads to smaller aerosol concentrations in AN_METCOM than AN_MET close to fire emission sources, with AN_METCOM having BC concentrations ~1.5 mg m^{-3} and OM concentrations ~30 mg m^{-3} lower than AN_MET on average, during the first phase of the flight. The decrease in concentration from assimilation continues in the eastern region during the second phase of the flight despite smaller analysis increments. Despite the negative increments over both eastern and western fires, away from the near-fire sources the majority of the increments are either zero or positive, with large positive values seen in the second-phase of the campaign. If the model-bias seen in Table 5.2 was solely down to the emissions we would expect an accurate 'scaling factor' to improve concentrations across the whole of South America and a too large 'scaling factor' to provide a positive bias throughout South America as well. The positive increments away from the fire sources, and the negative increments close to the fire sources, suggest that fire emissions are not the only source of model uncertainty and it is likely that transport, aerosol ageing and the eventual deposition of these aerosol species is contributing to the model bias and the underestimation of FC_NSCF compared to AN_METCOM.

Significant positive increments are also seen for carbonaceous aerosol species over populated regions such as São Paulo and Rio de Janeiro, as well as Northern Chile. Additionally, positive increments are seen over North-East Brazil on the arc of deforestation, which also corresponds to MOPITT CO analysis increments shown in Chapter 4, and could suggest a missing fire source. The impact of these positive increments is seen in AN_METCOM, with North-East Brazil having higher concentrations compared to AN_MET in the second phase of the campaign.

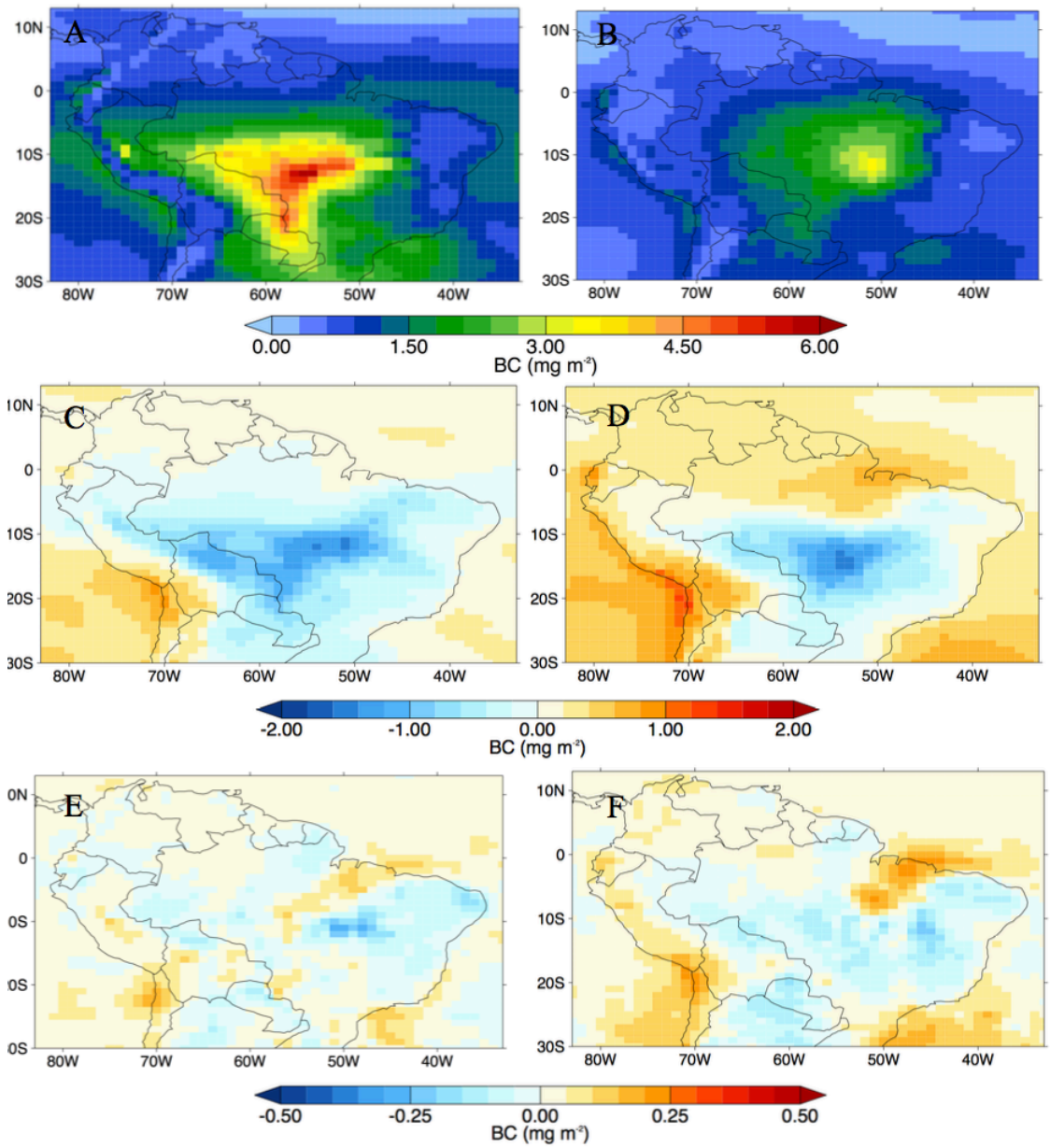

Figure 5.7 Impact of MODIS AOD assimilation on black carbon mass concentration in C-IFS for the 2012 tropical biomass burning season (Sept-Oct). The left panels show average results from the dry season (September 1-22) and the right panels show equivalent results from the dry-to-wet transition (September 23 – October 31). Panels (a, b) show mean analysis tropospheric BC columns (mg cm^{-2}) from the C-IFS simulation AN_METCOM. Panels (c, d) is AN_METCOM – AN_MET, or the average impact of assimilation at each 6-hour timestep. Panels (e, f) shows the average BC analysis increments from simulation AN_METCOM, for each 12-hour analysis step.

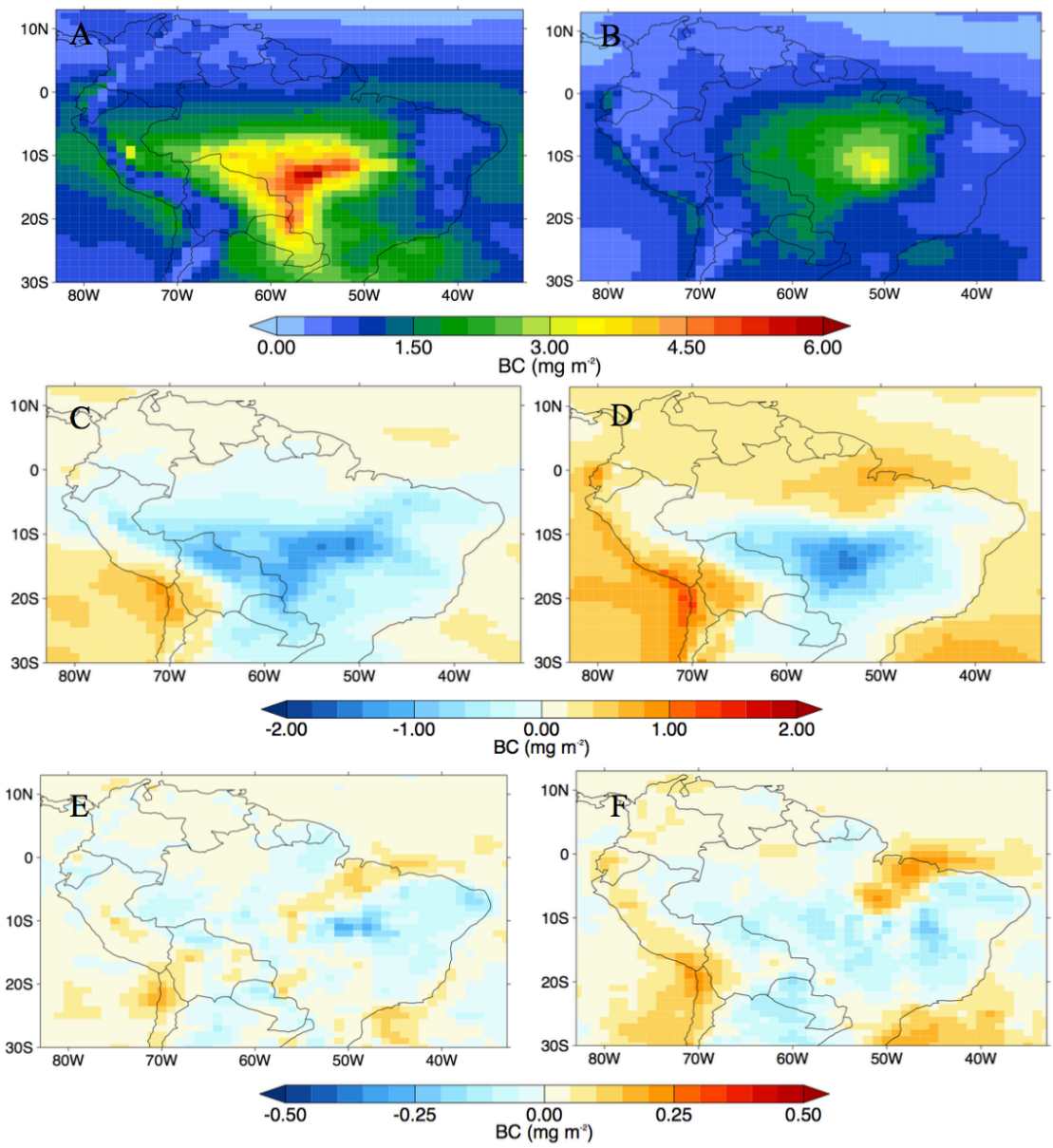

Figure 5.8 Impact of MODIS AOD assimilation on organic aerosol mass concentration in C-IFS for the 2012 tropical biomass burning season (Sept-Oct). The left panels show average results from the dry season (September 1-22) and the right panels show equivalent results from the dry-to-wet transition (September 23 – October 31). Panels (a, b) show mean analysis tropospheric OM columns (mg cm^{-2}) from the C-IFS simulation AN_METCOM. Panels (c, d) are AN_METCOM – AN_MET, or the average impact of assimilation at each 6-hour timestep. Panels (e, f) show the average OM analysis increments from simulation AN_METCOM, for each 12-hour analysis step.

Impact of fires on carbonaceous aerosol

The impact of AOD assimilation with altitude is shown in Figure 5.9 and Figure 5.10 for BC and OC, respectively, over the SAMBBA domain. The majority of negative analysis increments seen in the total column are distributed near the surface. Positive increments are seen at the surface of the longitude band that encompasses the increases seen over North-East Brazil in the total column increments. This longitude band also includes large negative increments and as such the zonal-mean averaging of the positive and negative values means that the increments are smaller than those seen in the total column. The negative increments at the surface impact the lowest 4 km in AN_METCOM, leading to smaller concentrations than seen in AN_MET, with larger differences seen during the first fire-intensive phase of the campaign. Above 4 km the difference between AN_METCOM and AN_MET is either near-zero or small and positive. These changes are most likely from positive increments away from the domain of the zonal means, and once again suggest that the ageing and deposition in the model is too rapid compared to reality. However, model concentrations at this altitude are generally very small.

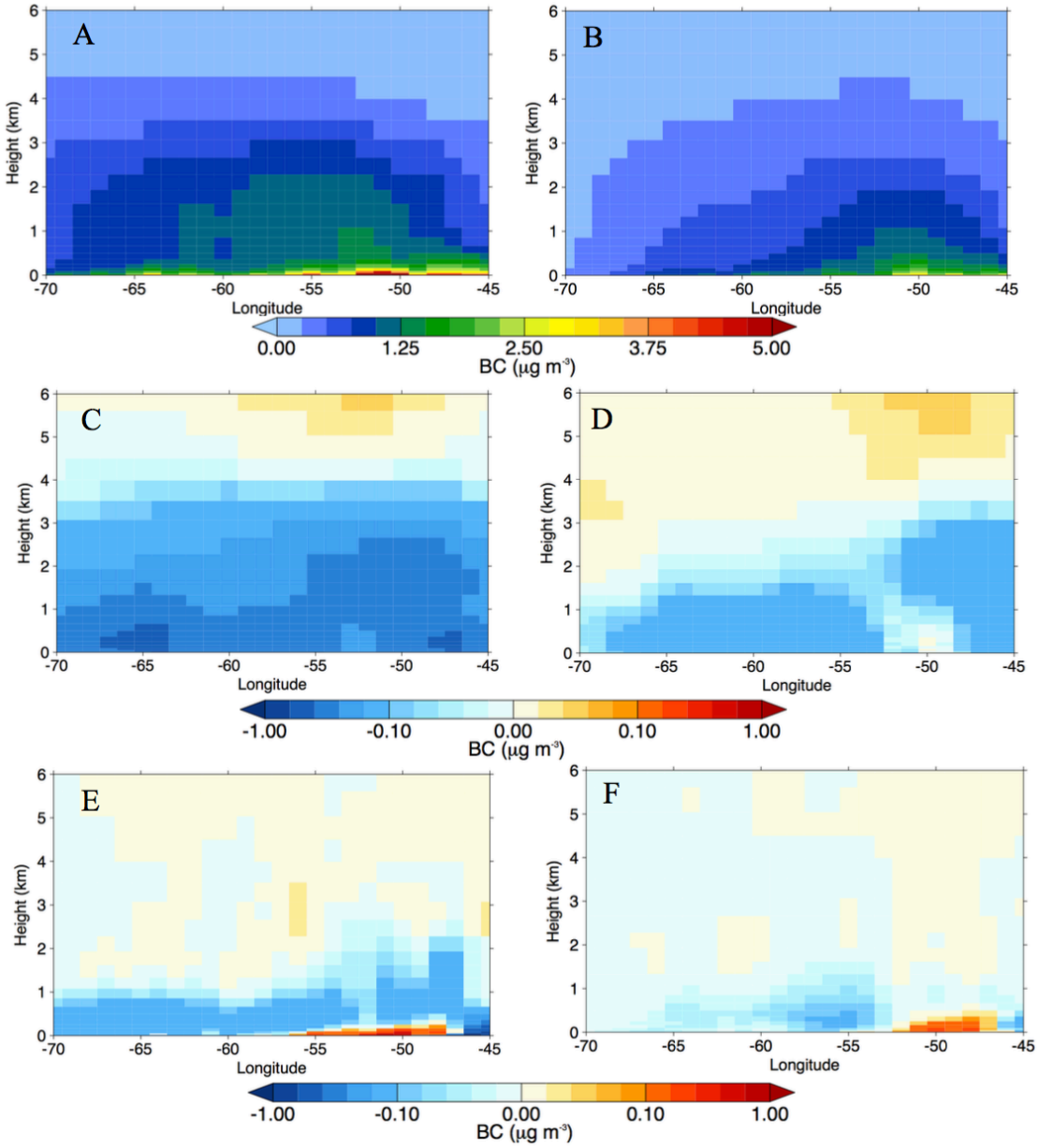

Figure 5.9 Impact of MODIS AOD assimilation on black carbon mass concentration latitude/height zonal mean cross section, over the latitudes sampled by the SAMBBA flights (5.5ºS to 12ºs), in C-IFS. The left panels show average results from the dry season (September 1-22) and the right panels show equivalent results from the dry-to-wet transition (September 23 – October 31). Panels (a, b) show mean analysis BC (µg cm^{-3}) from the C-IFS simulation AN_METCOM. Panels (c, d) are AN_METCOM – AN_MET, or the average impact of assimilation at each 6-hour timestep. Panels (e, f) show the average BC analysis increments from simulation AN_METCOM, for each 12-hour analysis step.

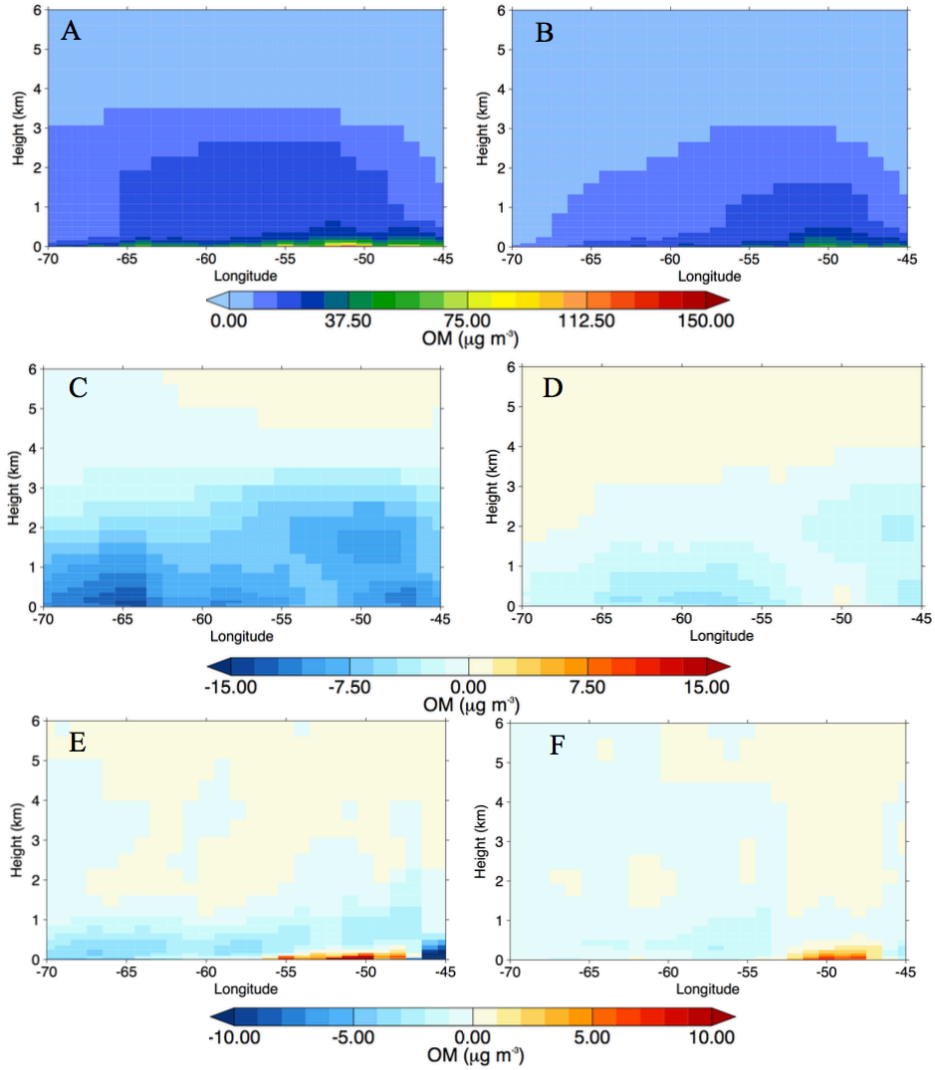

Figure 5.10 Impact of MODIS AOD assimilation on organic aerosol mass concentration latitude/height zonal mean cross section, over the latitudes sampled by the SAMBBA flights (5.5ºS to 12ºS), in C-IFS. The left panels show average results from the dry season (September 1-22) and the right panels show equivalent results from the dry-to-wet transition (September 23 – October 31). Panels (a, b) show mean analysis OM (μg cm^{-3}) from the C-IFS simulation AN_METCOM. Panels (c, d) are AN_METCOM – AN_MET, or the average impact of assimilation at each 6-hour timestep. Panels (e, f) show the average OM analysis increments from simulation AN_METCOM, for each 12-hour analysis step.

5.5 SAMBBA observations

Technical problems concerning both the SP2 and cToF-AMS instruments during the campaign means that aerosol observations are not available for every flight. The details of these technical problems are discussed along with in-depth descriptions for each flight in Darbyshire & Johnson, 2012. Aerosol mass concentrations of carbonaceous aerosol particles were highly variable during the flight campaign, with very low background concentrations and average concentrations at the maximum altitude of injection being ~1 μg m^{-3} and ~10 μg m^{-1} for BC and OM, respectively.

5.5.1 Campaign phases

Figure 5.11 shows the difference in carbonaceous aerosol vertical profiles between the different phases of the SAMBBA flight campaign. During the campaign aerosol concentrations were generally highest in the first 2-3 km, with significant concentrations up to the atmospheric boundary layer, before declining sharply. This is similar to the SAMBBA aerosol extinction lidar measurements discussed in Marenco et al., 2016. Simulation FOR_NSCF generally underestimates observations in the boundary layer, while AN_MET with GFAS emissions scaled by 3.4 overestimates, although both model runs predict higher concentrations in the free troposphere than those observed.

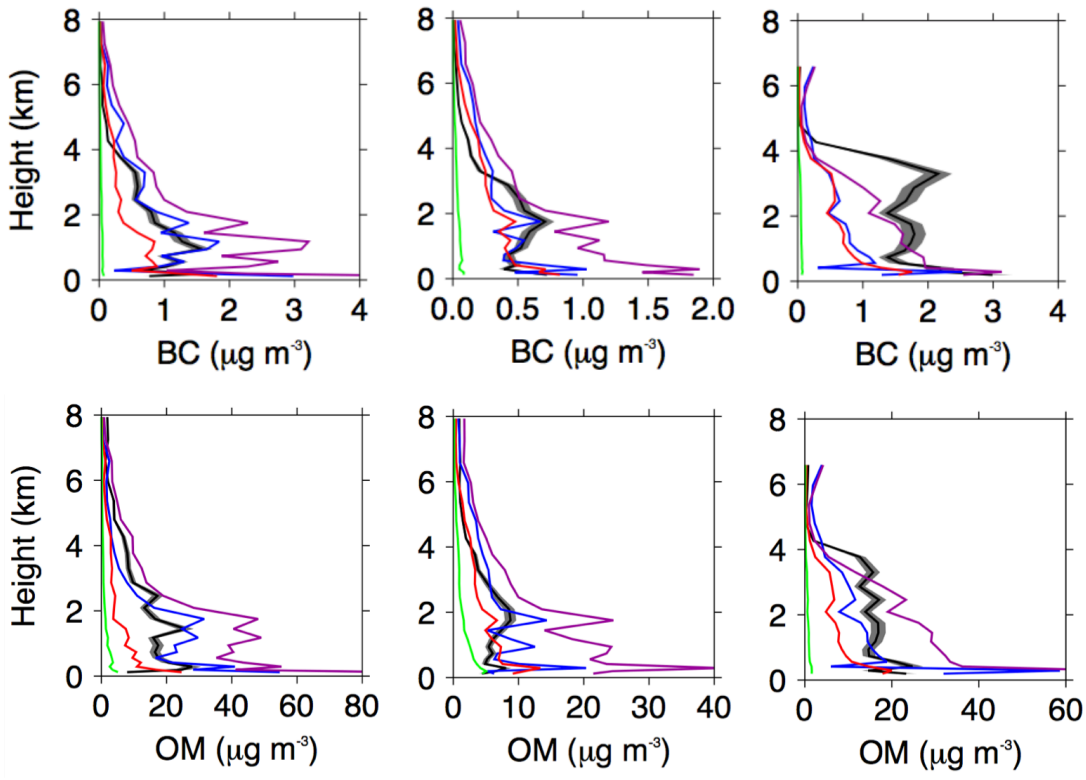

Figure 5.11 Comparison of mean BC and OM profiles (μg m^{-3}) between SAMBBA observations (black) and C-IFS simulations AN_METCOM (blue), FOR_NSCF (red) and AN_MET (purple). The three columns of panels from left to right represent: the western region phase 1, the western region phase 2 and the eastern region.

For flights in the western region AN_METCOM generally captures SAMBBA campaign phase averages in the boundary layer with a small overestimation near the surface. Simulation FOR_NSCF has a small underestimation compared to the observations and AN_METCOM during the first phase of the flight, but generally captures the second phase of the flight, suggesting the model captures background aerosol concentrations. Simulation AN_MET generally overestimates concentrations in the west throughout the profile, suggesting the 3.4 emission factor is too large. During the wet-to-dry phase of the flight the bias in AN_MET is more significant than during the dry phase. This 'persistence' could suggest an under-representative sink source in the model not removing BC and OM as quickly as in reality, although this would contradict the positive analysis increments seen outside of the campaign region in Section 5.4 and could just be

due to the excessive emissions caused by the 3.4 scaling factor. The decrease in observed OM from the dry season to the wet-to-dry transition suggest that loss processes are compensating for any potential increase in mass from Secondary Organic Aerosol (SOA) formation. Further evidence for this comes from the improved representation by FOR_NSCF and the increased overestimation by AN_MET during the wet-to-dry transition even though the model does not treat SOA formation.

Flights in the eastern region, showed maximum aerosol concentrations at higher altitudes, up to 4 km, where the injection heights from savannah/cerrado flaming fires are higher than those in the deforestation region. Observations also showed higher concentrations of BC (2.3 $\mu g\ m^{-3}$) at the maximum point of injection compared to the west (1.5 $\mu g\ m^{-3}$), although OM concentrations were similar. Due to surface-level emission injections, large negative biases in AN_MET and AN_METCOM BC concentrations are seen above 2 km, accompanied by an overestimation at the surface, although higher surface concentrations are seen in relation to the west. Despite the overestimation in AN_MET due to the scaling factor, the effect of emitting all emissions at the surface results in the altitude of maximum aerosol concentrations being lower than that observed by the aircraft over the eastern region. However, the lower injection height in the western region means this maximum-height is captured by model PBL mixing in both AN_MET and AN_METCOM. In simulation FOR_NSCF BC is generally underestimated to a greater extent in the Eastern region, with biases even at the surface suggesting these are not solely due to model injection height. OM shows a less significant negative bias above 2 km for AN_MET and AN_METCOM and a smaller but still significant bias throughout the profile for FOR_NSCF. Generally, OM concentrations are more accurately captured by the model than BC which corresponds with the smaller bias for OM compared to BC between AN_METCOM/FOR_NSCF in Table 5.2.

Figure 5.12 shows the correlation between the modelled and observed carbonaceous aerosol concentrations for the different flight phases. Flights during the first western phase (WR1) showed the lowest mean fractional bias (MFB) (-2%) for FOR_NSCF BC while the bias with observations in the eastern region (ER) were the largest (-41%). The opposite was the case for AN_MET which showed the largest MFB (89%) during WR1 and the lowest (23%) in the ER. For OM, FOR_NSCF showed the largest bias during

WR1 (-76%) with a more accurate representation during WR2 (-23%). The OM negative bias was also larger over the eastern region (-52%). The correlations show that the largest positive biases are associated with low observed concentrations, corresponding to high model concentrations most likely from the sampling of the small fires in flight B739 (discussed in Section 5.5.2 below).

Assimilating AOD in AN_METCOM significantly reduces concentrations compared to AN_MET. This decreases a result in an improved MFB compared to the observations for each flight phase and for both species, this suggests that AOD observations from MODIS are in-line with SAMBBA observations. The lack of a negative bias in MODIS AOD, due to the misinterpretation of plumes as clouds, is most likely due to AOD values not surpassing 3. although OM is reduced more significantly than BC and is better represented in AN_METCOM than FC_NSCF. However, there is an increase in the normalised mean bias (NMB) for eastern region BC which shows how the positive biases, relating to elevated aerosol concentrations, is made worse by the assimilation, as all emissions are injected at the surface.

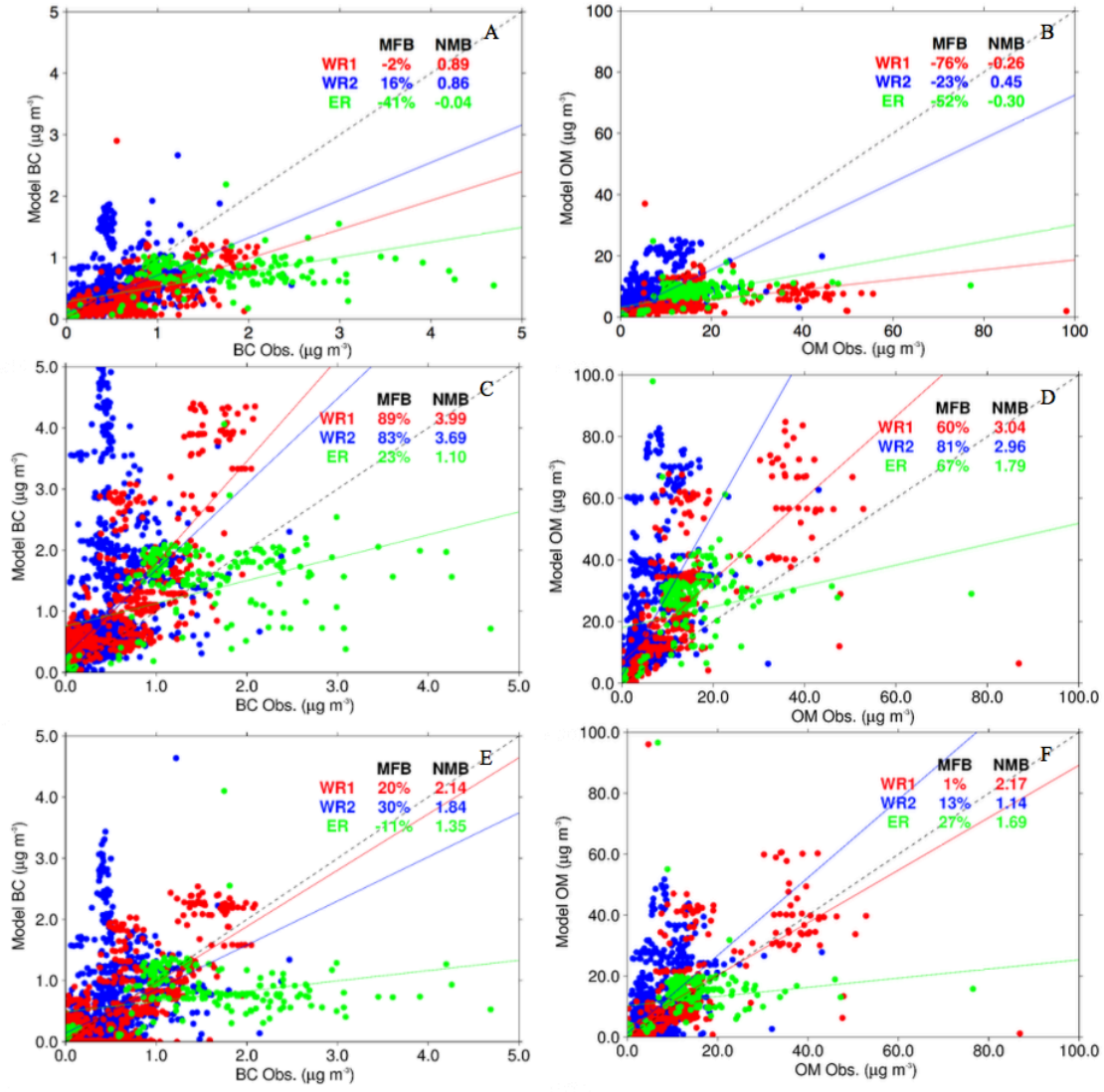

Figure 5.12 Correlation between SAMBBA BC (a, c, e) and OM (b, d, f) observations and C-IFS simulations in µg m^{-3}. (a, b) for FOR_NSCF, (c, d) for AN_MET and (e, f) for AN_METCOM. WR1 and WR2 refer to the first and second phases of the flights over the western regions and ER represents the Eastern cerrado region. Numbers in the panels give MFB mean fractional bias (MFB, %) between the observations and the model and the normalised mean bias (NMB).

5.5.2 Individual flights

Data from the SAMBBA flight campaign can be split further than just the different campaign phases, as multiple different flights sampled pristine regions, heavily polluted

regions and different fire types and sizes. In this section data from each individual flight will be assessed independently and compared against model simulations. Based on the CO evaluation in Chapter 4, the flights can be broadly classified into (outside the east/west split): large fires, small and medium fires and pristine regions. Correlation values for each individual flight are shown in Figure 5.13 and Figure 5.14 for OM and BC, respectively. In addition, Figure 5.15 and Figure 5.16 show average BC and OM vertical profiles from the SAMBA observations and simulations AN_METCOM, FOR_NSCF and AN_MET for each flight.

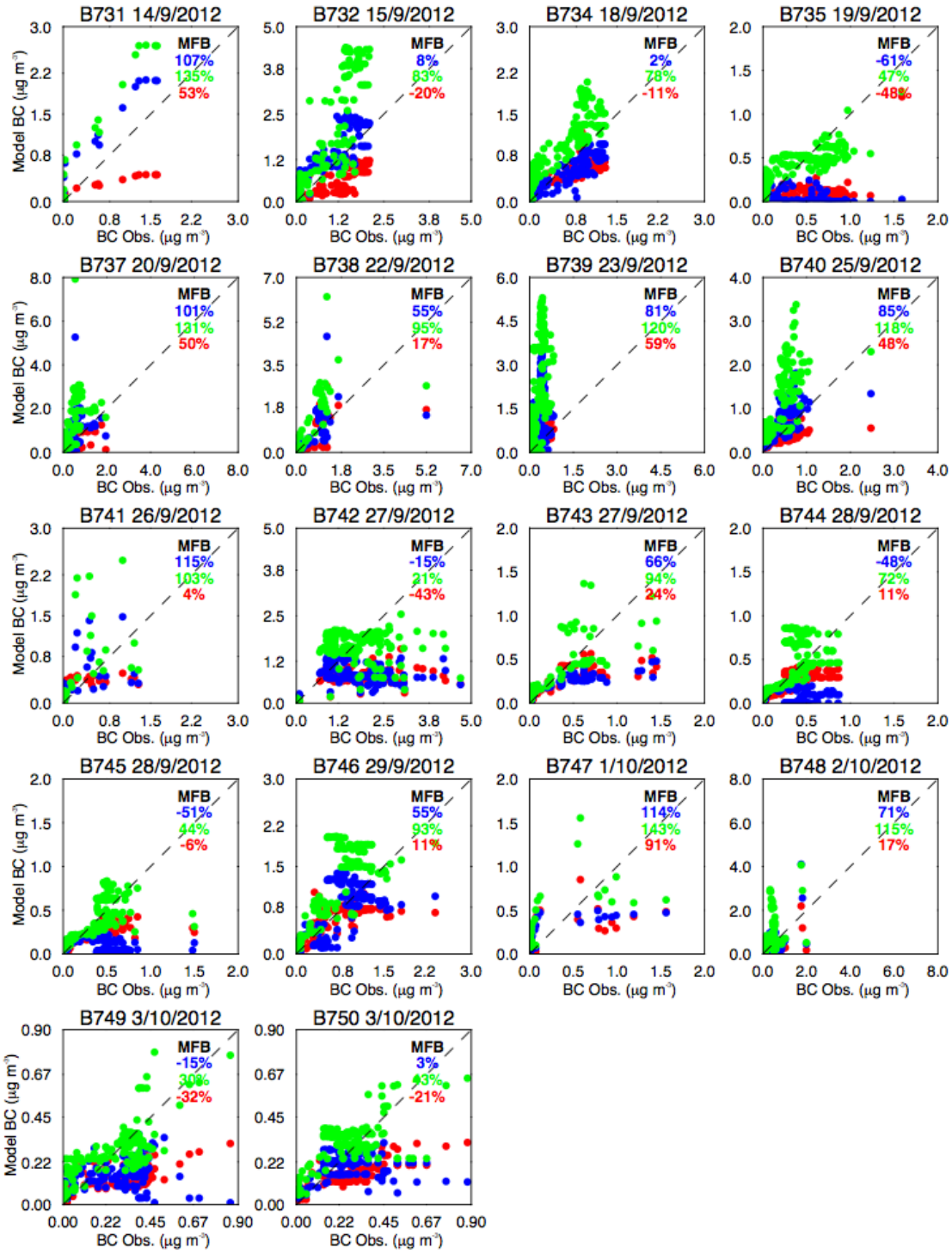

Figure 5.13 Correlations of BC concentrations between aircraft observations and C-IFS simulations AN_MET (green), AN_METCOM (blue) and FOR_NSCF (red) for 15 of the 20 flights during the SAMBBA aircraft campaign. Note the difference in y-axis and x-axis ranges for each panel.

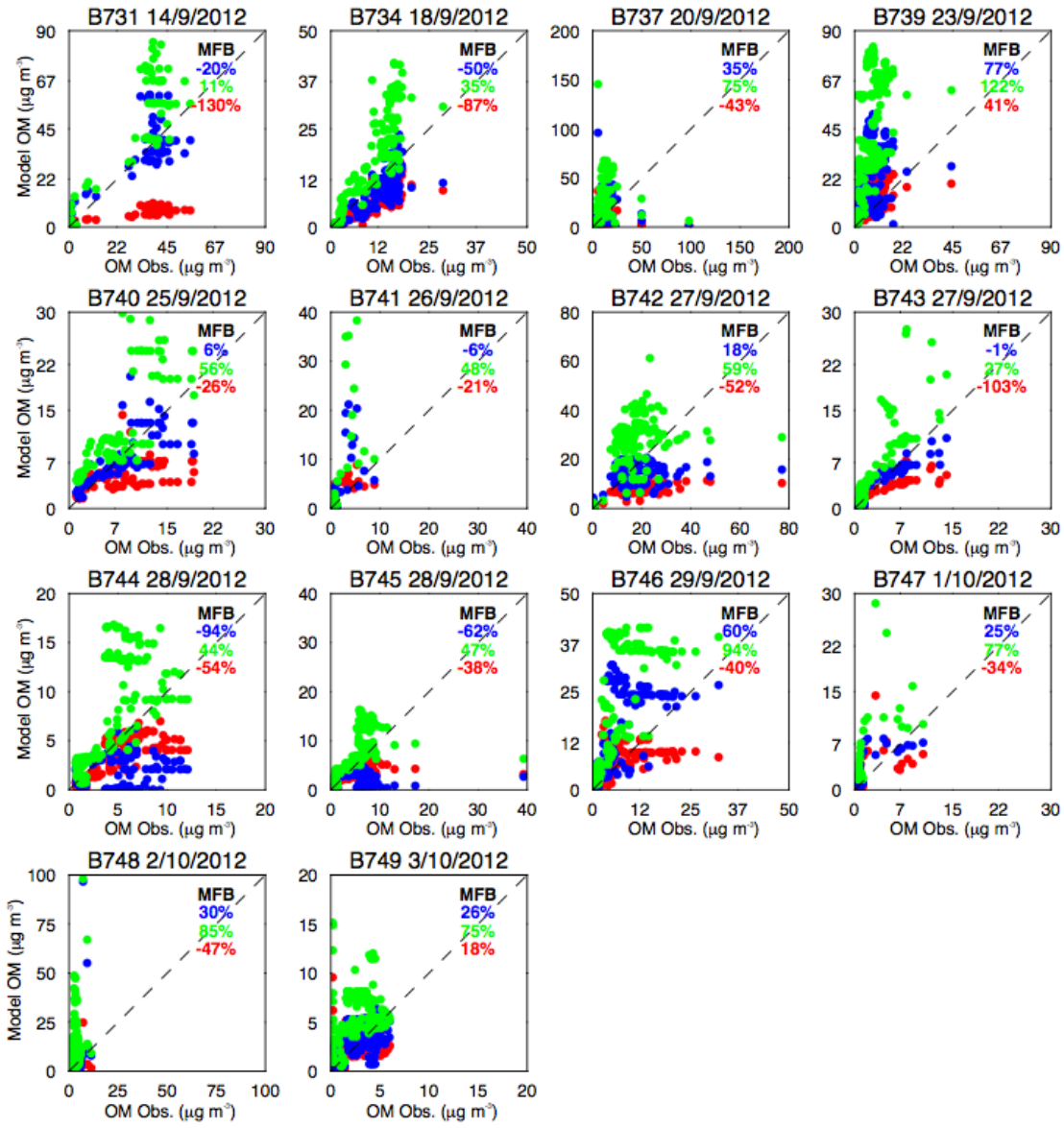

Figure 5.14 Correlations of OM concentrations between aircraft observations and C-IFS simulations AN_MET (green), AN_METCOM (blue) and FOR_NSCF (red) for 15 of the 20 flights during the SAMBBA aircraft campaign. Note the difference in y-axis and x-axis ranges for each panel.

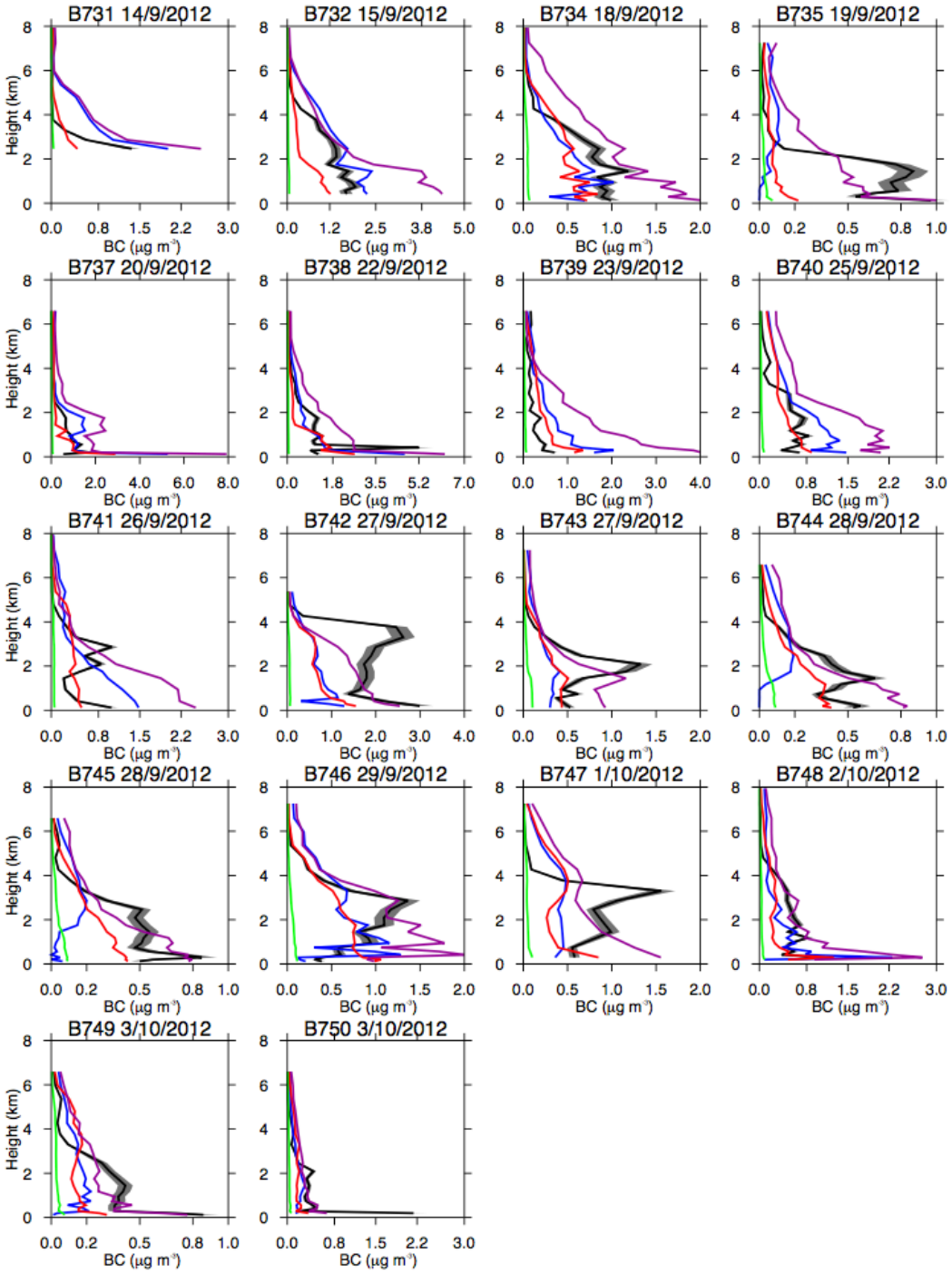

Figure 5.15 Average BC concentration profiles (µg m^{-3}) (black) from the SAMBBA aircraft campaign compared to simulations AN_MET (purple), AN_METCOM (blue), FOR_NSCF (red) and FOR_NBB (green) for 17 of the 20 SAMBBA flights.

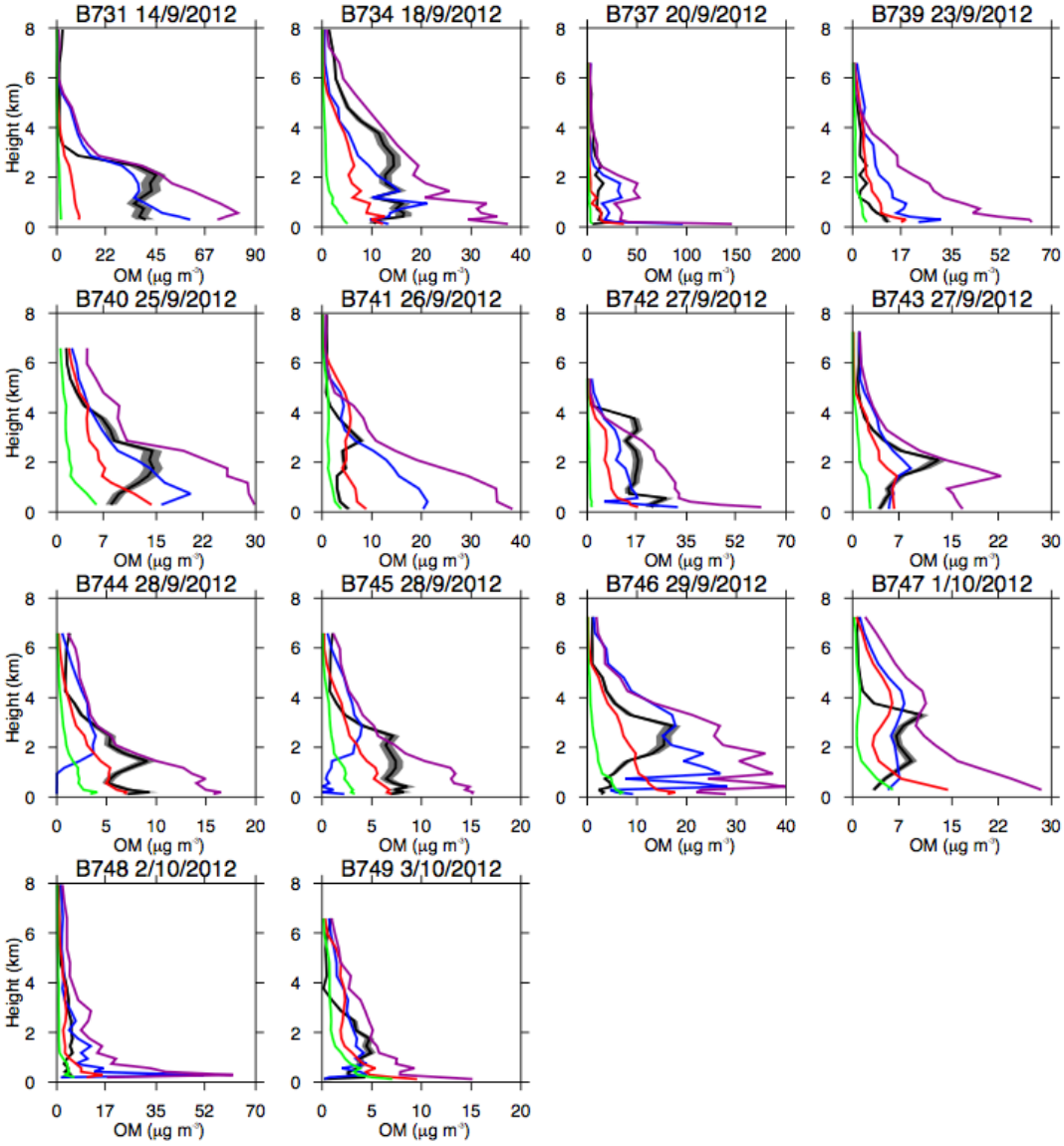

Figure 5.16 Average OM profiles (µg m^{-3}) (black) from the SAMBBA aircraft campaign compared to simulations AN_MET (purple), AN_METCOM (blue), FOR_NSCF (red) and FOR_NBB (green) for 15 of the 20 SAMBBA flights.

Near-fire plumes from flights B738 (16:45-17:15 GMT) and B746 (14:00-16:00 GMT) correspond to large smouldering fires (~300 ppb of CO Section 4.3) while the fire plume in B732 (14:00-15:30 GMT) corresponds to a large fresh fire. C-IFS with un-scaled GFAS emissions produces similar results to other primary emissions for the large smouldering fires, with overestimation near the surface and underestimation throughout

the rest of the boundary layer while the total MFB remains low and smaller than the other simulations. Although, unlike for other primary emissions, simulation FOR_NSCF significantly underestimates BC concentrations from the fresh plume. Simulation AN_MET, with scaled emissions, overestimates BC concentrations in all three plumes with concentrations from the fresh plume (B732) fire almost twice as large as that observed. The assimilation of AOD decreases concentrations in AN_METCOM and produces more realistic concentrations, reducing the MFB for BC from 94% to 55%. Biases in the vertical structure of AN_METCOM are similar to FC_NSCF although it does not underestimate observed BC concentrations in the fresh plume. OM observations were only available for flight B746 where FOR_NSCF underestimates OM while the overestimations for AN_MET and AN_METCOM are more significant. Simulation AN_METCOM overestimates OM values throughout the profile, unlike for BC where there was an underestimation at the altitude of maximum injection.

Flight B743 (19:30-20:00 GMT) sampled air above and around a large fire where concentrations are generally lower than when the flight directly sampled the plume. As with B732, FOR_NSCF and AN_METCOM capture near-surface concentrations while underestimating concentrations in the rest of the boundary layer. The increased emissions in AN_MET improve the vertical structure compared to the observations due to the rapid mixing within the PBL, although BC concentrations are still underestimated in the elevated aerosol layer (~2 km).

Near-fire plumes close to small and medium scale fires, identified as (<100m) and (<500m) respectively, were sampled in flights B731, B739 (12:45-16:00 GMT) and B740 (13:00-15:00 GMT). For flight B739, FOR_NSCF, AN_MET and AN_METCOM overestimate aerosol mass concentrations of BC and OM, with AN_MET overestimating BC observations in B739 by a factor of 7.5 and OM by a factor of 6, which is a larger bias than seen in other plumes. Overestimations are also seen for BC in B731 and B740, although less significantly. This larger overestimation is the opposite to that seen in the gas-phase comparison (Chapter 4) where both CO and NO_x where underestimated during these flights throughout the boundary layer. While the observations during these flights generally show elevated CO concentrations (>300 ppb) the aerosol concentrations are generally quite low, particularly in B739 where BC concentrations are under 0.5 $\mu g\ m^{-3}$.

On the occasions where high concentrations are seen in these flights, e.g. B740 (~13:45 GMT) and B731 (16:15-17:45 GMT), concentrations compare more closely to AN_MET while FOR_NSCF significantly underestimates concentrations, a result more similar to that seen for other tracers. The low observed aerosol concentrations from these smaller fires suggest BC emissions are smaller in reality than that assumed in the model.

Flights sampling the pristine northern regime (flights B735, B749, B750) showed lower aerosol concentrations than other flights, with BC values not exceeding 1 μg m^{-3} and OM not exceeding 10 μg m^{-3}. Compared to other flight conditions, simulation AN_MET does a relatively good job of capturing these pristine BC concentrations, although BC is still overestimated in the free-troposphere. OM concentrations are only available for flight B735 but show an overestimation by AN_MET throughout the profile and an overestimation by FOR_NSCF at the surface. The assimilation of AOD simulation AN_METCOM leads to an underestimation of BC but provides more realistic concentrations of OM. Flight B744 and B745 sampled areas of previous deforestation fires with elevated aerosol concentrations observed by the aircraft. Simulation FC_NSCF captures concentrations close to the surface while AN_METCOM underestimates OM and BC concentrations throughout the free troposphere. This suggests that MODIS AOD is not capturing these elevated concentrations after the fire.

5.5.3 OM/BC ratio

The single scattering albedo of biomass burning aerosols is related to the fraction of OM (positive SSA) and BC (negative SSA) in the particles. Therefore, an accurate modelling of the regional radiative effects of BBA is dependent on capturing the ratio of OM/BC. Figure 5.17 compares OM/BC from FOR_NSCF and AN_METCOM to that observed during the SAMBBA flight campaign. As the assimilation of AOD does not change the immediate contribution of different aerosol species to the total aerosol mass, the results from AN_MET are not shown here. Larger ratios (greater contribution of OM) are observed at the start of the flight campaign over the western region (flights B731-B740), with an average ratio of 28 compared to 11 during the second phase of the campaign.

Smaller ratios are also observed over the eastern cerrado region with flight B742 having an average ratio of 10.

Model results show a lot less variability compared to the observations, particularly near fresh plumes where modelled ratio remains constant while observations vary significantly. The variations in the observations are most likely due to different fuel types and burning efficiencies while emission factors used to produce the GFAS emission fluxes can only estimate the fuel type and do not provide different emission factors for different combustion types. During the dry season the western region generally shows a negative bias, indicating an underestimation of OM compared to BC. However, this changes to a positive bias by the end of the campaign. With the underestimation of BC at the end of the campaign compared to the positive bias at the start, the changing OM/BC ratio suggests that BC is being lost at a quicker rate than OM in the model and seems to be the main source of the ratio bias. The eastern cerrado regions shows a positive bias despite being a fire-intensive region implying that relative to OM, BC emissions in the cerrado are underestimated. Generally, FOR_NSCF and AN_METCOM ratios are similar in value, although the positive bias during the wet-to-dry transition is larger in FOR_NSCF. Overall, the ratios suggest that C-IFS aerosol would be more absorbing than reality during the dry season and less absorbing during the wet-to-dry transition and over the cerrado.

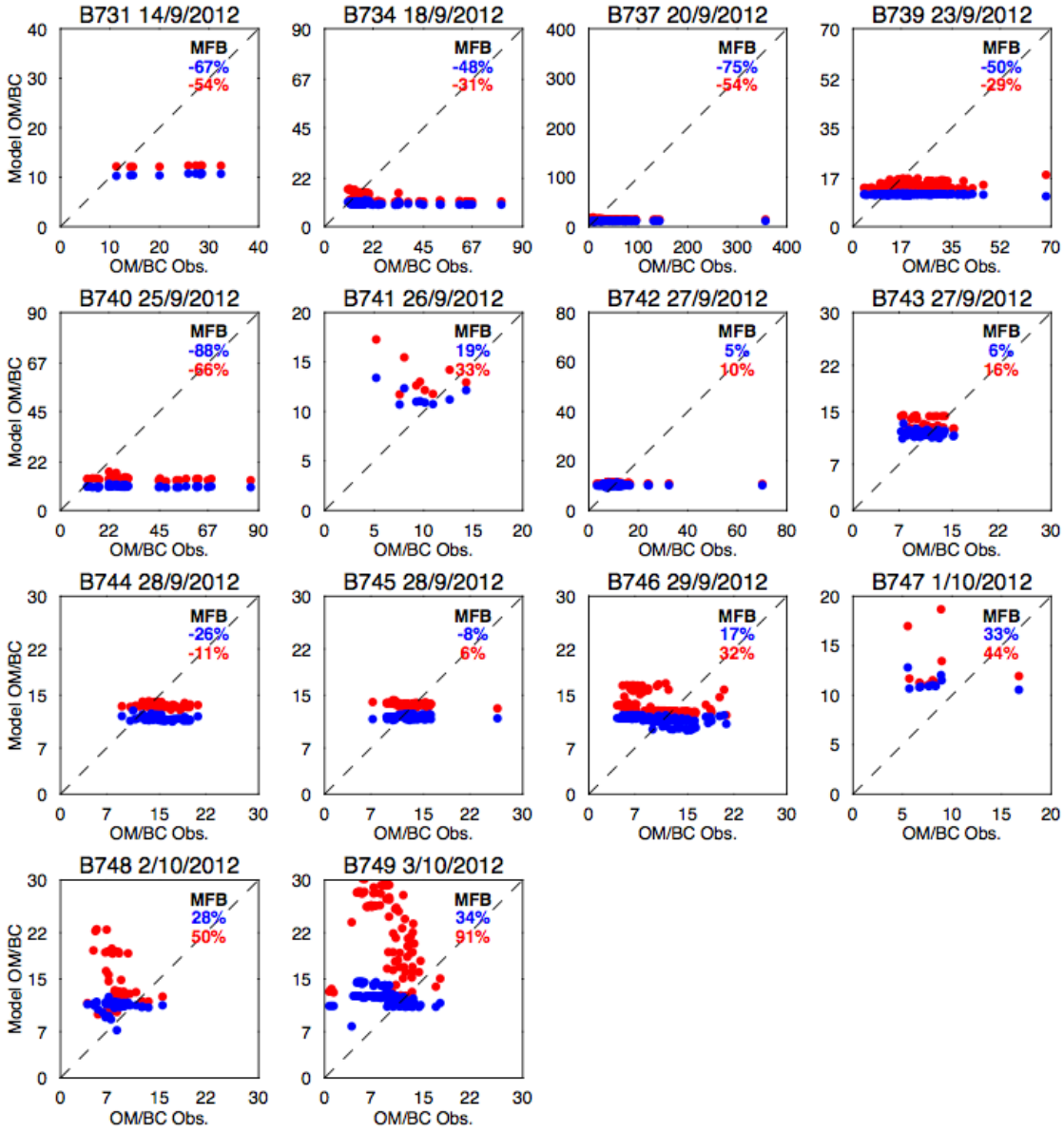

Figure 5.17 Correlations of OM/BC between aircraft observations and C-IFS simulations AN_METCOM (blue) and FOR_NSCF (red) for 15 of the 20 flights during the SAMBBA aircraft campaign. Note the difference in y-axis and x-axis ranges for each panel.

5.6 Impact of injection height

This section discusses the impact of the Plume Rise Model (PRM) on C-IFS concentrations through evaluation with SAMBBA observations. The model runs are

those used in Rémy et al., (2016), where they are compared to aerosol extinction measurements during the SAMBBA campaign, and are run on a separate IFS code branch with different model-setup to that discussed previously. Results from (Rémy et al., 2016) showed that the PRM compared well to the MPHP2 dataset for Africa and South America and generally produced more realistic concentrations for larger fires. The aim of this work is to identify how the injection height parameter captures OM + BC mass concentrations, which have already been shown to have different biases to AOD measurements, and compare to the full range of flights undertaken during the SAMBBA campaign. The impact of the PRM on the modelled vertical structure during the SAMBBA campaign can be seen in Figure 5.18 for BC and Figure 5.19 for OM.

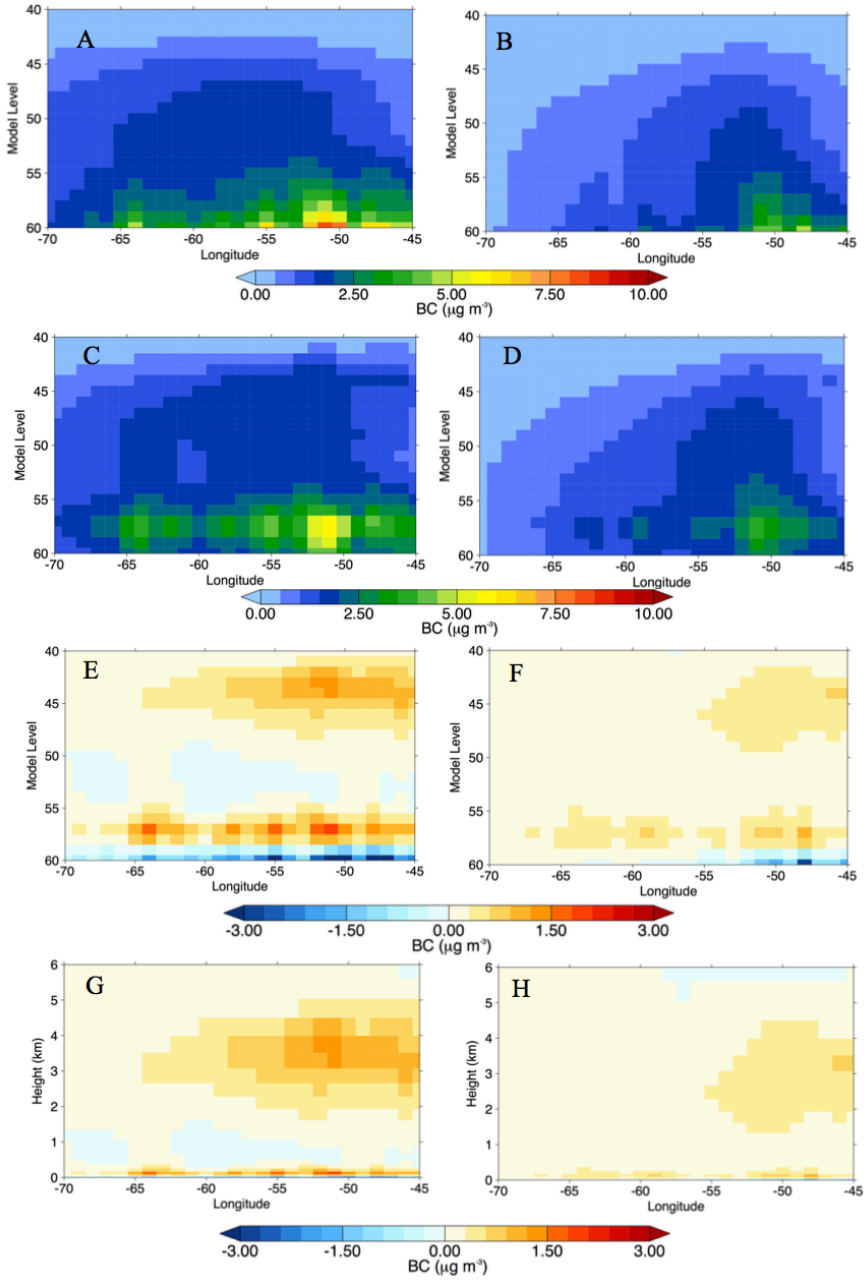

Figure 5.18 Impact of the plume rise model (PRM) on black carbon mass concentration longitude/height mean cross section, averaged over the latitudes sampled by the SAMBBA flights (5.5ºS to 12ºS), in C-IFS. The left panels show average results from the dry season (September 1-22) and the right panels show equivalent results from the dry-to-wet transition (September 23 – October 31). Panels (a, b) show mean analysis BC (µg cm^{-3}) from the C-IFS simulation AN_NINJ. Panels (c, d) show the C-IFS simulation AN_INJ, with the plume rise model. Panels (e, f) show the difference in between simulations AN_INJ and AN_NINJ.

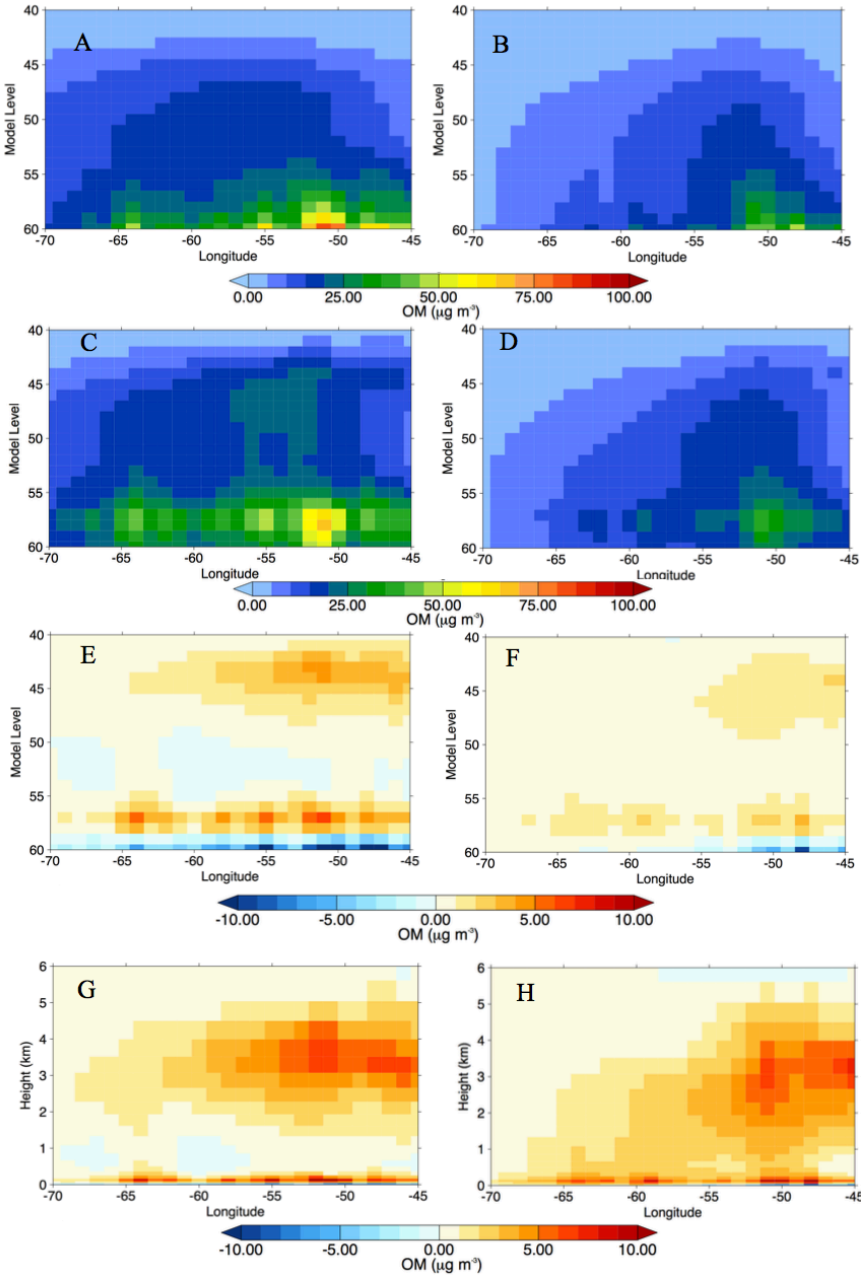

Figure 5.19 Impact of the plume rise model (PRM) on organic matter mass concentration longitude/height mean cross section, averaged over the latitudes sampled by the SAMBBA flights (5.5ºS to 12ºS), in C-IFS. The left panels show average results from the dry season (September 1-22) and the right panels show equivalent results from the dry-to-wet transition (September 23 – October 31). Panels (a, b) show mean analysis BC (µg cm^{-3}) from the C-IFS simulation AN_NINJ. Panels (c, d) show the C-IFS simulation AN_INJ, with the plume rise model. Panels (e, f) show the difference in between simulations AN_INJ and AN_NINJ.

Impact of fires on carbonaceous aerosol

Comparisons of the two different experiments AN_INJ, with injection height model by the PRM and AN_NINJ, without the injection height but run on the same branch, against average SAMBBA profiles for the three campaign phases are shown in Figure 5.20. Higher BC concentrations and a larger overestimation are seen for these experiments than seen for AN_METCOM in Section 5.5.1. In the eastern region, where a larger injection height was identified, there is a significant difference within the boundary layer between the two C-IFS experiments, with the vertical structure more accurately captured by AN_INJ than AN_NINJ. Despite this improvement in the vertical structure at the mean point of maximum injection, concentrations near the surface actually increase in AN_INJ compared to AN_NINJ. A comparison of the models during the campaign in Figure 5.18 and Figure 5.19 show that values are decreasing in AN_INJ compared to AN_NINJ but only at the lowest 2 model levels, which are altitudes (~100m) not sampled by the aircraft, during the eastern phase of the campaign.

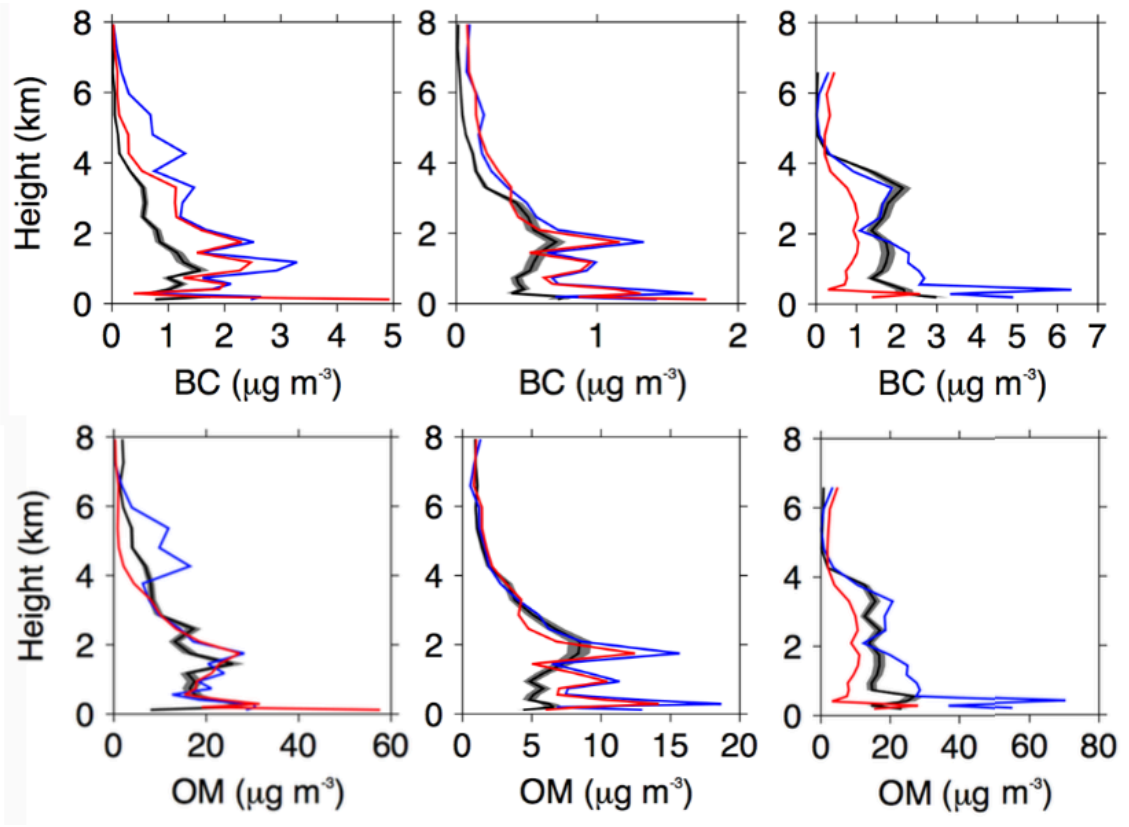

Figure 5.20 Comparison of mean BC and OM profiles (μg m^{-3}) between SAMBBA observations (black) and C-IFS simulations AN_NINJ (blue) and AN_INJ (red). The three columns from left to right represent: the western region phase 1, the western region phase 2 and the eastern region.

In the western region, there is a much smaller change from using PRM, as most of the aerosol species is emitted within the first 2 km, and the mixing within C-IFS compensates for any bias. There is an increase in the positive bias (particularly for BC) when PRM is used although, the significantly larger positive bias near the surface, seen in NINJ_AN is decreased by the PRM implementation. This is due to the aircraft sampling lower altitudes during the western-phase of the campaign. Increases in concentrations are also seen above the PBL for both OM and BC during the dry season when the PRM is used. This increases the positive bias seen in NINJ_AN and suggests that the PRM is injected emissions at too high an altitude, a result which has also been seen in previous evaluation studies (Archer-Nicholls et al., 2015).

Figure 5.21 shows the correlation between the modelled and observed carbonaceous aerosol concentrations for the different flight phases, showing the impact of the PRM. Similar results are seen to the AN_MET and AN_METCOM correlation values in Figure 5.12, with a more accurate OM field than BC due to MODIS AOD assimilation. As concentrations generally increase with the use of the PRM, the OM underestimation in the western region is improved using the PRM while the positive bias for BC is made worse. The values for AN_NINJ which show large underestimations in the eastern region are improved by the use of the PRM but increases are also seen in values that were not underestimated, leading to OM and BC being overestimated in the eastern region by AN_INJ.

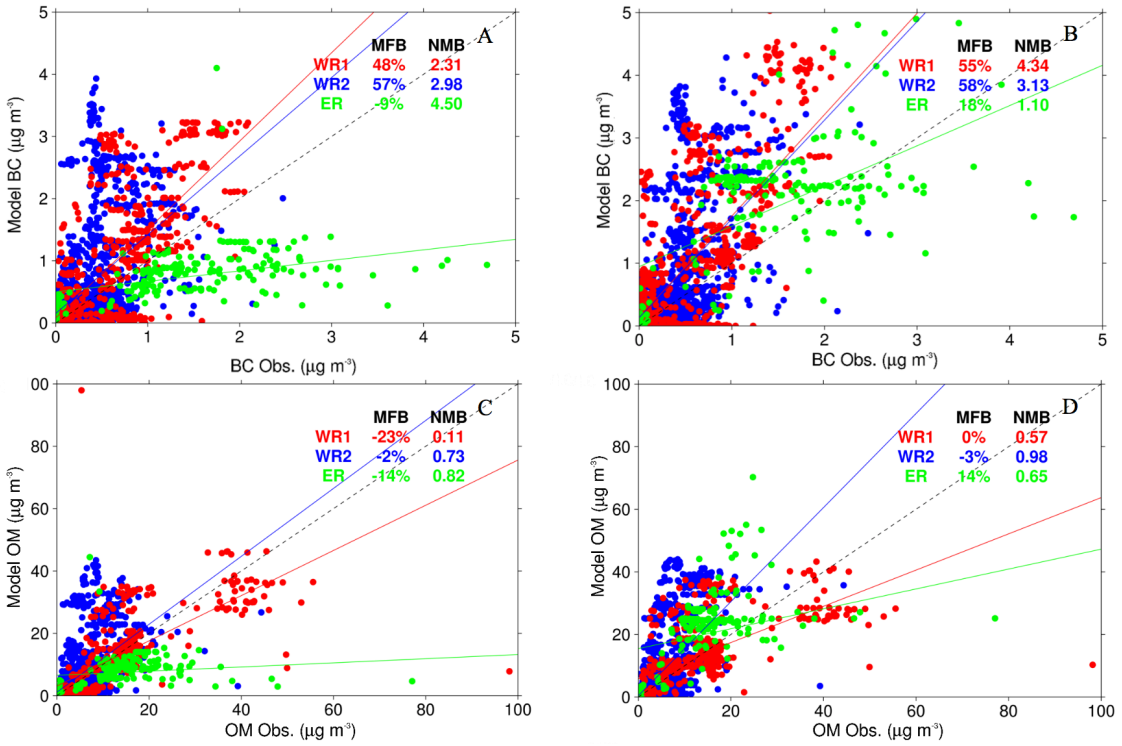

Figure 5.21 Correlation between SAMBBA BC (a, b) and OM (c, d) observations and C-IFS simulations in µg m^{-3}. (a, c) for AN_NINJ and (b, d) for AN_INJ. WR1 and WR2 refer to the first and second phases of the flights over the western regions and ER represents the Eastern cerrado region. The numbers in the panels give the mean fractional bias (MFB, %) between the observation and the model and the normalised mean bias (NMB).

Impact of fires on carbonaceous aerosol

The impact of the injection height from the PRM on C-IFS OM and BC tropospheric burdens is seen in Figure 5.22 and Figure 5.23, respectively. During the dry season, there is a significant increase in BC and OM concentrations with the PRM, with up to a ~30% increase in the eastern region where emissions are largest, while smaller but still significant increases are seen during the wet-to-dry transition. This implies that the lack of an injection height has a significant impact on the underestimation of total column metrics in the background model and that solely increasing the emissions will not necessarily improve representation.

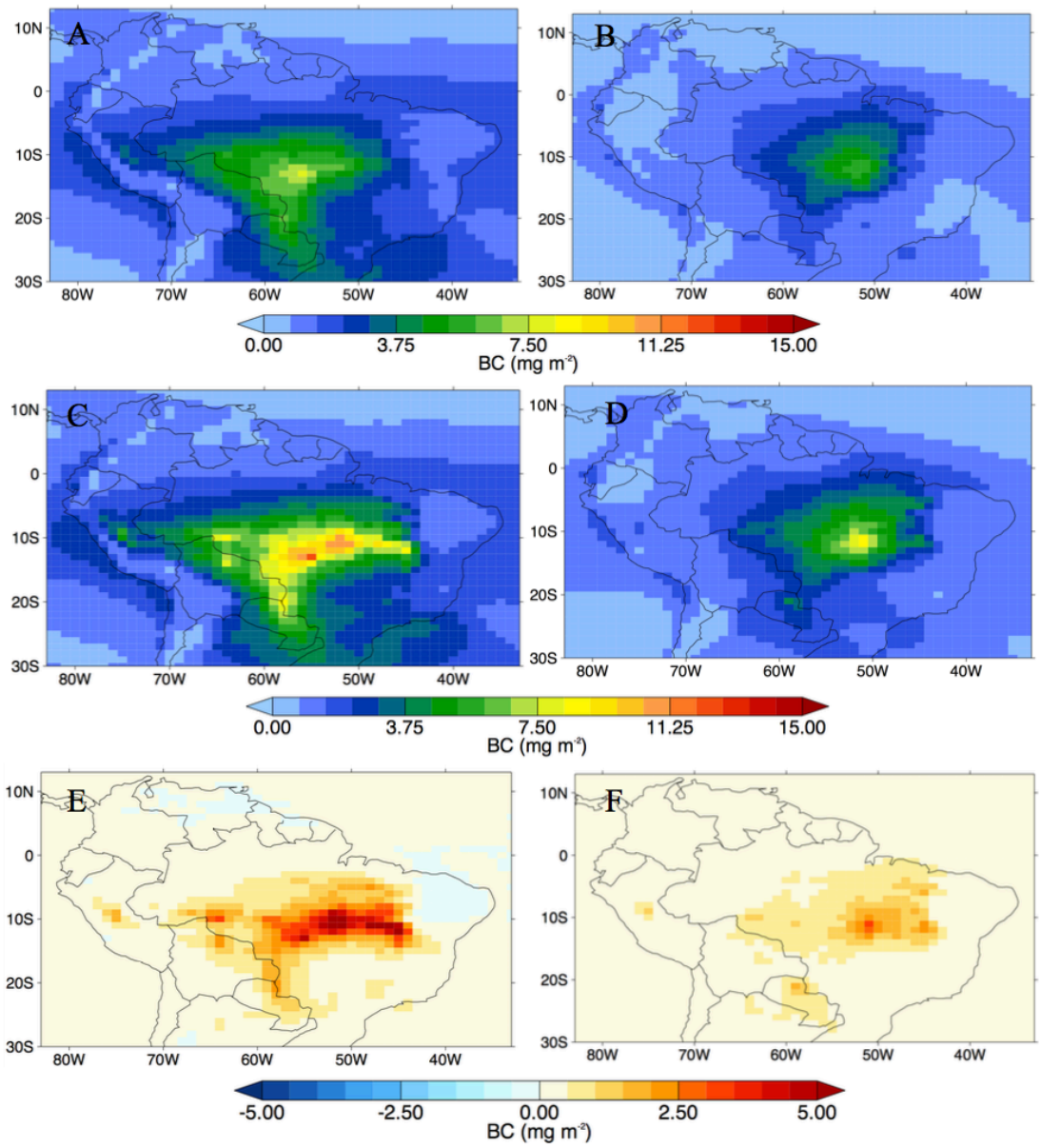

Figure 5.22 The impact of the plume rise model (PRM) on C-IFS simulated BC tropospheric column during the SAMBBA campaign. The left panels show average results from the dry season (September 1-22) and the right panels show equivalent results from the dry-to-wet transition (September 23 – October 31). (a, b) Total column BC (mg cm^{-2}) from C-IFS simulation AN_NINJ. (c, d) Total column from C-IFS simulation AN_INJ, with PRM. (e, f) Difference in BC column between simulations AN_INJ and AN_NINJ.

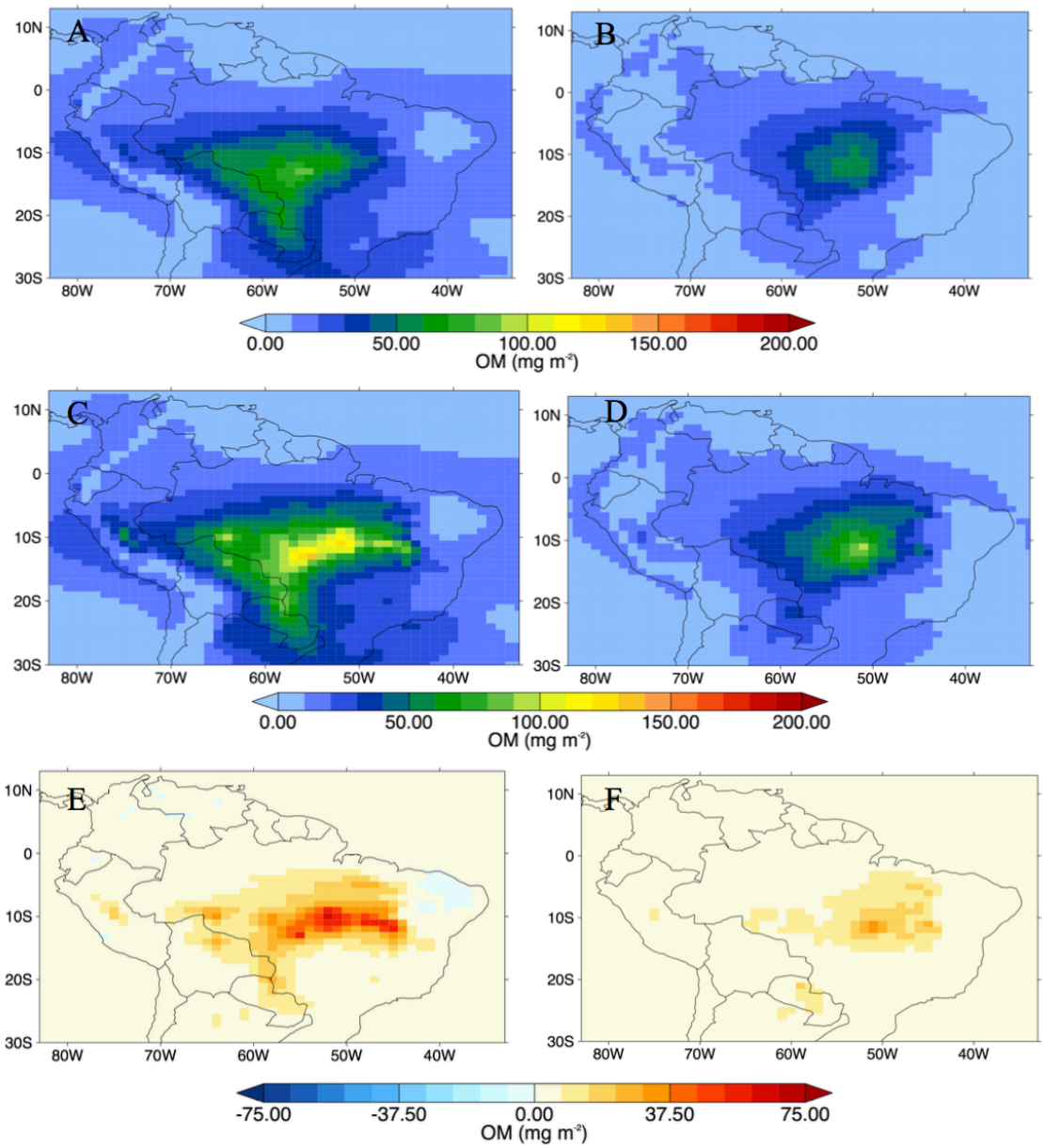

Figure 5.23 The impact of the plume rise model (PRM) on C-IFS simulated OM tropospheric column during the SAMBBA campaign. The left panels show average results from the dry season (September 1-22) and the right panels show equivalent results from the dry-to-wet transition (September 23 – October 31). (a, b) Total column OM (mg cm^{-2}) from C-IFS simulation AN_NINJ. (c, d) Total column from C-IFS simulation AN_INJ, with PRM. (e, f) Difference in BC column between simulations AN_INJ and AN_NINJ.

5.7 Summary

Aerosol concentrations from different C-IFS model runs have been evaluated against aircraft observations from the SAMBBA campaign, with the aim of assessing the impact of AOD assimilation, and the impact of injection height and emission scaling on biomass burning aerosols close to an emission source.

Comparing C-IFS model runs with and without assimilated MODIS AOD shows a biomass burning AOD (OMAOD + BCAOD) bias similar to that found in Kaiser et al., (2012). Globally, the factor 3.4 bias was used as the recommended scaling factor for GFAS fire emissions, assuming the bias was solely down to biomass burning emissions. Comparing BCAOD and OMAOD separately suggests that different scaling factors should be applied to each component of BBA, with BC underestimated to a greater extent than OM. Unlike for OM, the BCAOD bias is much larger than that found for the BC burden, implying that the assumed aerosol optical properties used to calculate AODs from mass concentrations are overestimating the impact of BC. Additionally, OM shows a more significant bias close to the emission sources while the bias in BC increases when considering the whole of South America. The bias for OM and BC is a lot smaller compared to SAMBBA observation than the bias between the model with and without AOD Assimilation, with the BC bias being 1.4 for SAMBBA compared to 3.31 for the AOD assimilation and the OM bias being 1.5 for SAMBBA and 2.36 for the AOD assimilation. These biases are similar to those seen for CO in chapter 4.

When evaluated by SAMBBA observations, the standard model run FOR_NSCF captures near-surface BC concentrations associated with deforestation fires during the dry-season but significantly underestimates OM. During the wet-to-dry season the representation of OM in FOR_NSCF generally improves but BC is now overestimated. Over the eastern region there is a large underestimation of both OM and BC by the model throughout the profile, suggesting emissions are too low in this region or the bias is due to the large injection heights. This bias is similar but smaller to the increased biases in the east for OM and BC mass concentrations compared to AN_METCOM. The more significant bias for OM for deforestation might be caused by the calculation of OM from OC, the factor of 1.5 used in C-IFS is on the lower end of the range of observed values of aerosol

mixtures impacted by biomass burning (Brito et al., 2014; Johnson et al., 2016) and a higher factor would reduce the bias. The improved model performance in WR2 suggest little impact of SOA formation, while the increase in BC bias suggests the BC lifetime is longer in the model than reality, however if the scaling for OM and OC was corrected OM concentrations are also likely to be too large during the dry season. Compared to the WRF-CHEM comparison from three flights in SAMBBA (Archer-Nicholls et al., 2015), the C-IFS experiment FOR_NSCF shows similar underestimation in the eastern region and overestimation during flight B739, but tends to underestimate observations from B731, when small fires were more prevalent, which is a similar bias to that seen for other primary tracers in Chapter 4 and for previous analysis of the GFAS emission inventory (Pereira et al., 2016; Reddington et al., 2016).

When emissions are scaled by 3.4 the model performs better in capturing aerosol concentrations in the eastern regions and OM in the WR1, but significantly overestimates concentrations in the western region. The lack of injection height in FOR_NSCF leads to a poor vertical structure although, increasing the emissions by 3.4 in AN_MET compensates for this somewhat, but also leads to an overestimation of concentrations near the surface. Overall, this suggests that emissions are underestimated in the model but not to the extent indicated in previous studies when modelled AOD has been compared to observations. As suggested in Reddington et al., (2016), which compared both surface PM2.5 and Aerojet AOD against GLOMAP during the SAMBBA campaign, using AOD observations to scale emissions fluxes can cause an additional bias.

The assimilation of MODIS AOD in AN_METCOM generally leads to an improved comparison with SAMBBA observations, despite the problems with AOD calculation in the model. Emissions are also scaled by 3.4 in AN_METCOM and over intensive fire regions analysis increments show the assimilation decreasing model values, i.e. working against the suggested increase in emissions. This decrease can be seen throughout the SAMBBA campaign where AN_METCOM values are always lower than AN_MET. As the control variable for AOD assimilation is the total aerosol mass, the partitioning of BC/OM is solely based on the model and as such the AOD assimilation does not improve the relative OM/BC ratio. This leads to a particularly improved representation of OM in the model by AOD assimilation due to the positive bias in the OM/BC ratio in the eastern

region and WR2. Either the large increase in bias by the emission factor or the erroneous assumed optical properties also leads to an overestimation of BC in the western region by AN_METCOM. This shows how important it is for a correct model representation in an assimilation product, the increased emissions added by the scaling factor are decreased by the assimilation but are not completely removed.

The implementation of a plume rise model (PRM) in GFAS emissions does improve model representation in the eastern region where injection heights were largest, suggesting this is the cause of the low bias in FOR_NSCF, but also adds an additional bias in the free troposphere over the western region. The injection heights also further highlight that emission fluxes are too large in the model with the scaling factor, even after assimilation, as the improved vertical structure in the eastern region also leads to an increased positive bias.

6 Global impact of composition data assimilation during the 2012 tropical fire season

6.1 Introduction

This chapter discusses the global impact of composition assimilation in C-IFS during the 2012 tropical fire season. A key focus is on how the assimilation improves the representation of elevated fire emissions and how they impact other species, which have been shown to be a significant sources of model bias. Another point of interest is how the assimilation of O_3, NO_2, CO and aerosol optical depth (AOD) impact atmospheric chemistry via changes in both the hydroxyl radical (OH) and the available radiation for photochemistry. Additionally, how AOD assimilation changes carbonaceous aerosol species in the model will also be assessed.

Previous composition assimilation studies using the IFS 4D-var data assimilation, while showing an improvement in model skill compared to independent observations of the species assimilated (Benedetti et al., 2009; Inness et al., 2013), have only performed limited evaluation of the impact on non-assimilated species, although large changes in OH have been reported in other assimilation studies (Miyazaki et al., 2015). Unlike these studies the impacts of assimilation will be seen over a 2 month period September-October 2012 rather than over a period of a few years. The skill of the assimilation will be assessed via comparison to previous model comparison studies as well as independent satellite observations of OMI tropospheric O_3 and HCHO as well as ground-based NOAA flask sites.

The chapter is structured as follows. Section 6.2 describes the impact of GFAS fire emissions on global modelled fields. Section 6.3 discusses the impact of assimilation and fires on gas-phase chemical species including O_3, CO and NO_2 which have assimilated datasets and HNO_3, propane and OH which are not. Section 6.4 details the impact of AOD assimilation on carbonaceous aerosol concentrations, while quantifying the global GFAS aerosol bias. Finally, Section 6.5 summarises the results from this chapter.

6.2 Assimilation setup

Information on the different experiments used in this chapter are shown in Table 5.1. Two different types of experiment are used, the analysis mode and the forecast mode. The analysis mode contains the 4D-var data assimilation system described in Chapter 3 while the forecast mode runs integrate forward in time from an analysis but without further use of observations. In these retrospective runs the forecast meteorology is relaxed to ERA-Interim, to reduce the computational cost. An additional assimilation was performed where the assimilation of AOD is allowed to impact the chemical species.

Name	Type	Emissions	Injection	Decription
AN_METCOM	analysis	GFAS × 3.4	Surface	Composition and meteorology data assimilated.
AN_MET	analysis	GFAS × 3.4	Surface	Only meteorological data assimilated.
AN_AER	analysis	GFAS × 3.4	Surface	Impact of AOD assimilation on radiation.
FOR	forecast	GFAS × 3.4	Surface	Relaxed forecast.
FOR_NSCF	forecast	GFAS	Surface	No GFAS scaling factor applied.
FOR_NBB	forecast	GFAS	Surface	No biomass burning emissions.

Table 6.1 Experiments run over the SAMBBA campaign period September - October 2012. Experiments designated 'analysis' are run in the analysis mode where observations constrain certain model parameters, the 'forecast' experiments are run using the forecast mode and the meteorology is relaxed to ERA-INTERIM.

The different satellite total columns or partial profiles assimilated in the experiments are shown in Table 3.2 and are discussed in more detail in Chapter 3. There was no MLS O_3 data with the correct quality flag for the first month of the simulation, and as a result the difference between September and October can be used as a proxy for a sensitivity of

Global impact of assimilation

MLS assimilation on atmospheric composition as all other total columns were assimilated throughout the simulations.

Instrument	Satellite	Species	Type
MODIS	EOS-AQUA/TERRA	AOD, FRP	Total optical depth (AOD)
MLS	EOS-AURA	O_3	Profiles
OMI	EOS-AURA	O_3	Total column
SBUV-2	NOAA	O_3	6 layer profiles
GOME-2	ERS-2	O_3	Profiles
IASI	METOP-A	CO	Total column
MOPITT	EOS-TERRA	CO	Total column
OMI	EOS-AURA	NO_2	Total column

Table 6.2 Composition satellite data assimilated in 'analysis' experiments.

For a global analysis, the impact of fire emissions and assimilation was defined for different global regions defined by climate and dominate vegetation which are summarised in Figure 6.1.

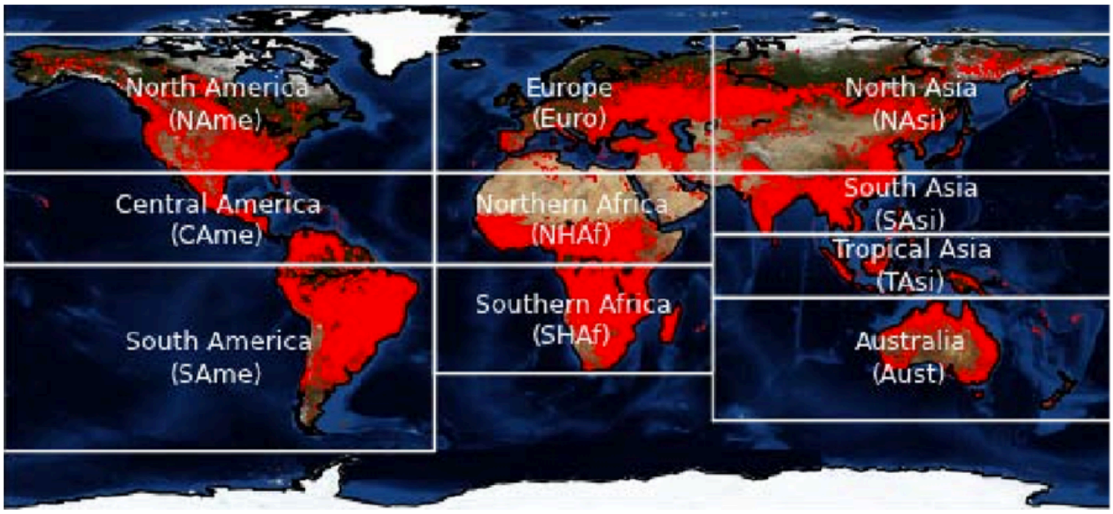

Figure 6.1 Regions of interest as defined in Kaiser et al., (2012).

6.3 Chemical assimilation

6.3.1 O_3

The impact of fire emissions on global O_3 concentrations is shown in Figure 6.2, showing significant increases in tropical fire regions of South American, sub-Saharan Africa, Australia and Indonesia. Maximum contributions (~40%) are seen in September on the arc-of-deforestation in the Amazon and on the west coast of sub-Saharan Africa, with a smaller impact of fires over both regions in October. In contrast, in Australia there is a larger impact of the fires in October. The majority of these emissions peak in regions where savannah fires are either the major contributor or provide a significant contribution, apart from Indonesia which is dominated by tropical and peat fires.

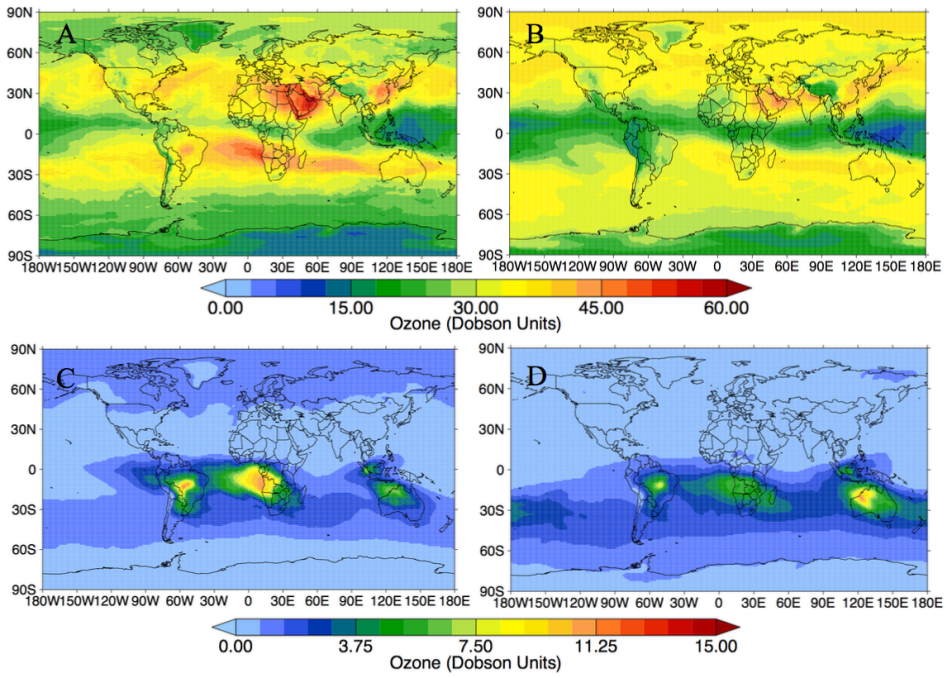

Figure 6.2 The impact of fires on C-IFS simulated O_3 tropospheric column. The left column shows average results for September 2012 and the right column shows equivalent results October 2012. (a, b) O_3 column concentrations for AN_MET (Dobson Units). (c,

Global impact of assimilation

d) Impact of fires on O_3 tropospheric concentrations (AN_MET –FOR_NBB) (Dobson Units).

Changes to the O_3 total column from composition data assimilation is shown in Figure 6.3. Larger differences are seen in October when there is MLS data available, thereby showing the importance of using such profile data in O_3 assimilation to constrain the stratospheric influence and improve the modelled concentrations in the troposphere. Analysis increments are significantly smaller than the difference between AN_MET and AN_METCOM, implying the increments are missing the impact of MLS.

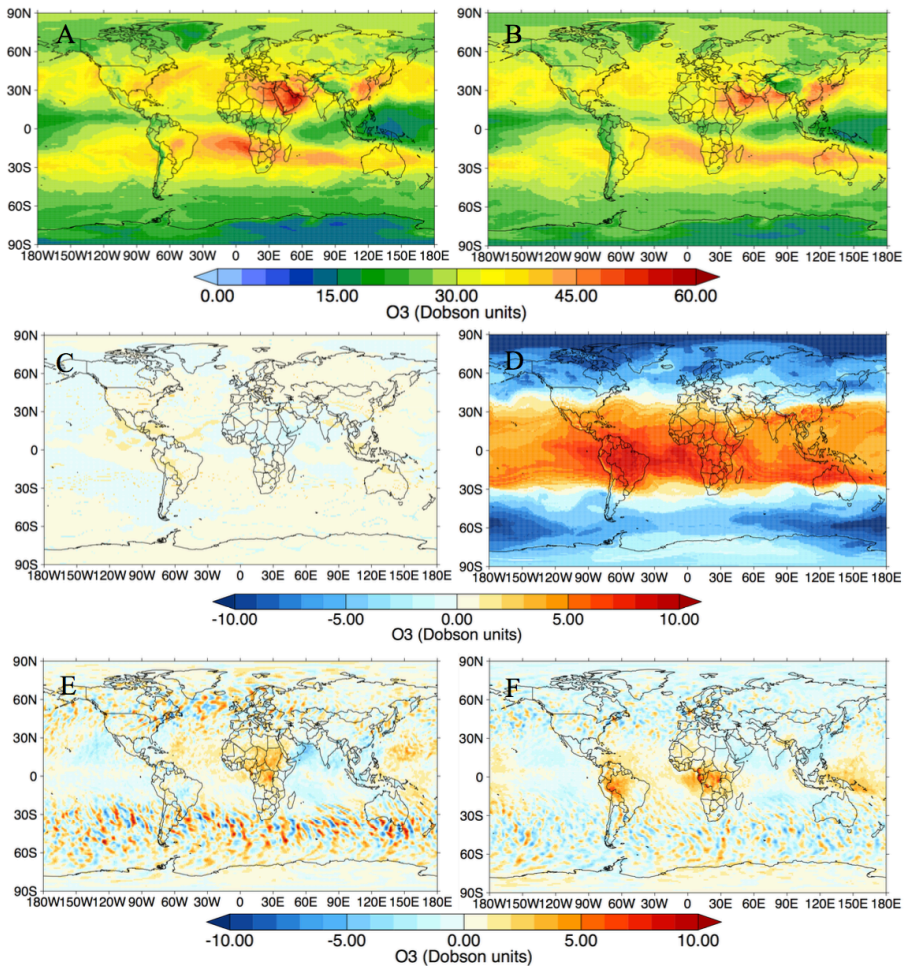

Figure 6.3 The impact of assimilation on C-IFS-simulated O_3 tropospheric column. The left panels show average results for September 2012 and the right panels show equivalent

results for October 2012. (a, b) O_3 column for AN_METCOM (Dobson units). Panels (c, d) show AN_METCOM – AN_MET, i.e. the average impact of assimilation at each 6-hour timestep. Panels (e, f) show the average column O_3 analysis increments from simulation AN_METCOM, for each 12-hour analysis step.

The time series showing the impact of assimilation over the different GFAS regions is shown in Figure 6.4, highlighting the changes when MLS is included after day 273 (October 1st). Overall, similar changes are seen to those presented in Inness et al., (2013) and Miyazaki et al., (2015), for the same time period, with increases in O_3 concentrations over the tropics after October with particularly large increases seen over Central America, Africa and South Asia. South America and Australia also show large increases, but are also impacted by the negative values in the southern latitudes. Negative changes can also be seen in the northern latitudes in North America, Europe and North Asia. Without the impact of MLS changes, as seen in the analysis increments, changes in concentrations are generally a lot smaller with only North Asia showing increments similar to the AN_METCOM – AN_MET model differences.

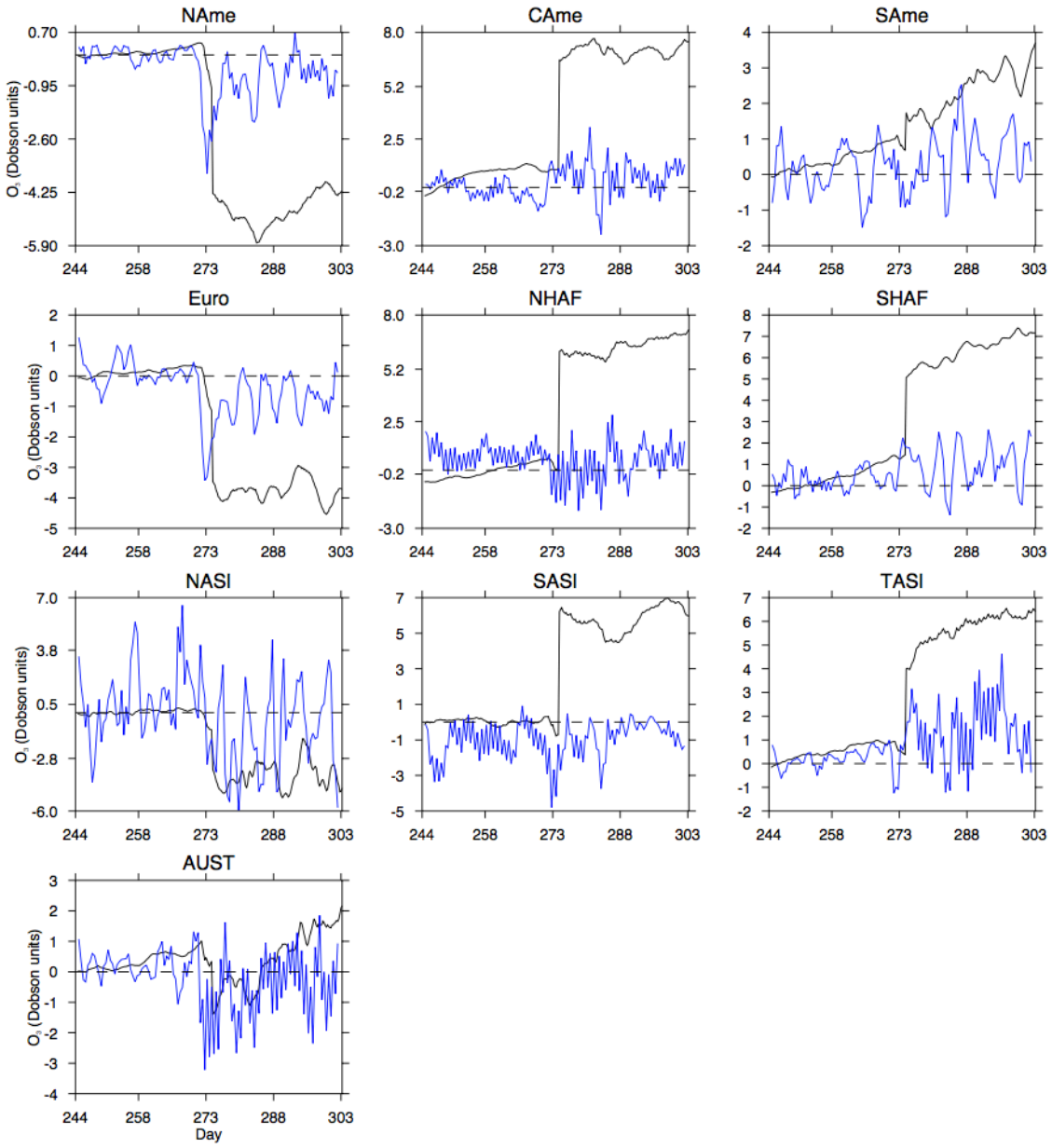

Figure 6.4 The impact of assimilation on O_3 concentrations for September-October 2012, for different regions. The black line shows AN_METCOM – AN_MET, or the average impact of assimilation at each 6-hour timestep. The blue line shows the average O_3 analysis increments from simulation AN_METCOM for each 12-hour analysis step. The labels for the different regions are given in Figure 6.1.

A comparison of simulations AN_MET and AN_METCOM to the RAL tropospheric partial ozone column product is given in in Figure 6.5. C-IFS slightly underestimates the

tropics and shows a small overestimation in both the northern and southern latitudes. Simulation AN_METCOM compares more accurately to the independent observations showing that the assimilation of OMI total column and MLS sub-column leads to more realistically modelled O_3 concentrations. Additionally, simulation AN_METCOM captures the increases in O_3 concentrations from tropical biomass burning over South America, Africa and Southern Atlantic. The increases are however, still small compared to the bias between C-IFS and OMI RAL (partial column 0-6 km), with the majority of the bias remaining after the assimilation, with the average bias in the tropics only falling from -3.55 to -2.93 DU.

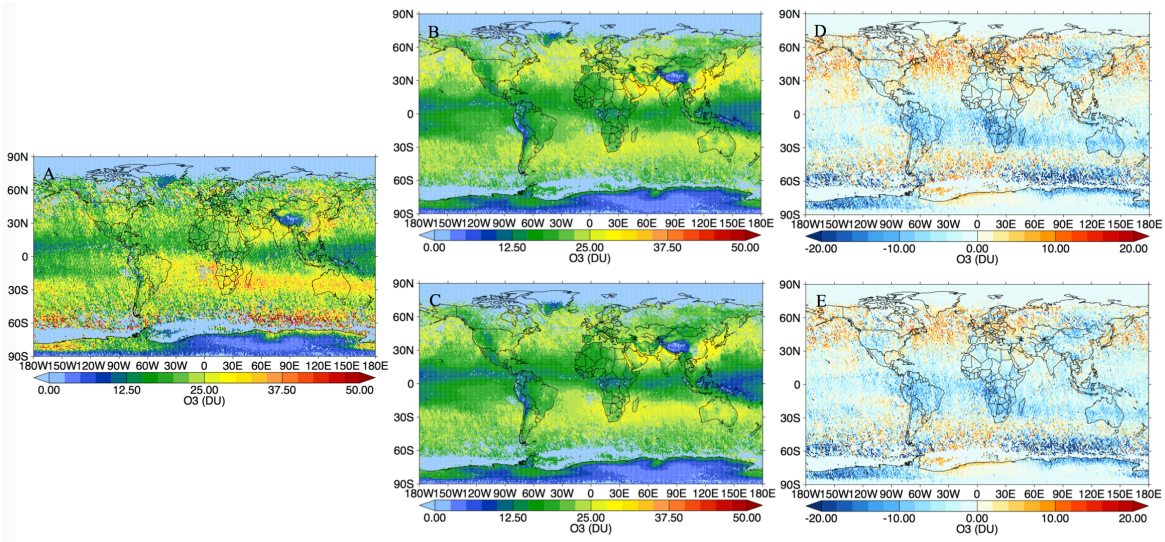

Figure 6.5 Comparison of C-IFS to OMI partial tropospheric ozone columns (0-6 km) for October 2012. (a) OMI satellite column (DU). (b, c) C-IFS partial column with applied averaging kernels for simulations AN_MET and AN_METCOM, respectively. (d, e) Difference between model and satellite partial column for AN_MET and AN_METCOM, respectively.

Figure 6.6 shows the impact of assimilation on O_3 zonal means to get an overview of the global differences. The positive differences over the tropics are predominantly seen at higher altitudes, showing the troposphere-stratosphere exchange could be an important cause of this. The negative changes due to assimilation in the northern and southern hemisphere troposphere are distributed more widely with altitude, suggesting the over-

estimation is also, and is the most likely reason why AN_METCOM shows the largest changes compared to the OMI partial column at these latitudes.

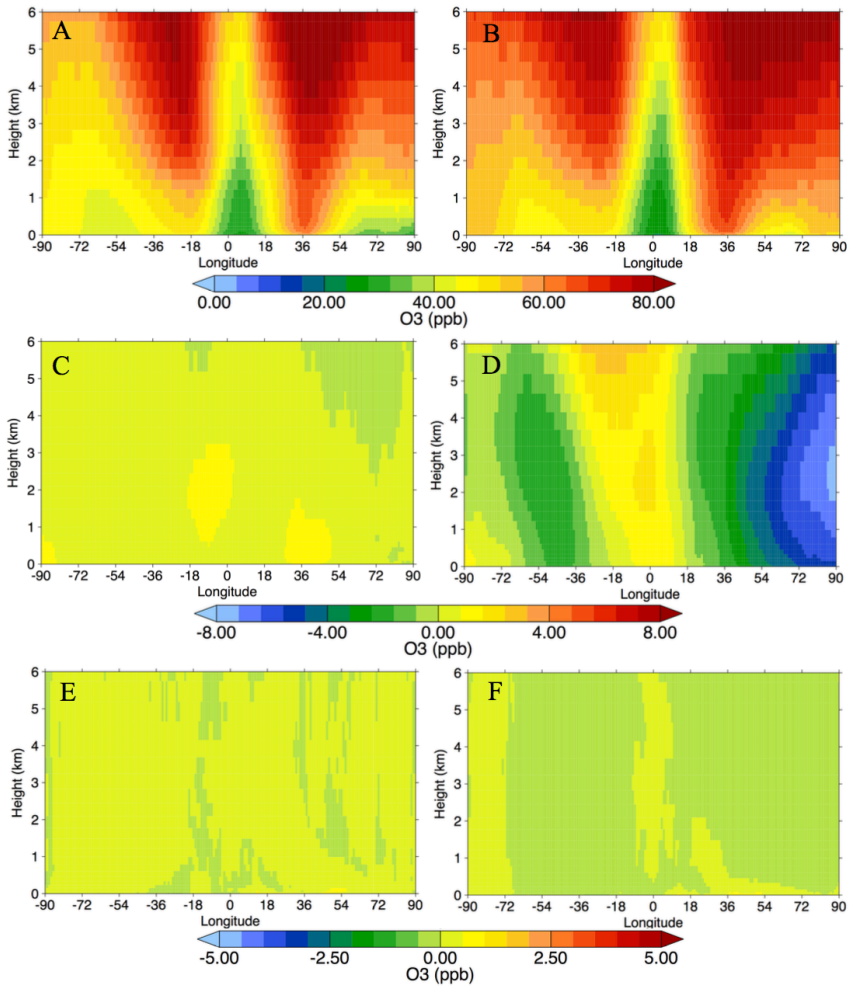

Figure 6.6 Zonal mean plots showing the average vertical impact of composition assimilation on O_3 concentrations in C-IFS for October 2012. The left panels show average results for September 2012 and the right panels equivalent results October 2012. (a, b) O_3 volume mixing ratio for AN_METCOM (ppb). (c, d) show AN_METCOM – AN_MET, i.e. the average impact of assimilation at each 6-hour timestep. (e, f) show the average O_3 analysis increments from simulation AN_METCOM, for each 12-hour analysis step.

6.3.2 CO

The impact of fire emissions on global CO concentrations are shown in Figure 6.7, showing, as expected, large increases in tropical fire regions of South American, sub-Saharan Africa, Australia and Indonesia. The distribution follows the increase in O_3 concentrations in Figure 6.2, although the highest concentrations are associated with the peat fires over Indonesia, rather than Savannah fires. Higher concentrations of CO are seen over tropics than the northern hemisphere due to the impact of fire emissions.

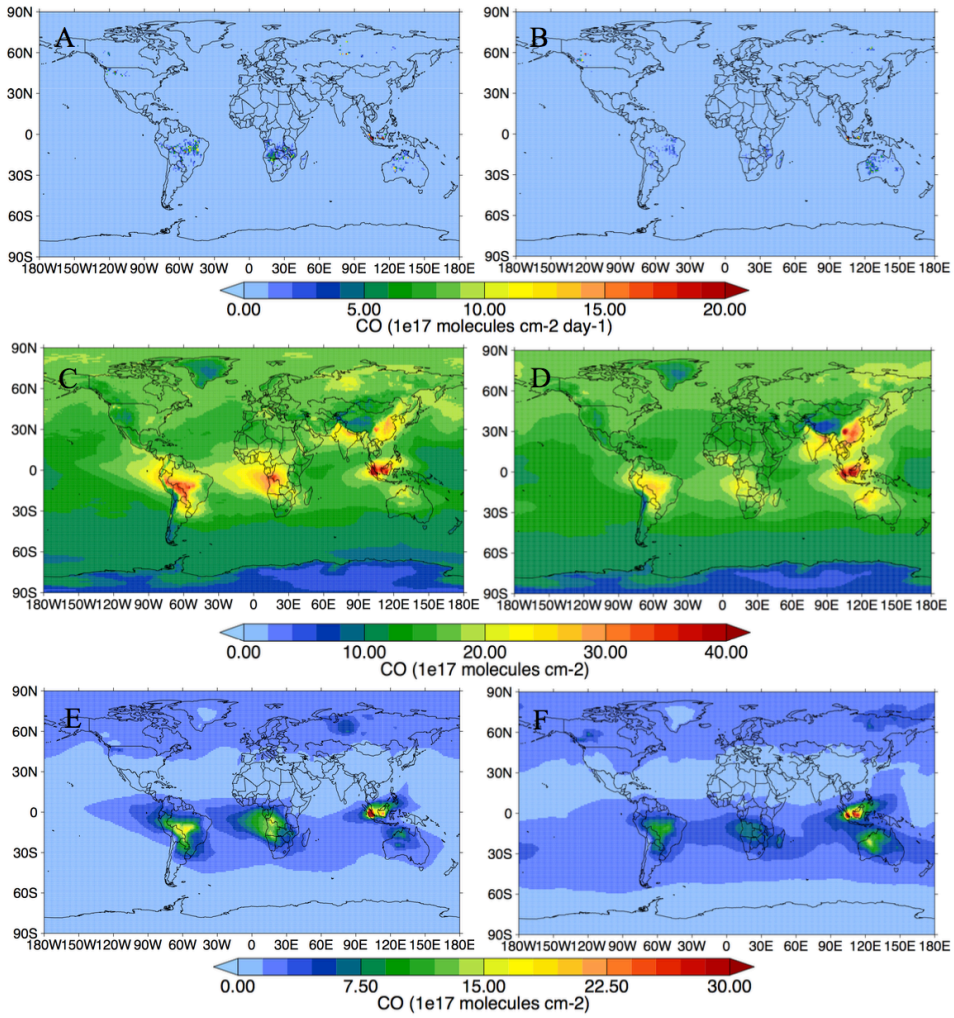

Figure 6.7 The impact of fires on C-IFS simulated CO tropospheric column. The left panels show average results for September 2012 and the right panels show equivalent results October 2012. (a, b) GFAS CO ($\times 10^{17}$ molec. cm^{-2} day^{-1}) flux. (c, d) CO column concentrations for AN_MET ($\times 10^{17}$ molec. cm^{-2}). (e, f) Impact of fires on CO tropospheric concentrations (AN_MET –FOR_NBB) ($\times 10^{17}$ molec. cm^{-2}).

Global impact of assimilation

Changes to the CO total column from composition data assimilation is shown in Figure 6.8. In September changes are seen over the cerrado region of South Africa and the savannah regions of Africa, suggesting a small underestimation (<5%) of the total column. However, the analysis increments suggest a less clear distinction between MOPITT and C-IFS CO with both decreases and increases seen in these tropical fire regions. This suggests that biases are due to misrepresentation of individual fires, with some being under-estimated and others over-estimated. Additionally, the large changes in the analysis increments over the south Atlantic are also likely influencing concentrations in simulation AN_METCOM in both regions.

Over Indonesia, both the AN_METCOM-AN_MET model differences and the analysis increments suggest decreases in CO concentrations from assimilation, with decreases up to 10% of the total column. This could imply that peat emission factors used in GFAS are producing CO concentrations that are too large compared to MOPITT CO. The recent 2015 -El Niño related fires in Indonesian fires and consequent observations showed that the emission factors from Akagi et al., (2011) and used in this study for peat fires are two low compared to in-situ observations (Huijnen et al., 2016). However, in this study C-IFS showed small positive biases compared to the MOPITT total column. This is concurrent with the over-estimation of CO in September-October 2012 from this study. This implies that the positive bias in CO concentrations over Indonesia is dominated by the uncertainty in the local CO loss (Duncan et al., 2003) and not due to too high emission factors.

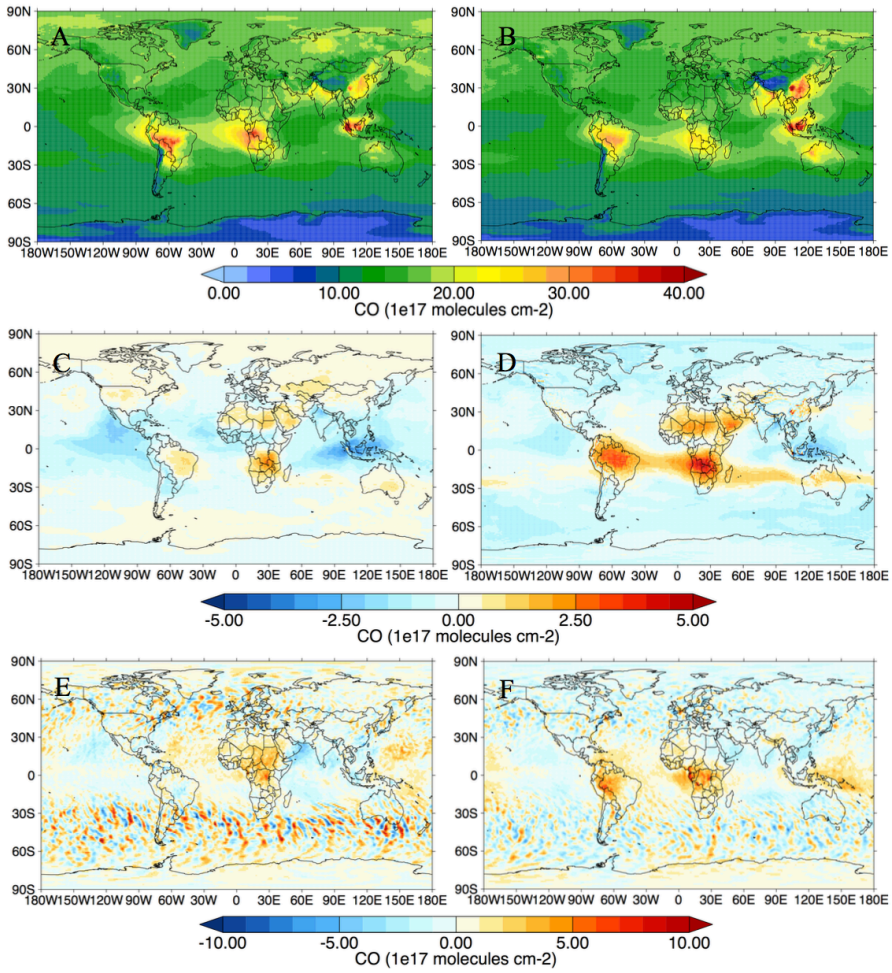

Figure 6.8 The impact of assimilation on C-IFS simulated CO tropospheric column. The left panels show average results for September 2012 and the right panels show equivalent results October 2012. (a, b) CO column concentrations for AN_METCOM ($\times 10^{17}$ molec. cm^{-2}). Panels (c, d) show AN_METCOM – AN_MET, or the average impact of assimilation at each 6-hour timestep. Panels (e, f) show the average CO analysis increments from simulation AN_METCOM, for each 12-hour analysis step.

As with O_3, more significant changes from assimilation are seen for CO in October. Analysis increments show larger increases over the western Amazon and Sub-Saharan Africa, areas where fire emissions are smaller but where concentrations might be impacted by the transport of fire emissions. The AN_METCOM – AN_MET differences are larger than the analysis increments during October and imply an impact from the assimilation of MLS O_3 on CO concentrations, with increases in CO corresponding to

increases in O_3. The changes in CO are, however, small compared to the CO total column, with the maximum value being the decrease over tropical Asia (-3.30×10^{17} molecules cm^{-2}), corresponding to peat fires. The negative values over tropical Asia are improved after October although the increments remain low throughout.

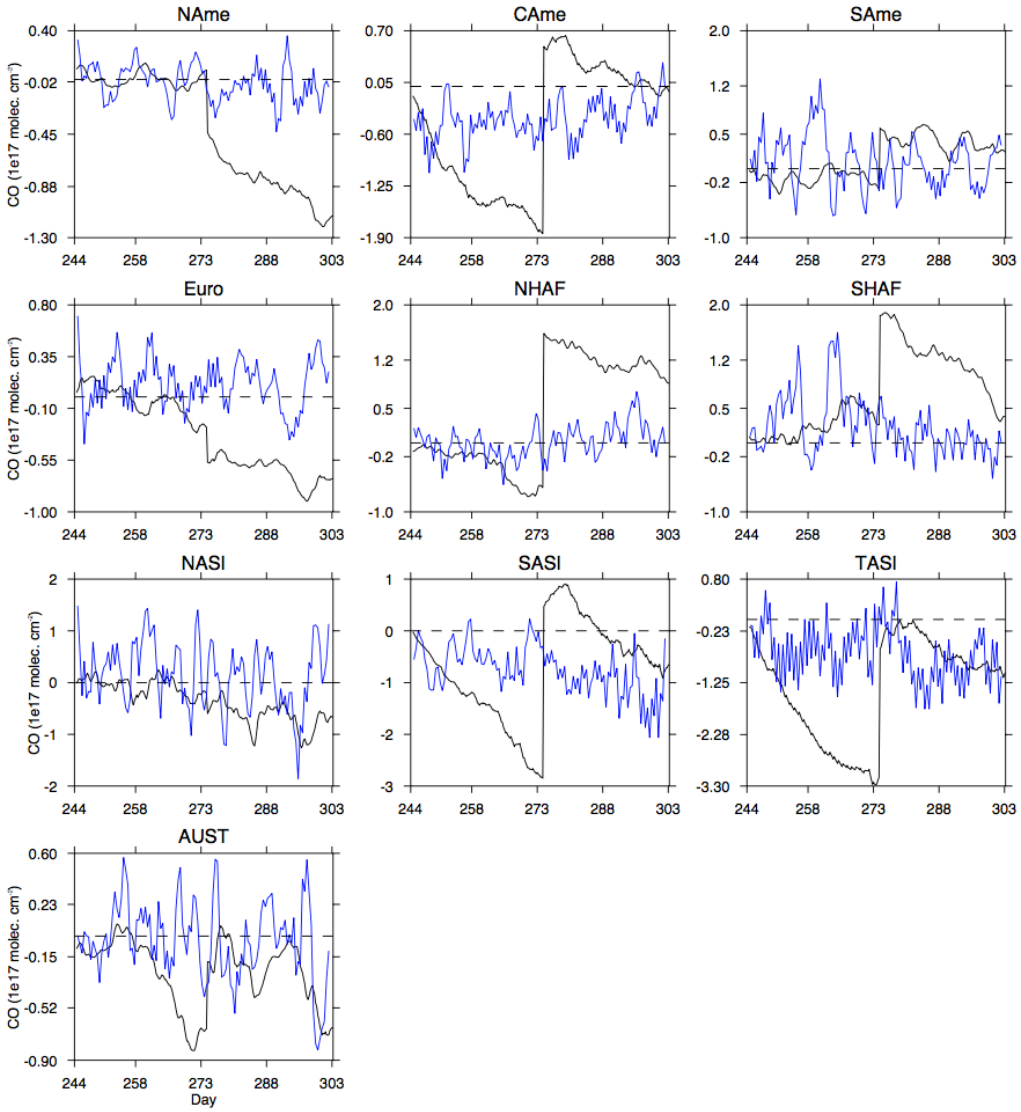

Figure 6.9 The impact of assimilation on CO concentrations for September-October 2012, for different regions. The black line represents, AN_METCOM – AN_MET, or the average impact of assimilation at each 6-hour timestep. The blue line shows the average CO analysis increments from simulation AN_METCOM, for each 12-hour analysis step. The labels for the different regions are given in Figure 6.1.

Global impact of assimilation

Figure 6.10 shows the impact of assimilation on CO zonal means. The difference between AN_MET and AN_METCOM is dominated by the large negative increments over the tropics relating to peat fires, masking positive changes from tropical savannah fires, in September and are enhanced by increasing O_3 concentrations in October from MLS. Smaller positive changes are seen in the Northern Hemisphere relating to increases over North Africa.

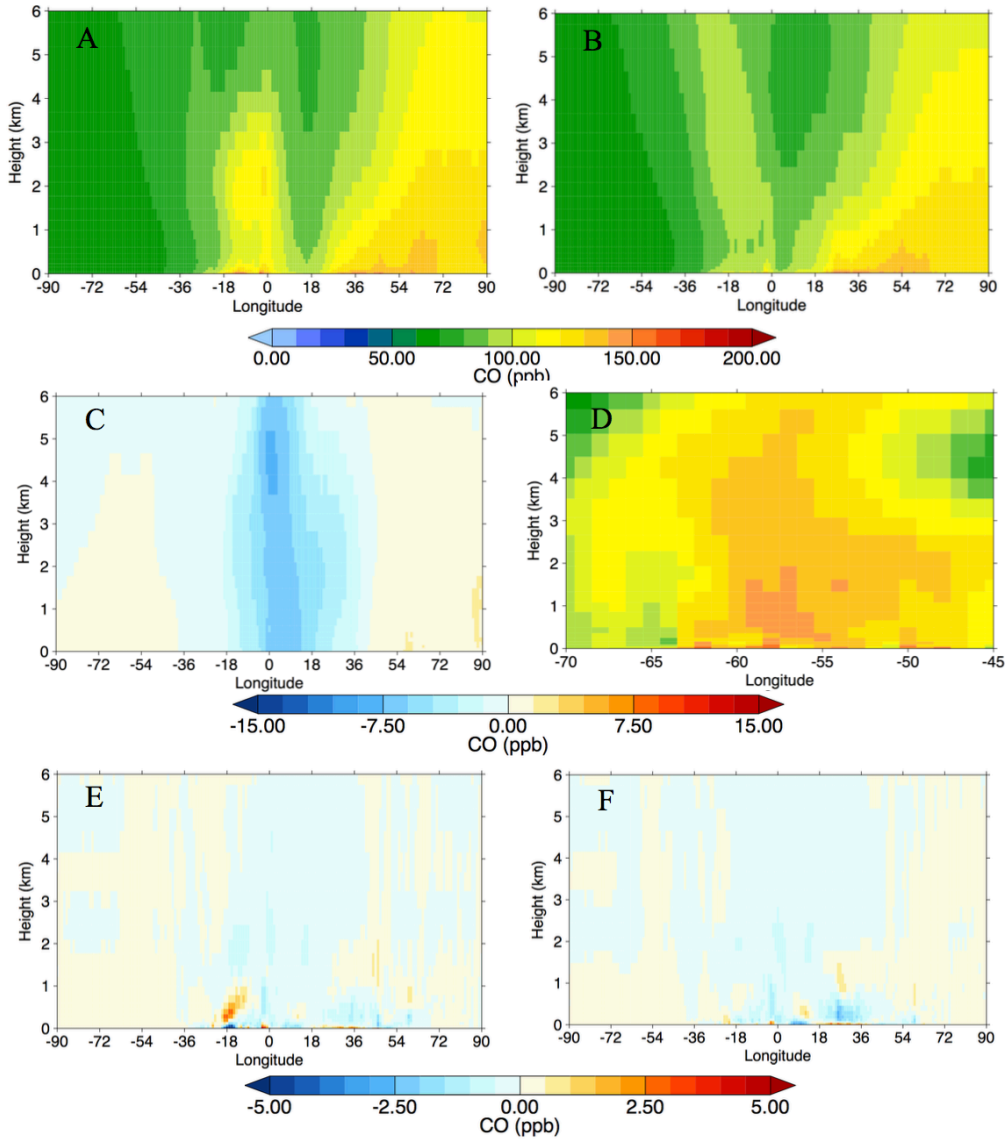

Figure 6.10 Zonal means showing the average vertical impact of composition assimilation on CO concentrations in C-IFS for October 2012. The left panels show average results for September 2012 and the right panels show equivalent results October 2012. (a, b) CO volume mixing ratios for AN_METCOM (ppb). (c, d) Difference between simulations AN_METCOM – AN_MET, i.e. the average impact of assimilation at each 6-hour timestep. (e, f) The average CO analysis increments from simulation AN_METCOM, for each 12-hour analysis step.

6.3.3 NO_2

The impact of fire emissions on global NO_2 concentrations are shown in Figure 6.11, showing significant increases in the tropical fire regions of South American, sub-Saharan Africa and Australia. These emissions dominate in the Southern Hemisphere but provide a much smaller contribution to the global budget than the urban emissions in the Northern Hemisphere. Sub-Saharan Africa and Australian fires are predominantly Savanah vegetation, which is also the case for the eastern fire regions in South America, and these fires seemingly dominate the contribution of fires to the total NO_x concentrations. This is probably due to the higher Modified Combustion Efficiency (MCE) (Jaffe & Wigder, 2012), implying a larger contribution of flaming fires, due to the more open canopy of Savannah fires. The MCE is the most important factor contributing to NO_x production from fires in emission inventories as it is assumed that while plants do have varying nitrogen content there is little variation on average between biomes(Jaffe & Wigder, 2012).

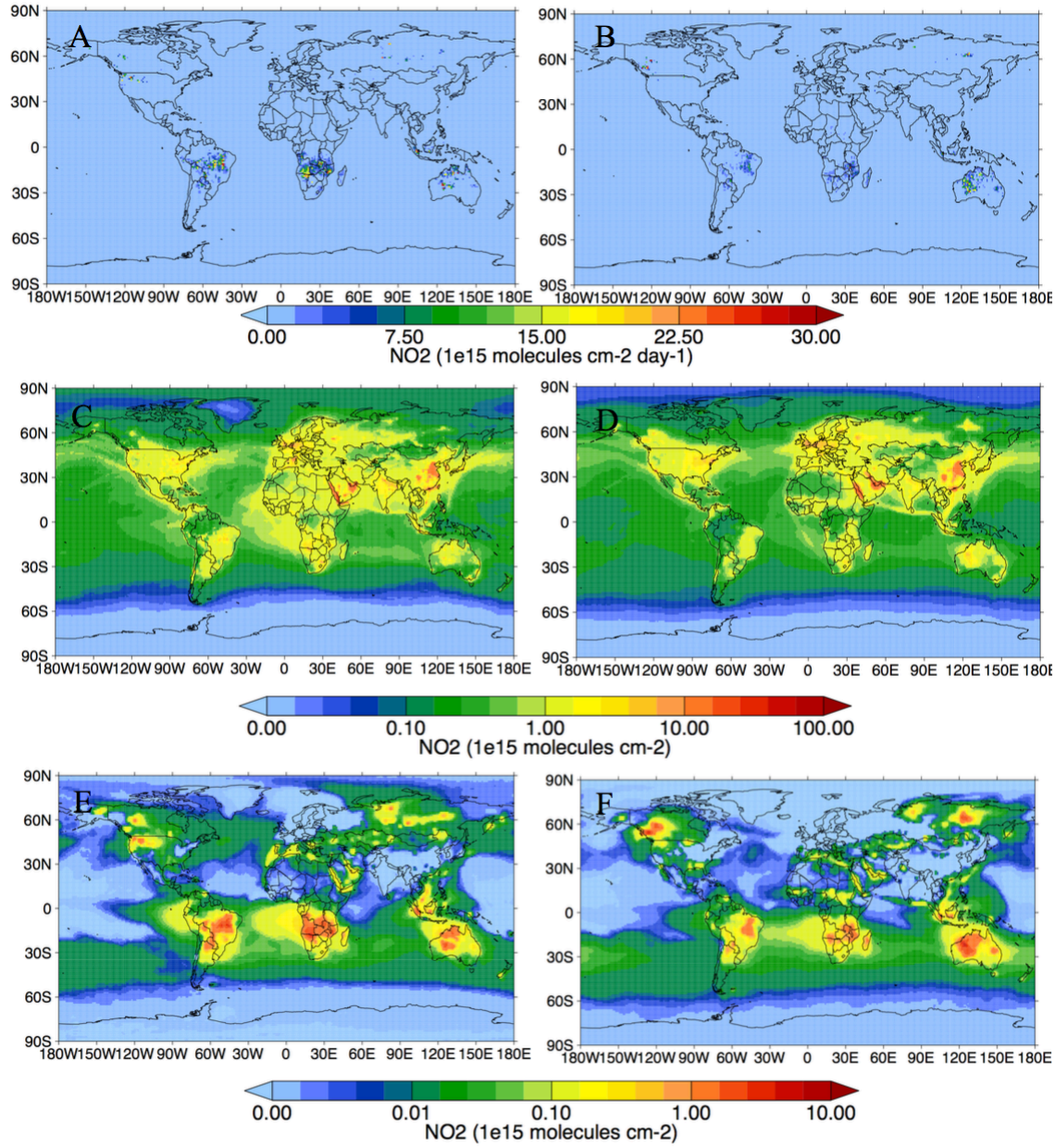

Figure 6.11 The impact of fires on C-IFS simulated NO_2 tropospheric column. The left panels show average results for September 2012 and the right panels show equivalent results for October 2012. (a, b) GFAS NO_x ($\times 10^{15}$ molec. cm^{-2} day^{-1}) flux. (c, d) NO_2 column concentrations for AN_MET ($\times 10^{15}$ molec. cm^{-2}). (e, f) Impact of fires on NO_2 tropospheric concentrations (AN_MET –FOR_NBB) ($\times 10^{15}$ molec. cm^{-2}).

Changes to the NO_2 total column from composition data assimilation is shown in Figure 6.12. In September changes are seen over the majority of fire and urban emission sources,

with additional changes seen over the tropical oceans in October after the assimilation of MLS. The analysis increments, unlike for CO and O_3, are larger than the AN_METCOM-AN_MET simulation differences, with particularly large values over emission source regions. This difference is due to the short lifetime of NO_2 (order of days) relative to O_3 and CO which means that analysis NO_2 shows little improvement over time and needs to constantly be improved, leading to 'large' total increments for each assimilation window. Additionally, NO_2 increments appear to be split into longitudinal bins with positive increases seen between 90°W – 30°W and 90°E-180°E and negative increments between 30°W-90°E, with large increments in these region over areas with little predicted NO_2 e.g. Northern Atlantic Ocean.

Global impact of assimilation

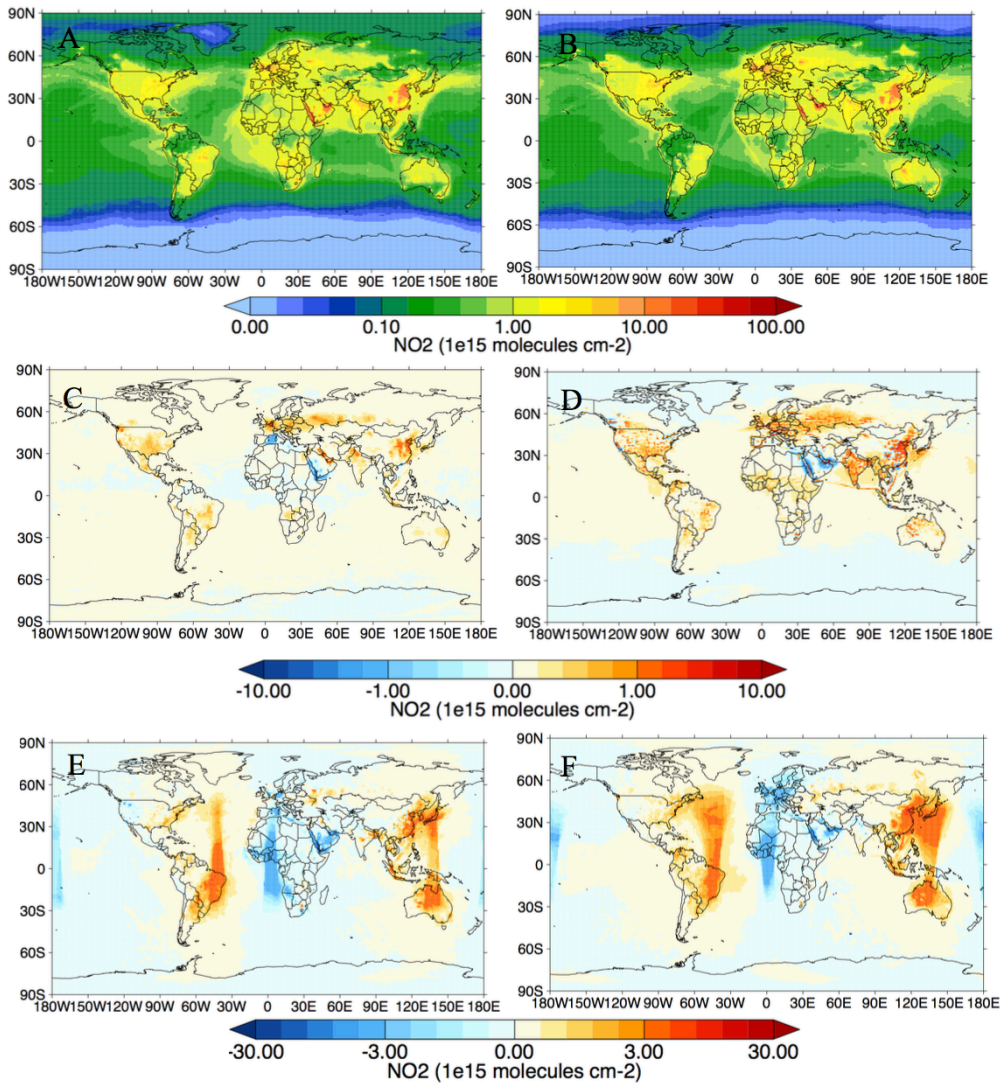

Figure 6.12 The impact of assimilation on C-IFS simulated NO_2 tropospheric column. The left panels show average results for September 2012 and the right panels show equivalent results October 2012. (a, b) NO_2 column concentrations for AN_METCOM ($\times 10^{15}$ molec. cm^{-2}). Panels (c, d) show the difference between simulations AN_METCOM – AN_MET, i.e. the average impact of assimilation at each 6-hour timestep. Panels (e, f) show the average NO_2 analysis increments from simulation AN_METCOM, for each 12-hour analysis step.

The time series showing the impact of assimilation over the different GFAS regions is shown in Figure 6.13. The analysis increments are significantly larger than the AN_METCOM-AN_MET difference throughout the time window, due to increments

being a ‘total’ increase over each 12-hr period. With a NO_x lifetime at the surface that could be only a few hours, near a major underestimated source of NO_x a significant amount of NO_x can added by the assimilation system and seen in the increments. Generally, the assimilation increases the concentrations of NO_x over urban and emissions sources, although there are negative values over urban sources in both the Arabian Peninsula and the Mediterranean. The positive analysis increments are also significantly larger than the main fire emission fluxes over the main tropical fire seasons. This is despite recent studies implying an under-estimation of NO_x emissions over Riyadh in the EDGAR emission inventory (Beirle et al., 2011), but could be explained by the influence of dust particles in the up-take of HNO_3 halting the reformation of NO_2 from HNO_3 (Fairlie et al., 2010).

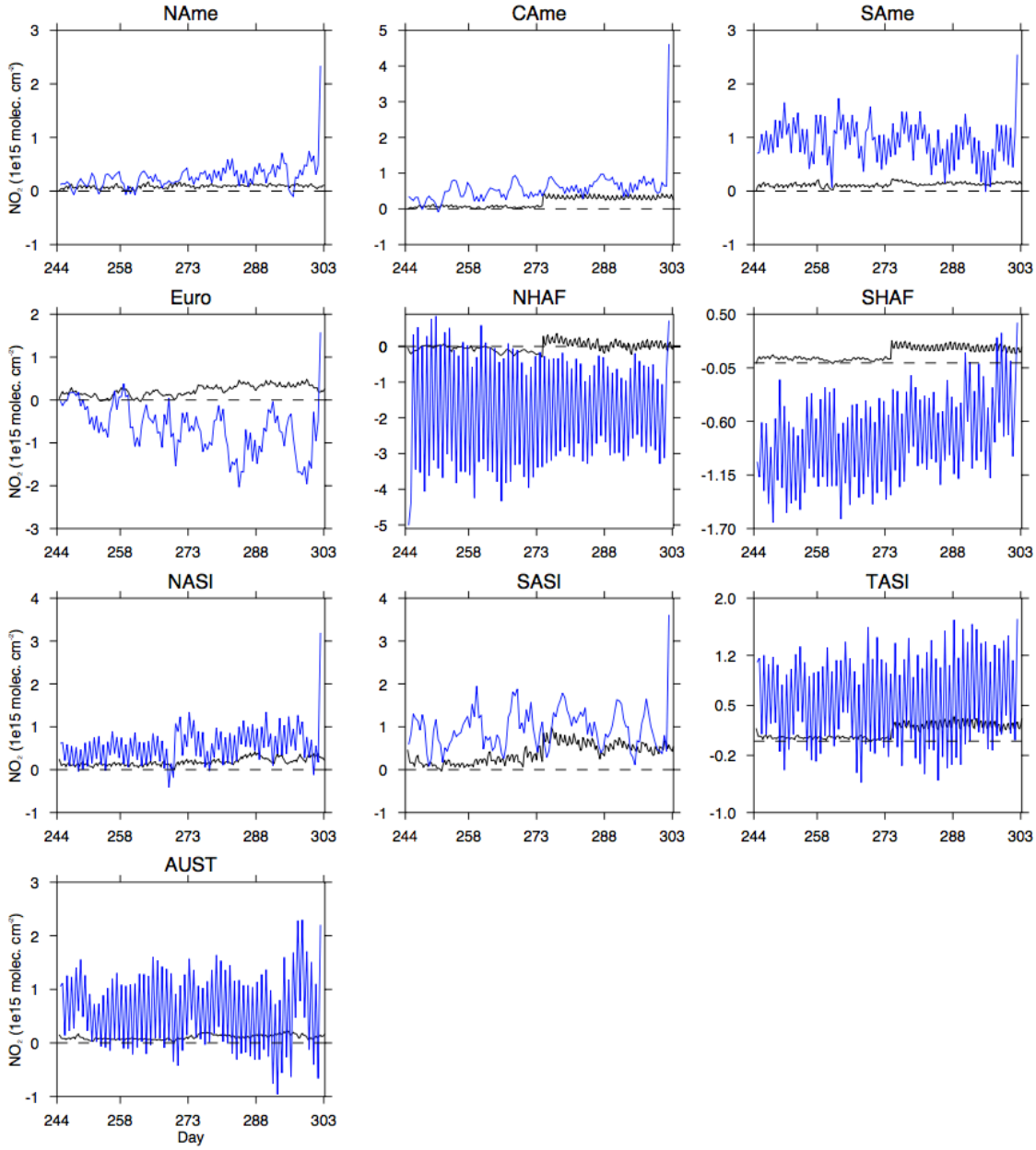

Figure 6.13 The impact of assimilation on NO_2 concentrations for September-October 2012, for different regions. The black line represents, AN_METCOM – AN_MET, or the average impact of assimilation at each 6-hour timestep. The blue shows the average NO_2 analysis increments from simulation AN_METCOM, for each 12-hour analysis step. The region labels are explained in Figure 6.4.

Global impact of assimilation

For Europe, and all of Africa the analysis increments are negative while the AN_METCOM – AN_MET difference is positive. Such a difference between AN_METCOM - AN_MET and the analysis increments could imply that the assimilation of other species is influencing the concentration of NO_2. However, CO increments are small over Europe and the negative increments there are also present in September, when there was limited change from O_3 assimilation. Compared to the OMI product in Figure 6.14, C-IFS shows an underestimation over Europe which corresponds to the positive AN_MET-AN_METCOM difference. However, concentrations over both the Mediterranean and North Africa are lower for OMI than C-IFS and are likely the cause of the negative analysis increments in and around Europe. The spread of the negative increments into central Europe and the positive increments over the Northern Atlantic could suggest potential inaccuracies in the model error-correlation matrices.

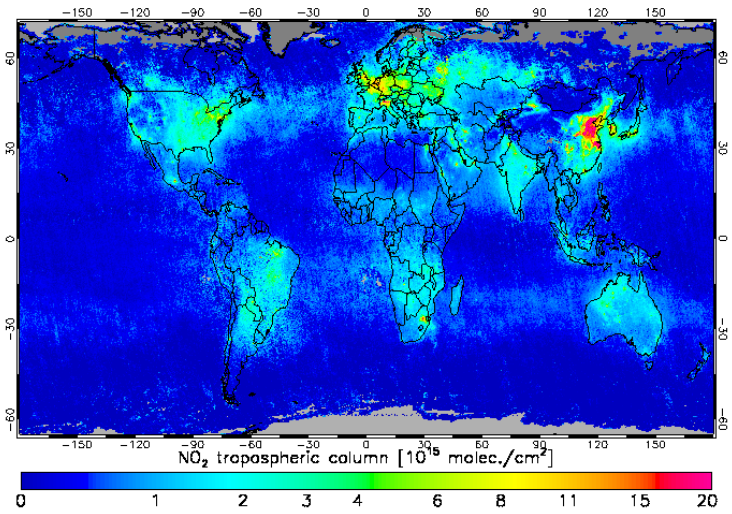

Figure 6.14 Average OMI NO_2 total column ($\times 10^{15}$ cm^{-2}) for September 2012, from TEMIS.

Figure 6.15 shows the impact of assimilation on NO_2 zonal means. The positive increments over both the tropics and northern hemisphere are all at the surface, indicating that they are emissions related. The negative increments are just above the surface which would imply an underestimation of the NO_2 loss process. However, the vertical distribution of increments is solely based on the model and as such the impact from assimilation may be incorrectly distributed. The global zonal means also show the more

relative persistence of northern hemisphere NO_2 increments compared to the tropics due to higher concentration of OH in the tropics controlling the loss processes.

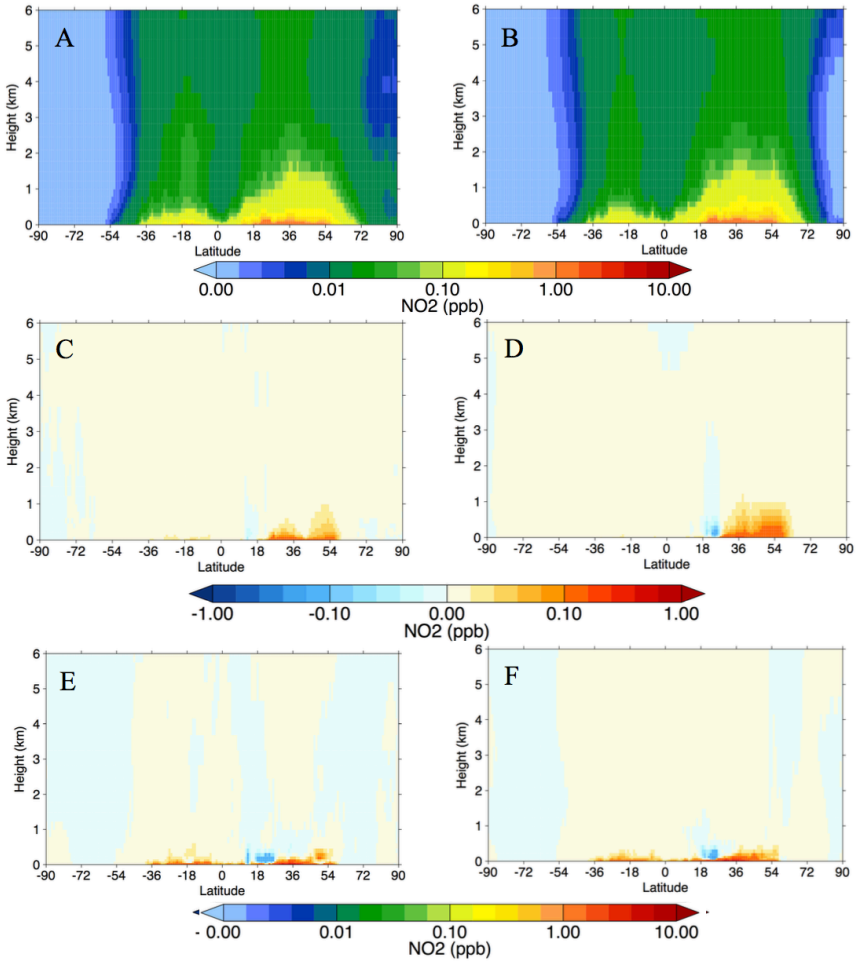

Figure 6.15 Zonal mean plots showing the average vertical impact of composition assimilation on NO_2 concentrations in C-IFS for October 2012. The left panels show average results for September 2012 and the right panels show equivalent results October 2012. (a, b) NO_2 volume mixing ratio for AN_METCOM (ppb). (c, d) Difference between simulations AN_METCOM – AN_MET, i.e. the average impact of assimilation at each 6 hour timestep. (e, f) The average NO_2 analysis increments from simulation AN_METCOM, for each 12-hour analysis step.

6.3.4 Hydroxyl radical

As the most important atmospheric oxidant, and its participation in many chemical reactions, the hydroxyl radical (OH) is significantly impacted by changes in concentrations of other atmospheric species. As OH is not a control variable in the C-IFS assimilation system, increments are not directly calculated at the assimilation step and changes in values are purely down to the model reacting to changes in concentrations from other assimilated species. Ozone assimilation impacts OH as elevated O_3 concentrations promote the production of OH through the photochemical production of $O(^1D)$. NO_2 and CO increments both impact the production of O_3 with the NO_x null-cycle also able to regenerate OH in the presence of VOCs. The main loss processes of both species are oxidation with the OH radical with NO_2 and OH forming HNO_3 and CO and OH forming CO_2 with the peroxide radical (HO_2). Additionally, CO is formed from the oxidation of CH_4 by OH, a process that contributes about half of the background CO (Duncan et al., 2007).

The impact of composition assimilation in C-IFS on the modelled OH radical tropospheric column is shown in Figure 6.16 for September and Figure 6.17 for October 2012. Increases in concentrations are seen over both months for Eurasia, North America, South America and Australia. For September 2012 OH shows a strong positive-correlation with NO_2 increments with large positive increases in OH over urban emissions in the Northern Hemisphere, as well as fire emissions in the tropics. These locations also show a small increase in O_3, despite no MLS assimilation, suggesting that increase in NO_x concentrations lead to increases in OH via O_3 with concentrations of OH most likely kept high due to the presence of VOCs in these regions.

For October 2012, as seen in Figure 6.17, when a full suite of observations is assimilated, there are smaller positive changes in the Northern Hemisphere due to decreases in O_3 concentrations by MLS. Large negative changes in OH occur over the Arabian Peninsula and Northern Africa corresponding to large decreases in NO_2 and O_3. Despite smaller NO_2 increments in the tropics positive increases in OH concentrations remain high due to O_3 assimilation. Finally, negative O_3 changes over the South Atlantic and South Pacific lead to smaller concentrations of OH there.

Global impact of assimilation

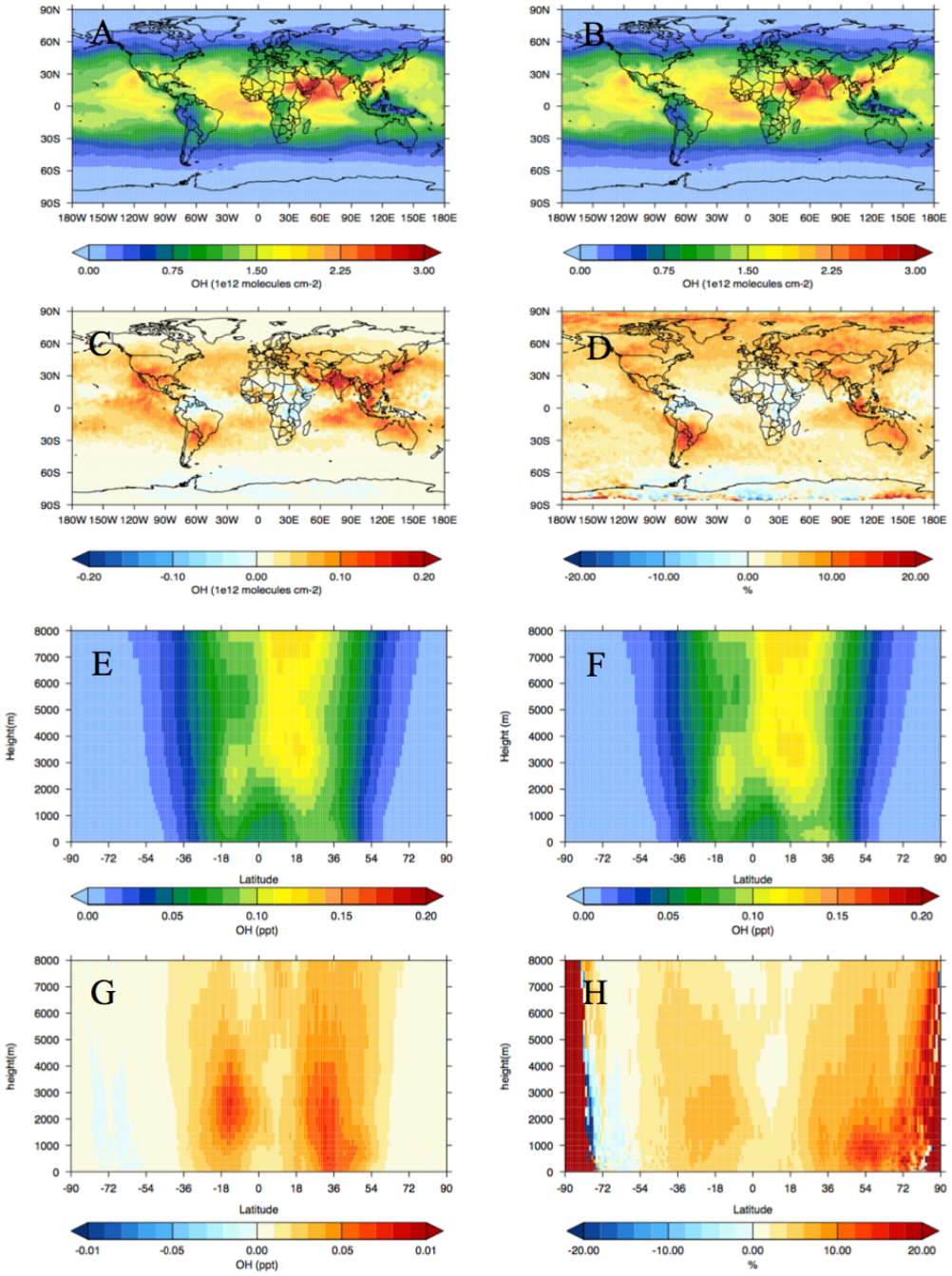

Figure 6.16 Impact of assimilation on OH total columns and zonal means for September 2012. (a) AN_MET OH total column ($\times 10^{12}$ molec. cm^{-2}). (b) AN_METCOM OH total column ($\times 10^{12}$ molec. cm^{-2}). (e) AN_MET OH zonal mean (ppt) (f) AN_METCOM OH zonal mean (ppt). (c, g) Difference between simulations AN_METCOM – AN_MET, i.e the average impact of assimilation at each 6-hour timestep. (d, h) The percentage change from assimilation at each 6 hour timestep.

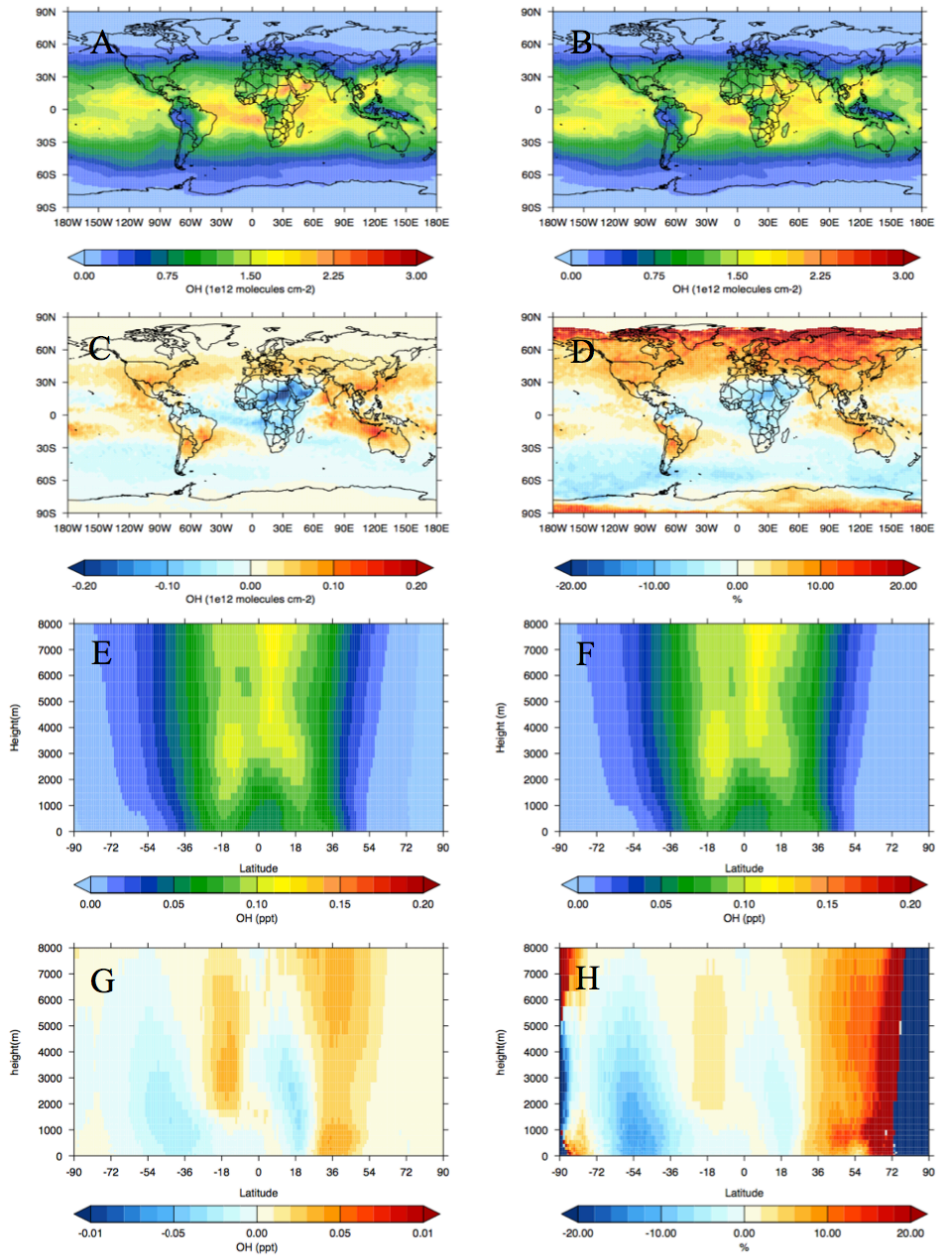

Figure 6.17 As Figure 6.15 but for October 2012.

The interhemispheric (NH/SH) ratio in mean OH concentration for C-IFS without assimilation is 1.24, which is an overestimate compared to the methyl-chloroform derived observed ratio of 0.97 ± 0.12 (Patra et al., 2014). This suggests C-IFS OH values are either too large in the Northern Hemisphere or too small in the Southern Hemisphere. This is similar to, but slightly more accurate, than the ACCMIP (the Atmospheric

Chemistry and Climate Model Intercomparison Project) model average of 1.28 ± 0.10 (Naik et al., 2013). In Patra et al., 2014 TM5, which the chemistry scheme in C-IFS is based on, had a NH/SH OH ratio of 1.28 for the year 2000, as this value is similar to the 1.24 seen in this study it seems that the bias compared to observations is due to the chemical scheme in the model rather than the 2 month timeframe of the experuiment. A smaller NH/SH would actually be expected for September-October due to higher O_3 concentrations in the Soutehrn hemisphere during thius time period.

The assimilation of the different chemical species increases the bias to 1.31 as OH concentrations in the Northern Hemisphere are increased, moving the value away from the derived observations Patra et al., (2014). This suggests that the correction of chemical species to observations can add an additional error and that the modelled chemistry (in this case for OH) has fundamental inaccuracies. However, the long-term analysis dataset in Miyazaki et al., (2015) showed decreases in OH concentrations in the NH and increases in the SH and an improvement in the NH/SH ratio compared to observations. In Miyazaki et al., (2015) OH was include in the state vector which enabled the relationship between the concentrations and emissions of related species to be calculated at the analysis step by the background error correlations. This calculation meant that OH concentrations were changed when increases or decreases in NO_2 and CO increments where related an inaccurate loss via OH, unlike for C-IFS where OH changes from assimilation only change after the concentrations have been perturbed.

6.3.5 Organic compounds

Many different organic chemical species were included in the C-IFS chemical scheme used in AN_MET and AN_METCOM, all of which showed small changes from assimilation resulting from the impact on OH. As the simulations were only run for a couple of months the larger differences were seen for compounds which reacted more rapidly with OH and hence had shorter atmospheric lifetimes. Propane (C_3H_8) is used here to assess the impact of assimilation on OH, this is due to the atmospheric lifetime of propane being around 14 days (Rosado-Reyes & Francisco, 2007) and as such can be impacted by OH changes over the 2-month simulation. Additionally, propane

observations are available globally by NOAA via flask measurements (Figure 6.18). Propane is primarily emitted from oil and natural gas production and as a short lived species is sensitive to local/regional emissions. Recent studies have highlighted the recent increases of propane in the united states and its impact on O_3 concentrations (Helmig et al., 2016).

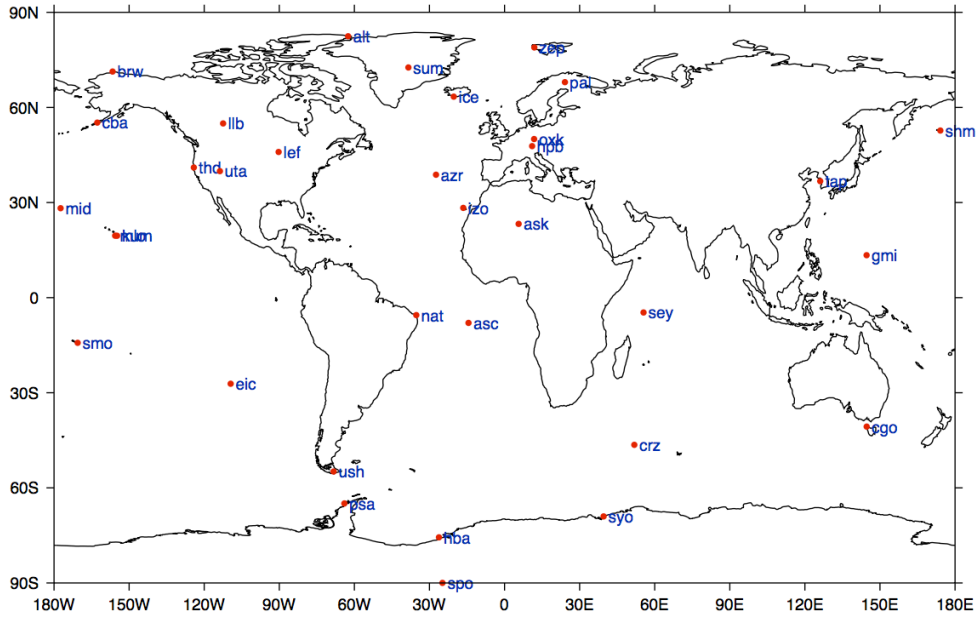

Figure 6.18 Available NOAA flasks sites with propane concentrations for September - October 2012. NOAA station codes: Alt: Alert, Canada; asc:ascension island, UK; ask: Assekrem, Algeria; azr: Terecia Island, Azores; brw: Barrow, USA; cba: Cold Bay, USA; cgo: Cape Grim, Australia; crz: Crozet Island, France; eic: Easter Island, Chile; gmi: Mariana Islands, Guam; hba: Halley Station, Antartica; HBP: Hohenpeissenberg, Germany; ice: Storhofdi, Iceland; izo: Tenerife, Spain; kum: Cape Kumukahi, USA; lef: Park Falls, USA; lib: Lac La Biche, Canada; mid: Midway, USA; mlo: Mauna Lao, USA; nat: Farol De Mae, Brazil; oxk: Ochsenkopf, Germany; pal: Pallas-Sammaltunturi, Finland; sey: Mahe Island, Seychelles; shm: Shemya Island, USA; smo: Tutuila, American Samoa; spo: South Pole, Antartica; sum: Summit, Greenland; syo: Syowa Station, Antartica; tap: Tae-ahn, Korea; thd: Trinidad Head, USA; ush: Ushuaia, Argentina; uta: Wendover, USA; zep: Ny-Alesund, Norway and Sweden.

Global impact of assimilation

The impact of composition assimilation in C-IFS on modelled propane is shown in Figure 6.19 for September and Figure 6.20 for October 2012. Total changes in concentrations are small but the differences are anti-correlated to the changes seen in OH in Section 6.3.4, with decreases seen over both months for Eurasia, North America, South America and Australia and increases over North Africa in September.

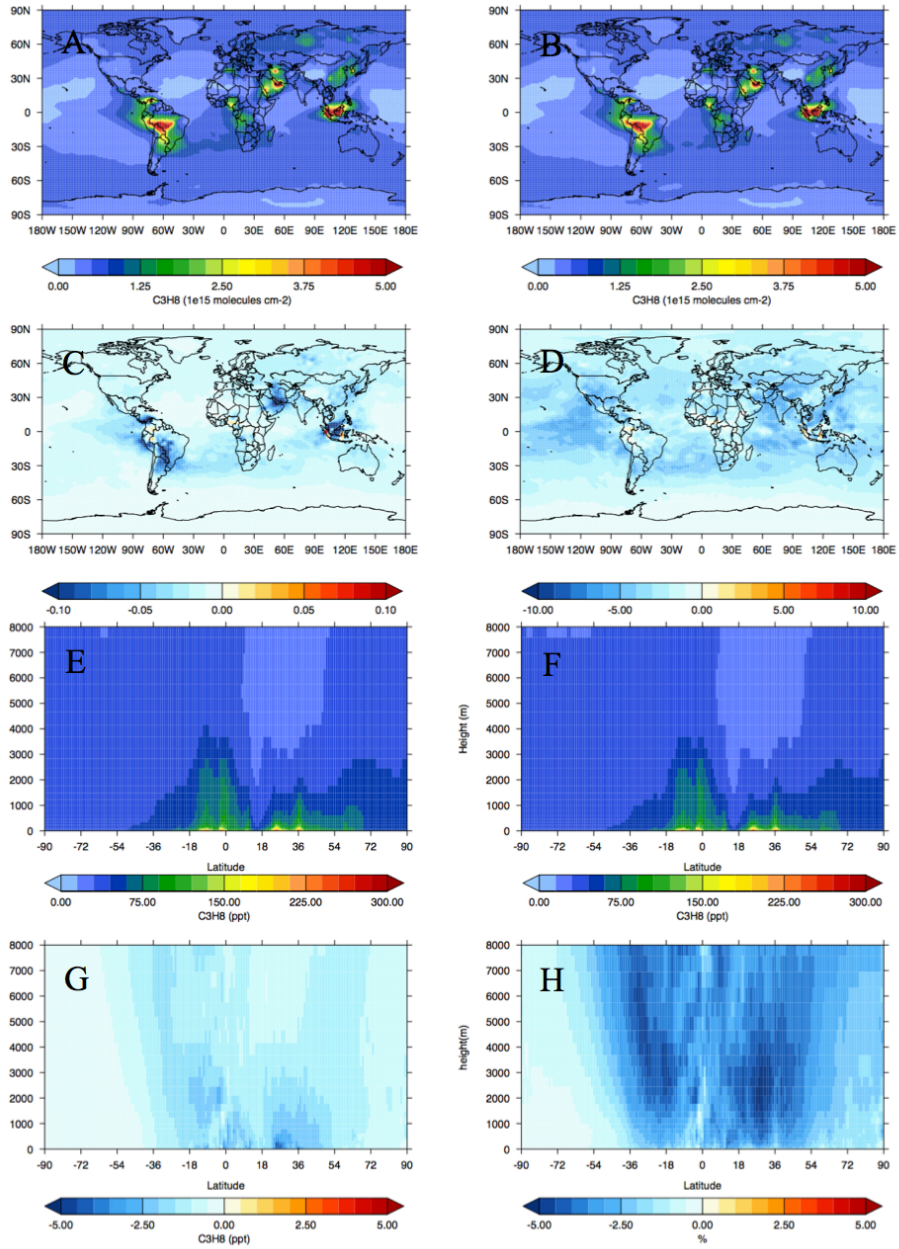

Figure 6.19 Impact of assimilation on C_3H_8 total columns and zonal means for September 2012. (a) AN_METCOM C_3H_8 total column ($\times 10^{15}$ molec. cm^{-2}). (b) AN_MET C_3H_8 total column ($\times 10^{15}$ molec. cm^{-2}). (e) AN_MET OH zonal mean (ppt). (f) AN_METCOM

Global impact of assimilation

C_3H_8 zonal mean (ppt). (c, g) Difference AN_METCOM – AN_MET, i.e. the average impact of assimilation at each 6 hour timestep. (d, h) The percentage change from assimilation at each 6-hour timestep.

Global impact of assimilation

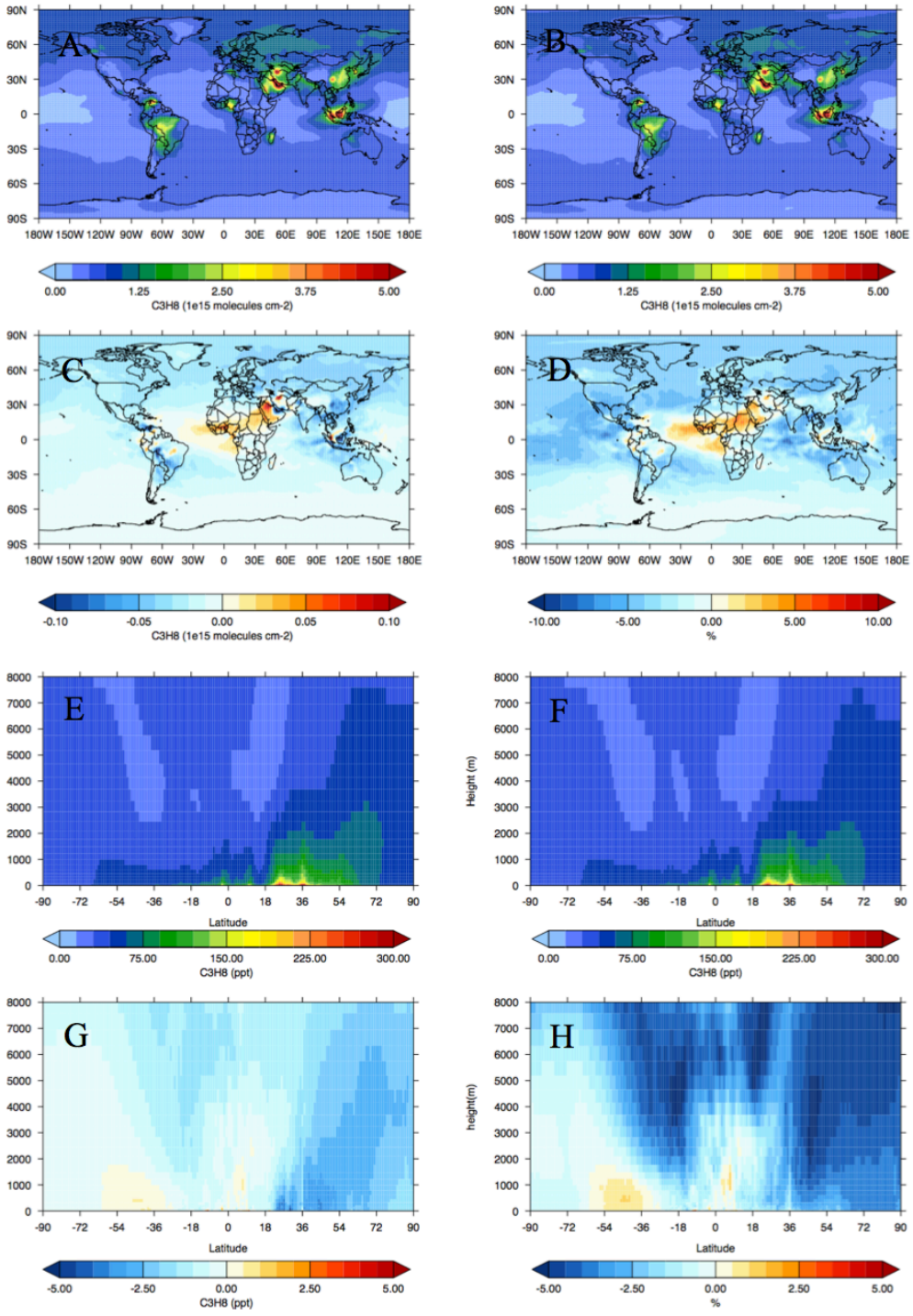

Figure 6.20 As Figure 6.19 but for October 2012.

Comparisons of propane from simulations AN_MET and AN_METCOM to NOAA flask sites are given in Figure 6.21. Generally, observed concentrations of propane are significantly larger than modelled concentrations over the northern hemisphere where emissions from oil and natural gas production are largest. The model compares realtivilty

well to sites with low propane concentrations such as remote sites at Halley and Syowa stations Farol de Mae in Brazil. This suggests the majority of the model bias is duw to low emissions rather than propane loss via OH. This is similar to earlier studies which have shown that top-down emission estimates are well above inventory estimates (Helmig et al., 2016).

As this is a model comparison to surface observations changes from assimilating total column observations are very small. However, changes can be seen in the tropics with the assimilation decreasing propane concentrations as the OH budget is changed. These increases are small compared to the model-surface observations differences, as the majority of bias is thought to be due to emissions rather than loss process, but shows that assimilating total column gas phase species is changing the OH budget significantly enough to impact other tracers. However, the change from assimilation does in some case worsen the representation of propane in the model , showing that as with the increase in the NH/SH OH bias from assimilation the chemistry of the OH radical needs to be considered at the assimilation step.

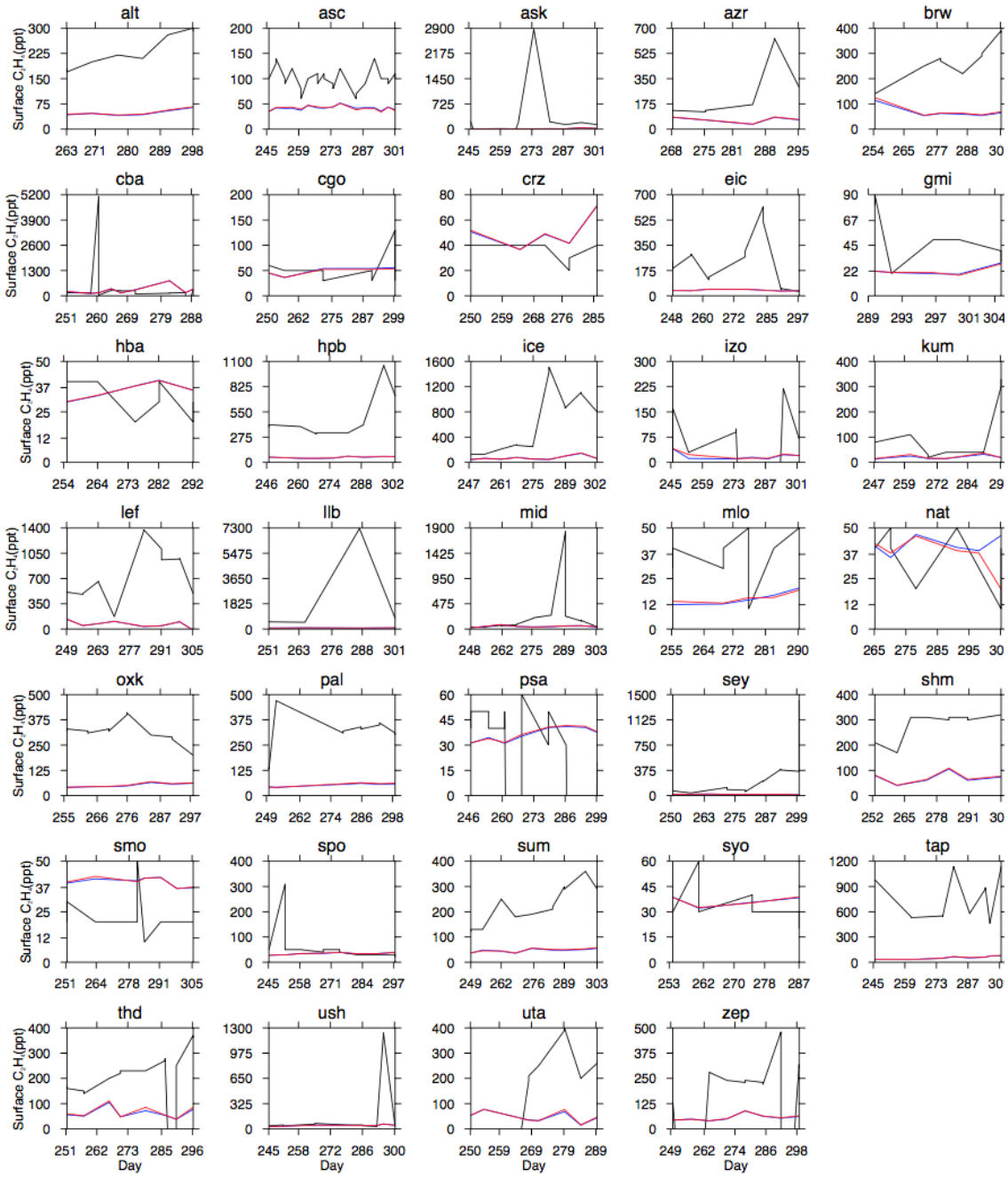

Figure 6.21 Comparison of propane concentrations from individual surface NOAA flask sites to C-IFS. (black) is observations, (red) is AN_MET and (blue) is AN_METCOM.

6.3.6 Nitric acid

The impact of composition assimilation in C-IFS on modelled nitric acid (HNO_3) is shown in Figure 6.22 for September and Figure 6.23 for October 2012. The changes from assimilation are positively correlated to NO_2 increments relating to biases in NO_2 emissions. As HNO_3 is the main product of NO_x oxidation increased emissions of NO_2 lead to increases in HNO_3. This leads to larger changes in HNO_3 relative to species solely impacted by OH changes, such as propane in Section 6.3.5. The large changes in HNO_3 also help show that the assimilation of NO_2 is significantly increasing urban and fires sources of NO_2, which is often difficult to see in NO_2 global concentrations due its short lifetime. Over the Arabian Peninsula the negative NO_2 increments lead to negative changes in HNO_3 concentrations. This is line with an increased up-take of HNO_3 due to more dust, however this uptake is not included in the model and HNO_3 concentrations are decreasing due to lower NO_2 concentrations.

That HNO_3 shows significant increase in concentration from OMI NO_2 assimilation near the fire source regions suggests that other important NO_y species will also be impacted. PAN is rapidly formed from NO_2 and oxygenated VOCs and is a reservoir for NO_2 allowing it to be reformed down-wind. If increases in NO_2 assimilation also increases PAN by a similar amount as HNO_3 then O_3 concentrations downwind of fire plumes will also likely be increased by assimilation.

6.4 AOD assimilation

The impact of MODIS AOD assimilation is shown in Figure 6.24. Compared to MODIS AOD in Figure 6.24b, C-IFS underestimates AOD over fire-dominated regions in South America, Indonesia and Sub-Saharan Africa and over urban regions in both India and China. Additionally, background AOD over the oceans is slightly larger in the observations than the standalone model. The AN_METCOM analysis field with MODIS AOD assimilated is shown in Figure 6.24c and displays increases in concentrations, providing a more accurate model representation while providing global coverage. Despite the improvement compared to MODIS, AN_METCOM shows larger concentrations of AOD compared to MODIS AOD directly over fire sources while still underestimating

concentrations over India and China. These differences in AOD between MODIS and AN_METCOM are most likely caused by the use of total aerosol mass as the control variable in AOD assimilation. This means that the assumed optical properties used to calculate AOD are used in both the calculation of the total mass column as well as the subsequent calculation of AOD and if inaccurate could add a source of bias.

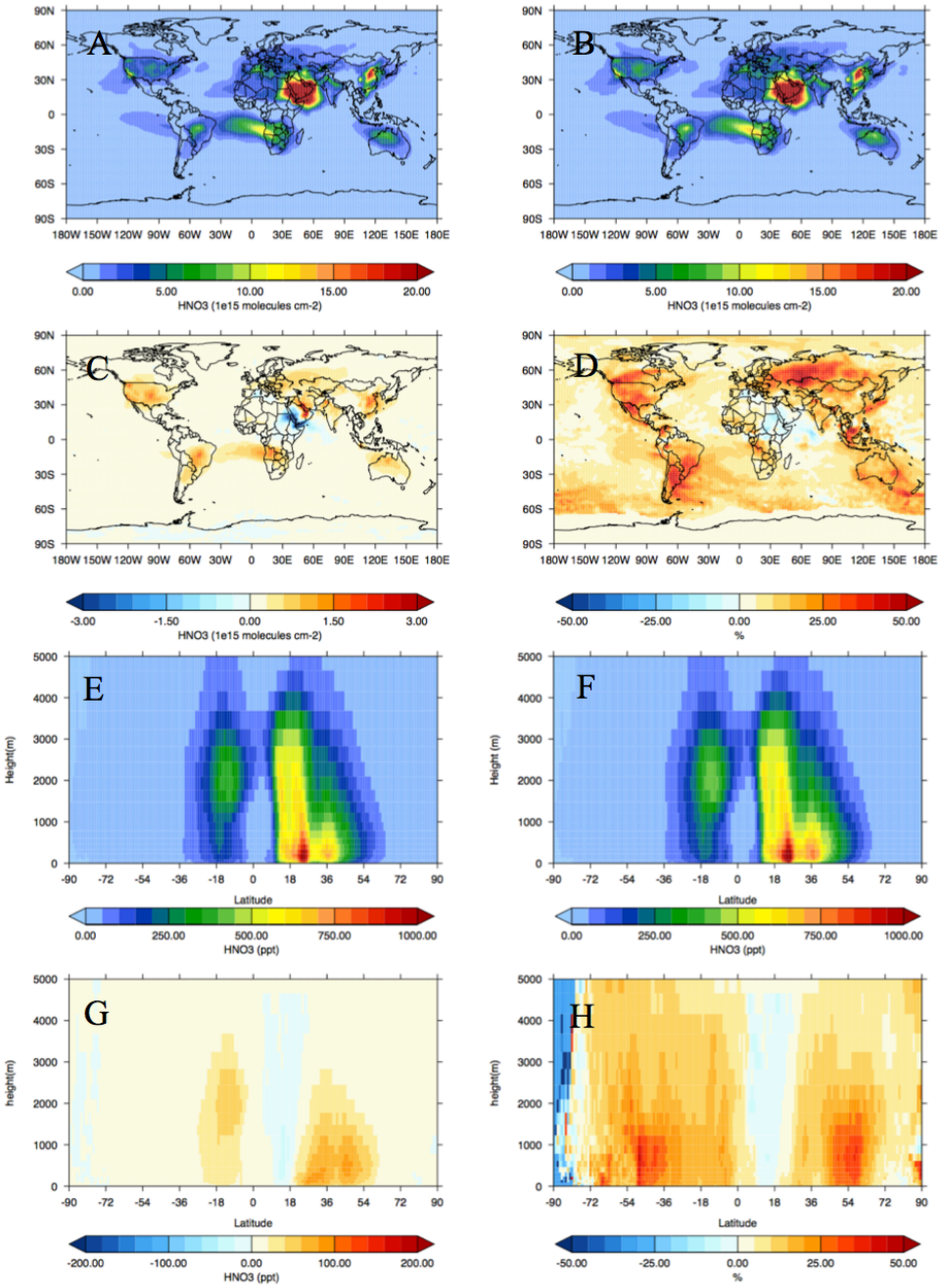

Figure 6.22 Impact of assimilation on HNO_3 total columns and zonal means for September 2012. (a) AN_METCOM total column ($\times 10^{15}$ molec. cm^{-2}). (b) AN_MET HNO_3 total column ($\times 10^{15}$ molec. cm^{-2}). (e) AN_MET OH zonal mean (ppt). (f) AN_METCOM HNO_3 zonal mean (ppt). (c, g) Difference AN_METCOM – AN_MET, i.e. the average impact of assimilation at each 6-hour timestep. (d, h) The percentage change from assimilation at each 6 hour timestep.

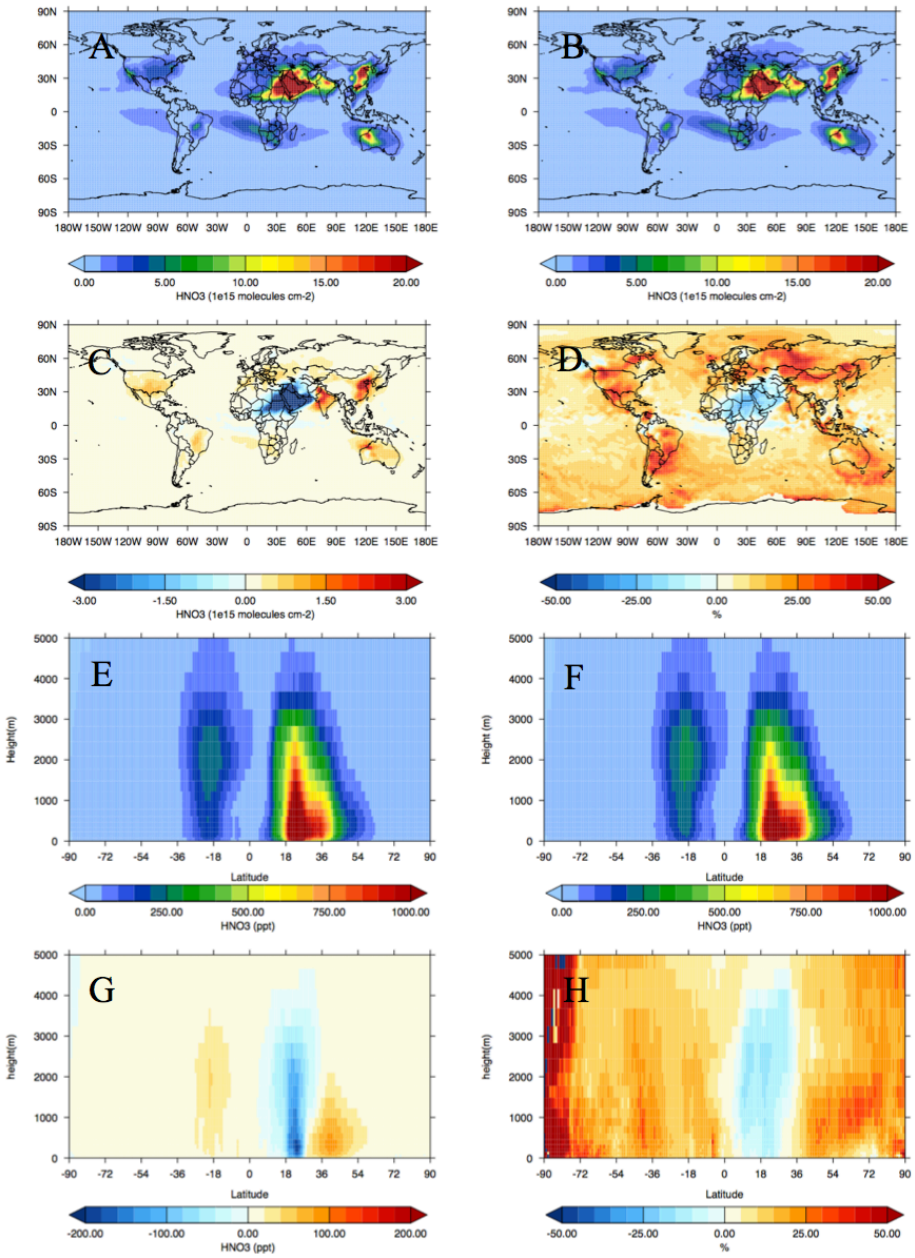

Figure 6.23 As Figure 6.22 but for October 2012

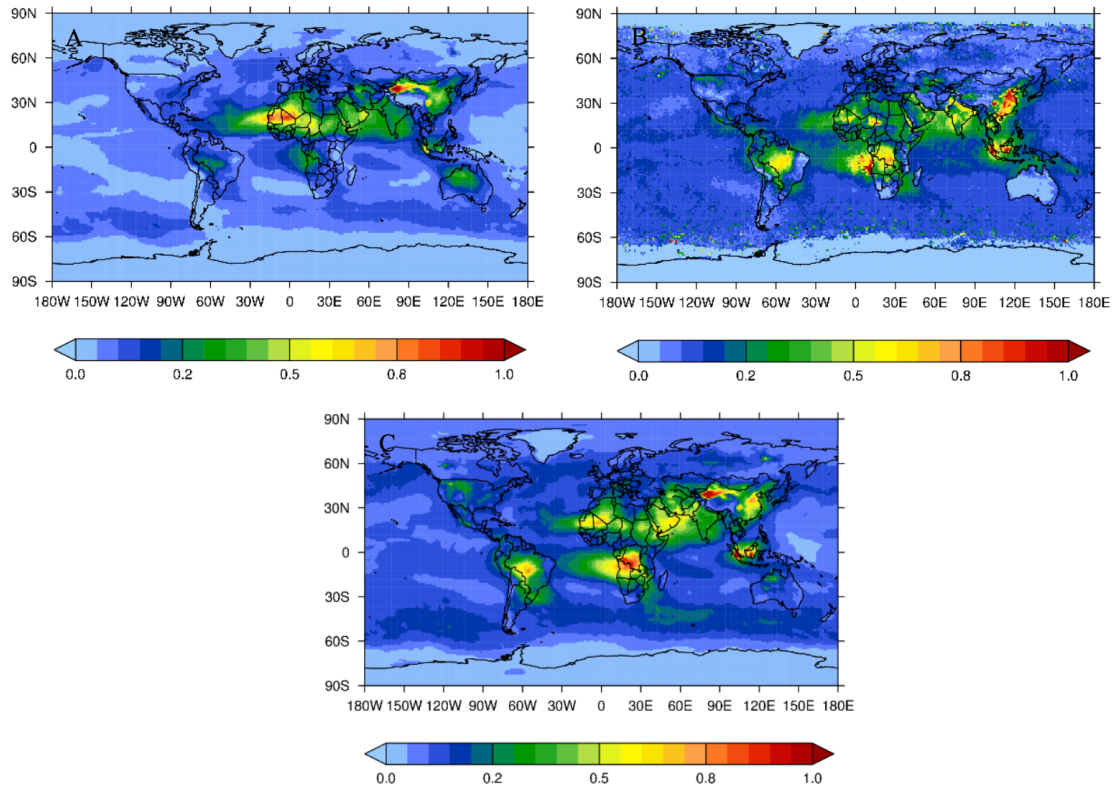

Figure 6.24 Impact of AOD assimilation in C-IFS on average AOD fields for September - October 2012. (a) Simulation FOR_NSCF. (b) MODIS retrievals. (c) Simulation AN_METCOM AOD.

6.4.1 Impact of fires

The impact of fire emissions on carbonaceous aerosol concentrations is shown in Figure 6.25 for Black Carbon (BC) and Figure 6.26 for Organic Matter (OM), after GFAS aerosol emissions have been scaled by 3.4. Fire emissions dominate global concentrations of carbonaceous aerosol during the tropical fire season, as concentrations in the tropics are larger than urban emissions in the Northern Hemisphere. The two different carbonaceous aerosol types in the model are generally co-located as they both have the same fixed ageing time between their hydrophilic and hydrophobic parts of 1.16 days. Elevated concentrations from tropical fire emissions can be seen throughout the tropics and the Southern hemisphere.

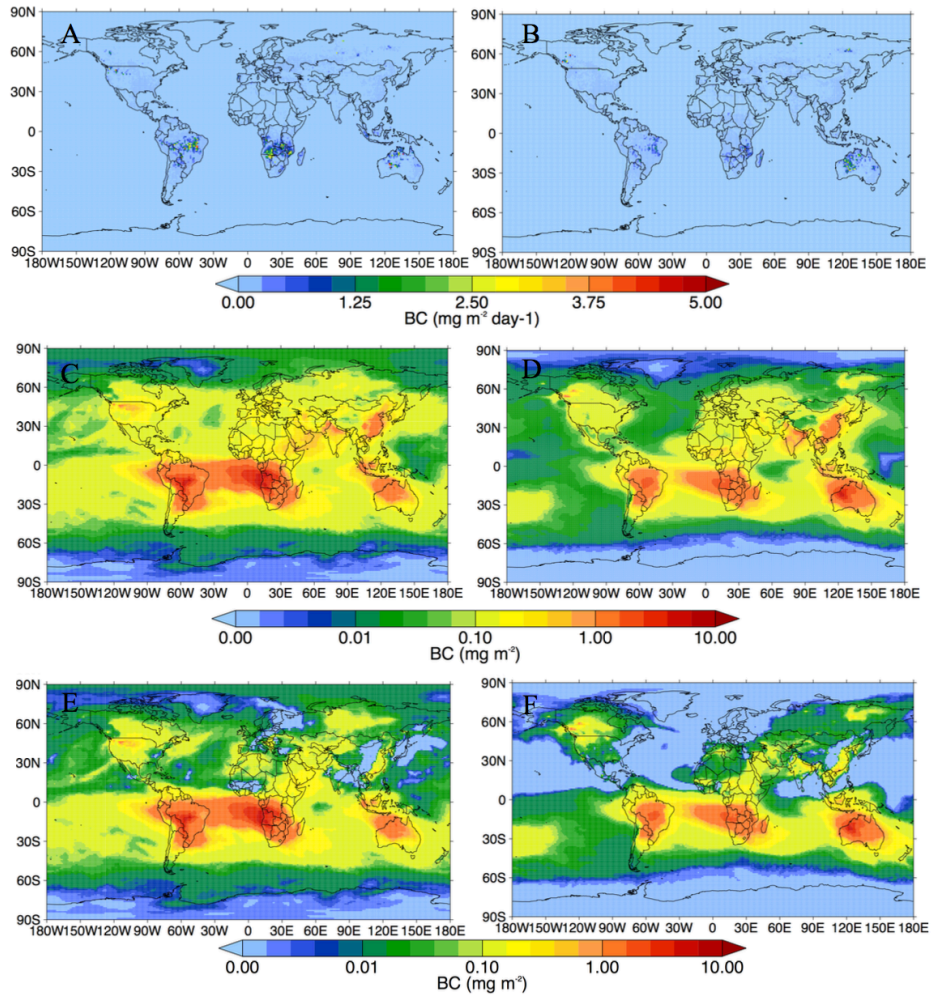

Figure 6.25 The impact of fires on C-IFS simulated BC tropospheric column. The left panels show average results for September 2012 and the right panels show equivalent results for October 2012. (a, b) GFAS BC (mg m^{-2} day^{-1}) flux. (c, d) BC column concentrations for AN_MET (mg m^{-2}). (e, f) Impact of fires on BC tropospheric concentrations (AN_MET –FOR_NBB) (mg m^{-2}).

Global impact of assimilation

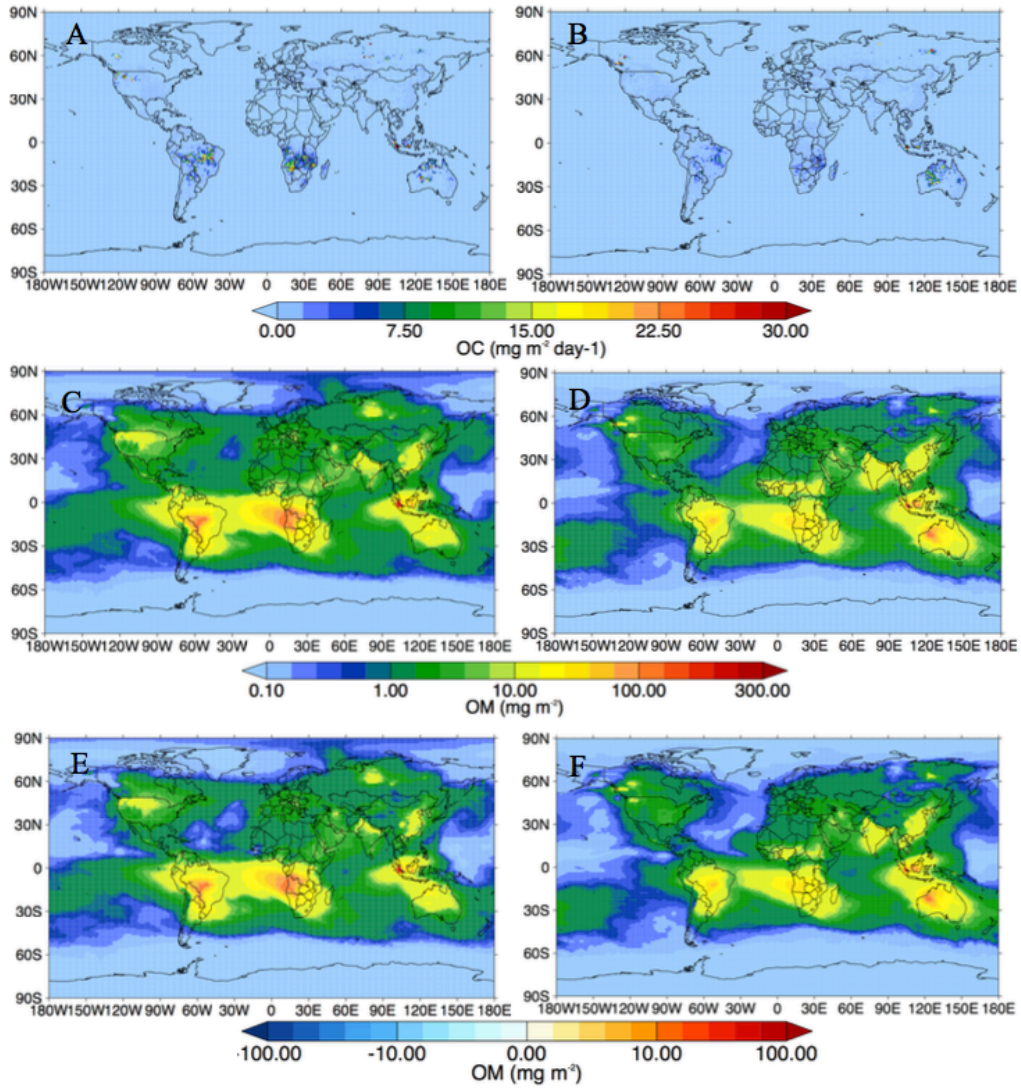

Figure 6.26 The impact of fires on C-IFS simulated OM tropospheric column. The left panels show average results for September 2012 and the right panels show equivalent results October 2012. (a, b) GFAS OC (mg m^{-2} day^{-1}) flux. (c, d) OM column concentrations for AN_MET (mg m^{-2}). (e, f) Impact of fires on BC tropospheric concentrations (AN_MET –FOR_NBB) (mg m^{-2}).

Figure 6.27 shows the impact of the GFAS scaling factor on mean global values of AOD, OMAOD and BCAOD. Figure 6.27a, d and g show concentrations from the C-IFS experiment FOR_NSCF, the standard C-IFS run, which shows a large underestimation compared to the analysis product AN_METCOM (Figure 6.27c, f and i), This is comparable to the results from AOD comparisons during both the original

implementation of GFAS aerosol emissions (J. W. Kaiser et al., 2012) and in an earlier C-IFS/SAMBBA evaluation (Rémy et al., 2016), which compared the impact on BCAOD and OMAOD. Figure 6.27b, e and h show aerosol concentrations from the C-IFS experiment FOR where GFAS carbonaceous aerosols emissions are increased by a factor of 3.4, as is standard in C-IFS and other models using GFAS. This change has a significant impact on global concentrations and generally improves the comparison to AN_METCOM, although concentrations are now larger than that seen in AN_METCOM, over the main tropical fire-regions while remote regions are still underestimated.

Table 6.3 shows the ratio between the AN_METCOM and FOR_NSCF for numerous different carbonaceous aerosol metrics. Generally, the larger ratios (biases) are seen near the tropical source regions (South America, Southern Africa and Tropical Asia). The global AODBC + AODOM (AODBB) bias is larger than that seen in Kaiser et al., (2012) (3.4) for July-December 2010, potentially due to the sole focus on the tropical fire season in this study. Biases for all regions were larger than that shown in Kaiser et al., (2012), with the most significant change from Kaiser et al., (2012) seen away from the main fires in North America and the smallest close to fires in South America.

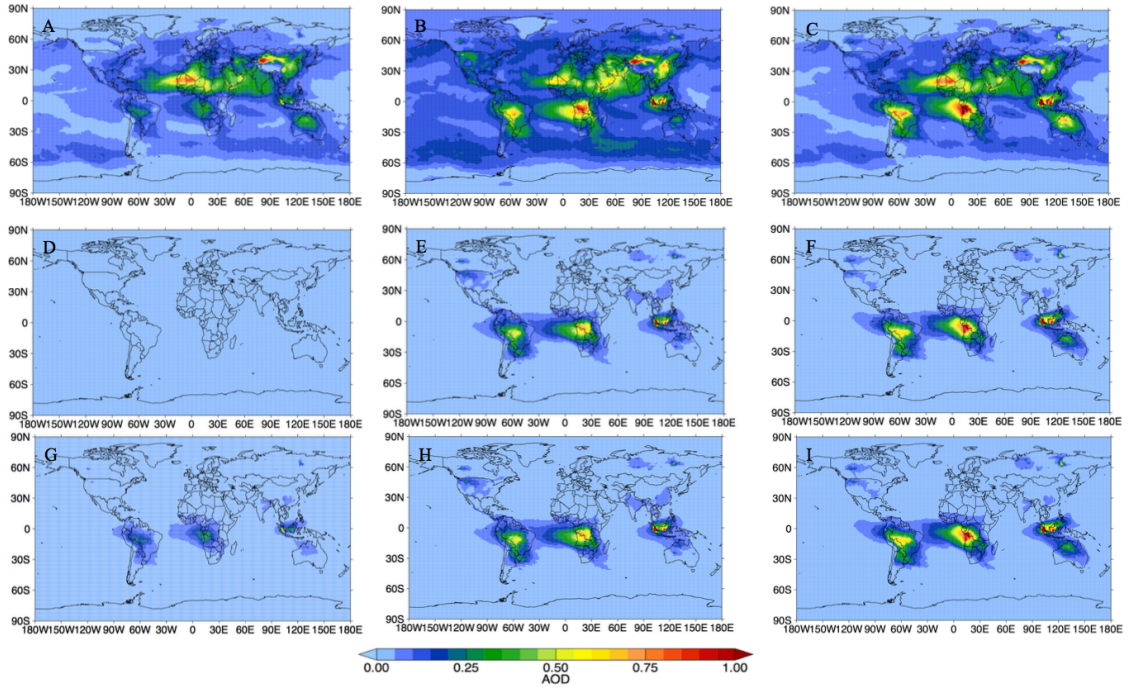

Figure 6.27 Impact of GFAS scaling factor on AODs for September-October 2012. First row (a, d, e) is experiment FOR_NSCF without unmodified GFAS emissions, second row (d, e, f) is from experiment AN_MET and the third row (g, h, i) is from AN_METCOM). The first column (a, b, b) is AOD, the second column (d, e, f) is BCAOD and the third column (g, h, i) is OMAOD.

Significant global differences from this scaling factor is seen for BCAOD (14.8) and OM AOD (2.46) which was not investigated in Kaiser et al., (2012), but has previously been suggested in Rémy et al., (2016), although a much larger BCAOD bias is seen in this study. This implies that the biases are different for OM and BC, either relating to their separate emission factors or loss processes. Furthermore, while the bias for the OM burden is similar to OMAOD, the BC burden bias is significantly smaller than BCAOD suggesting that assumed optical properties used to calculate the BCAOD are contributing to the bias. The relative size of the bias between BC and BCAOD for different regions generally remains the same suggesting this bias is constant and systematic. The spatial bias of both BC and OM are similar, suggesting that the ratio of the two remains the same after emissions and that inaccurate emission factors are responsive for less modelled BC compared to reality than OM.

Global impact of assimilation

Region	AOD	BBAOD	BCAOD	OMAOD	BC	OM	BBAOD Kaiser (2012)
Global	1.65	4.15	14.83	2.46	3.99	2.78	3.40
NAme	1.99	4.48	14.59	2.65	4.34	3.06	2.20
CAme	1.24	3.50	17.05	1.95	3.26	2.33	-
SAme	2.41	4.26	17.48	2.42	3.89	2.56	4.10
Euro	1.38	3.20	5.47	2.26	2.47	2.59	2.40
NHAF	1.01	2.68	10.11	1.54	2.32	1.68	-
SHAF	2.42	4.98	16.48	2.93	4.09	3.32	-
NASI	1.36	3.39	5.64	2.42	2.75	2.74	2.30
SASI	1.32	2.46	5.84	1.55	1.79	1.67	3.00
TASI	1.77	4.48	34.28	2.40	3.10	2.53	-
AUST	1.19	2.92	8.82	1.75	2.76	1.81	-

Table 6.3 Ratio of different aerosol metrics between experiment FOR_NSCF and AN_METCOM.

6.4.2 Impact of assimilation on carbonaceous aerosol mass

Figure 6.28 and Figure 6.29 show the difference between AN_METCOM and AN_MET (i.e. the difference from assimilation) as well as the analysis increments for both BC and OM respectively. AN_METCOM, although assimilating MODIS AOD has aerosol GFAS emissions scaled by 3.4, this is theoretically done to provide a more accurate model field for assimilation. However, negative analysis increments are calculated over tropical fire emission source regions for both OM and BC, suggesting that aerosol emissions are too large in C-IFS when this scaling factor is applied. This is despite larger bias than 3.4 seen in Table 6.3 over tropical fire source regions. Away from the near-fire sources, particularly over the Southern Atlantic and Pacific, the majority of the increments are large and positive, suggesting FOR_NSCF under-estimates these concentrations. If the model bias seen in Table 6.3 was solely down to the emissions we would expect an accurate 'scaling factor' to improve concentrations across the whole globe and a too large

'scaling factor' to provide a consistent bias. The positive increments away from the fire sources and the negative increments close to the fire sources suggests that fire emissions are not the only source of model uncertainty and it is likely that transport, aerosol ageing and the eventual deposition of these aerosol species is contributing to the model bias and the under-estimation of FOR_NSCF compared to AN_METCOM.

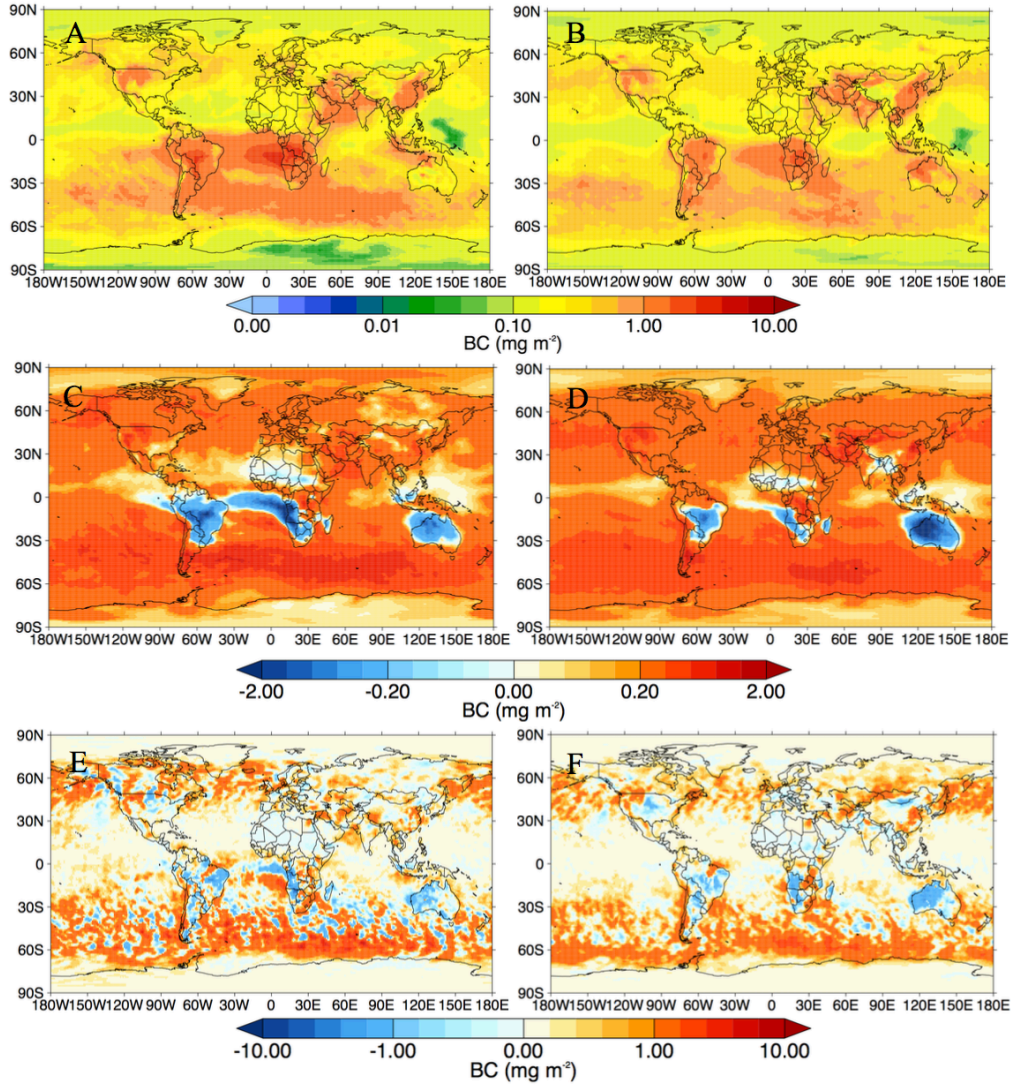

Figure 6.28 The impact of assimilation on C-IFS simulated BC tropospheric column. The left panels show average results for September 2012 and the right panels show equivalent results for October 2012. (a, b) BC column concentrations for AN_METCOM (mg m^{-2}). Panels (c, d) show AN_METCOM – AN_MET, i.e. the average impact of assimilation at each 6-hour timestep. Panels (e, f) show the average BC analysis increments from simulation AN_METCOM, for each 12-hour analysis step.

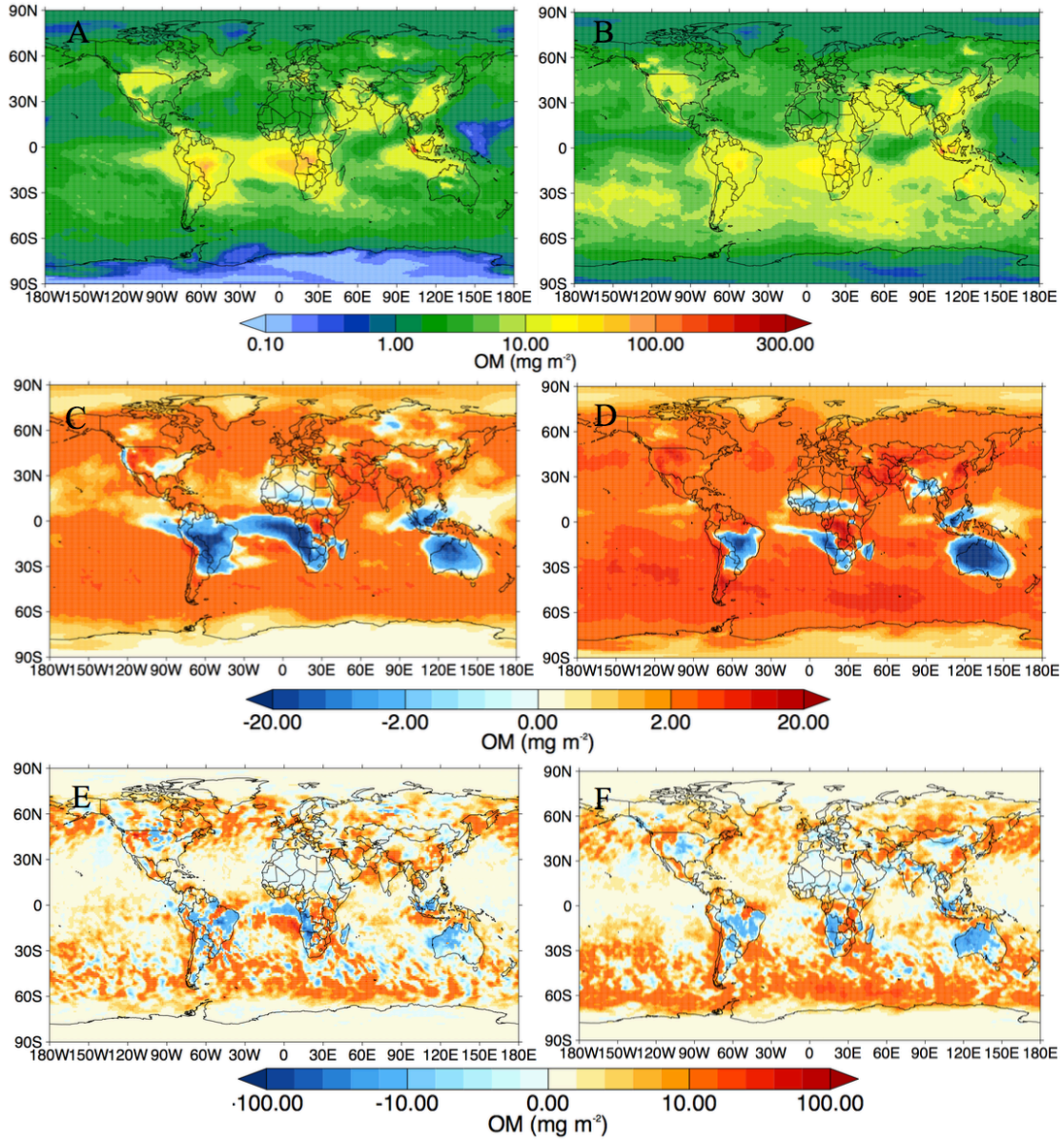

Figure 6.29 The impact of assimilation on C-IFS simulated BC tropospheric column. The left panels show average results for September 2012 and the right panels show equivalent results for October 2012. (a, b) BC column concentrations for AN_METCOM (mg m^{-2}). Panels (c, d) show AN_METCOM – AN_MET, i.e. the average impact of assimilation at each 6-hour timestep. Panels (e, f) show the average BC analysis increments from simulation AN_METCOM, for each 12-hour analysis step.

6.4.3 Impact of AOD assimilation on the gas phase

The additional impact of AOD assimilation on O_3 concentrations is shown in Figure 6.30. Compared to the assimilation without the AOD impact in Figure 6.4 a much more significant negative change is seen over the Arabian Peninsula. Similar changes from the AOD assimilation are also seen for OH and NO_2 and imply that the increase in AOD over this region, is leading to a decrease in concentration of these species. As the assimilation of AOD only impacts the incoming radiation the changes seen in O_3, OH and NO_2 due to increased dust concentrations leading to the uptake of more HNO_3 into the nitrate aerosol phase.

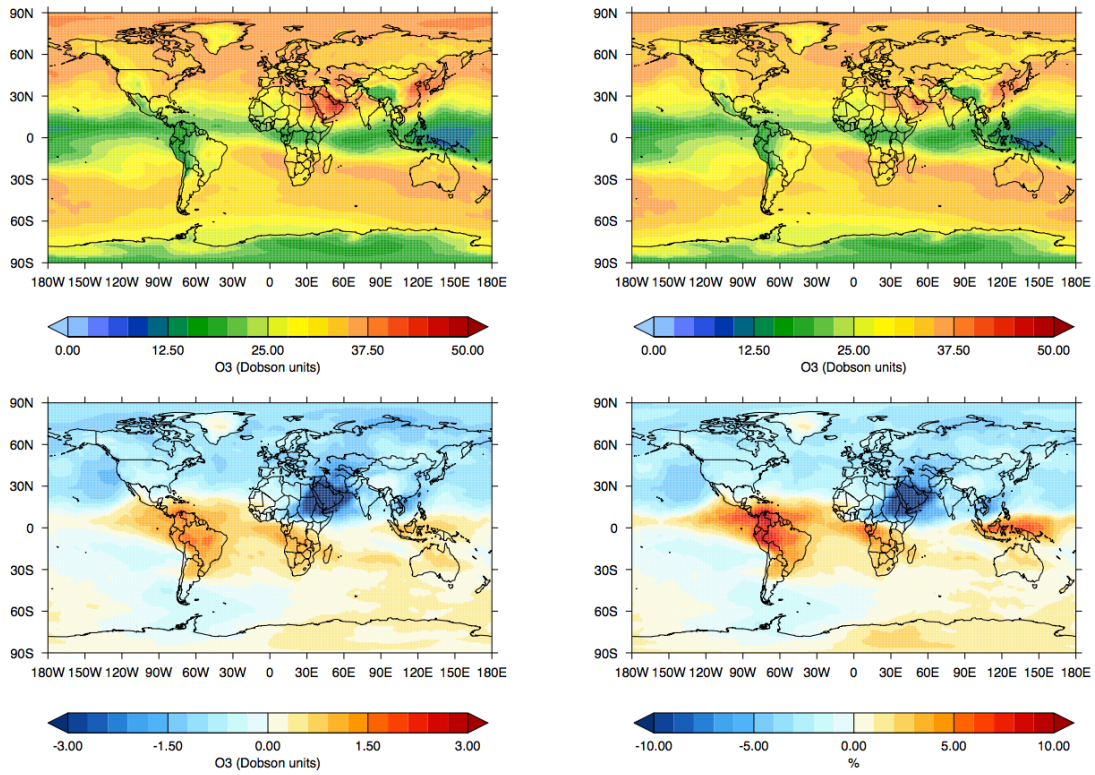

Figure 6.30 Impact of assimilation, including AOD, on O_3 total columns and zonal means for September and October 2012. (a) AN_AER O_3 total column (DU). (b) AN_MET O_3 total column (DU). (c) Difference AN_METCOM – AN_MET, i.e. the average impact of assimilation at each 6-hour timestep. (d) The percentage change from assimilation at each 6-hour timestep.

6.5 Summary

The impact of composition assimilation on both gas and aerosol species for September-October 2012, along with the skill of the model to capture global tropical fires and other emission sources, has been assessed. This has been done by comparing the free-running model to the assimilated datasets as well as to independent observations.

C-IFS suggests a significant impact of biomass burning emissions on tropical O_3 concentrations during the tropical fire seasons, with a 20-30% increase in the tropospheric column over fire source regions in South America, Sub-Saharan Africa and Australia. The assimilation increases concentrations of O_3 in these fire-dominated regions, while decreasing concentrations in the northern latitudes, which are dominated by urban emissions. The assimilation of MLS has a significant impact, with much smaller AN_METCOM-AN_MET differences in September compared to October. This indicates the importance of accounting for, and removing, the stratospheric O_3 contribution to the total column in improving tropospheric O_3 concentrations. Despite the decreases in the tropics and increases in the northern latitudes, in comparison to the RAL O_3 partial column C-IFS O_3 is still significantly biased in these regions. This suggests that the assimilation of a separate tropospheric column into C-IFS would significantly impact the changes seen by assimilation. Additionally, the implication of an extra negative bias over the tropical fire regions is that fire emissions have an even larger impact on O_3 concentrations than that suggested by C-IFS.

There are only small changes from assimilation on CO concentrations, with the over-estimation of peat fires over Indonesia being the most significant change. Significant changes in the AN_METCOM-AN_MET difference from September and October differences show that the MLS assimilation during October also impacted CO concentrations, with more significant increases over tropical land masses despite lower fire emissions. The increase in CO concentrations over North Africa is not seen in the CO analysis increments so suggests an impact from the assimilation of other species, this region corresponds to decreases in both NO_2 and O_3 assimilation suggesting that the loss of these species is having a positive impact on CO lifetime in this region.

Global impact of assimilation

The largest analysis increments are seen in NO_x concentrations mostly due to OMI NO_2 assimilation, as the assimilation both corrects for the large underestimation of NO_x and has to constantly correct NO_x concentration due to its short lifetime, unlike other species whose increments decrease over time. There is also evidence of OMI NO_2 assimilation improving the O_3 field as changes in O_3 concentrations are seen over regions with large NO_2 increments, before the assimilation of MLS in October. In comparison to OMI NO_2 emission inversion in (Miyazaki et al., 2012) changes to global concentrations of NO_2 are small despite the large analysis increments this may be due to the short-term nature of this study but could imply that correcting the emissions directly for short-lived species short as NO_2 does a better job at correcting global concentrations as more information is retained in the next analysis time-step. Negative analysis increments for NO_2 were seen over the Arabian Peninsula, previous studies have indicated the lifetime of modelled NO_x. AOD assimilation significantly increases aerosol concentrations in this region and the inclusion of AOD assimilation impacting the gas phase decreases concentrations of the species further. This implies that the positive bias in the model is due to the lower AOD in the model and despite the lack of conversion of HNO_3 to nitrate aerosol in C-IFS the background error covariance matrix reduces NO_2 when AOD increases over Arabian Peninsula.

Changes to the OH field from assimilation were seen between AN_MET and AN_METCOM despite OH not being included in the state vector, with changes up to 10% of the total column. Changes in OH concentrations are generally positively correlated to changes in O_3 concentrations which are, in turn, impacted by NO_2 concentrations in September. This leads to decreases in concentrations over North Africa and the ocean and increased concentrations over other land masses. With these changes the NH/SH ratio actually worsens in comparison to the methylchloroform-derived observations, which is the opposite to the composition assimilation study Miyazaki et al., 2015, which included OH in the state vector. Changes in OH concentrations from assimilation consequently impacted concentrations of non-assimilated species whose lifetime is dependent on OH. Changes from assimilation of up to 5% were seen from propane, although these changes are small compared to the bias in C-IFS compared to NOAA flask-site observations. Larger changes were seen from assimilation on HNO_3 due

to the significant changes from NO_2 assimilation and the rapid reaction of NO_2 with OH that forms nitric acid.

Comparing C-IFS model runs with and without assimilated MODIS AOD result in a biomass burning AOD (OMAOD + BCAOD) bias larger (4.2) than that found in Kaiser et al., (2012) due to the large number of fires during September-October. Globally, the ×3.4 bias was used to recommend a scaling factor for GFAS fire emissions, assuming the bias was solely down to biomass burning emissions. Comparing BCAOD and OMAOD separately suggests that different scaling factors should be applied to each component of BBA, with BC underestimated to a greater extent than OM. Unlike for OM, BCAOD bias is a lot larger than that found for the BC burden, implying that the assumed aerosol optical properties used to calculate AODs from mass concentrations over-estimate the impact of BC. Larger model biases for both OM and BC were found closer to fire emission sources and the relative bias between the two-species remained the same globally.

The assimilation of MODIS AOD actually decreases carbonaceous aerosol concentrations directly over tropical fire emissions, despite the larger biases between the model run without scaling factor and AN_METCOM over these regions. These decreases and negative increments show that the assimilation is working against the increase in emissions implemented in Kaiser et al., (2012) and that at the source the aerosol fire emissions are not as low as previously suggested. Significant positive increments and changes from assimilation are seen away from these fire source regions, correcting for the known model-underestimation of black carbon over the Southern Atlantic and Pacific. The fact that the scaling of emissions leads too large concentrations directly over the fire intensive regions but does not correct for the bias in the remote regions suggests that the source of this bias is a too rapid aerosol loss scheme rather than underestimated aerosol fire emissions.

7 Conclusions

7.1 Summary of results

The overall objective of this thesis was to investigate the impact of fire emissions on atmospheric composition, during the 2012 tropical dry season, using reactive gas and aerosol assimilation. This work represents the first application of the trace gas observations from the SAMBBA aircraft campaign, to complement the observed aerosol fields. The main modelling tool employed has been the ECMWF Composition – Integrated Forecast System (C-IFS). This is a large model with a state-of-the-art representation of atmospheric chemistry coupled to a detailed data assimilation system. The model underpins the ECMWF Copernicus Atmospheric Monitoring System (CAMS) and is used to produce daily global analyses of atmospheric composition. It is a complex modelling system, and in that sense limited in the sensitivity experiments that can be performed. However, given its pre-eminent role in current and future studies of atmospheric composition, it is important to evaluate it against independent observations.

As discussed in Chapter 2 there are large uncertainties associated with the processes which are important in determining the total impact of fires on the earth system. Fire emissions are major source of this uncertainty due to their large spatial and temporal variability. C-IFS uses satellite-based GFAS fire emissions in conjunction with assimilated composition datasets to try and compensate for this bias and produce a 'best estimate' of modelled fire impacts, for global atmospheric composition forecasts. The skill of this system in fire-dominated regions is uncertain and needs to be evaluated against independent observations which, in the case of this study, includes the observations from the SAMBBA campaign. Through this evaluation we can determine the skill of the background model and the assimilated data-sets and determine impacts of emission bias, injection height and model lifetime on O_3 and aerosol concentrations.

The first aim of the thesis (Chapter 1) was to investigate the impact of fire emissions on ozone and aerosol concentrations. Simulations with C-IFS show that on average throughout the lowest 6 km fires contributed 4.53 ppb of O_3 (9% of total) in South

America, 5.68 ppb in Australia (11%) and 7.65 ppb in Sub-Saharan Africa (16%). There is, however, a significantly higher contribution closer to fires with an average increase of 11.3 ppb (28% of total) over the SAMBBA domain. Surface concentrations are smaller (15 ppb) but show a larger contribution of fire emissions (51%), although they remain significantly lower than the 40 ppb threshold known to damage plant and human health. Overall, for the period studied, 4% of the total tropospheric O_3 column is from biomass burning, which compares to the 4-5% predicted by the Global Modelling Initiative CTM in Ziemke et al., (2009) and 3.5% calculated from emissions in Jaffe and Wigder, (2012). These values are annual estimates while the calculated C-IFS estimates are for the tropical dry season suggesting O_3 is slightly low compared to other estimates.

For carbonaceous aerosol concentrations C-IFS suggests that during the tropical season fires contribute 0.65 mg m^{-2} of OM (64% of total) and 0.06 mg m^{-2} of BC (49% of total). This figure for BC is similar to the 40% contribution determined by bottom-up inventories (T. C. Bond et al., 2013). If the GFAS scaling factor is used the contribution rises to 89% for BC and 95% for OM. The relative contribution of BC to the total aerosol mass is 9.6% for Sub-Saharan Africa, showing a similar contribution to HADGEM3, but an underestimation compared to the 12% observed over Africa during the DABEX campaign (Johnson et al., 2016). Compared to SAMBBA observations C-IFS predicts a 7.6% contribution of BC over the western region and a 9.1% contribution of the eastern region, this compares to observed values of 8.9% and 5.1% for the eastern and western region, respectively. This suggests that the model would underestimate the amount of absorbing aerosol particles over Africa and overestimate the amount over the deforestation region in South America.

Carbon monoxide, generally used as a tracer of biomass burning, in C-IFS generally compares well to SAMBBA observations. The assimilation of CO shows only small positive increments over tropical fires in South America, Sub-Saharan Africa and Australia, indicating a small bias in comparison to MOPITT. Large negative increments are, however, seen over peat fires in Indonesia, implying that at least for the 2012 fire season that these fires are over-estimated in C-IFS.

C-IFS model runs do not capture the vertical structure of CO SAMBBA observations due to the lack of prescribed injection height in the simulations, with larger fires showing

overestimation near the surface and underestimation at the mean height of maximum injection. This work has also provided evidence of small fires in the deforestation region being under-estimated, as evidenced by CO and other tracers in the GFAS emissions. This is most likely due to either the regional dry-matter conversion factor estimated from GFED or a blocking of FRP measurements by forest canopies. The relatively small C-IFS analysis increments globally, that are similar to those seen over the Amazon, suggest that the FRP approach in GFAS is generally capturing most fires in savannah-dominated regions, where fires are generally larger.

Previous SAMBBA studies have focussed on the aerosol measurements, with little attention on observations of the gas-phase species apart from CO. O_3 concentrations during the SAMBBA flight campaign were highly variable, depending on proximity to fires, with near-surface concentrations in the background up to ~30 ppb lower than that observed near-plumes. C-IFS sensitivity simulations show an increase in O_3 concentrations from fire emissions but show a persistent under-estimation compared to both SAMBBA observations and OMI partial column (0-6 km) throughout the Amazon. This bias suggests a larger contribution of fires to O_3 concentrations in the Amazon than that predicted by C-IFS, which is further supported by the global increase in O_3 concentrations over the tropics when both MLS and OMI are assimilated into C-IFS. Despite these increases, C-IFS still underestimates SAMBBA observations in the Amazon and the OMI partial column (0-6 km) over both South America and Sub-Saharan Africa, by around 5-10 DU, implying that the assimilation of these measurements do not fully constrain O_3. That O_3 enhancements from fires are still underestimated after assimilation highlights the potential benefits of assimilating a tropospheric column O_3 measurement into C-IFS.

This O_3 bias appears to be predominantly caused by a significant underestimation of NO_x in the model compared to SAMBBA observations. As CO is relatively well captured by the model the bias is not likely to be due to missing fires in the GFAS inventory. However, due to its short life-time NO_x is more severely impacted by the lack of parameterised injection height in the model. Sensitivity studies with the TOMCAT 3-D model reveal how a prescribed injection height can improve model representation of both NO_x and O_3 compared to both SAMBBA and OMI. The fact that a bias still exists after an injection

height is specified, and for a separate experiment when emissions are scaled by 3.4, suggests that the total NO_x flux is still too low. This implies that published emission factors for both tropical and savannah fires in Andreae and Merlet (2001) are most likely too small. Furthermore, the bias in NO_2 concentrations in the free troposphere over the Amazon western region suggests an impact of PAN that is not captured by the model. These increases in NO_x are also associated with large observed O_3 concentrations not captured by the model, leading to a larger C-IFS O_3 bias in the free-troposphere.

The assimilation of OMI NO_2 improves the modelled representation of NO_2, particularly in the eastern region indicating that NO_2 fields are improved by assimilation even when the emissions are not adjusted. Additionally, before the assimilation of MLS stratospheric ozone in October the majority of O_3 increases in the tropics are correlated with NO_2 increases, implying that NO_2 assimilation does improve O_3 model skill. Despite these increases, C-IFS still shows essentially no NO_x in the free troposphere above the western deforestation region even after OMI assimilation, this is despite observations suggesting concentrations between 0.2 and 0.5 ppb. This shows how the assimilation struggles to increase concentrations when the model predicts concentrations close to zero and is potentially the cause of the C-IFS bias compared to the OMI total column in this region. Additionally, as this bias is predominantly in the free-troposphere the impact of the total column assimilation is limited by the dependence on the model's vertical distribution. Globally, the assimilation of NO_2 increases concentrations over fire-dominated regions in Australia and South America, but not Sub-Saharan Africa. This difference is due to the distinct longitudinal differences from assimilation seen in the analysis increments where increases and decreases in NO_2 concentrations are seen which are not consistent with OMI observations. This is likely due to incorrect background error covariance matrices for the assimilation of OMI NO_2.

A second aim of the thesis was to investigate the impact of assimilation on non-assimilated chemical species, particularly with reference to the DAS-CHASER assimilation system which includes these additionally species in the state vector. The chemical scheme used in C-IFS does react to the changes in assimilation, which is illustrated, for example, by increases in OH where O_3 increases. However, as this impact is solely after the analysis step, the changes in non-assimilated species only occur after

an adjustment in concentrations and not because of the adjustment. This leads to changes to the OH field which actually increase the OH NH/SH bias compared to observations, in contrast to assimilation experiments which include OH in the state vector. Changes to organic chemical species, whose lifetimes are dependent on OH, from assimilation are also small in comparison to the bias seen between C-IFS and observations. Changes in HNO_3 after assimilation are larger than the organic species due to the short lifetime of NO_2 and help highlight how NO_2 concentrations are being increased by OMI assimilation. Also, when impacts from AOD assimilation on the radiative budget are included in the analysis, decreases in O_3, NO_2 and OH concentrations are seen over the Arabian Peninsula suggesting changes in photochemical loss due to an increase in aerosol optical depth (AOD).

The third research aim addresses how assimilation of AOD affects simulated aerosol properties. A significant number of satellite-based fire emission inventories use a so-called scaling factor to reproduce observations of AOD. In comparisons to SAMBBA observations in the Amazon, BC and OM mass concentrations with the suggested ×3.4 scaled GFAS emissions over-estimate observed concentrations. Interestingly, the non-scaled emissions provide a more accurate comparison. The assimilation of AOD also works against this scaling factor, causing negative analysis increments in BC and OM over South America, Sub-Saharan Africa and Australia, while increasing concentrations in the remote regions, implying an impact of aerosol lifetime on model bias. The original GFAS scaling-factor was calculated by establishing the difference between black carbon AOD (BCAOD) and organic matter AOD (OMAOD) before and after MODIS AOD assimilation in C-IFS. Work in this thesis has shown that BCAOD and OMAOD have different biases after AOD assimilation, and that the bias for BCAOD is significantly larger than that for BC total burden. This implies that the size of the scaling factor was exaggerated by the BCAOD calculation with assumed optical properties. Additionally, the bias between the un-scaled emission run and the SAMBBA observations is smaller still than the bias between the OM and BC burden before and after AOD is assimilated, indicating the bias for C-IFS is different compared to AOD measurements and mass concentration measurements. While the assimilation of AOD does significantly improve model representation of BC and OM, particularly compared to the scaled emission experiment, the use of the scaling factors in the run with AOD assimilation often leads to

an overestimation compared to some SAMBBA observations. This is also the most likely reason why there is a larger global bias between the run with assimilation and the run without scaled emissions compared to that seen in Kaiser et al. (2012).

Evaluation by the SAMBBA observations also suggest a different model bias for organic matter and black carbon. Organic matter is under-estimated to a greater extent than BC over deforestation fires during the dry season. This might be due to calculation of OM from OC, which is on the low end of the scale compared to other observations. This is concurrent with previous studies of the make-up of aerosol particles from SAMBBA which showed high contribution of sulfate aerosol in the make-up of aerosol particles over the deforestation region. During the wet-to-dry transition modelled concentrations of OM compare better than BC and the OM/BC ratio changes from being biased towards BC to being biased towards OM. This suggests that BC lifetime in the model is too large compared to reality and if OM is scaled from OC correctly, OM lifetime may also be too large. This is the opposite to the positive increments seen for OM and BC in the analysis away from the main fire-regions, which may suggest that either the observations are not sufficiently representative or highlight a difference in bias seen in the model compared to AOD measurements and mass concentration measurements.

Another, key source of uncertainty in fire modelling is correctly accounting for the vertical distribution of emissions. The use of the Plume Rise Model (PRM) improves the vertical structure of modelled BC and OM compared to SAMBBA observations in the eastern cerrado regions, but shows limited impact in the western deforestation region where injection heights were lower. While improving the vertical structure of BC and OM, the use of the PRM actually increases the OM and BC positive bias compared to the observations, further indicating that scaled emissions overestimate reality. The changes from injection also significantly alter the total column burden of BC and OM, suggesting that an inaccurate injection height is contributing to the underestimation of AOD by the model and the underestimation of NO_2 compared to OMI.

7.2 Suggestions for further work

This thesis has highlighted the underestimation of O_3 concentrations, the overestimation of aerosol emissions and different biases between OM and BC for tropical fires within the framework of the state-of-the-art C-IFS model. The impact of these model biases on the simulation earth system should be investigated further. This would help quantify the 'true' impact of composition changes from fires and might indicate further climate-feedbacks from fires that need to be considered in the future. Additionally, the particularly high SAMBBA-observed O_3 concentrations from savannah fires in the Amazon should be investigated with regards to future scenarios due to both the predicted 'savanna-fication' of the Amazon and the recently highlighted positive trend in burned area in this region, in contrast to the western deforestation region.

In terms of scaling GFAS aerosol fire emissions, different model biases have been seen in this study and others (Reddington et al., 2016) compared to AOD and non-AOD aerosol measurements. The use of AOD measurements to constrain and 'scale' aerosol fire emissions should be discouraged until a better understanding of the bias added by the modelled AOD calculation is determined. The new, ongoing development of CIFS-GLOMAP, which implements the GLOMAP microphysical scheme into C-IFS, should also be evaluated against SAMBBA observations and the impact of AOD assimilation in GLOMAP investigated. The inclusion of GLOMAP in the HADGEM3 model has already shown improvements compared to the classic aerosol when evaluated using aerosol extinction measurements from SAMBBA (Johnson et al., 2016).

Although the assimilation of certain species has been shown to improve the C-IFS representation of fire emissions, the assimilation of different products and further development of the assimilation method will most likely improve the representation further. Primarily the assimilation of total column satellite observations is still critically dependent on the vertical distribution assumed in the model. The use of more vertical information such as tropospheric profiles for MOPITT should be explored, particularly in relation to fire emissions where the vertical structure can be complex and modelling can be difficult. Additionally, this work has highlighted the significant difference between the OMI partial ozone column and the C-IFS product, with OMI total column

and MLS stratospheric column assimilated. The impact of Assimilating this partial column directly could improve model representation further and the assimilation of this product, or other tropospheric O_3 columns, should be assessed and evaluated against in-situ observations such as ozonesondes, In-Service Aircraft for a Global Observing System (IAGOS), and European Monitoring and Evaluation Programme (EMEP). Furthermore, for aerosol representation to change beyond the relative ratio of its constituents already in the model, the effect of including the individual aerosol species in the state vector should be tested and the assimilation of non-AOD satellite data such as CALIOP observed aerosol particle-size, which is not affected by radiative processes, should be considered. Finally, while the assimilation in C-IFS has been shown to improve the model representation of assimilated species in this study and others, for a more accurate capture of other important non-assimilated species such as OH, these should also be included in the state vector.

Top priorities for C-IFS system:

1. The AOD scaling factor derived in Kaiser et al., 2012 should not be used to constrain and scale fire emissions within C-IFS.
2. For the better modelling of OH and other chemical species OH should be include within the state vector and be more directly changed by assimilation.
3. O_3 assimilation only slightly improves the model field compared to independent tropospheric ground and satellite observations. The assimilation of tropospheric O_3 products within the C-IFS system should be considered.

8 References

Achard, F., Eva, H. D., Stibig, H.-J., Mayaux, P., Gallego, J., Richards, T., & Malingreau, J.-P. (2002). Determination of deforestation rates of the world ' s humid tropical forests. *Science*, *297*(August), 999–1002. https://doi.org/10.1126/science.1070656

Ainsworth, E., Yendrek, C. R., Sitch, S., Collins, W. J., & Emberson, L. D. (2012). The effects of tropospheric ozone on net primary productivity and implications for climate change. *Annual Review of Plant Biology*, *63*(March), 637–661. https://doi.org/10.1146/annurev-arplant-042110-103829

Akagi, S. K., Yokelson, R. J., Wiedinmyer, C., Alvarado, M. J., Reid, J. S., Karl, T., … Wennberg, P. O. (2011). Emission factors for open and domestic biomass burning for use in atmospheric models. *Atmospheric Chemistry and Physics*, *11*(9), 4039–4072. https://doi.org/10.5194/acp-11-4039-2011

Andela, N., Kaiser, J. W., Heil, A., Leeuwen, T. T. Van, Wooster, M. J., Werf, G. R. Van Der, … Schultz, M. G. (2013). Assimilation System (GFASv1), *2013*(June).

Andela, N., Kaiser, J. W., Werf, G. R. Van Der, & Wooster, M. J. (2015). New fire diurnal cycle characterizations to improve fire radiative energy assessments made from MODIS observations. *Atmos. Chem. Phys.*, 8831–8846. https://doi.org/10.5194/acp-15-8831-2015

Andela, N., Morton, D. C., Giglio, L., Chen, Y., van der Werf, G. R., Kasibhatla, P. S., … Randerson, J. T. (2017). A human-driven decline in global burned area. *Science*, *356*(6345), 1356–1362. https://doi.org/10.1126/science.aal4108

Andreae, M. O., & Merlet P. (2001). Emission of trace gases and aerosols from biomass burning. *Global Biogeochemical Cycles*, *15*(4), 955–966.

Andreae, M. O., & Rosenfeld, D. (2008). Earth-Science Reviews Aerosol – cloud – precipitation interactions . Part 1 . The nature and sources of cloud-active aerosols. *Earth-Science Reviews Journal*, *89*, 13–41. https://doi.org/10.1016/j.earscirev.2008.03.001

Anenberg, S., Horowitz, L. W., & Tong, D. Q. (2010). An Estimate of the Global Burden of Anthropogenic Ozone and Fine Particulate Matter on Premature Human Mortality Using ... Fine Particulate Matter on Premature Human Mortality Using. *Environ Health*

References

Perspect., (June), 1–15. https://doi.org/10.1289/ehp.0901220

Archer-Nicholls, S., Lowe, D., Darbyshire, E., Morgan, W. T., Bela, M. M., Pereira, G., … McFiggans, G. (2015). Characterising Brazilian biomass burning emissions using WRF-Chem with MOSAIC sectional aerosol. *Geoscientific Model Development*, *8*(3), 549–577. https://doi.org/10.5194/gmd-8-549-2015

Archer-Nicholls, S., Lowe, D., Schultz, D. M., & McFiggans, G. (2016). Aerosol–radiation–cloud interactions in a regional coupled model: the effects of convective parameterisation and resolution. *Atmos. Chem. Phys.*, *16*(9), 5573–5594. https://doi.org/10.5194/acp-16-5573-2016

Archibald, A. T., Levine, J. G., Abraham, N. L., Cooke, M. C., Edwards, P. M., Heard, D. E., … Pyle, J. A. (2011). Impacts of HOx regeneration and recycling in the oxidation of isoprene: Consequences for the composition of past, present and future atmospheres. *Geophysical Research Letters*, *38*(5), 1–6. https://doi.org/10.1029/2010GL046520

Archibald, S., Nickless, A., Govender, N., Scholes, R. J., & Lehsten, V. (2010). Climate and the inter-annual variability of fire in southern Africa: A meta-analysis using long-term field data and satellite-derived burnt area data. *Global Ecology and Biogeography*, *19*(6), 794–809. https://doi.org/10.1111/j.1466-8238.2010.00568.x

Arnold, S. R., Emmons, L. K., Monks, S. A., Law, K. S., Ridley, D. A., Turquety, S., … Long, Y. (2015). Biomass burning influence on high-latitude tropospheric ozone and reactive nitrogen in summer 2008: A multi-model analysis based on POLMIP simulations. *Atmospheric Chemistry and Physics*, *15*(11), 6047–6068. https://doi.org/10.5194/acp-15-6047-2015

Artaxo, P., Gatti, L. V., Leal, A. M. C., Longo, K. M., Freitas, S. R. De, Lara, L. L., … Rizzo, L. V. (2005). Química atmosférica na Amazônia: a floresta e as emissões de queimadas controlando a composição da atmosfera amazônica. *Acta Amazonica*, *35*(2), 185–196. https://doi.org/10.1590/S0044-59672005000200008

Artaxo, P., Martins, J. V., Yamasoe, M. A., Procópio, A. S., Pauliquevis, T. M., Andreae, M. O., … Leal, A. M. C. (2002). Physical and chemical properties of aerosols in the wet and dry seasons in Rondônia, Amazonia. *Journal of Geophysical Research D: Atmospheres*, *107*(20), 1–14. https://doi.org/10.1029/2001JD000666

Ashmore, M. R. (2005). Assessing the future global impacts of ozone on vegetation. *Plant, Cell*

References

and Environment, *28*(8), 949–964. https://doi.org/10.1111/j.1365-3040.2005.01341.x

Balkanski, Y., Schulz, M., Claquin, T., & Guibert, S. (2007). Reevaluation of Mineral aerosol radiative forcings suggests a better agreement with satellite and AERONET data. *Atmos. Chem. Phys.*, (2001), 81–95.

Beirle, S., Boersma, K. F., Platt, U., Lawrence, M. G., & Wagner, T. (2011). Megacity Emissions and Lifetimes of Nitrogen Oxides Probed from Space. *Science*, *333*, 1737–1739.

Bela, M. M., Longo, K. M., Freitas, S. R., Moreira, D. S., Beck, V., Wofsy, S. C., … Artaxo, P. (2015). Ozone production and transport over the Amazon Basin during the dry-to-wet and wet-to-dry transition seasons. *Atmospheric Chemistry and Physics*, *15*(2), 757–782. https://doi.org/10.5194/acp-15-757-2015

Bellouin, N., Quaas, J., Morcrette, J.-J., & Boucher, O. (2013). Estimates of aerosol radiative forcing from the MACC re-analysis. *Atmospheric Chemistry and Physics*, *13*(4), 2045–2062. https://doi.org/10.5194/acp-13-2045-2013

Benedetti, a., Morcrette, J.-J., Boucher, O., Dethof, a., Engelen, R. J., Fisher, M., … Suttie, M. (2009). Aerosol analysis and forecast in the European Centre for Medium-Range Weather Forecasts Integrated Forecast System: 2. Data assimilation. *Journal of Geophysical Research*, *114*(D13), D13205. https://doi.org/10.1029/2008JD011115

Bergthórsson, P., & Döös, B. R. (1955). Numerical Weather Map Analysis. *Tellus*, *7*(3), 329–340. https://doi.org/10.1111/j.2153-3490.1955.tb01170.x

Bistinas, I., Harrison, S. P., Prentice, I. C., & Pereira, J. M. C. (2014). Causal relationships versus emergent patterns in the global controls of fire frequency. *Biogeosciences*, *11*(18), 5087–5101. https://doi.org/10.5194/bg-11-5087-2014

Bond, T. C., Doherty, S. J., Fahey, D. W., Forster, P. M., Berntsen, T., Deangelo, B. J., … Zender, C. S. (2013). Bounding the role of black carbon in the climate system: A scientific assessment. *Journal of Geophysical Research Atmospheres*, *118*(11), 5380–5552. https://doi.org/10.1002/jgrd.50171

Bond, W. J., & Keeley, J. E. (2005). Fire as a global "herbivore": The ecology and evolution of flammable ecosystems. *Trends in Ecology and Evolution*, *20*(7), 387–394. https://doi.org/10.1016/j.tree.2005.04.025

References

Boucher, O., Randall, D., Artaxo, P., Bretherton, C., Feingold, G., Forster, P., … Zhang, X. Y. (2013). *Clouds and Aerosols. In: Climate Change 2013: The Physical Science Basis. Contribution of Working Group I to the Fifth Assessment Report of the Intergovernmental Panel on Climate Change*. Cambridge.

Bouttier, F., Miller, M., Hortal, M., & Isaksen, L. (2001). The Development of 12- hourly 4D-Var. *ECMWF Technical Memoranda A*, (September).

Bowman, D. M. J. S., Balch, J. K., Artaxo, P., Bond, W. J., Carlson, J. M., Cochrane, M. a, … Pyne, S. J. (2009). Fire in the Earth system. *Science (New York, N.Y.)*, *324*(5926), 481–484. https://doi.org/10.1126/science.1163886

Brito, J., Rizzo, L. V., Morgan, W. T., Coe, H., Johnson, B., Haywood, J., … Artaxo, P. (2014). Ground-based aerosol characterization during the South American Biomass Burning Analysis (SAMBBA) field experiment. *Atmospheric Chemistry and Physics*, *14*(22), 12069–12083. https://doi.org/10.5194/acp-14-12069-2014

Calvo, A. I., Alves, C., Castro, A., Pont, V., Vicente, A. M., & Fraile, R. (2013). Research on aerosol sources and chemical composition: Past, current and emerging issues. *Atmospheric Research*, *120–121*, 1–28. https://doi.org/10.1016/j.atmosres.2012.09.021

Cariolle, D., & Teyssèdre, H. (2007). A revised linear ozone photochemistry parameterization for use in transport and general circulation models: multi-annual simulations. *Atmos. Chem. Phys.*, *7*(9), 2183–2196. https://doi.org/10.5194/acp-7-2183-2007

Clerbaux, C., Edwards, D. P., Deeter, M., Emmons, L., Lamarque, J. F., Tie, X. X., … Gille, J. (2008). Carbon monoxide pollution from cities and urban areas observed by the Terra/MOPITT mission. *Geophysical Research Letters*, *35*(3), 1–6. https://doi.org/10.1029/2007GL032300

Cochrane, M. A. (2003). Fire science for rainforests. *Nature*, *421*(6926), 913–919. https://doi.org/10.1038/nature01437

Cook, P. A., Savage, N. H., Turquety, S., Carver, G. D., O'Connor, F. M., Heckel, A., … Pyle, J. A. (2007). Forest fire plumes over the North Atlantic: p-TOMCAT model simulations with aircraft and satellite measurements from the ITOP/ICARTT campaign. *Journal of Geophysical Research Atmospheres*, *112*(10), 1–20. https://doi.org/10.1029/2006JD007563

References

Cooper, O. R., Parrish, D. D., Ziemke, J., Balashov, N. V., Cupeiro, M., Galbally, I. E., … Zbinden, R. M. (2014). Global distribution and trends of tropospheric ozone: An observation-based review. *Elementa: Science of the Anthropocene*, *2*, 29. https://doi.org/10.12952/journal.elementa.000029

Courtier, P.; Andersson, E.; Heckley, W.; Pailleux, J.; Vasiljevic, D.; Hamrud, M.; Hollingsworth, A.; Rabier, F.; Fisher, M. (1998). The ECMWF implementation of three-dimensional variational assimilation (3D-Var). I: Formulation. *Quarterly Journal of the Royal Meteorological Society*, *124*(1994), 1783–1807.

Courtier, P., Thepaut, J. N., & Hollingsworth, a. (1994). A Strategy for Operational Implementation of 4d-Var, Using an Incremental Approach. *Quarterly Journal of the Royal Meteorological Society*, *120*(519), 1367–1387. https://doi.org/10.1002/qj.49712051912

Crutzen, P. J., Heidt, L. E., Krasnec, J. P., Pollock, W. H., & Seiler, W. (1979). Biomass burning as a source of atmospheric gases CO, H2, N2O, NO, CH3Cl and COS. *Nature*, *282*(5736), 253–256. Retrieved from http://dx.doi.org/10.1038/282253a0

Daley, R. (1991). *Atmospheric Data Analysis*. Cambridge: Cambridge University Press.

Darbyshire, E., & Johnson, B. (2012). The SAMBBA Campaign : A Summary of Research Flights. *SAMBBA Summary*.

Deeter, M. N., Edwards, D. P., Gille, J. C., Emmons, L. K., Francis, G., Ho, S. P., … Novelli, P. C. (2010). The MOPITT version 4 CO product: Algorithm enhancements, validation, and long-term stability. *Journal of Geophysical Research-Atmospheres*, *115*, 1–13. https://doi.org/Artn D07306\nDoi 10.1029/2009jd013005

Deeter, M. N., Emmons, L. K., Francis, G. L., Edwards, D. P., Gille, J. C., Warner, J. X., … Drummond, J. R. (2003). Operational carbon monoxide retrieval algorithm and selected results for the MOPITT instrument. *Journal of Geophysical Research*, *108*(D14), 4399. https://doi.org/10.1029/2002JD003186

Dentener, F., Kinne, S., Bond, T., Boucher, O., Cofala, J., Generoso, S., … Hoelzemann, J. J. (2006). and Physics Emissions of primary aerosol and precursor gases in the years 2000 and 1750 prescribed data-sets for AeroCom. *Atmos. Chem. Phys.*, (year 1750), 4321–4344.

Donkelaar, A. Van, Martin, R. V, Levy, R. C., Arlindo, M., Krzyzanowski, M., Chubarova, N.

References

E., … Cohen, A. J. (2011). Satellite-based estimates of ground-level fi ne particulate matter during extreme events : A case study of the Moscow fi res in 2010. *Atmospheric Environment*, *45*(34), 6225–6232. https://doi.org/10.1016/j.atmosenv.2011.07.068

Doughty, C. E., Flanner, M. G., & Goulden, M. L. (2010). Effect of smoke on subcanopy shaded light , canopy temperature , and carbon dioxide uptake in an Amazon rainforest. *Global Biogeochemical Cycles*, *24*, 1–10. https://doi.org/10.1029/2009GB003670

Duncan, B. N., Bey, I., Chin, M., Mickley, L. J., Fairlie, T. D., Martin, R. V, & Matsueda, H. (2003). Indonesian wildfires of 1997: Impact on tropospheric chemistry. *Journal of Geophysical Research-Atmospheres*, *108*, *D15*(D15), 4458. https://doi.org/10.1029/2002jd003195

Edwards, D. P., Emmons, L. K., Hauglustaine, D. A., Chu, D. A., Gille, J. C., Kaufman, Y. J., … Drummond, J. R. (2004). Observations of carbon monoxide and aerosols from the Terra satellite: Northern Hemisphere variability. *Journal of Geophysical Research D: Atmospheres*, *109*(24), 1–17. https://doi.org/10.1029/2004JD004727

Emberson, L. D., Ashmore, M. R., Cambridge, H. M., Simpson, D., & Tuovinen, J. (2000). Modelling stomatal ozone flux across Europe. *Environmental Pollution*, *109*.

Engelen, R. J., Serrar, S., & Chevallier, F. (2009). Four-dimensional data assimilation of atmospheric CO2 using AIRS observations. *Journal of Geophysical Research*, (August), 398–430. Retrieved from http://dx.doi.org/10.1002/047172372X.ch11

Fairlie, T. D., Jacob, D. J., Dibb, J. E., Alexander, B., Avery, M. A., Van Donkelaar, A., & Zhang, L. (2010). Impact of mineral dust on nitrate, sulfate, and ozone in transpacific Asian pollution plumes. *Atmospheric Chemistry and Physics*, *10*(8), 3999–4012. https://doi.org/10.5194/acp-10-3999-2010

Felzer, B., Reilly, J., Melillo, J., Kicklighter, D., Sarofim, M., Wang, C., … Zhuang, Q. (2005). Future effects of ozone on carbon sequestration and climate change policy using a global biogeo- chemical model. *Clim. Change*, 345–373. https://doi.org/10.1007/s10584-005-6776-4

Fischer, E. V., Jaffe, D. A., Reidmiller, D. R., & Jaeglé, L. (2010). Meteorological controls on observed peroxyacetyl nitrate at Mount Bachelor during the spring of 2008. *Journal of Geophysical Research Atmospheres*, *115*(3), 1–18. https://doi.org/10.1029/2009JD012776

References

Fisher, M. (1998). Background error covariance modelling. *ECMWF Newsl.*, *106*, 23–28. Retrieved from ftp://beryl.cerfacs.fr/pub/globc/exchanges/daget/DOCS/sem2003_fisher.pdf%5Cnpapers2://publication/uuid/265DCC42-4A9C-482A-B2CF-74866FCC2312

Flemming, J., Huijnen, V., Arteta, J., Bechtold, P., Beljaars, A., Blechschmidt, A. M., … Tsikerdekis, A. (2015). Tropospheric chemistry in the integrated forecasting system of ECMWF. *Geoscientific Model Development*, *8*(4), 975–1003. https://doi.org/10.5194/gmd-8-975-2015

Flemming, J., Inness, A., Flentje, H., Huijnen, V., Moinat, P., Schultz, M. G., & Stein, O. (2009). Model Development Coupling global chemistry transport models to ECMWF ' s integrated forecast system. *Geoscientific Model Development*, *3*, 253–265.

Forbes, R. M., Tompkins, A. M., & Untch, A. (2003). A new prognostic bulk microphysics scheme for the ECMWF forecast model. *JPL Publ.*, *649*.

Forster, P., Ramaswamy, V., Artaxo, P., Berntsen, T., & Betts, R. (2007). Changes in atmospheric constituents and in radiative forcing. *Climate Change 2007: The Physical Science Basis. Contribution of Working Group I to the Fourth Assessment Report of the Intergovernmental Panel on Climate Change*.

Freitas, S. R., Longo, K. M., & Andreae, M. O. (2006). Impact of including the plume rise of vegetation fires in numerical simulations of associated atmospheric pollutants. *Geophysical Research Letters*, *33*(July), 1–5. https://doi.org/10.1029/2006GL026608

Freitas, S. R., Longo, K. M., Chatfield, R., Latham, D., Dias, M. A. F. S., Andreae, M. O., … Unesp, F. E. G. (2007). Including the sub-grid scale plume rise of vegetation fires in low resolution atmospheric transport models. *Atmos. Chem. Phys.*, 3385–3398.

Freitas, S. R., Longo, K. M., Trentmann, J., & Latham, D. (2010). Sensitivity of 1-D smoke plume rise models to the inclusion of environmental wind drag. *Atmos. Chem. Phys.*, 585–594.

Giglio, L., Csiszar, I., & Justice, C. O. (2006). Global distribution and seasonality of active fires as observed with the Terra and Aqua Moderate Resolution Imaging Spectroradiometer (MODIS) sensors. *Journal of Geophysical Research*, *111*(G2), G02016. https://doi.org/10.1029/2005JG000142

References

Giglio, L., Descloitres, J., Justice, C. O., & Kaufman, Y. J. (2003). An enhanced contextual fire detection algorithm for MODIS. *Remote Sensing of Environment*, *87*(2–3), 273–282. https://doi.org/10.1016/S0034-4257(03)00184-6

Giglio, L., Randerson, J. T., Van Der Werf, G. R., Kasibhatla, P. S., Collatz, G. J., Morton, D. C., & Defries, R. S. (2010). Title: Assessing variability and long-term trends in burned area by merging multiple satellite fire products Assessing variability and long-term trends in burned area by merging multiple satellite fire products. *Biogeosciences*, *7*(2008), 1171–1186. https://doi.org/10.5194/bg-7-1171-2010

Giglio, L., van der Werf, G. R., Randerson, J. T., Collatz, G. J., & Kasibhatla, P. (2006). Global estimation of burned area using MODIS active fire observations. *Atmospheric Chemistry and Physics*, *6*(4), 957–974. https://doi.org/10.5194/acp-6-957-2006

Ginoux, P., Chin, M., Tegen, I., Prospero, J. M., Holben, B., Dubovik, O., & Lin, S.-J. (2001). Sources and distributions of dust aerosols simulated with the GOCART model. *Journal of Geophysical Research*, *106*(D17), 20255. https://doi.org/10.1029/2000JD000053

Goode, J. G., Yokelson, R. J., Susott, R. a., & Ward, D. E. (1999). Trace gas emissions from laboratory biomass fires measured by open-path Fourier transform infrared spectroscopy: Fires in grass and surface fuels. *Journal of Geophysical Research*, *104*(D17), 21237. https://doi.org/10.1029/1999JD900360

Granier, C., Bessagnet, B., Bond, T., D'Angiola, A., Denier van der Gon, H., Frost, G. J., … Vuuren, D. P. (2011). Evolution of anthropogenic and biomass burning emissions of air pollutants at global and regional scales during the 1980–2010 period. *Climatic Change*, *109*(1–2), 163–190. https://doi.org/10.1007/s10584-011-0154-1

Granier, C., & J.F. Lamarque, A. Mieville, J.F. Muller, J. Olivier, J. Orlando, J. Peters, G. Petron, G. Tyndall, S. W. (2005). POET, a database of surface emissions of ozone precursors, available on internet at http://www.aero.jussieu.fr/projet/ACCENT/POET.php.

Hantson, S., Arneth, A., Harrison, S. P., Kelley, D. I., Prentice, I. C., Rabin, S. S., … Ciais, P. (2016). The status and challenge of global fire modelling. *Biogeosciences*, 3359–3375. https://doi.org/10.5194/bg-13-3359-2016

Haywood, J., & Boucher, O. (2000). Estimates of the direct and indirect radiative forcing due to tropospheric aerosols: A review. *Review of Geophysics*, (1999), 513–543.

References

Heil, A., Werf, G. R. Van Der, Wooster, M. J., Schultz, M. G., & Gon, H. D. Van Der. (2010). Assessment of the Real-Time Fire Emissions (GFASv0) by MACC, (July).

Helmig, D., Rossabi, S., Hueber, J., Tans, P., Montzka, S. A., Masarie, K., … Smale, D. (2016). Reversal of global atmospheric ethane and propane trends largely due to US oil and natural gas production. *Nature Communications*, *9*(June). https://doi.org/10.1038/NGEO2721

Hodgson, A. K., Morgan, W. T., O'Shea, S., Bauguitte, S., Allan, J. D., Darbyshire, E., … Coe, H. (2017). Near-field emission profiling of Rainforest and Cerrado fires in Brazil during SAMBBA 2012. *Atmos. Chem. Phys. Discuss.*, *2017*, 1–33. https://doi.org/10.5194/acp-2016-1019

Hollingsworth, a., Engelen, R. J., Benedetti, a., Dethof, a., Flemming, J., Kaiser, J. W., … Schultz, M. G. (2008). Toward a Monitoring and Forecasting System For Atmospheric Composition: The GEMS Project. *Bulletin of the American Meteorological Society*, *89*(8), 1147–1164. https://doi.org/10.1175/2008BAMS2355.1

Hortal, M., & Simmons, A. J. (1991). Use of Reduced Gaussian Grids in Spectral Models. *Monthly Weather Review*. https://doi.org/10.1175/1520-0493(1991)119<1057:UORGGI>2.0.CO;2

Hudman, R. C., Jacob, D. J., Cooper, O. R., Evans, M. J., Heald, C. L., Park, R. J., … Ryerson, T. (2004). Ozone production in transpacific Asian pollution plumes and implications for ozone air quality in California. *Journal of Geophysical Research D: Atmospheres*, *109*(23), 1–14. https://doi.org/10.1029/2004JD004974

Huijnen, V., Flemming, J., Kaiser, J. W., Inness, A., Leita, O, J., … Eremenko, M. (2012). Hindcast experiments of tropospheric composition during the summer 2010 fires over western Russia. *Atmospheric Chemistry and Physics*, *12*(9), 4341–4364. https://doi.org/10.5194/acp-12-4341-2012

Huijnen, V., Williams, J., van Weele, M., van Noije, T., Krol, M., Dentener, F., … Pätz, H.-W. (2010). The global chemistry transport model TM5: description and evaluation of the tropospheric chemistry version 3.0. *Geoscientific Model Development*, *3*(2), 445–473. https://doi.org/10.5194/gmd-3-445-2010

Huijnen, V., Wooster, M. J., Kaiser, J. W., Gaveau, D. L. A., Flemming, J., Parrington, M., … van Weele, M. (2016). Fire carbon emissions over maritime southeast Asia in 2015 largest

References

since 1997. *Scientific Reports*, *6*(1), 26886. https://doi.org/10.1038/srep26886

Huneeus, N., Schulz, M., Balkanski, Y., Griesfeller, J., Prospero, J., Kinne, S., … Physics, P. (2011). Global dust model intercomparison in AeroCom phase I. *Atmos. Chem. Phys.*, 7781–7816. https://doi.org/10.5194/acp-11-7781-2011

Hurst, D. F., Griffith, D. W. T., & Cook, G. D. (1994). Trace Gas Emissions from Biomass Burning in Tropical Australian Savannas. *Journal of Geophysical Research*, *99*(D8), 16441–16456. https://doi.org/10.1029/94JD00670

Inness, A., Baier, F., Benedetti, A., Bouarar, I., Chabrillat, S., Clark, H., … Zerefos, C. (2013). The MACC reanalysis: an 8 yr data set of atmospheric composition. *Atmospheric Chemistry and Physics*, *13*(8), 4073–4109. https://doi.org/10.5194/acp-13-4073-2013

Jacob, D., , Liu, H., , Mari, C., & , Yantosca, R. (2000). Harvard Wet Deposition Scheme for GMI. *Harvard University Atmospheric Chemistry Modeling Group*.

Jaegle ́L, Quinn, P. K., Bates, T. S., Alexander, B., & Oceanic, N. (2011). Global distribution of sea salt aerosols : new constraints from in situ and remote sensing observations. *Atmos. Chem. Phys.*, (2004), 3137–3157. https://doi.org/10.5194/acp-11-3137-2011

Jaffe, D. a., & Wigder, N. L. (2012). Ozone production from wildfires: A critical review. *Atmospheric Environment*, *51*, 1–10. https://doi.org/10.1016/j.atmosenv.2011.11.063

Janhäll, S., Andreae, M. O., & Pöschl, U. (2010). Biomass burning aerosol emissions from vegetation fires : particle number and mass emission factors and size distributions. *Atmos. Chem. Phys.*, *10*, 1427–1439.

Jiang, Z., Worden, J. R., Worden, H., Deeter, M., Jones, D. B. A., Arellano, A. F., & Henze, D. K. (2017). A 15-year record of CO emissions constrained by MOPITT CO observations. *Atmospheric Chemistry and Physics*, *17*(7), 4565–4583. https://doi.org/10.5194/acp-17-4565-2017

Johnson, B. T., Haywood, J. M., Langridge, J. M., Darbyshire, E., Morgan, W. T., Szpek, K., … Bellouin, N. (2016). Evaluation of biomass burning aerosols in the HadGEM3 climate model with observations from the SAMBBA field campaign. *Atmos. Chem. Phys.*, *16*(22), 14657–14685. https://doi.org/10.5194/acp-16-14657-2016

Jolly, W. M., Cochrane, M. a, Freeborn, P. H., Holden, Z. a, Brown, T. J., Williamson, G. J., & Bowman, D. M. J. S. (2015). Climate-induced variations in global wildfire danger from

References

1979 to 2013. *Nature Communications*, *6*(May), 7537. https://doi.org/10.1038/ncomms8537

Kaiser, J. W., Benedetti, A., Flemming, J., Heil, A., Schultz, M. G., Werf, G. R. Van Der, … Kingdom, U. (2011). FROM FIRE OBSERVATIONS TO SMOKE PLUME FORECASTING IN THE MACC, *2010*(January).

Kaiser, J. W., Heil, a., Andreae, M. O., Benedetti, a., Chubarova, N., Jones, L., … van der Werf, G. R. (2012). Biomass burning emissions estimated with a global fire assimilation system based on observed fire radiative power. *Biogeosciences*, *9*(1), 527–554. https://doi.org/10.5194/bg-9-527-2012

Kalnay, E. (2002). *Atmospheric Modeling, Data Assimilation and Predictability*. Cambridge: Cambridge University Press.

Kirkman, G. A., Gut, A., Ammann, C., Gatti, L. V, Cordova, A. M., Moura, M. A. L., … Meixner, F. X. (2002). Surface exchange of nitric oxide, nitrogen dioxide, and ozone at a cattle pasture in Rondonia, Brazil. *Journal of Geophysical Research-Atmospheres*, *107*(D20). https://doi.org/8083\r10.1029/2001jd000523

Koppmann, R., von Czapiewski, K., & Reid, J. S. (2005). A review of biomass burning emissions, part I: gaseous emissions of carbon monoxide, methane, volatile organic compounds, and nitrogen containing compounds. *Atmospheric Chemistry and Physics Discussions*, *5*(5), 10455–10516. https://doi.org/10.5194/acpd-5-10455-2005

Kurpius, M. R., & Goldstein, A. H. (2003). Gas-phase chemistry dominates O3 loss to a forest, implying a source of aerosols and hydroxyl radicals to the atmosphere. *Geophysical Research Letters*, *30*(7), 1371. https://doi.org/10.1029/2002GL016785

Lahoz, W. A., & Schneider, P. (2014). Data assimilation : making sense of Earth Observation. *Frontiers in Environmental Science*, *2*(May), 1–28. https://doi.org/10.3389/fenvs.2014.00016

Lamarque, J.-F., Bond, T. C., Eyring, V., Granier, C., Heil, a., Klimont, Z., … van Vuuren, D. P. (2010). Historical (1850–2000) gridded anthropogenic and biomass burning emissions of reactive gases and aerosols: methodology and application. *Atmospheric Chemistry and Physics*, *10*(15), 7017–7039. https://doi.org/10.5194/acp-10-7017-2010

Lamsal, L. N., Martin, R. V., Van Donkelaar, A., Celarier, E. A., Bucsela, E. J., Boersma, K. F.,

References

… Wang, Y. (2010). Indirect validation of tropospheric nitrogen dioxide retrieved from the OMI satellite instrument: Insight into the seasonal variation of nitrogen oxides at northern midlatitudes. *Journal of Geophysical Research Atmospheres*, *115*(5), 1–15. https://doi.org/10.1029/2009JD013351

Landgraf, J., & Crutzen, P. J. (1998). An Efficient Method for Online Calculations of Photolysis and Heating Rates. *Journal of the Atmospheric Sciences*, *55*, 863–878. https://doi.org/10.1175/1520-0469(1998)055<0863:AEMFOC>2.0.CO;2

Latham, D. (1994). PLUMP: A one-dimensional plume predictor and cloud model for fire and smoke managers. *Tech. Rep. INT–GTR–314, Intermountain Research Station, USDA Forest Service*.

Laursen, K. K., Hobbs, V., & Radke, F. (1992). Some trace gas emissions from the North American biomass fires with an assessment of regional and global fluxes from biomass burning. *Journal of Geophysical Research*, *97*(D18), 20687–20701.

Lawless, a. S., Gratton, S., & Nichols, N. K. (2005). An investigation of incremental 4D-Var using non-tangent linear models. *\Qjrms*, *131*, 459–476. https://doi.org/10.1256/qj.04.20

Lelieveld, J., Evans, J. S., Fnais, M., Giannadaki, D., & Pozzer, A. (2015). The contribution of outdoor air pollution sources to premature mortality on a global scale. *Nature*, *525*(7569), 367–371. Retrieved from http://dx.doi.org/10.1038/nature15371

Leung, F. Y. T., Logan, J. A., Park, R., Hyer, E., Kasischke, E., Streets, D., & Yurganov, L. (2007). Impacts of enhanced biomass burning in the boreal forests in 1998 on tropospheric chemistry and the sensitivity of model results to the injection height of emissions. *Journal of Geophysical Research Atmospheres*, *112*(10), 1–15. https://doi.org/10.1029/2006JD008132

Levelt, P. F., Oord, G. H. J. Van Den, Dobber, M. R., Mälkki, A., Visser, H., Vries, J. De, … Saari, H. (2006). The Ozone Monitoring Instrument. *TRANSACTIONS ON GEOSCIENCE AND REMOTE SENSING*, *44*(5), 1093–1101.

Lightfoot, P. D., Cox, R. A., Crowley, J. N., Destriau, M., Hayman, G. D., Jenkin, M. E., … Zabel, F. (1992). Organic peroxy radicals: Kinetics, spectroscopy and tropospheric chemistry. *Atmospheric Environment Part A, General Topics*, *26*(10), 1805–1961. https://doi.org/10.1016/0960-1686(92)90423-I

References

Lobert, J. M., & Warnatz, J. (1993). Emissions from the Combustion Process in Vegetation. *Fire in the Environment: Its Ecological, Atmospheric and Climatic Importance*.

Lorenc, A. C. (1986). Analysis methods for numerical weather prediction. *Quarterly Journal of the Royal Meteorological Society*, *112*(474), 1177–1194. https://doi.org/10.1002/qj.49711247414

Marenco, F., Johnson, B., Langridge, J. M., Mulcahy, J., Benedetti, A., Remy, S., … Artaxo, P. (2016). On the vertical distribution of smoke in the Amazonian atmosphere during the dry season. *Atmos. Chem. Phys.*, 2155–2174. https://doi.org/10.5194/acp-16-2155-2016

Marlon, J. R., Bartlein, P. J., Carcaillet, C., Gavin, D. G., Harrison, S. P., Higuera, P. E., … Prentice, I. C. (2008). Climate and human influences on global biomass burning over the past two millennia. *Nature Geoscience*, *1*(October 2008), 697–702. https://doi.org/10.1038/ngeo468

Martin, M. V., Logan, J. A., Kahn, R. A., Leung, F., Nelson, D. L., & Diner, D. J. (2010). Smoke injection heights from fires in North America : analysis of 5 years of satellite observations. *Atmos. Chem. Phys.*, 1491–1510.

Mason, S. A., Trentmann, J., Winterrath, T., Yokelson, R. J., Christian, T. J., Carlson, L. J., … Andreae, M. O. (2006). Intercomparison of Two Box Models of the Chemical Evolution in Biomass-Burning Smoke Plumes. *Journal of Atmospheric Chemistry*, *55*(3), 273–297. https://doi.org/10.1007/s10874-006-9039-5

Mauzerall, D. L., Logan, J. A., Jacob, D. J., Anderson, B. E., Blake, D. R., Bradshaw, J. D., … Talbot, B. (1998). Photochemistry in biomass burning plumes and implications for tropospheric ozone over the tropical South Atlantic. *Journal of Geophysical Research*, *103*(D7), 8401. https://doi.org/10.1029/97JD02612

McKeen, S. A., Wotawa, G., Parrish, D. D., Holloway, J. S., Buhr, M. P., Hübler, G., … Meagher, J. F. (2002). Ozone production from Canadian wildfires during June and July of 1995. *Journal of Geophysical Research Atmospheres*, *107*(14), 1–25. https://doi.org/10.1029/2001JD000697

McMeeking, G. R., Kreidenweis, S. M., Baker, S., Carrico, C. M., Chow, J. C., Collett, J. L., … Cyle E., W. (2009). Emissions of trace gases and aerosols during the open combustion of biomass in the laboratory. *Journal of Geophysical Research Atmospheres*, *114*(19), 1–20. https://doi.org/10.1029/2009JD011836

References

Metzger, S., Dentener, F., Krol, M., Jeuken, A., & Lelieveld, J. (2002). Gas/aerosol partitioning 2. Global modeling results. *Journal of Geophysical Research D: Atmospheres*, *107*(16), 1–23. https://doi.org/10.1029/2001JD001103

Metzger, S., Dentener, F., Pandis, S., & Lelieveld, J. (2002). Gas/aerosol partitioning: 1. A computationally efficient model. *Journal of Geophysical Research Atmospheres*, *107*(16). https://doi.org/10.1029/2001JD001102

Michou, M., Laville, P., Serça, D., Fotiadi, A., Bouchou, P., & Peuch, V.-H. (2005). Measured and modeled dry deposition velocities over the ESCOMPTE area. *Atmospheric Research*, *74*(1), 89–116. https://doi.org/10.1016/j.atmosres.2004.04.011

Miyazaki, K., Eskes, H. J., & Sudo, K. (2012). Global NO x emission estimates derived from an assimilation of OMI tropospheric NO 2 columns. *Atmospheric Chemistry and Physics*, *12*(5), 2263–2288. https://doi.org/10.5194/acp-12-2263-2012

Miyazaki, K., Eskes, H. J., & Sudo, K. (2015). A tropospheric chemistry reanalysis for the years 2005-2012 based on an assimilation of OMI, MLS, TES, and MOPITT satellite data. *Atmospheric Chemistry and Physics*, *15*(14), 8315–8348. https://doi.org/10.5194/acp-15-8315-2015

Miyazaki, K., Eskes, H., Sudo, K., Boersma, K. F., Bowman, K., & Kanaya, Y. (2016). Decadal changes in global surface NOx emissions from multi-constituent satellite data assimilation. *Atmospheric Chemistry and Physics Discussions*, *0*(2), 1–48. https://doi.org/10.5194/acp-2016-529

Monahan, E. C., Spiel, D. E., & Davidson, K. L. (1986). A Model of Marine Aerosol Generation Via Whitecaps and Wave Disruption. In E. C. Monahan & G. Mac Niocaill (Eds.), *Oceanic Whitecaps: And Their Role in Air-Sea Exchange Processes* (pp. 167–174). Dordrecht: Springer Netherlands. https://doi.org/10.1007/978-94-009-4668-2_16

Monks, P. S., Archibald, A. T., Colette, A., Cooper, O., Coyle, M., Derwent, R., … Williams, M. L. (2015). Tropospheric ozone and its precursors from the urban to the global scale from air quality to short-lived climate forcer. *Atmospheric Chemistry and Physics*, *15*(15), 8889–8973. https://doi.org/10.5194/acp-15-8889-2015

Monks, P. S., Granier, C., Fuzzi, S., Stohl, A., Williams, M. L., Akimoto, H., … von Glasow, R. (2009). Atmospheric composition change - global and regional air quality. *Atmospheric Environment*, *43*(33), 5268–5350. https://doi.org/10.1016/j.atmosenv.2009.08.021

References

Morcrette, J.-J., Boucher, O., Jones, L., Salmond, D., Bechtold, P., Beljaars, a., … Untch, a. (2009). Aerosol analysis and forecast in the European Centre for Medium-Range Weather Forecasts Integrated Forecast System: Forward modeling. *Journal of Geophysical Research*, *114*(D6), D06206. https://doi.org/10.1029/2008JD011235

Moritz, M. A., Batllori, E., Bradstock, R. A., Gill, A. M., Handmer, J., Hessburg, P. F., … Syphard, A. D. (2014). Learning to coexist with wildfire. *Nature*, *515*(7525), 58–66. https://doi.org/10.1038/nature13946

Moritz, M. a., Parisien, M.-A., Batllori, E., Krawchuk, M. a., Van Dorn, J., Ganz, D. J., & Hayhoe, K. (2012). Climate change and disruptions to global fire activity. *Ecosphere*, *3*(6), art49. https://doi.org/10.1890/ES11-00345.1

Myhre, G., Shindell, D., Bréon, F.-M., Collins, W., Fuglestvedt, J., Huang, J., … Zhang, H. (2013). Anthropogenic and Natural Radiative Forcing. *Climate Change 2013: The Physical Science Basis. Contribution of Working Group I to the Fifth Assessment Report of the Intergovernmental Panel on Climate Change*, 659–740. https://doi.org/10.1017/CBO9781107415324.018

Navon, I. (2009). *Data assimilation for numerical weather prediction: A Review*. Berlin: Springer.

Neirynck, J., Gielen, B., Janssens, I. a, & Ceulemans, R. (2012). Insights into ozone deposition patterns from decade-long ozone flux measurements over a mixed temperate forest. *Journal of Environmental Monitoring : JEM*, *14*(6), 1684–1695. https://doi.org/10.1039/c2em10937a

Oikawa, P. Y., Ge, C., Wang, J., Eberwein, J. R., Liang, L. L., Allsman, L. A., … Jenerette, G. D. (2015). Unusually high soil nitrogen oxide emissions influence air quality in a high-temperature agricultural region. *Nat Commun*, *6*, 8753. https://doi.org/10.1038/ncomms9753

Oliveira, P. H. F., P. Artaxo, C. Pires, S. De Lucca, A. Procopio, B. Holben, J. Schafer, L. F. Cardoso, S. C. Wofsy, and H. R. R. (2007). The effects of biomass burning aerosols and clouds on the CO 2 flux in Amazonia. *Tellus*, 338–349. https://doi.org/10.1111/j.1600-0889.2007.00270.x

Oliver, J., Peters, J., Granier, C., Petron, G., Muller, J. F., And, & Wallens, S. (2003). *Present and future surface emissions of atmospheric compounds, POET report #2*.

References

Osborne, S. R., Haywood, J. M., Francis, P. N., & Dubovik, O. (2004). Short-wave radiative effects of biomass burning aerosol during SAFARI2000. *Quarterly Journal of the Royal Meteorological Society*, *130*(599), 1423–1447. https://doi.org/10.1256/qj.03.134

Pacifico, F., Folberth, G. A., Sitch, S., Haywood, J. M., Rizzo, L. V., Malavelle, F. F., & Artaxo, P. (2015a). Biomass burning related ozone damage on vegetation over the Amazon forest: A model sensitivity study. *Atmospheric Chemistry and Physics*, *15*(5), 2791–2804. https://doi.org/10.5194/acp-15-2791-2015

Pacifico, F., Folberth, G. A., Sitch, S., Haywood, J. M., Rizzo, L. V, Malavelle, F. F., & Artaxo, P. (2015b). Biomass burning related ozone damage on vegetation over the Amazon forest: a model sensitivity study. *Atmos. Chem. Phys.*, *15*(5), 2791–2804. https://doi.org/10.5194/acp-15-2791-2015

Parrington, M., Palmer, P. I., Lewis, A. C., Lee, J. D., Rickard, A. R., Di Carlo, P., … Leigh, R. J. (2013). Ozone photochemistry in boreal biomass burning plumes. *Atmospheric Chemistry and Physics*, *13*(15), 7321–7341. https://doi.org/10.5194/acp-13-7321-2013

Paton-walsh, C., Emmons, L. K., & Wiedinmyer, C. (2012). Australia ' s Black Saturday fi res e Comparison of techniques for estimating emissions from vegetation fi res. *Atmospheric Environment*, *60*, 262–270. https://doi.org/10.1016/j.atmosenv.2012.06.066

Patra, P. K., Krol, M. C., Montzka, S. A., Arnold, T., Atlas, E. L., Lintner, B. R., … Young, D. (2014). Observational evidence for interhemispheric hydroxyl-radical parity. *Nature*, *513*. https://doi.org/10.1038/nature13721

Paugam, R., Wooster, M., & Atherton, J. (2015). Development and optimization of a wildfire plume rise model based on remote sensing data inputs – Part 2. *Atmospheric Chemistry and Physics Discussions*, 9815–9895. https://doi.org/10.5194/acpd-15-9815-2015

Paugam, R., Wooster, M., Freitas, S., & Martin, M. V. (2016). A review of approaches to estimate wildfire plume injection height within large-scale atmospheric chemical transport models. *Atmos. Chem. Phys.*, 907–925. https://doi.org/10.5194/acp-16-907-2016

Pechony, O., & Shindell, D. T. (2010). Driving forces of global wildfires over the past millennium and the forthcoming century. *Proceedings of the National Academy of Sciences of the United States of America*, *107*(45), 19167–19170. https://doi.org/10.1073/pnas.1003669107

References

Pereira, G., Siqueira, R., Rosário, N. E., Longo, K. L., Freitas, S. R., Cardozo, F. S., … Wooster, M. J. (2016). Assessment of fire emission inventories during the South American Biomass Burning Analysis (SAMBBA) experiment. *Atmospheric Chemistry and Physics*, *16*(11), 6961–6975. https://doi.org/10.5194/acp-16-6961-2016

Pope, R. J., Chipperfield, M. P., Savage, N. H., Ordóñez, C., Neal, L. S., Lee, L. A., … Richards, N. A. D. (2014). Evaluation of a regional air quality model using satellite column NO2: treatment of observation errors and model boundary conditions and emissions. *Atmospheric Chemistry and Physics Discussions*, *14*(15), 21749–21784. https://doi.org/10.5194/acpd-14-21749-2014

Pope, R. J., Richards, N. A. D., Chipperfield, M. P., Moore, D. P., Monks, S. A., Arnold, S. R., … Feng, W. (2016). Intercomparison and evaluation of satellite peroxyacetyl nitrate observations in the upper troposphere-lower stratosphere. *Atmospheric Chemistry and Physics*, *16*(21), 13541–13559. https://doi.org/10.5194/acp-16-13541-2016

Power, M. J., Marlon, J., Ortiz, N., Bartlein, P. J., Harrison, S. P., Mayle, F. E., … Zhang, J. H. (2007). Changes in fire activity since the Last Glacial Maximum : an assessment based on a global synthesis and analysis of charcoal data. *Climate Dynamics*, *30*(7–8), 887–907. https://doi.org/10.1007/s00382-007-0334-x

Rap, A., Spracklen, D. V, Mercado, L., Reddington, C. L., Haywood, J. M., Ellis, R. J., … Butt, N. (2015). Fires increase Amazon forest productivity through increases in diffuse radiation. *AGU Publications*, 4654–4662. https://doi.org/10.1002/2015GL063719.Received

Real, E., Law, K. S., Weinzierl, B., Fiebig, M., Petzold, A., Wild, O., … Blake, D. (2007). Processes influencing ozone levels in Alaskan forest fire plumes during long-range transport over the North Atlantic. *Journal of Geophysical Research Atmospheres*, *112*(10), 1–19. https://doi.org/10.1029/2006JD007576

Reddington, C. L., Spracklen, D. V., Artaxo, P., Ridley, D. A., Rizzo, L. V., & Arana, A. (2016). Analysis of particulate emissions from tropical biomass burning using a global aerosol model and long-term surface observations. *Atmospheric Chemistry and Physics*, *16*(17), 11083–11106. https://doi.org/10.5194/acp-16-11083-2016

Reddy, M. S., Boucher, O., Bellouin, N., Schulz, M., Balkanski, Y., Dufresne, J. L., & Pham, M. (2005). Estimates of global multicomponent aerosol optical depth and direct radiative

References

perturbation in the Laboratoire de Météorologie Dynamique general circulation model. *Journal of Geophysical Research D: Atmospheres*, *110*(10), 1–16. https://doi.org/10.1029/2004JD004757

Reid, J. S., Koppmann, R., Eck, T. F., & Eleuterio, D. P. (2005). A review of biomass burning emissions part II: intensive physical properties of biomass burning particles. *Atmospheric Chemistry and Physics*, *5*(3), 799–825. https://doi.org/10.5194/acp-5-799-2005

Rémy, S., Veira, A., Paugam, R., Sofiev, M., Kaiser, J. W., Marenco, F., … Hair, J. W. (2016). Two global climatologies of daily fire emission injection heights since 2003. *Atmospheric Chemistry and Physics Discussions*, (August 2013), 1–42. https://doi.org/10.5194/acp-2015-1048

Richter, A. (2009). Nitrogen oxides in the troposphere – What have we learned from satellite measurements? *The European Physical Journal Conferences*, *1*(x), 149–156. https://doi.org/10.1140/epjconf/e2009-00916-9

Roderick, M. L., Farquhar, G. D., Berry, S. L., & Noble, I. R. (2001). On the direct effect of clouds and atmospheric particles on the productivity and structure of vegetation. *Oecologia*, 21–30. https://doi.org/10.1007/s004420100760

Rosado-Reyes, C. M., & Francisco, J. S. (2007). Atmospheric oxidation pathways of propane and its by-products: Acetone, acetaldehyde, and propionaldehyde. *Journal of Geophysical Research Atmospheres*, *112*(14). https://doi.org/10.1029/2006JD007566

Rummel, U., Ammann, C., Kirkman, G. A., Moura, M. A. L., Foken, T., Andreae, M. O., … Group, C. (2007). and Physics Seasonal variation of ozone deposition to a tropical rain forest in southwest Amazonia. *Atmos. Chem. Phys.*, 5415–5435.

Russell, L. M. (2003). Aerosol Organic-Mass-to-Organic- Carbon Ratio Measurements. *Environ. Sci. Technol.*, *37*(13), 2982–2987.

Saatchi, S., Asefi-Najafabady, S., Malhi, Y., Aragao, L. E., Anderson, L. O., Myneni, R. B., & Nemani, R. (2013). Persistent effects of a severe drought on Amazonian forest canopy. *Proceedings of the National Academy of Sciences of the United States of America*, *110*(2), 565–570. https://doi.org/10.1073/pnas.1204651110

Sander, S. P. (2003). Chemical kinetics and photochemical data for use in atmospheric studies Evaluation 15. *JPL Publ.*, *06–2*(14), 523 pp.

References

Sandu, A., & Chai, T. (2011). Chemical Data Assimilation—An Overview. *Atmosphere*, *2*(4), 426–463. https://doi.org/10.3390/atmos2030426

Saunois, M., Bousquet, P., Poulter, B., Peregon, A., Ciais, P., Canadell, J. G., … Zhu, Q. (2016). The global methane budget 2000-2012. *Earth System Science Data*, *8*(2), 697–751. https://doi.org/10.5194/essd-8-697-2016

Schultz, M. G., Heil, A., Hoelzemann, J. J., Spessa, A., Thonicke, K., Goldammer, J. G., … Bolscher, M. Van. (2008). Global wildland fire emissions from 1960 to 2000. *Global Biogeochemical Cycles*, *22*, 1–17. https://doi.org/10.1029/2007GB003031

Schumann, U., & Huntrieser, H. (2007). The global lightning-induced nitrogen oxides source. *Atmos. Chem. Phys. Atmospheric Chemistry and Physics*, *7*, 3823–3907. https://doi.org/10.5194/acpd-7-2623-2007

Scott, A. C., & Glasspool, I. J. (2006). The diversification of Paleozoic fire systems and fluctuations in atmospheric oxygen concentration. *Proceedings of the National Academy of Sciences of the United States of America*, *103*(29), 10861–10865. https://doi.org/10.1073/pnas.0604090103

Seinfeld, J., & Pandis, S. (2016). *Atmospheric Chemistry and Physics: From Air Pollution to Climate Change* (3rd Editio). Wiley.

Shi, Y., Matsunaga, T., Saito, M., Yamaguchi, Y., & Chen, X. (2015). Comparison of global inventories of CO<inf>2</inf> emissions from biomass burning during 2002-2011 derived from multiple satellite products. *Environmental Pollution*, *206*, 479–487. https://doi.org/10.1016/j.envpol.2015.08.009

Silva, R. a, West, J. J., Zhang, Y., Anenberg, S. C., Lamarque, J.-F., Shindell, D. T., … Zeng, G. (2013). Global premature mortality due to anthropogenic outdoor air pollution and the contribution of past climate change. Supporting Information. *Environmental Research Letters*, *8*(3), 34005. https://doi.org/10.1088/1748-9326/8/3/034005

Sinha, P., Hobbs, P. V, Yokelson, R. J., Bertschi, I. T., Blake, D. R., Simpson, I. J., … Novakov, T. (2003). Emissions of trace gases and particles from savanna fires in southern Africa. *Journal of Geophysical Research: Atmospheres (1984–2012)*, *108*(D13). https://doi.org/10.1029/2002JD002325

Sitch, S., Cox, P. M., Collins, W. J., & Huntingford, C. (2007). Indirect radiative forcing of

References

climate change through ozone effects on the land-carbon sink. *Nature*, *448*(August), 791–794. https://doi.org/10.1038/nature06059

Stein, O., Flemming, J., Inness, A., Kaiser, J. W., & Schultz, M. G. (2012). Global reactive gases forecasts and reanalysis in the MACC project. *Journal of Integrative Environmental Sciences*, *8168*(October 2014), 1–14. https://doi.org/10.1080/1943815X.2012.696545

Stevenson, D. S., Dentener, F. J., Schultz, M. G., Ellingsen, K., Noije, T. P. C. Van, Wild, O., … Bey, I. (2006). Multimodel ensemble simulations of present-day and near-future tropospheric ozone. *Atmos. Chem. Phys.*, *111*. https://doi.org/10.1029/2005JD006338

Stocker, T. F., & D. Qin, G.-K. Plattner, M. Tignor, S.K. Allen, J. Boschung, A. Nauels, Y. Xia, V. B. and P. M. M. (eds. . (2013). *IPCC, 2013: Climate Change 2013: The Physical Science Basis. Contribution of Working Group I to the Fifth Assessment Report of the Intergovern- mental Panel on Climate Change*. Cambridge, United Kingdom and New York, NY, USA, 1535 pp.

Stockwell, C. E., Jayarathne, T., Cochrane, M. A., Ryan, K. C., Putra, E. I., Saharjo, B. H., … Yokelson, R. J. (2016). Field measurements of trace gases and aerosols emitted by peat fires in Central Kalimantan, Indonesia, during the 2015 El Niño. *Atmospheric Chemistry and Physics*, *16*(18), 11711–11732. https://doi.org/10.5194/acp-16-11711-2016

Swetnam, T. W., & Betancourt, J. L. (1990). Fires-Southern Oscillation Relations in the Southwestern United States. *Science*, *249*(4972), 1017–1020.

Talukdar, R. K., Burkholder, J. B., Schmoltner, A.-M., Roberts, J. M., Wilson, R. R., & Ravishankara, A. R. (1995). Investigation of the loss processes for peroxyacetyl nitrate in the atmosphere: UV photolysis and reaction with OH. *Journal of Geophysical Research*, *100*(D7), 14163. https://doi.org/10.1029/95JD00545

Textor, C., Schulz, M., Guibert, S., Kinne, S., Balkanski, Y., Bauer, S., … Boucher, O. (2006). Analysis and quantification of the diversities of aerosol life cycles within AeroCom. *Atmos. Chem. Phys.*, 1777–1813.

Thomas, P. A., & Packham, J. R. (2007). Introduction : Forest basics. *Ecology of Woodlands and Forests: Description, Dynamics and Diversity*.

Trémolet, Y. (2007). Incremental 4D-Var convergence study. *Tellus, Series A: Dynamic Meteorology and Oceanography*, *59*(5), 706–718. https://doi.org/10.1111/j.1600-

References

0870.2007.00271.x

Tuomisto, J. T., Wilson, A., Evans, J. S., & Tainio, M. (2006). Uncertainty in Mortality Response to Airborne Fine Particulate Matter : Combining European Air Pollution Experts, 1–24.

Van Der Werf, G. R., Randerson, J. T., Giglio, L., Collatz, G. J., Mu, M., Kasibhatla, P. S., … Van Leeuwen, T. T. (2010). Global fire emissions and the contribution of deforestation, savanna, forest, agricultural, and peat fires (1997-2009). *Atmospheric Chemistry and Physics*, *10*(23), 11707–11735. https://doi.org/10.5194/acp-10-11707-2010

Van Der Werf, G. R., Randerson, J. T., Giglio, L., Gobron, N., & Dolman, A. J. (2008). Climate controls on the variability of fires in the tropics and subtropics. *Global Biogeochemical Cycles*, *22*(3), 1–13. https://doi.org/10.1029/2007GB003122

Vautard, R., Szopa, S., Beekmann, M., Menut, L., Hauglustaine, D. A., Rouil, L., & Roemer, M. (2006). Are decadal anthropogenic emission reductions in Europe consistent with surface ozone observations ? *Geophysical Research Letters*, *33*, 2–5. https://doi.org/10.1029/2006GL026080

Wang, Z., Chappellaz, J., Park, K., & Mak, J. E. (2008). Large Variations in Southern. *Science*, *205*(December), 2002–2005. https://doi.org/10.1126/science.1197257

Ward, D. E., Susott, R. a., Kauffman, J. B., Babbitt, R. E., Cummings, D. L., Dias, B., … Setzer, a. W. (1992). Smoke and fire characteristics for cerrado and deforestation burns in Brazil - BASE-B experiment. *Journal of Geophysical Research*, *97*(92), 14601–14619. https://doi.org/10.1029/92JD01218

Warneke, C., Roberts, J. M., Veres, P., Gilman, J., Kuster, W. C., Burling, I., … De Gouw, J. A. (2011). VOC identification and inter-comparison from laboratory biomass burning using PTR-MS and PIT-MS. *International Journal of Mass Spectrometry*, *303*(1), 6–14. https://doi.org/10.1016/j.ijms.2010.12.002

Waters, J. W., Froidevaux, L., Harwood, R. S., Jarnot, R. F., Pickett, H. M., Read, W. G., … Walch, M. J. (2006). The Earth Observing System Microwave Limb Sounder (EOS MLS) on the aura satellite. *IEEE Transactions on Geoscience and Remote Sensing*, *44*(5), 1075–1092. https://doi.org/10.1109/TGRS.2006.873771

Wesely, M. ., & Hicks, B. . (2000). A review of the current status of knowledge on dry

References

deposition. *Atmospheric Environment*, *34*(12), 2261–2282. https://doi.org/10.1016/S1352-2310(99)00467-7

Wesely, M. L. (1989). Parameterization of surface resistances to gaseous dry deposition in regional-scale numerical models. *Atmospheric Environment (1967)*, *23*(6), 1293–1304. https://doi.org/10.1016/0004-6981(89)90153-4

Wiedinmyer, C., Akagi, S. K., Yokelson, R. J., Emmons, L. K., Al-Saadi, J. a., Orlando, J. J., & Soja, a. J. (2010). The Fire INventory from NCAR (FINN) – a high resolution global model to estimate the emissions from open burning. *Geoscientific Model Development Discussions*, *3*(4), 2439–2476. https://doi.org/10.5194/gmdd-3-2439-2010

Wittig, V. E., Ainsworth, E. A., Naidu, S. L., Karnosky, D. F., & Long, S. P. (2009). Quantifying the impact of current and future tropospheric ozone on tree biomass, growth, physiology and biochemistry: A quantitative meta-analysis. *Global Change Biology*, *15*(2), 396–424. https://doi.org/10.1111/j.1365-2486.2008.01774.x

Wooster, M. J., Roberts, G., Perry, G. L. W., & Kaufman, Y. J. (2005). Retrieval of biomass combustion rates and totals from fire radiative power observations: FRP derivation and calibration relationships between biomass consumption and fire radiative energy release. *Journal of Geophysical Research Atmospheres*, *110*(24), 1–24. https://doi.org/10.1029/2005JD006318

Wooster, M. J., Zhukov, B., & Oertel, D. (2003). Fire radiative energy for quantitative study of biomass burning: Derivation from the BIRD experimental satellite and comparison to MODIS fire products. *Remote Sensing of Environment*, *86*(1), 83–107. https://doi.org/10.1016/S0034-4257(03)00070-1

Worden, H. M., Deeter, M. N., Frankenberg, C., George, M., Nichitiu, F., Worden, J., … Warner, J. X. (2013). Decadal record of satellite carbon monoxide observations. *Atmospheric Chemistry and Physics*, *13*(2), 837–850. https://doi.org/10.5194/acp-13-837-2013

World Health Organization. (2006). WHO Air quality guidelines for particulate matter, ozone, nitrogen dioxide and sulfur dioxide: global update 2005: summary of risk assessment. *Geneva: World Health Organization*, 1–22. https://doi.org/10.1016/0004-6981(88)90109-6

World Health Organization. (2014). *Burden of disease from Household Air Pollution for 2012*

References

Summary of results (Vol. 35).

Xu, W., Wooster, M. J., Kaneko, T., He, J., Zhang, T., & Fisher, D. (2017). Major advances in geostationary fire radiative power (FRP) retrieval over Asia and Australia stemming from use of Himarawi-8 AHI. *Remote Sensing of Environment*, *193*, 138–149. https://doi.org/10.1016/j.rse.2017.02.024

Yokelson, R. J., Susott, R., Ward, D. E., Reardon, J., & Griffith, D. W. T. (1997). Emissions from smoldering combustion of biomass measured by open-path Fourier transform infrared spectroscopy. *Journal of Geophysical Research*, *102*(D15), 18865. https://doi.org/10.1029/97JD00852

Young, P. J., Archibald, A. T., Bowman, K. W., Lamarque, J., Naik, V., Stevenson, D. S., & Tilmes, S. (2013). Pre-industrial to end 21st century projections of tropospheric ozone from the Atmospheric Chemistry and Climate Model Intercomparison Project (ACCMIP), (February), 2063–2090. https://doi.org/10.5194/acp-13-2063-2013

Ziemke, J. R., Chandra, S., Duncan, B. N., Schoeberl, M. R., Torres, O., Damon, M. R., & Bhartia, P. K. (2009). Recent biomass burning in the tropics and related changes in tropospheric ozone. *Geophysical Research Letters*, *36*(15), 1–5. https://doi.org/10.1029/2009GL039303